Geochemical And Sedimentological Investigations Of Youngest Toba Tuff Ashfall Deposits

Emma Gatti

Sidney Sussex College

A dissertation submitted for the degree of Doctor of Philosophy

University of Cambridge

— September 2012 —

DECLARATION

This dissertation is the result of my own work and includes nothing which is the outcome of work done in collaboration, except where specifically indicated in the text. I confirm that it does not exceed the word limit required by the degree committee of Geography and does not contain work that has been submitted for a degree, diploma or other qualification at any other university.

.....

Emma Gatti

Acknowledgements

I owe an enormous debt of gratitude to many people who assisted well beyond their duty during my PhD, and taught me about science, volcanoes, rivers, India, England, and, more generally, about life.

Firstly I thank my supervisor Clive Oppenheimer. His insight, critical thinking and gentle direction have made this thesis far more than it would otherwise have been. His kind assistance always made me feel prepared. This helped me to carry on and bring this work to conclusion. He also tried to teach me good English manners. That did not work out fine.

Secondly, I am very grateful for the support and teaching of my second supervisor Phil Gibbard, who has worked closely with me on the project in the past three years. His wisdom, patience and gentle manners really made working with him a pleasure. He also tried to teach me good English manners, and that did not work out either.

The generous support of the Domestic Research Scholarship and the Cambridge European Trust has provided me with a solid foundation from which to do my research. Without them this thesis would not have been possible, nor would I have had the opportunity to work in Cambridge for four years. Travel in India, Malaysia and Indonesia has been fully sponsored by the Cambridge-India Partnership Fund and the SMUTS Memorial Fund, both of the University of Cambridge. Dame Sandra Dawson is especially to be thanked for her nurturing of my project in England and in India. The William Vaughan Lewis and Philip Lake Fund from the Department of Geography have allowed me to undertake my second field work in Malaysia and Indonesia. The Dudley Stamp Memorial Award (Royal Geographical Society), the William George Fearnsides Fund (Geological Society of London) and Sidney Sussex College sponsored the laboratory analyses.

I particularly thank Hema Achyuthan (University of Chennai), a role model for all women who wish to pursue a career in science. Without her my field work in India would not have being possible. Hema introduced me to the Indian view of life, in which nothing is perfect but you have to let problems go, especially in science. She was right.

I owe especial thanks to Igor Villa (University of Milano Bicocca) for continuously encouraging me to aim higher. His insights into the world of geochemistry, mineralogy and dark chocolate have been invaluable. He has been my teacher since my undergraduate days, and I hope he feels proud of his old "*studentessa*".

This research would have not been possible without the assistance of Chiara Petrone, Jason Day, Steve Boreham, Chris Jeans and Chris Rolfe. Their knowledge and continuous support exceed their role as technicians, making them outstanding scientists in their own right. In particular, Chris Jeans' garden parties provided many of my best memories in Cambridge. His famous Christmas roast pork is an experience that should not be missed.

During my project several friends helped me generously. I owe a great debt of gratitude to Jamie Blundell, who —way beyond his mission as my boyfriend— helped me in understanding how to write a scientific paper and corrected all my written creations. I got angry with him so many times that just for putting up with my ego and supporting me through difficult times, he deserves acknowledgement. During the past two years he taught me everything I know about cycling, tennis, football, rugby, basketball, handball, mountain biking, squash, badminton, real tennis, golf, ping-pong, archery, shooting, poker, snooker, darts and the Victoria Line engineering works. We went a long way together, through good and bad, and I hope that the exciting adventures are still to come.

Alex Diment is a fine editor disguised in a Zoologist's clothing. He spent days with me, teaching me how to edit my own work. I am profoundly grateful to have met him on my journey. If this thesis meets the requirements for a PhD, it is also thanks to him. Besides, since work is not everything, he provided me with accommodation for the last five months, he celebrated with me when there was no one else

around, and he took me to eat zebra steak for the first time in my life. He made my last months in Cambridge memorable.

Simon Wongsuwarn is the best of house mates. He put up with me when I was down, and gave me beer when I needed it. He sat next to me when I was lonely, and kept me company in the hardest moments, when the rain seemed as if it would never stop (June 2012) and the future bright as a November day (July 2012). Because I know that friends are rare, and no success is the result of a single effort, I consider him an integral part of my accomplishments.

Eszter Kovac is an incredible woman who shared with me two crazy holidays in Italy, one year of absolutely failed rowing experiences, tears and laughter. She is hilarious and deep at the same time, and I loved to have her around. She also helped me during the proof-reading process, and wrote with me several applications in the middle of the night, tolerating without complaint my complete absence of organization. She has heard me complaining about everything so many times that I am surprised she still hangs out with me.

I spent the last three years living with a group of amazing people from every part of the world. I won't forget 19 Saxon Road and our nights in front of the TV watching The Wire ("Those are for you McNutty!") and The Apprentice ("Stuart the brand, you are fired!"), our Sunday breakfasts at Hot Numbers, and our joint effort to try to avoid the Council Tax. For this I thank the 19 Saxon Road Crew: Jamie Blundell, Simon Wongsuwarn, Dino Ott, Sabrina Jahn and Alex Silver. In particular, Alex gave us a free TV and paid for the TV licence throughout 2011, although he had been living in Japan since 2010. So, thank you Alex. We made the most of it.

I also thank my fieldwork companions: Naomi Matthews, Adam Durant, Christina Neudorf, Clair Harris, Ceri Ben Shipton, Kathryne Price, Kate Connell, Jinu Koshy, Janaradhana B., Racha Raj and Alpa Sridhar. It was —to all extent— a mind-blowing experience. I would leave again right now if I had the chance.

I am particularly grateful to Sacha Jones, the writer of an impressive 700 page thesis on the Toba super-eruption. It seems that everything I did, she had done before me. Her help, suggestions and hints about living in India were life saving.

I thank all my special editors and proof-readers who assisted me in polishing the language of my thesis: Amy Donovan, Tehnuka Ilanko, Kayla Iacovino, Amy Prendergast, Helena van der Merwe, Eszter Kovac, Alex Diment, Marie Edmonds and Derek Birch.

Life in the Department of Geography would have not been the same without my PhD companions: Maria Angelica Godoi, Paul van der Vegt, Sebastian Gibson, Karolina Lesczcynska, Tobias Gerken, Lex Hoffmann (also invaluable San Francisco hotel companion), Priti Nigam, Andre Silveira and Isayvani Naicker. I owe you all interesting dinners involving rum on fire, Risk games in which one becomes as tense as a violin string, and general day-to-day amusements in Downing College Hall. Without you, my life would have been a simple sequence of days in and out of the office.

During the last few months, the only social activity that kept me sane was kick-boxing. For this I thank the company of Einat Elmalem who shared with me the mind-numbing experience of boxercise first, and kick boxing after. We met late, but I hope our friendship will last.

Finally, I must thank my mum and dad. Everything I am, think and feel comes ultimately from them. I hope I have made them proud.

‘Happy families are all alike; each unhappy family is unhappy in its own way’

Leo Tolstoy

‘Primary ash are all alike; each reworked ash is reworked in its own way’

A Geologist version

Summary

The ~ 73 ka 'super-eruption' of the Toba caldera in Sumatra is the largest known eruption of the Quaternary. The products of this eruption, the Youngest Toba Tuff (YTT), have been implicated in global and regional climate deterioration with widespread ecological effects.

In this thesis I study the YTT co-ignimbrite ashfall, in particular the mechanisms of transport, sedimentation and preservation of ash deposits. I use distal marine and terrestrial ash sediments: a) to estimate the volume of YTT ash fallout; b) to quantify variability in the geochemistry of YTT ash; c) to assess the reliability of YTT ash as a chronostratigraphic marker; and d) to determine local influences on the reworking of YTT ash deposits.

Following the introductory chapters, I address topics a) and b) through detailed investigations of published physical and chemical evidence. Chapter three shows that particle size and sediment thickness do not decline exponentially with distance from the eruption vent, highlighting the limitations of current methods of volume estimation for co-ignimbrite super-eruptions. Chapter four analyses geochemical variation in 72 YTT samples, and reveals the signatures of magma chamber zonation and post-depositional alteration.

I address topics c) and d) through fieldwork in six locations, and detailed analysis of ash samples from a wide variety of local depositional environments. Chapter five uses high-resolution stratigraphic analysis of the YTT layer in the Son Valley, India, to show that variable deposition and sediment reworking may compromise the reliability of the ash layer as an isochronous marker for interpreting archaeological sequences. Chapter six combines a new understanding of the mechanisms of reworking, using new data on microscopic characteristics of reworked ash at four sites in Malaysia to demonstrate the necessity of accounting for reworking in palaeoenvironmental reconstructions.

I conclude that accurate analyses of distal ash deposits can reliably determine the chemical properties of the YTT eruption, and that a detailed understanding of deposition and reworking processes is essential to inference of the environmental impacts of super-eruptions.

Table Of Contents

Table of Figures

Table of Tables

Chapter 1. Introduction

Super-eruptions are rare and extreme volcanic events that have not been experienced in recorded human history. As a working definition, eruptions producing 1000 km^3 or more (bulk volume) of magma may loosely be considered 'super-eruptions' (Figure 1-1). One of the most recent is the Youngest Toba Tuff (YTT) eruption, which occurred at what is now Lake Toba, in Sumatra, Indonesia. The lake resulted from the collapse of the Toba caldera after several very large explosive eruptions, culminating in the YTT eruption ~ 73 ka ago. In addition to voluminous ignimbrites, the YTT eruption produced a tephra fall deposit estimated at ~ 800 km^3 Dense Rock Equivalent (DRE) consisting of fine volcanic ash (equivalent to a solid cube of rock measuring 9 km in each dimension). The ash is found to have a thickness of 1 cm as far as 4000 km from the vent. To put this into context, the 2010 eruption of Eyjafjallajökull, which caused the largest disruption in European civil aviation since World War II, deposited no more than 8 mm of ash at a maximum 60 km from the volcano (Bonadonna et al., 2011).

YTT ash deposits have been discovered in over 100 terrestrial and marine sites in southern Asia, covering an area of at least 1.3×10^7 km^2, equivalent to the combined areas of the United States and Canada. The thickness of the YTT deposits ranges from 0.1 mm in deep ocean sediments to 7 m in river valleys. These variations reflect various factors operating on what might be considered the primary ash fallout (i.e., reworking by various agents). The exceptional amount of ash erupted and the distance the ash reached suggest that the YTT is possibly the largest volcanic eruption of the last 2 million years.

This thesis considers several YTT ash sites in a variety of environmental contexts, and focuses on the interactions between ash and the receiving environment. In particular, it examines the mechanisms of transport, aggradation and preservation of the metres-thick tephra sequences in terrestrial sites. The dynamics of sedimentation of distal tephra are important to a wide range of fields including Quaternary studies, Volcanology, Geochronology and Archaeology. The applications of tephrostratigraphy span from single grain micron-scale analyses to kilometre-scale stratigraphic correlations: geochemical and isotopic investigations on single ash grains can

determine the age and provenance of the ash, and this in turn can be used to link geological sequences thousands of kilometres apart. Recently, tephrostratigraphy has been applied to palaeoenvironmental studies, which use the tephra as a chronostratigraphic marker to enable identification of abrupt environmental changes (possibly associated with ash deposition itself), and dating in archaeological reconstructions.

This chapter introduces the YTT eruption (**1.1**), the rationale and goals of the thesis (**1.2**), and concludes with a synopsis of the rest of the thesis (**1.3**).

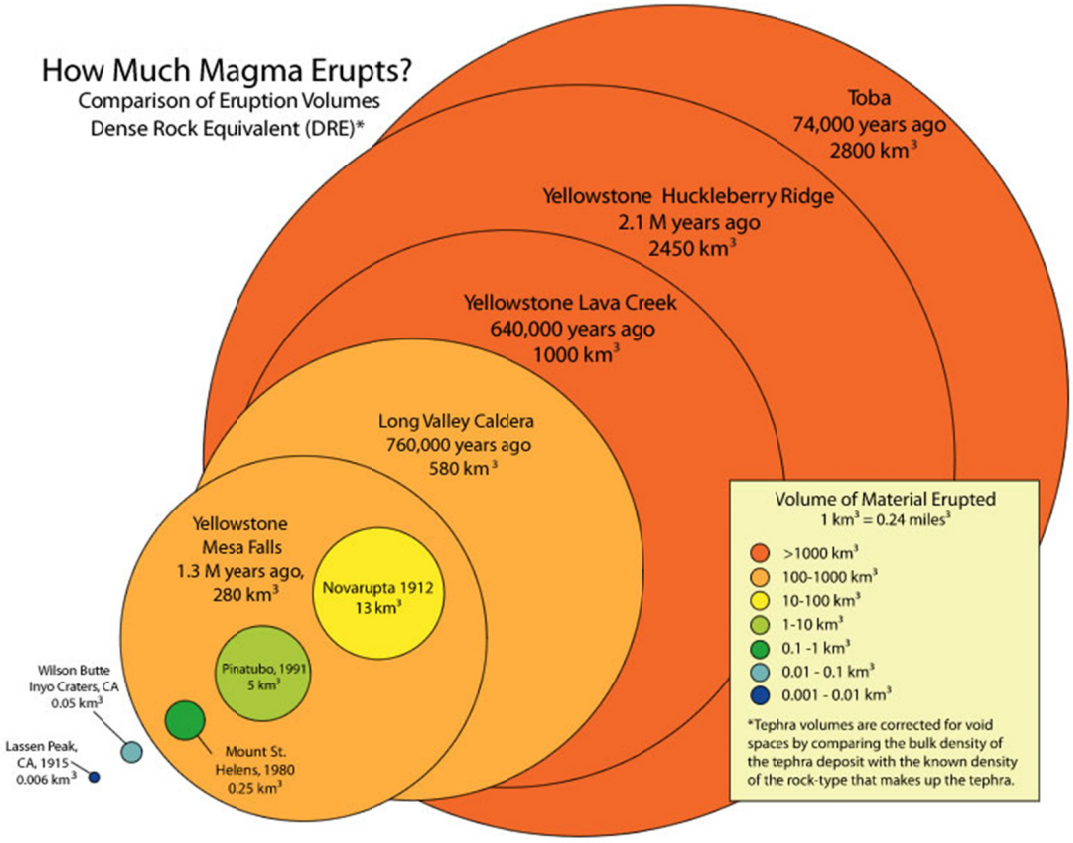

Figure 1-1 Comparison of eruption sizes based on the volume of magma. Toba is considered the largest eruption to have occurred in the past 2 million years, with 2800 km^3 of material erupted, of which 800 km^3 is fine ash. This is more than the entire volume of Mount Everest (2300 km^3) Picture courtesy of the USGS volcano Hazard Program.

1.1 The ~ 73 ka Toba super-eruption

The Toba caldera, in north Sumatra, Indonesia, is the largest resurgent Quaternary caldera on Earth (Figure 1-2). It measures 100 km x 30 km, and it is partially occupied by the Toba lake, the largest volcanic lake on the planet (Rose and Chesner, 1990). The caldera consists of Permo-Carboniferous metamorphic rocks, Miocene sedimentary rocks, and Quaternary volcanics (Aldiss and Ghazali, 1984). Toba is part of the active volcanic arc that follows the NW trend of Sumatra (Page, 1979), generated by the subduction of the Indian-Australian plate beneath continental Eurasian (McCarthy and Elders, 1997; Masturyono et al., 2001). The plate is characterised by a 2 km ridge (the Investigator Ridge Fracture Zone) that subducts directly beneath Toba (Nishimura, 1981). Its location probably coincides with a bend in the subducting ridge, which might accentuate volatile release beneath the volcano (Fauzi et al., 1996).

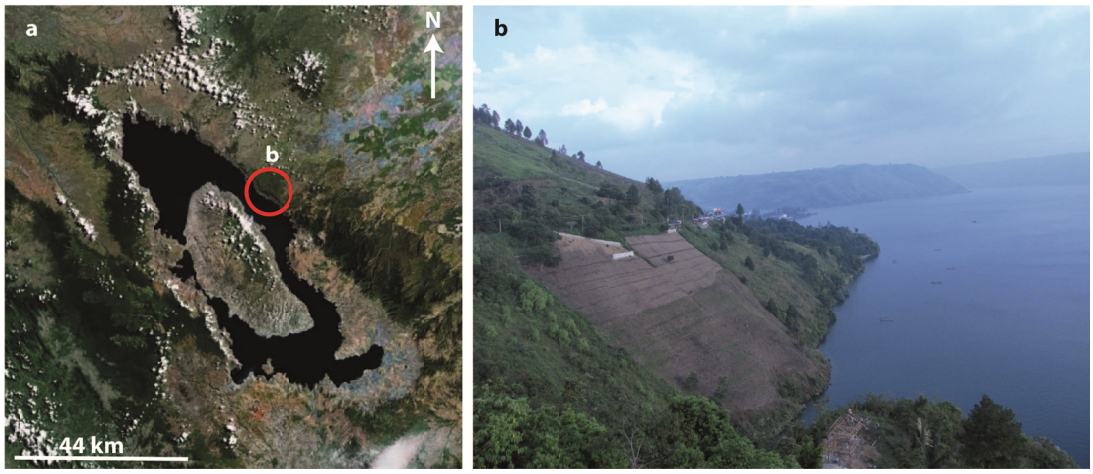

Figure 1-2 a) The Toba caldera in Sumatra from Google Earth; b) View of the western side of Toba caldera and the Toba lake from Prapat.

The caldera complex consists of four overlapping calderas (Nishimura et al., 1984; Chesner and Rose, 1991), each of which is associated with an ignimbrite eruption (Chesner and Rose, 1991; Chesner et al., 1991). The Haranggaol Dacite Tuff (HDT) is the oldest ignimbrite recognised around Lake Toba. This is a densely welded tuff exposed in the northern caldera walls, up to 100 m thick near Haranggaol (Figure 1-3). Chesner and Rose (1991) estimated that the HDT erupted a dense-rock equivalent (DRE) volume of ~ 35 km^3 of material (Table 1-1). The only published date for the HDT eruption is a fission track age of 1.2 Ma by Nishimura et al. (1977), as summarized in Table 1-1.

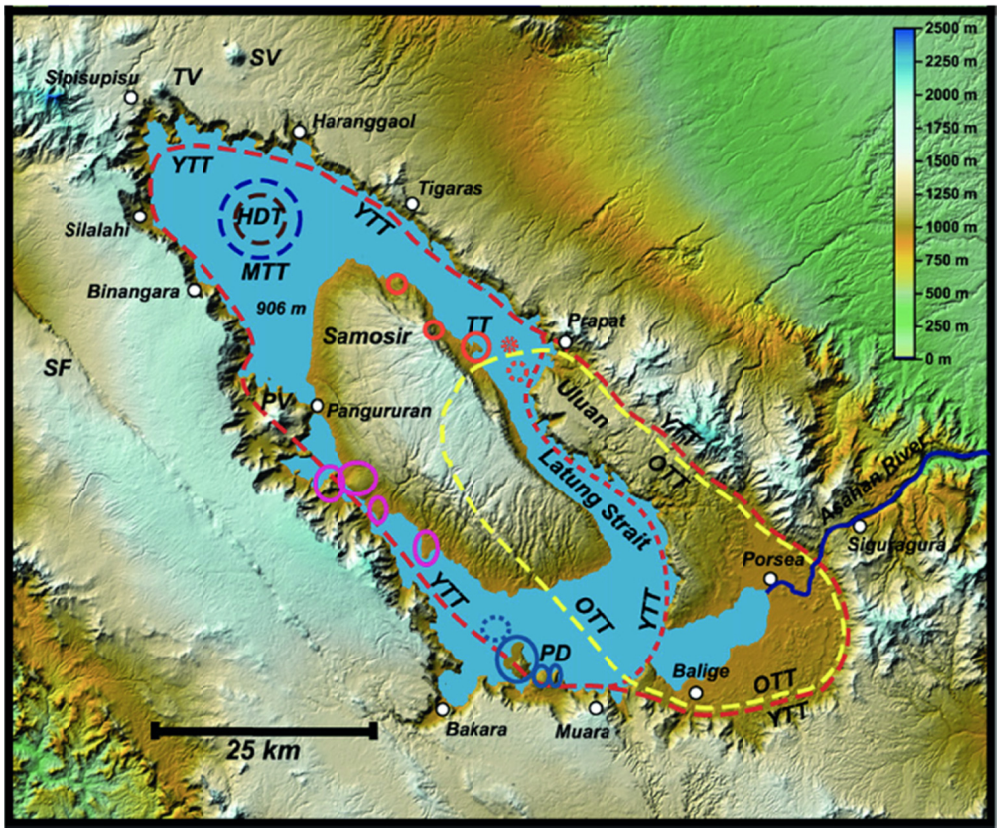

Figure 1-3 Toba caldera complex location (from Chesner, 2012). The inner YTT collapse fault is shown with short red dashes. The Samosir lava domes are outlined by orange circles.

The Oldest Toba Tuff (OTT) is exposed along the western scarp of the Uluan peninsula, and in the walls of the southern and eastern portions of the caldera (Figure 1-3, Chesner, 2012). The only places in which it has been identified outside the present caldera are in the deeply incised Asahan River canyons and in a fault block north of the lake (Chesner, 2012). Chesner (1998) described the OTT as a densely welded rhyolite tuff (69–74 wt. % SiO_2) distinguished from Youngest Toba Tuffs by its reverse polarity (Table 1-1). The OTT has been dated by $^{40}Ar/^{39}Ar$ at 840 ka (Diehl et al., 1987, Table 1-1). Knight et al. (1986) estimated an initial DRE volume of ~ 500 km^3. Yet OTT ash deposits have recently been identified in deep-sea cores in the Indian Ocean and south China Sea (Dehn, 1991; Pattan et al., 1999; Lee et al., 2004), increasing the estimated DRE volume to ~ 2300 km^3.

The third, or Middle Toba Tuff (MTT), is limited to the northern walls of the caldera, overlying the HDT (Figure 1-3). Chesner and Rose (1991) estimated that this eruption ejected a minimum of ~ 60 km^3 DRE of ignimbrite. Sanidine dated by $^{40}Ar/^{39}Ar$ provided an age of 501 ka (Chesner et

al., 1991, Table 1-1). The MTT has the same mineralogy as that of the other Toba tuffs, but it can be distinguished from them by its whole rock and mineral chemistry as well as its strontium isotopic composition (Chesner, 2012). Dehn et al. (1991) identified MTT ash in deep-sea cores from the Indian Ocean, but Chesner (2012) argues against dispersal of the MTT beyond Sumatra.

Table 1-1 Characteristics and ages of the four eruptions of the Toba Caldera Complex.

Unit	Thickness (m)	Volume (km^3)	Age	Method	References
Youngest Toba Tuff (YTT)	< 400	2800	73.88 ± 0.32 ka	$^{40}Ar/^{39}Ar$	Storey et al. (2012)
			74 ka	Average	Oppenheimer (2002)
			73 ± 4 ka	$^{40}Ar/^{39}Ar$	Chesner et al. 1991
			75 ka	Oxygen isotope stratigraphy	Ninkovich et al. (1979)
			74.9 ± 12 ka; 73.5 ± 3 ka	K/Ar	Ninkovich et al. (1978a)
Middle Toba Tuff (MTT)	> 140	60	0.50 Ma	$^{40}Ar/^{39}Ar$	Chesner et al. (1991)
Oldest Toba Tuff (OTT)	> 300	500	0.84 Ma	$^{40}Ar/^{39}Ar$	Diehl et al. (1987)
Haranggaol Dacite Tuff (HDT)	< 200	35	1.2 Ma	Fission track	Nishimura et al. (1977)

The Youngest Toba Tuff (YTT) is the youngest of the three major rhyolitic tuffs of Quaternary age associated with the Toba caldera (Chesner et al., 1991, Table 1-1). The eruption is partially responsible for the collapsed structure visible today (Figure 1-3); a resurgent dome formed within the caldera, consisting of two half-domes separated by a longitudinal structure called the Prapat graben (Bellier and Sebrier, 1994). Today the collapsed caldera includes all the previous calderas. The steep slopes of the caldera walls suggest the caldera collapsed along a ring fracture structure (Figure 1-2). From crude stratigraphical evidence the total magma volume of the YTT has been estimated as ~ 2800 km^3 DRE, of which the ashfall accounts for ~ 800 km^3 DRE (Rose and Chesner, 1987; Chesner and Rose, 1991; Gardner et al., 2002). Proximal plinian pumice fall deposits of the YTT have not been found. This led Rose and Chesner (1987) to conclude that the YTT fallout is entirely of co-ignimbrite origin. Such eruptions develop a buoyant cloud from pyroclastic density currents, rather than from the vent (Figure 1-4). In cases where the density of

the particle-gas mixture is too high for a given initial vertical momentum, the material rising from the eruptive column cannot become buoyant, and forms a collapsing fountain (Sparks et al., 1986). These formations generate dense pyroclastic flows that travel on the ground surface (Sparks and Wilson, 1976). The flows segregate into a dense lower part and an upper dilute part (Sparks and Huang, 1980). As fine ash and gas escape from the dense lower flow into the upper part, the latter is progressively enriched in ash and gases, and becomes buoyant because of the expansion of the gas (Textor et al., 2003). This generates the co-ignimbrite cloud, a buoyant cloud rising above the pyroclastic flows and carrying large quantities of ash and magmatic gases (Sigurdsson and Carey, 1989; Woods and Wohletz, 1991). Since fine-grained and low-density particles are more likely to enter the buoyant plume, the resulting remaining pyroclastic deposits are depleted in those types of particle (Andrews and Manga, 2012).

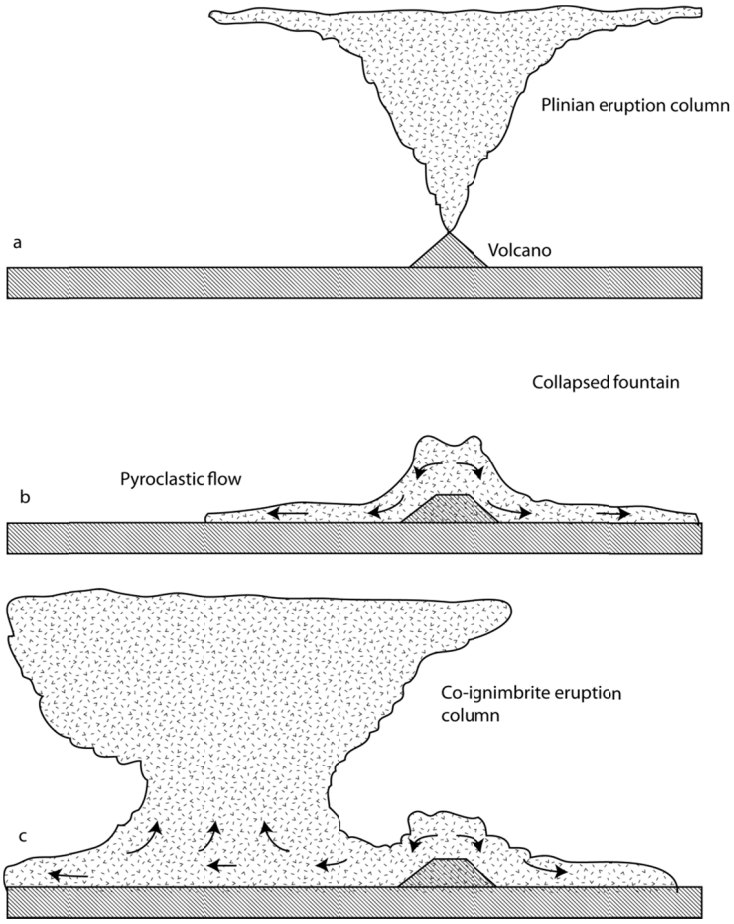

Figure 1-4 Schematic representation of a) plinian eruptive column, b) fountain generating lateral pyroclastic flows after the collapse of the plinian column, c) development of the co-ignimbrite cloud formed as the buoyant mixture of fine ash rises off the pyroclastic flow (modified from Woods and Wohletz, 1991).

Figure 1-5 Thick YTT semi-welded pyroclastic density current deposits on the eastern scarp of Samosir Island.

The tuffs deposited by this colossal eruption are known as the YTT, and consist of thick intracaldera tuffs, an extensive outflow sheet, and distal ash. Intracaldera tuffs are less than 100 m thick, and are exposed between Prapat and Porsea (Figure 1-5, Chesner, 1998). By contrast, the outflow sheet exceeds 100 m in thickness and covers between ~ 20,000 km^2 to ~ 30,000 km^2 of northern Sumatra (Aldiss and Ghazali, 1984). Rose and Chesner (1987) crudely estimated volumes of 1000 km^3 (DRE) caldera fill and 1000 km^3 (DRE) of outflow sheets.

The distal ash has been reported to cover an area of at least 1.3×10^7 km^2 in southern and southeaster Asia (Figure 1-6). YTT ash deposits have been identified at terrestrial locations in India (Korisettar et al., 1988; Acharyya and Basu, 1993; Kale et al., 1993; Mishra et al., 1995; Shane et al., 1995; Karmalkar et al., 1998; Westgate et al., 1998), Malaysia (Ninkovich et al., 1978b; Rose and Chesner, 1990; Chesner et al., 1991; Shane et al., 1995) and possibly in Bangladesh (Acharyya an Basu, 1993). Equivalent material has been recognised in sea-floor sediments in the Indian Ocean, the Bengal Fan, the South China Sea and the Arabian Sea (Ninkovich, 1979; Pattan et al.,

1999; Buhring et al., 2000; Gasparotto et al., 2000; Huang et al., 2001; Liang et al., 2001; Schulz et al., 2002; Liu et al., 2006).

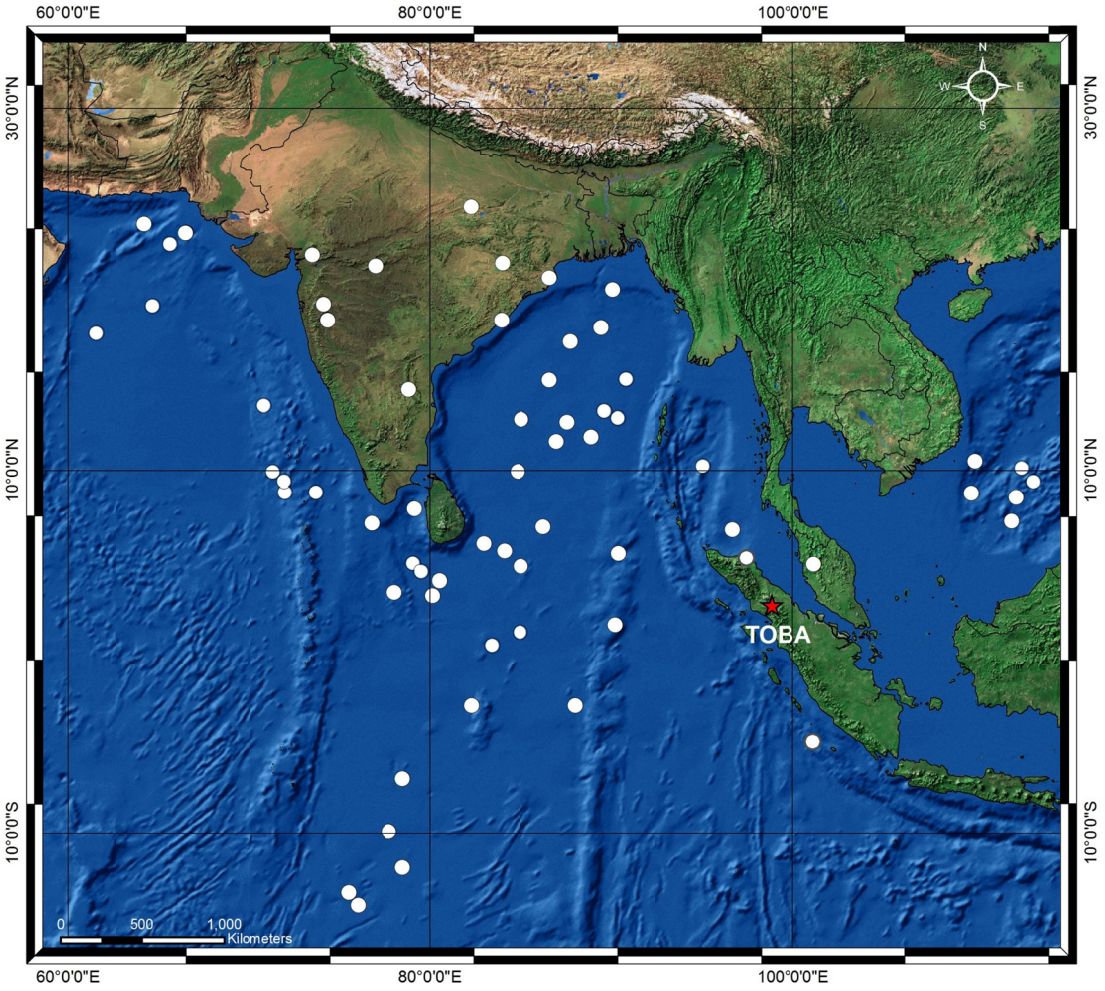

Figure 1-6 The distribution of the YTT. Each point represents a marine core or terrestrial site where YTT has been identified.

The distance reached by the ash (more than 4000 km from the caldera) is another of the remarkable characteristics of the YTT eruption. Baines and Sparks (2005) suggested that co-ignimbrite clouds generated from super-eruptions (M > 6.5) could cover continent-sized areas. They argued that the large source area (i.e., the area covered by pyroclastic flows) would produce a higher magma flux, which in turn governs the cloud development and entrainment height (the height at which the cloud starts expanding horizontally). They therefore suggested that the larger the eruption, the higher the column (this principle is based on a model by Woods, 1988). If the magnitude of the eruption is large enough to produce a large source area and an elevated

magmatic flux, then the model by Baines and Sparks (2005) shows that the eruption can generate giant clouds with diameters of a few thousands km, whose neutral buoyancy height can reach the stratosphere.

Because of the extreme diameter these giant clouds' radial expansion speeds are greater than typical stratospheric wind speeds and thus they are initially insensitive to winds. This allows the clouds to expand in all directions, developing diameters greater than 600 km (Baines and Sparks, 2005). The spin velocity increases with the size: thus the expansion of the giant clouds becomes controlled by a balance between gravity and Earth's rotational forces. The Coriolis forces transform the giant clouds into spinning bodies of nearly fixed proportions. The constraints of the Earth's rotation transforms the ash clouds into compact, rigid-body-like structures, and this helps to maintain the clouds' integrity, so that they can carry on spinning for some time, before they become unstable owing to baroclinic disturbances and break up into eddies.

Recently, Herzog and Graf (2010) questioned the assumption that the size of the source, magma flux and the neutral buoyancy height are effectively correlated. They suggested that co-ignimbrite clouds are inefficient in terms of vertical transport, because they are produced by multiple updrafts developing from the pyroclastic flow, all characterised by the same energy. They argued that the energy of each single updraft is not enough to produce a sustained umbrella cloud in the stratosphere for the time necessary to produce the spinning cloud suggested by Baines and Sparks (2005).

Ninkovich et al. (1978a) provided the first age estimation for the YTT deposit. They obtained a K-Ar age of 73.5 ± 3 ka on sanidine from sample 72-0-60 from Prapat (Malaysia). The same method on biotite from sample Id680 from Si Gura Gura (Sumatra) provided an age of 74.9 ± 12 ka (Table 1-1). Chesner et al. (1991) obtained a mean age of 73 ± 4 ka for a welded tuff from Samosir Island and for an ash sample from Malaysia. Both these samples were dated using laser-fusion $^{40}Ar/^{39}Ar$ on individual sanidine phenocrysts. Later, Zielinski et al. (1996a) suggested an age of 71±5 ka based on a peak in volcanic sulphur in an ice-core from Greenland. More recently, Oppenheimer (2002) proposed a mean age of ~ 73 ka, while Williams et al. (2009) suggested an average age of 73 ± 2 ka. Storey et al. (2012) recently dated sanidine collected from YTT in the Lenggong valley (Malaysia) with $^{40}Ar/^{39}Ar$ and obtained an age of 73.88 ± 0.32 ka (Table 1-1). Earlier literature

refers to the YTT as dating 74 ka (Williams and Clarke, 1995; Oppenheimer, 2002) or 71 ka (Zielinski et al., 1996a; Zielinski et al., 1996b; Zielinski, 2000).

The YTT eruption has been calculated to have lasted 7-14 days (Table 1-2), on a grain-size deposition model (Ninkovich et al., 1978b; Ledbetter and Sparks, 1979). The plume column has been estimated to have been 31 ± 5 km high, on the basis of a linear relationship between the height of the umbrella cloud and the magnitude of the eruption (Chesner and Rose, 1991; Woods and Wohletz, 1991). These calculations are highly model-dependent and the estimations are heavily influenced by assumption. Herzog and Graf (2010) recently modelled the spread of a co-ignimbrite plume in three dimensions, and suggested that the maximum overshooting of such an eruption does not depend linearly on the magnitude. They recalculated the initial parameters and suggested that in cases of large co-ignimbrite eruption (radius > 70 km) the maximum overshoot height is expected to reach around 20 km.

Rampino and Self (1992; 1993) used the assessed duration and maximum column height to obtain the H_2SO_4- burden emitted by the volcano, essential to determining the climatic effect of the eruption. By studying compositions of YTT pumices and welded tuffs, they were able to suggest 1×10^{15} g of sulphate aerosols were released from the erupted magma, together with 2×10^{16} g of fine dust. Another study estimated the dissolved amount of sulphate from the composition of pyrrhotite inclusions in magnetite, and suggested that the eruption ejected a minimum of ~ 3.5×10^{15} g of H_2S (Rose and Chesner, 1990) and 1×10^{16} g of sulphur aerosol into the stratosphere (Chesner et al., 1991). However, Scaillet et al. (1998) questioned this estimate which was based upon the low solubility and diffusivity of sulphur in low temperature silicic melts. A recent study on the YTT melt inclusions by Chesner and Luhr (2010) determined a sulphur content of just 6–32 ppm by using microprobe analyses of the YTT melt inclusions. They estimated a syn-eruptive production of H_2SO_4 of 10^{14} g, two orders of magnitude less than the earlier calculation, although this estimate neglects the possibility of a separate gas/fluid phase before the eruption. It is fair to say that we have no reliable estimate of the sulphur yield of the YTT eruption. Table 1-2 summarise the extrapolated eruptive parameters.

Table 1-2 Modelled and estimated YTT volcanic parameters (modified from Woods ad Wohletz, 1991). Column height by a) Herzog and Graf (2010) and b) Woods and Wohletz, (1991); total volume and duration of the eruption by Chesner and Rose (1991); mass of sulphur from Chesner and Luhr, (2010) and Rose and Chesner, (1990).

Total volume erupted (km^3 DRE)	Volume of ash elutriated (km^3 DRE)	Duration of co-ignimbrite column	Mass eruption rate from vent (10^9 kg s^{-1})	Column height (km)	Mass of sulphur aerosol (g)
2840	840	7-14 days	7.1	20[a] to 30[b]	10^{14} or 10^{15}

The YTT magma was sourced from a compositionally zoned magma chamber (Chesner, 1998). The compositional zoning results from the crystal fractionation occurring in the YTT source magma chamber during ~ 150 ka cycles (Bachmann and Bergantz, 2008). The result is a magma that is more evolved near the chamber roof and less evolved at deeper levels. A model described by de Silva et al. (2006) suggested that eventually water saturation and roof-magma density contrasts lead to the caldera collapse and consequent ignimbrite eruption.

1.2 Recent Toba activity

The ~ 73 ka Toba eruption left a 2 km deep, steep-walled caldera, with a flat floor covered by a thick accumulation of welded YTT. Immediately following the eruption, Lake Toba began to fill with water (Chesner et al., 1996). The most evident post-eruption feature is Samosir Island, a resurgent dome that was lifted at least 1100 m to its present position (Figure 1-2a). It is unclear when resurgence began and ended, but a ^{14}C date of 33,090 ± 570 (Chesner et al., 2000) on organic-rich lake sediments collected near the highest elevations on Samosir indicated that about 33 ka ago Samosir Island was still beneath lake level. Samosir Island is covered by the sediments of the Samosir Formation, which were deposited on the sub-lacustrine caldera floor after the filling of the Toba Lake. The formation comprises fining-upwards sequences of debris flow, volcanic breccias, and conglomerates, overlain by laminated tuffaceous sand and silt, diatomaceous clay and volcanic ash (Figure 1-7, Marel, 1947; Van Bemmelen, 1970).

Since the YTT eruption, volcanic activity has continued at Toba. The northern area of Samosir Island (Pintubatu) includes active hot springs and fumaroles, and the area along the lake shore beneath Parapat and Samosir is intensely hydrothermally altered. Several overlapping lava domes

have been identified on northeaster Samosir Island and near Tuk-Tuk (Figure 1-3). Two small andesitic centres, the Tandukbenua and Singgalang volcanoes, are located outside the northern side of the main caldera. Both cones rise ~ 500 m above the YTT outflow sheet and appear to have formed since the YTT eruption. An intracaldera volcano, the Pusikbukit volcano, developed after the eruption and now rises over 1000 m above lake level (Chesner, 2012). Pusikbukit has not erupted in historical times, but an active solfatara is present on its northeaster flank (Chesner et al., 1996).

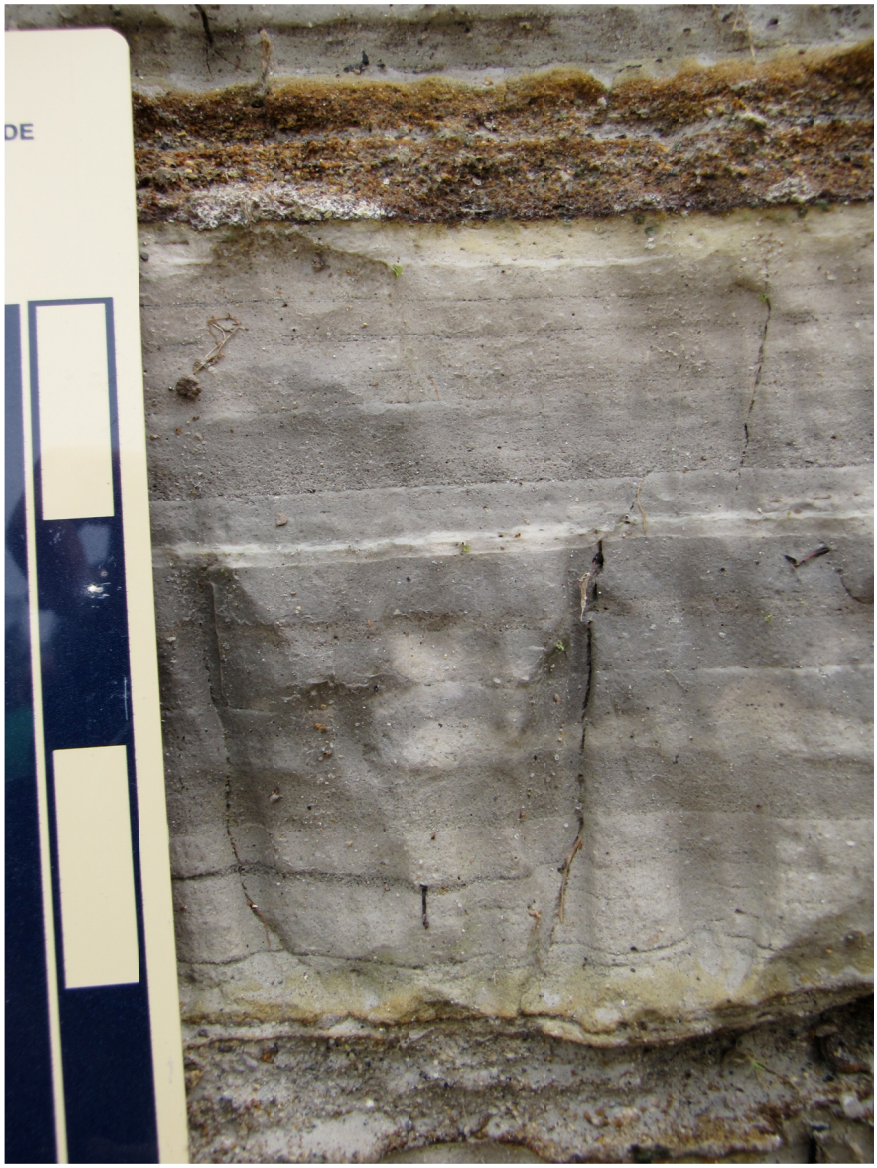

Figure 1-7 Laminated tuffaceous sand and silt, diatomaceous clay and volcanic ash from the Samosir Formation identified on the northern part of Samosir Island. The Samosir Formation is a post-YTT volcaniclastic deposits emerged from water when Samosir became resurgent, *ca*. 30 ka. Scale divisions: 2 cm.

1.3 The potential impact of the ~ 73 ka Toba super-eruption

Ever since the discovery of tephra beyond the Indian Ocean (Ninkovich, 1979), there has been speculation concerning the possible effects of the YTT eruptive event. The discussion has touched upon climate, environmental and palaeoanthropological aspects. Here each of these is addressed in turn.

1.3.1 Climatic impact

It has been suggested that the YTT eruption was responsible for an extended cooling period and consequent icesheet advance at the beginning of the last ice age (Rampino and Self, 1992; Rampino and Self, 1993; Ambrose, 1998). Since volcanic sulphur aerosols are known to be the principal cause of volcanic-generated climatic perturbations, several studies have attempted to estimate the amount of sulphur emitted during the YTT event **(§ 1.1**).

The postulated exceptional mass of sulphur released has prompted several hypotheses concerning the effect of the super-eruption on climatic deterioration. Rampino and Self (1982; 1992; 1993) proposed that the YTT led to a 'volcanic winter': a surface cooling of up to 5 °C caused by increased atmospheric opacity, similar to post-nuclear war scenarios. This global cooling effect, they argued, would have lasted for several years, generating up to 12 °C of cooling. A negative feedback would consequentially have developed, precipitating the Earth into a millennium of cold climate (Rampino and Self, 1993).

A key paper by Zielinski et al. (1996a) argued against the 'volcanic winter' hypothesis, emphasising that the eruption and the millennium of cooling that occurred afterwards are unrelated. They reported a volcanic sulphate peak at about 71,100 ± 5000 year in the Greenland ice-core GISP2 (Yang et al., 1996; Zielinski et al., 1996a; Zielinski et al., 1996b), and equated it to the YTT event (Figure 1-8). Yet they showed that the ~ 1000 years of cooling between the interstadial 20 (IS20, ~ 74.5 ka) and interstadial 19 (IS19, ~ 69 ka) that Rampino and Self (1992) identified as a post-YTT cooling effect, was already underway before the eruption occurred (cf. Jouzel et al., 1987; Bond et al., 1993, Leuschner and Sirocko, 2000). This demonstrated that the YTT occurred too late to have initiated a major millennial-scale glacial period. Furthermore, it suggested that, despite the record's indicating an increased amount of SO_2^{-4}, the sulphur emission

was insufficient to trigger significant climatic change. Nevertheless, they noticed that the climate system between IS20 and IS19 was in 'shifting mode' (i.e. highly sensitive to perturbations), and this instability could have amplified the effects of the Toba aerosols. They concluded that the magnitude and long residence time of aerosols resulted in a complex environmental feedback, which might have been responsible for a 200 years period of enhanced cooling at the beginning of the 71 ka stadial event. Yet, Oppenheimer (2002) argued that the apparent perturbations in the ice-core chemistry could reflect post-deposition reactions occurring in the highly acidic YTT horizon, and pointed out that no other ice core has yet been reported a similar peak at ~ 70 ka. However, a recent work of Svensson et al. (2012) linked the Greenland (NGRIP) and Antarctic (EDML) ice cores at the Toba eruption, using matching patterns of bipolar volcanic spikes. Nine volcanic spikes identified in both cores allowed a unique match, confirming with decadal precision that the Toba event occurred between the onsets of Greenland Interstadials (GI) 19 and 20 and the Antarctic counterpart Antarctic Isotope Maxima (AIM) 19 and 20 (Figure 1-8).

A recent study simulated a 100-times-Pinatubo sulphur emission scenario (a putative YTT eruption) to investigate its possible impact on the regional climate (Timmreck et al., 2010; Timmreck et al., 2012). They found that even under interglacial conditions (capable of amplifying the eruption impact), the effects of the YTT on climate were reduced to minor changes, such as two years of reduced precipitation, anomalously strong fluvial discharges and a few decades of possible vegetation changes in which trees were replaced by grasses. They concluded that the climate changes arising from the YTT eruption were insufficient in terms of temporal scale to have drastic, lasting consequences for the biota, including humans (Timmreck et al., 2012).

There is no general consensus on the climatic impact of the YTT ashfall. The initial hypotheses are strongly challenged by the evidence of more limited sulphur emissions and the lack of clear evidence of long-term global climatic shock (cf. Kilian et al., 2006). More recent studies emphasise the role of the YTT eruption in environmental change on the local to regional rather than global scale.

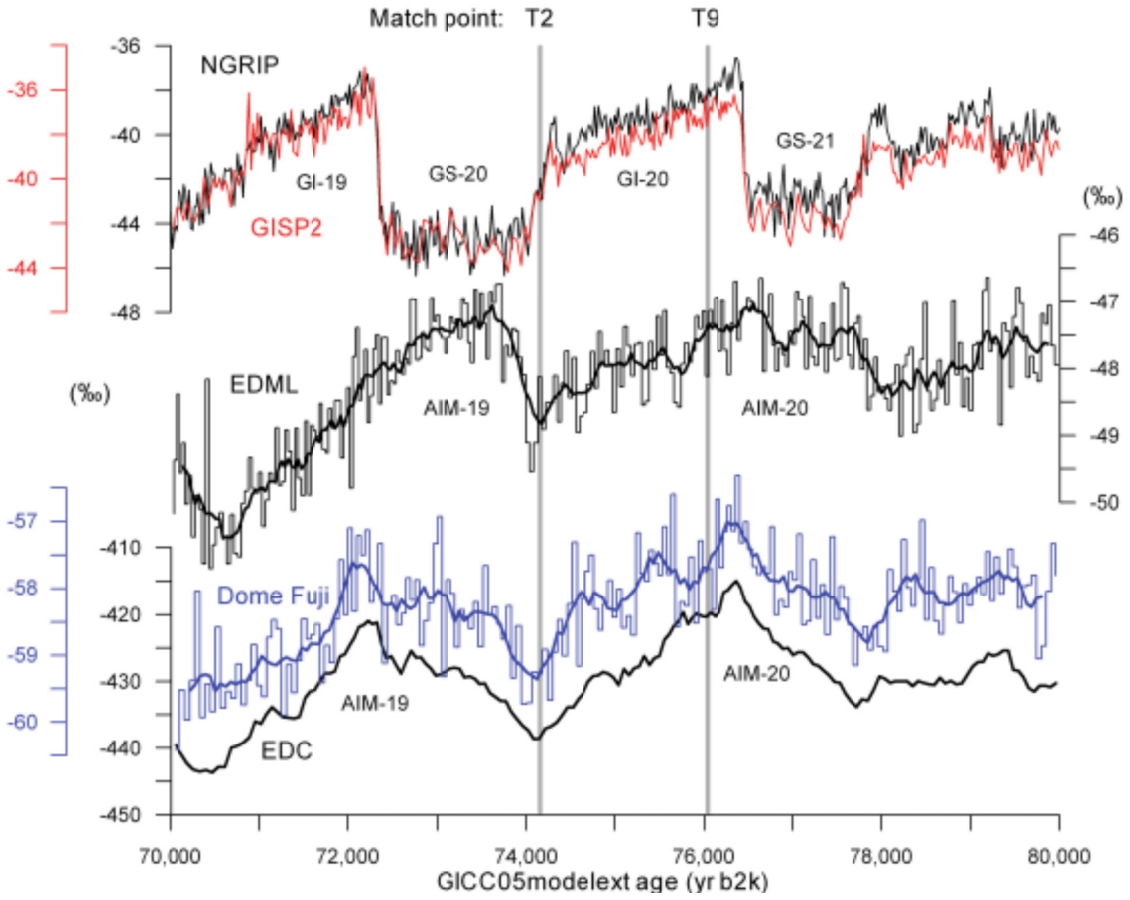

Figure 1-8 Synchronization of the NGRIP (North Greenland Ice Core Projects), GISP2 (Greenland Ice Core Projects 2), EDML (EPICA Dronning Maud Land), EDC (EPICA dome C) and Dome Fuji 1 isotopic profiles around Greenland Interstadial 20 (GI 20) and the Antarctic Isotope Maxima (AIM) 19 and 20, based on the Toba volcanic match. All records show $\delta^{18}O$ except EDC that is δD. Nine volcanic spikes have been used as match points to synchronize the records (T1-T9). Match points T1 to T4, whose ages fall in the interval 74.1-74.5, are the best candidates to represent the Toba event. T2 is considered the most probable due to an abrupt shift in the d-excess close to the marker (from Svensson et al., 2012).

1.3.2 Environmental impact

Following the argument of Rampino and Self (1992), several studies hypothesised the environmental impact that such a climatic shift could have induced in the ecosystems of southern Asia.

Models. Robock et al. (2009) simulated the environmental impact of a 100-times-Pinatubo model scenario by applying a two-dimensional climatic model and found that the vegetation distribution in South Asia changed dramatically as a result of the reduction of sunlight induced by the large aerosol cloud.

Terrestrial proxies. Williams et al. (2009) analysed terrestrial pollen from sediments from the northern Bay of Bengal. They found a distinct change in Indian vegetation from tree and shrub before, to more open vegetation immediately following the eruption. Van der Kaars et al. (2012) studied pollen collected from the marine core BAR94-25, in the northwest of Sumatra, and suggested that the YTT instantaneously destroyed the local pine forests on Sumatra. Ambrose (2003) and Williams et al. (2009) investigated stable carbon isotopes in carbonate nodules from above and beneath the ash in the Son Valley**,** India. The results suggested an increase in C_4 and decrease in C_3 plants immediately following the YTT, corroborating the conclusion that the YTT caused a shift in local vegetation from trees to open grassland. Haslam et al. (2010) measured stable carbon isotopes from south central India, and found the same dramatic climatic shift to drier/cooler conditions after the eruption. These authors suggested that such an environmental shift lasted at least several centuries (Haslam et al., 2010; Haslam et al., 2011).

Marine proxies. Schulz et al. (2002) analysed monsoon-influenced proxies extracted from core SO130-289 KL, from the northern Arabian Sea. They showed substantial interstadial/stadial fluctuations in sea-surface temperatures during the Toba interval, confirming that the Late Pleistocene was characterised by climatic instability in the region (Figure 1-9). However, the monsoon oscillations recorded by the proxies did not appear to have been influenced by the YTT event. These studies overall suggest that the YTT had a strong impact on the environment (especially the vegetation) of local areas directly affected by the ashfall (i.e. Sumatra and India) but had only a minor impact on monsoonal circulation.

These discoveries initiated a reconsideration of previous conceptions of the impact of the YTT event. Oppenheimer (2002) noted that there was a large range of uncertainty in estimates of important eruptive parameters, including eruption volume, height of eruptive plume, duration of the eruption and the amount and duration of stratospheric sulphur aerosol. He suggested that the data did not provide compelling evidence for strong and enduring climatic impact.

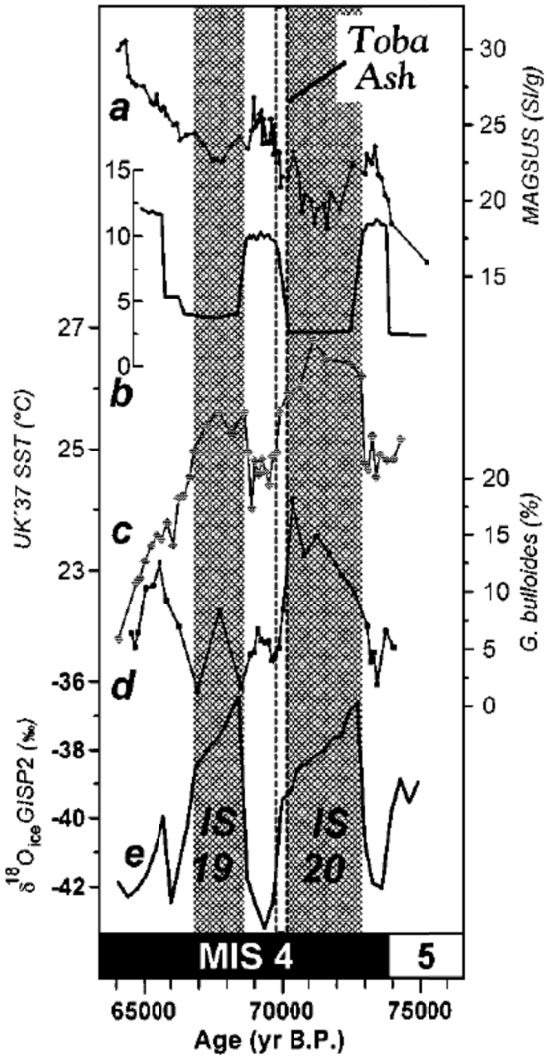

Figure 1-9 Palaeoclimatic proxy data from the Arabian Sea core SO90-93KL. Magnetic susceptibility (MAGSUS), sediment accumulation rate, sea-surface temperature and relative abundance of the plankton foraminifer *Globigerina bulloides* all show relative instability in the time window 64,000-76,000 yr ago., independently from the YTT event (from Schulz et al., 2002). MIS= Marine Isotope Stage; IS= Inter-Stadial. (a) Magnetic Susceptibility (MAGSUS); (b) sediment accumulation rate; (c) U^{k}_{37} –based sea-surface temperatures; (d) relative abundance of the planktic foraminifer *Globigerina bulloides;* (e) GISP2 δ $^{18}O_{ice}$ record.

Recently Van der Kaars et al. (2012) pointed out that the changes determined from pollen analyses were clearly linked to long-term trends initiated a few thousand years before the YTT eruption. Since the Late Pleistocene was characterised by oscillating climate and unstable monsoons (Campo et al., 1982; Prell and Kutzbach, 1987; Prell and Kutzbach, 1992; Kudrass et al., 2001; Clemens and Prell, 2003; van der Kaars et al., 2010; Xiao et al., 2011), the changes in pollen assemblages detected by Williams et al. (2009) could have been linked to externally-driven factors rather than volcanically-induced effects. This explanation has been further supported by

Blinkhorn et al. (2012), who re-calculated the carbon isotope ratios from specific YTT sediments sites in southern India. They obtained values related to local morphological changes rather than the presence (or absence) of the ash. Williams (2012a) concluded that the resolution of the sediments in which the proxies (both marine and terrestrials) are preserved is too low to isolate the environmental changes related exclusively to the YTT ashfall.

1.3.3 Human impact and archaeological evidences

A major motive for studies of the ~ 73 ka Toba super-eruption is the need to understand the effects that the YTT event might have had on the prehistoric human populations living in Asia and elsewhere at the time of the eruption. Rampino and Self (1992 and 1993) after proposing the 'volcanic winter' hypothesis, argued that the supposed millennium of cold climate generated by the YTT eruption might have led to a crash in ancient modern-human population size.

Ambrose (1998) developed the idea further, proposing the concept of a 'volcanic winter bottleneck'. The author suggested that YTT ashfall were responsible for a Late Pleistocene human bottleneck (Figure 1-10, Ambrose, 1998). He speculated that the feedback caused by the volcanic winter could have induced low primary productivity and famine; thus the YTT might have had a substantial impact on human populations (Ambrose, 1998). Gathorne-Hardy and Harcourt-Smith (2003) argued against the YTT 'bottleneck' hypothesis, stating that there was little fossil and genetic evidence to support it.

Archaeological work by Petraglia et al. (2007) in southern India supported the 'low-impact' hypothesis of Oppenheimer (2002), Schulz et al. (2002) and Gathorne-Hardy and Harcourt-Smith (2003). The archaeologists suggested that the impact of the ash was minimal and very short-lived, since the technology of the stone tools recovered both below and above the ash was the same (Petraglia et al., 2007). Williams (2012a) reminds us, however, that the Optically Stimulated Luminescence (OSL) dates constraining the sediment ages below and above the ash have substantial uncertainties (81–67 ka above and 83–71 ka below the ash) and so they cannot exclude the possibility of long (millennial scale) abandonment of the area.

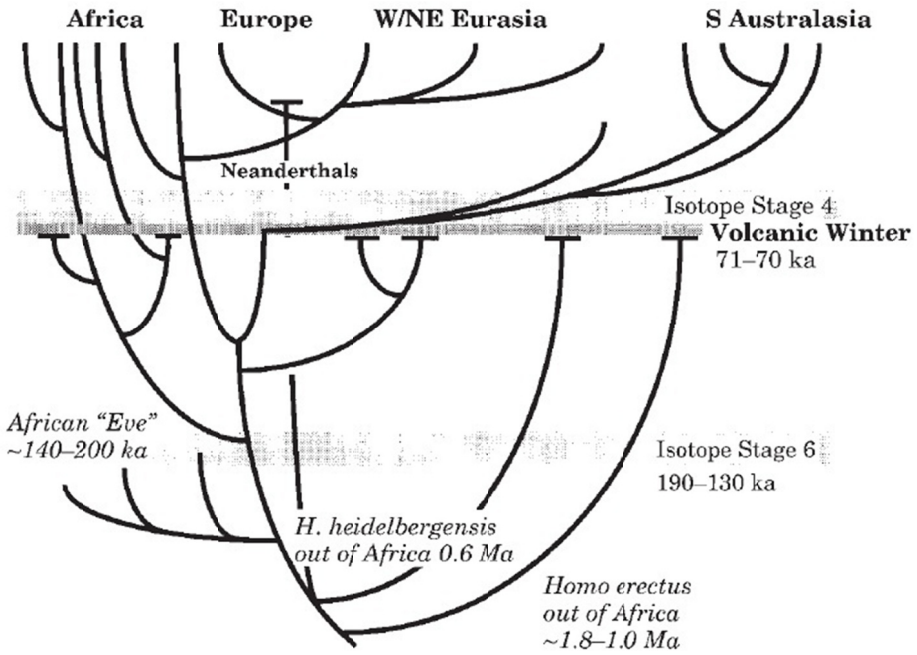

Figure 1-10 The Late Pleistocene 'volcanic winter' bottleneck proposed by Ambrose, (1998). Population subdivision due to dispersal within Africa during the early Late Pleistocene is followed by bottlenecks caused by the Toba-induced volcanic winter (from Ambrose, 1998).

Jones (2010) proposed that different areas gave rise to different palaeoanthropological responses to the YTT event, with some parts of south Asia serving as refugial areas whilst others were more severely affected. This concept was supported by Oppenheimer (2012), who suggested that ancient modern-humans were strongly affected by the YTT consequences, but recovered afterwards thanks to the abundance of local environmental diversities available in India. These conditions lessened the severity of a local genetic 'bottleneck' and enabled rapid re-colonisation (Oppenheimer, 2009).

1.4 Research rationale and objectives

The previous sections have shown that much work has gone into understanding the impact of the YTT eruption. This section discusses the many questions that remain unanswered, and addresses them in terms of the aims of the thesis. The initial goal of this study was to re-examine and determine the environmental impacts caused by the YTT ashfall.

In his reviews, Williams (2012a, 2012b) suggested that a fundamental issue that needed to be addressed when considering the environmental impact of the YTT is the availability of high-

resolution, accurate environmental proxy records directly related to the tephra. Jones (2010) recommended the addressing of two issues: the rate of accumulation of the secondary tephra and the time/seasonality of the eruption, since the local climate could drastically amplify or reduce the effects of the tephra accumulation (cf. Todesco et al., 2004; Favalli et al., 2006). Three objectives were therefore established in this study: a) to find high resolution proxies directly related to the YTT; b) to assess the rate of accumulation of reworked deposits; and c) to investigate the time and seasonal setting of the eruption.

However, while reviewing the literature on the subject, several recurring issues related to the use of the tephra deposits were identified. Accordingly, the research was reoriented to focus on the following questions:

1) What is the primary thickness of the YTT? Thickness, together with grain size, is the most important and discussed characteristic of the tephra, since it is used in models and simulations to assess the eruption's environmental impact (i.e. Rose and Chesner, 1987, Robock et al., 2009). However, the thickness varies substantially from site to site. Several previous studies used an approximated average thickness, but it is not clear how such constraints were obtained. It is therefore necessary to understand how the ash is distributed and accumulated, the variability of particle sizes and how the deposit's thickness varies with distance from the source, and to assess the uncertainty inherent in estimating these physical factors.

2) What is the geochemical variation in YTT glass? Geochemical fingerprinting is the accepted method by which YTT deposits are identified and correlated (Westgate and Gorton, 1981). Because of the large body of literature available, it is common to use geochemical data from published studies for comparison with new results. The question therefore arises of the extent to which analyses performed in different laboratories are comparable. Could the depositional environment modify the geochemistry of the glass? The variability of the major chemical components in the YTT has not hitherto been closely examined. Yet, given the large amount of geochemical data collected for the YTT since the 1930s, it seems appropriate to compare the available chemical evidence and in addition to investigate the causes and effects of chemical variations.

3) How reliable are previous reconstructions of the YTT environmental impacts? Assessments of the environmental impact of the YTT are typically based upon evaluation of proxies collected from sediments immediately under- and overlying the YTT horizon. However, several studies have used the YTT as chronostratigraphic marker without distinguishing whether the material was primary ash (deposited during fallout and instantaneously preserved in situ) or secondary ash (redeposited ash material possibly mixed with non-volcanic clastic products). Reworking processes such as erosion, fluvial and aeolian transport, floods, soil flow and landslides can disturb the tephra sequence, depositing the ash on younger or older sediments. The reliability of the YTT as a chronostratigraphic marker in sedimentary sequences therefore needs to be studied.

4) **Which mechanisms are behind the transport, accumulation and preservation of the thick, widespread, YTT fall deposits?** The largest part of the YTT tephra in distal deposits at terrestrial sites is composed of 'secondary' tephra, metres-thick sequences of reworked volcanic material, occasionally mixed with non-volcanic sediments (Figure 1-11). As will be shown in chapters five and six, the characteristics of the YTT tephra are therefore a consequence of a range of environmental processes acting, with the passage of time, upon and interacting with the ash. Thus, in order to isolate the impact of the YTT on the receiving ecosystems (using environmental proxies collected from the tephra sediments), it is necessary first to determine how the ash has been modified by local factors, and whether the tephra are suitable for palaeoenvironmental reconstruction. The recent discovery of new sites in the Malaysia peninsula has finally allowed the interpretation of the interactions between YTT ash and the receiving environment.

The objectives of the present study derive from the desire to answer the questions proposed by previous studies and the challenges exposed during review of the literature on the YTT eruption. As a consequence, it was decided directly to address the four questions identified above, and indirectly, in relation to the results, to discuss the suggestions of Williams (2012a) and Jones (2010). Hence, keeping the main goal in mind (**re-examine and determine the environmental impacts caused by the YTT ashfall**) this thesis tackles the following objectives:

a) to review the literature on particle size and thickness of the YTT fallout and synthesise the evidence to re-evaluate the volume of the co-ignimbrite ash.

b) to review and synthesise published and new evidence on the YTT glass compositions (mostly from distal tephra fall deposits) and to evaluate agents of any variability discovered.

c) to assess the reliability of the YTT tephra as a chronostratigraphic marker in the Son Valley, India.

d) to evaluate the mechanisms of tephra reworking, and assess the reliability of tephra sediments for palaeoenvironmental reconstructions.

The next section offers a synopsis of the remaining chapters of the dissertation.

Figure 1-11 Reworked YTT deposits in Jwalapuram, southern India. The reworked volcanic material can reach 7 m in thickness in this area.

1.5 Thesis structure

This work is based on sedimentological and stratigraphic data collected during two field seasons in 2009 (India) and 2010 (India, Malaysia, Indonesia), as well as geochemical analyses of ash collected in the field. The backbone of the thesis is the study of the dynamics of the ash and its receiving environment, focusing on distal tephra deposits.

Following this introduction, **Chapter two** outlines the methods and techniques employed to acquire primary data. **Chapters three** and **four** review the physical and chemical parameters of the YTT as reported in the literature. Chapter three discusses the most recent volume calculations and proposes an alternative estimate, taking into account the variation (or lack of) in thickness with distance from source. The size of the YTT ash finer-grained (< 60 μm) particles is poorly correlated with distance from the source. Below a certain grain-size the motion of the particle is dominated by the viscosity of the air rather than by the inertia of the particle itself (as particles get smaller, the Reynolds number of the fluid goes down). Fine ash particles therefore behave more analogously to the motion of a feather in honey. Given this, and the complex wind conditions to which the YTT was exposed, it seems implausible to model the YTT volume using a simple exponential decay of the ash thickness with distance from the source.

Chapter four compares the chemical features of the YTT, investigating the differences between YTT preserved in different environmental contexts. Here the aim was the study of post-depositional leaching arising from environmental factors; however it was discovered that major variations are driven by the compositional stratification of the magma in the pre-eruptive reservoir. This is consistent with compositional zonation in the magma chamber, and highlights a strong correlation between time of eruption and composition of ash ejected.

In the second part of the thesis new samples collected in the field were used to investigate the interactions between ash and receiving environment. **Chapter five** deals with the YTT deposits in the Son valley, India. Field investigations here indicate that hydrological processes such as lateral accretion and overbank floods removed and redeposited the ash several times after the eruption. This chapter discusses the consequences of such mechanisms for the application of the YTT as a chronostratigraphic marker for palaeoenvironmental and archaeological studies.

Chapter six discusses the characteristics of reworked tephra deposits, the differences between primary and secondary ash, and the mechanisms that underpin the accumulation and preservation of tephra. The sediments in the Lenggong valley, Malaysia, show that reworked deposits have variable textural and mineralogical features, and that such features can overlap with the characteristics considered unique to primary ash. The analyses suggest that the ash accumulated during a short period of time, thus implying that the possible impact of the YTT on local landscape lasted for a few decades. The evidenced depositional processes suggest that reworked tephra might not be suitable for palaeoenvironmental reconstruction.

1.6 Comments on the authorship of journal papers revised as chapters

Chapters three, four, five and six of this thesis are based on manuscripts that have been submitted to journals for publication and involved co-authorship. I am first author of these works and the contributions from my co-authors went no further than typical levels of support from co-supervisors and colleagues, i.e. in the provision of comments and suggestions on early versions of the manuscripts.

Specifically, Chapter 3 is the updated and revised version of the paper in press: Gatti, E., and Oppenheimer, C. 2012. "Utilization of distal tephra records for understanding climatic and environmental consequences of the Youngest Toba Tuff". In: L. Giosan, D. Fuller, R. Flad, and P. Clift (Eds.), Climates, Past Landscapes and Civilizations, American Geophysical Union Monograph Series, Washington DC. I conducted all the analyses presented in this chapter, wrote the manuscript and drew the figures. Chapter four is based on the submitted article: Gatti, E., Achyuthan, H., Villa, I., Gibbard, P., and Oppenheimer, C. "Geochemical patterns in distal and proximal Toba glass", *Bulletin of Volcanology*. I conducted all the analyses presented in the chapter, wrote the manuscript and drew the figures. Prof. Achyuthan assisted with the collection of the samples in India; Prof. Villa helped with the interpretation of the geochemical plots; my supervisors Phil Gibbard and Clive Oppenheimer revised the chapter. Chapter five is based on the published article: Gatti, E., Durant, A.J., Gibbard, P., Oppenheimer, C., (2011), "Youngest Toba Tuff in the Son Valley, India: a weak and discontinuous stratigraphic marker", *Quaternary Reviews,* (30), 3925-3934. I collected the field analyses (see **Chapter two**), drew all the images and

wrote the manuscript. Dr. Durant assisted with the collection of data during the fieldwork and commented on the geological interpretations; Gibbard and Oppenhemeir commented on the draft of the manuscript. **Chapter six** is based on the published article: Gatti E., Mokhtar, S., Talib, K., Rashidi, A., Gibbard, P., Oppenheimer, C., "Depositional processes of reworked tephra: a case study from the Late Pleistocene Younger Toba Tuff deposits in the Lenggong Valley, Malaysia", *Quaternary Research*. I collected the samples in Malaysia (see **Chapter two**), ran the analyses, wrote the manuscript and drew all the figures and tables. Prof. Mokhtar and Master students Kariunnisa Talib and Akin Rashidi helped with the field work in Malaysia, while Prof. Gibbard and Prof. Oppenheimer commented on the draft of the manuscript before submission.

Chapter 2. Research Methods

This chapter briefly outlines the field and laboratory techniques that have been used in this study. It focuses on the sample preparation methods and technical procedures used in this thesis, rather than providing a detailed treatment of the principles behind each analytical technique (since these are long-established methods). Localities sampled during the fieldworks are summarised in paragraph 2.1. Further details of each site are given in the relevant chapters. Methods of data analyses (e.g. GIS-based) are also described in the appropriate chapters rather than in this section.

2.1 Field methods

Six sites were investigated during two field campaigns in 2009 and 2010 in India, Malaysia and Indonesia (Figure 2-1 and Table 2-1). The samples of Toba ash presented in this work were collected by the author in each of these locations, except for the samples from Jwalapuram, in India (**Chapters three and four**), which were provided by Dr. Sacha Jones.

Table 2-1 List of sites visited, with the corresponding analyses conducted. PS= Particle Size; MS= Magnetic Susceptibility; EPMA= Electron Probe Micro Analyser; LA-ICP-MS=Laser Ablation Inductively Coupled Plasma Mass Spectrometry.

Site	Field work	Sample Collection	PS	MS	EPMA	LA-ICP-MS
Jwalapuram (IN)	✓	✓	✓		✓	✓
Son Valley (IN)	✓	✓				
Bori (IN)	✓	✓	✓		✓	✓
Morgaon (IN)	✓	✓	✓		✓	✓
Lenggong (MYS)	✓	✓	✓	✓	✓	✓
Lake Toba (IND)	✓	✓				

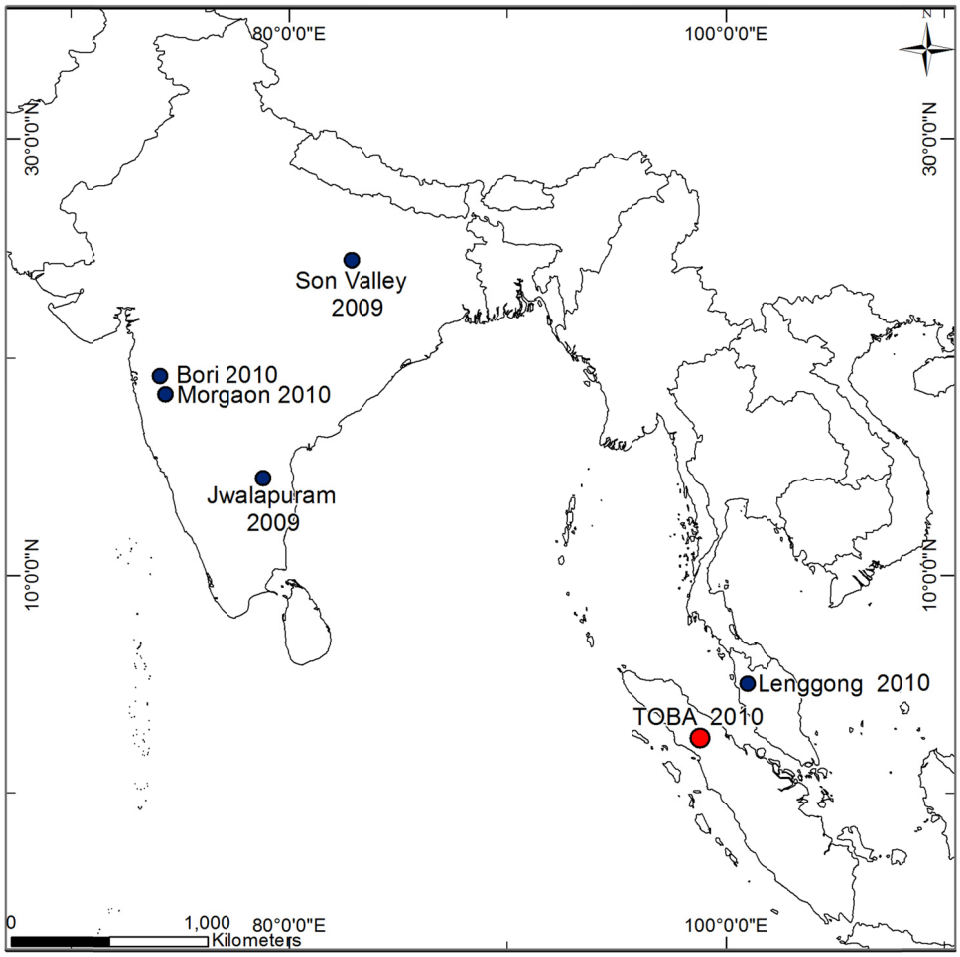

Figure 2-1 Sites sampled by the author for this work

Figure 2-2 The ash reported in chapter six was collected from Kampung Luat, Lenggong valley (Malaysia).

Samples were collected from fresh, clean surfaces and stored in plastic bags (Figure 2-2). They were then shipped to the UK for analysis (Table 2-1). Field mapping of the Son Valley (**Chapter five**) was conducted by the author with support from Dr. Adam Durant. Samples collected in the Son Valley did not reach the UK in time to be made available for the research.

2.2 Laboratory methods

The following section outlines the procedures and techniques applied to the samples collected. Preliminary analyses were conducted using a scanning electron microscope (SEM) and associated energy-dispersive spectrometer (EDS) at the Department of Anatomy at the University of Cambridge. The author conducted all the analyses, except where specifically indicated.

2.2.1 Electron probe microanalyses

Major and rare element geochemical fingerprinting is a routine procedure applied to determine the composition of volcanic ash and relate it to its volcano of origin (Westgate and Gorton, 1981; Stokes et al., 1992). Subsequent to preliminary analyses e.g. run to verify that the collected sediments were ash, the samples were chemically characterised, in order to compare them with verified YTT samples. The Electron Probe Micro-Analyser (EPMA) is a particle-beam analytical technique used to establish the composition of small areas on specimens. It can estimate major elements in areas as small as ~ 10 μm, making it suitable for geochemical analysis of small tephra particles. This technique uses a beam of accelerated electrons that is focused on the surface of the grain, producing characteristic x-rays. These x-rays are detected at particular wavelengths, and their intensities are measured to determine concentrations. Individual elements can be detected because each has a specific range of wavelengths that it emits.

Samples were prepared for EPMA using 5% HCl and placed in an ultrasonic bath for 10 minutes to remove secondary carbonates. Samples in the fraction 63-125 μm were mounted, impregnated, polished and coated with carbon (Figure 2-3). Glass compositions were analysed in the Department of Earth Sciences, University of Cambridge on a Cameca SX-100 with one energy-dispersive and five wavelength-dispersive spectrometers. The accuracy was ± 1% for major elements, detection limits ranged from 1 to 20 ppm, and the spatial resolution was about 1 μm. A

beam current of 15 keV 2nA was applied to measure Na, Si, K, Ca, Ti, Fe, Al, Mg. Na was counted at the beginning to minimise the consequences of Na loss. The analyses were normalised excluding water. Internal standards were: Jadeite (Na), Diopside (Si, Ca), Corundrum (Al), Periclase (Mg), Orthoclase (K), Apatite (P). The secondary standard used was sample JLP3-11s, provided by Sacha Jones. The scanning electron microscope (SEM) used was equipped with a secondary and backscatter electron imaging system.

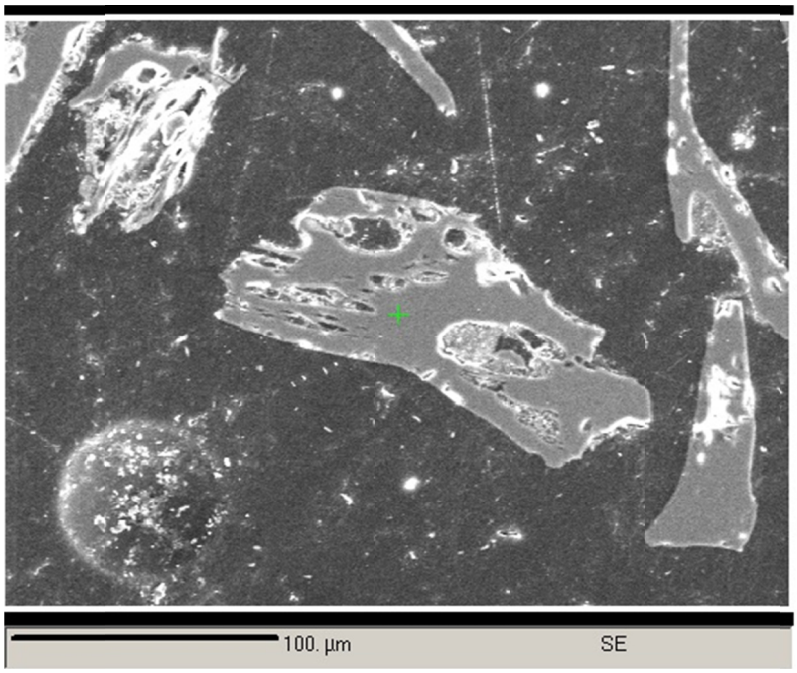

Figure 2-3 Ash grains as they appear under the EMPA camera. Grains were mounted on epoxy resin and polished with diamond powder in order to remove the surface impurities and expose the inner part of the glass.

2.2.2 Laser ablation ICP-MS

Trace element composition is valuable for differentiation of minor differences between eruptions of the same volcanic system (Westgate et al., 1994; Pearce et al., 2008a). In this case, it was necessary to verify that the samples collected were YTT and not OTT and MTT, and work with YTT glasses only. The laser ablation ICP-MS (Inductively Coupled Plasma Mass Spectrometer) is a micro-analytical technique that combines the micrometer-scale resolution of the laser probe with the sensitivity of the ICP-MS. A pulsed laser beam is used to ablate a small quantity of material, which is transported into the Ar plasma of the ICP-MS instrument by a stream of Ar carrier gas.

Trace element compositions of individual phases were measured using a New Wave UP213 Nd-YAG laser ablation system (an artificially grown Y-Al garnet doped with a small quantity of Nd) interfaced to a Perkin-Elmer Elan DRC II ICP-MS in the Department of Earth Sciences, University of Cambridge. Helium was used as the ablation gas, and was delivered to the sample ablation cell via a mass controller system (MKS Instruments, Cheshire, England). The helium flow rate was precisely controlled at 0.7 L min^{-1}. The helium flow carrying the ablated sample material was joined with an argon stream from the ICP-MS at 0.8 L min^{-1} before entering the plasma.

A 60 μm diameter laser beam, with a laser repetition rate of 10 Hz and laser power of ~ 0.2 mJ (8 Jcm^{-1}) was used throughout the study. The spot size was chosen as a compromise between signal intensity and the size of the grains in the samples. The ICP-MS data acquisition settings were 1 sweep per reading, 80 readings, and 1 replicate; total data acquisition lasted 58 s. The first 20 s were gas blanked for each spot, and then put through laser analysis. There was a 45 s gas rinse out time after each spot to allow the element signals to return to baseline levels before moving to the next spot. The data were acquired at a rate of about one point per 0.7 s. The ICP-MS dwell times were selected on the basis of the isotope abundance and elemental concentration in the samples.

For data processing and calculation of concentrations, Glitter Software (GEMOC, Australia) was used to process the raw data files. For all the data, NIST 610 trace elements in a glass matrix 3 mm wafer (National Institute of Standards and Technology, Gaithersburg, Maryland, USA) was used for calibration of element sensitivity. The certificate values of 500 ppm nominal for each element are not reliable, so instead the published and widely agreed values from Pearce et al. (1997) were used. The CaO (or for olivines, MgO) content of each sample was used for internal standard normalisation of the trace element signals. Calibration accuracy was verified by analysing NIST 612, 614, BCR-2G and T1-G (MPI DING standard, Mainz) as unknown samples and recoveries were typically 90-110% of the values in the GEOREM database. In addition, several analyses of the United States Geological Survey (USGS) standards BIR-1, BCR-2, BHVO-2 and were conducted during the study to verify calibration accuracy. These standards were analysed as glasses prepared from the rock powder available from USGS. Less than 10% ICP-MS drift was seen during the single day of measurements.

2.2.3 Malvern Mastersizer 2000 particle size analyser

Characterisation of particle sizes of tephra deposits is vital to investigation of the methods of transport and sedimentation (Folk and Ward, 1957; Passega, 1964; Folk, 1966; McLaren, 1981), and to understanding the dynamics of post-deposition accumulation of the ash (Charman et al., 1995; Koniger and Stollhofen, 2001). Grains between 0.001 and 1000 μm were studied using laser diffraction, a technique that measures the intensity of light scattered as a laser beam passes through the dispersed sample. Samples were cleaned of secondary carbonates using 5% HCl and 10 minutes in an ultrasonic bath; 7% sodium pyrophosphate solution ($Na_2P_2O_7$) was added to the solution to separate clay particles. All samples were centrifuged (3500 rpm for 13 min) to separate the supernatant, and thoroughly cleaned using deionised water. Laser-scatter analysis was conducted using a Malvern Mastersizer 2000 in the Department of Geography, University of Cambridge. The average from four analyses per sample was used. Grain-size statistics (Folk and Ward, 1957) were calculated using both the Malvern software SOP (Standard Operating Procedures) and GRADSTAT software, following Blott and Pye (2001).

2.2.4 Magnetic susceptibility

The magnetic susceptibility indicates the degree of magnetisation of a material in response to an applied magnetic field. This technique was used to study the potential changes to tephra deposits during reworking. The magnetic susceptibility of the samples was measured using a Bartington magnetic susceptibility MS2 meter and MS2B dual frequency sensor in the Department of Geography, University of Cambridge. Cleaned bulk sediments were placed in 10 cm^3 plastic pots, and samples were dried overnight in an oven (at 42°C). The data were acquired using Multisus software. The background magnetic field was measured before and after each sample reading in order to test for natural drift in the Earth's magnetic field. The mass specific magnetic susceptibility of each sample (expressed in 10^{-8} $m^3 kg^{-1}$) was calculated by subtracting the mean of the two background measurements from the mean of the two sample measurements and dividing the resulting value by the dry mass of the sample.

Chapter 3. Particle size, thickness and volume of the YTT co-ignimbrite ashfall

Based on Gatti and Oppenheimer (2012)

Abstract

Estimation of the volume of the co-ignimbrite fallout is a fundamental part of any estimate of the overall magnitude of the YTT eruption. To date, this quantity remains poorly characterised. This chapter presents particle sizes and thicknesses of distal YTT deposits from the literature and original work, in order to examine the variations of these parameters with distance from the vent. Thickness data are used to compare two techniques for volume calculation, the Pyle (1989) method, which estimates the volume by extrapolating the exponential thinning of the ash sheet with distance, and the Bonadonna and Houghton (2005) method, which applies a voronoi tessellation, calculating the volume by weighing the individual thickness measurements. After discussing volume estimation methods, I address analyses of particle size distributions. It is found that the median size of the finer particles shows no variation with distance, particularly beyond 1000 km from source. No ash deposits beyond 1000 km from the vent show exponential thinning decay in relation to the distance from the vent. Furthermore, the isopach map built from the available data shows that several wind systems affected the distribution of the tephra, and that for areas a distance > 2000 km from the vent the isopachs cannot be constructed because of lack of data. The study concludes that exponential models cannot be applied to the YTT ashfall. This chapter argues that without knowledge of the atmospheric conditions prevailing during the eruption no model can provide better than an order-of-magnitude estimate of the tephra fallout volume. It concludes that the voronoi is the fastest and simplest method of providing a first order estimate of the minimum volume. This approach yields a minimum amount of co-ignimbrite ash between 770 km^3 and 2000 km^3 (dense rock equivalent).

3.1 Introduction

The impact of a pyroclastic eruption on terrestrial ecosystems depends heavily on the quantity and dispersal of ash that is erupted (Pollack et al., 1976). Estimating the volume of ash ejected is therefore a crucial goal when studying a co-ignimbrite eruption such as the YTT, which ejected vast quantities of fine ash. The essential concept behind the estimation of volume of ash is simple: samples of ash that are known to have come from a specific eruption (verified using geochemical

fingerprinting; **Chapter four**) are measured in terms of their geographical position and thickness at that point. It is possible to obtain a rough volume estimate by multiplying the average thickness of the observed deposits by the area covered by the sample sites. This, however, will be a crude estimate since the ash is never distributed uniformly. Effects of prevailing winds, sedimentation and air and sea currents will all act to deform the ash cloud, and the resulting distribution of the ash will therefore be highly non-uniform. The key question is 'Can we use knowledge about how ash disperses and measurement of ash size and thickness to improve on the crude volume estimate?'.

Answering this question is the main aim of this chapter. There are, however, significant problems in applying standard volume calculations to the YTT co-ignimbrite deposit. For example, YTT deposits span the west through to the northeast quadrants around the caldera. They do not define a downwind area with clear elliptical isopachs, nor are they described by spherical isopachs, since ash has not been reported in the south and southeast of Sumatra. Other parameters such as the height of the eruptive column and the season of the eruption, which could constrain the model, are unknown. For these reasons, tephra volume estimates for large eruptions, and especially super-eruptions, have large errors (Self, 2006). This chapter first demonstrates that the distal YTT co-ignimbrite deposits are mostly composed of fine and ultrafine particles. It then shows that the size of the fine particles, beyond a threshold distance, no longer decreases exponentially with distance from the vent, and examines the implications of this behaviour for the thickness of the deposits. Finally, attempts to calculate the total volume of ash ejected using two methods and the results are discussed.

3.2 Methods of volume calculation in ignimbrite and co-ignimbrite eruptions

Various methods have been developed to estimate ash volumes by using thickness from recovered distal ash. For example, Thorarinsson and Sigvaldason (1972) observed that tephra fall deposits from Hekla thinned exponentially with distance from the vent. Since then, several techniques have been applied to calculate volumes on the basis of exponential decay of ash thickness with distance. Pyle (1989a) developed this principle, formulating the volume (V) as follows: $V = 13.08\, T_0 b_t^2$, where T_0 and b_t are, respectively, the extrapolated maximum deposit thickness

at the vent and the distance over which the thickness of the tephra sheet decays by half (Pyle, 1989a). Extrapolation to an arbitrary thickness is possible assuming the exponential thickness decay and an elliptical isopach distribution. The method presented by Pyle is based on the formula:

$$T = T_0 \, exp(-kr) \qquad (1)$$

where r= distance from the vent, $k = ln2/b_t$, T_0 = extrapolated maximum deposit thickness; T=tephra thickness at a certain r distance from the vent. A summary of the Pyle method is illustrated in Figure 3-1. The integration results in the simplified equation for the total volume of ash:

$$V = 13.08 \, T_0 b_t^2 \qquad (2)$$

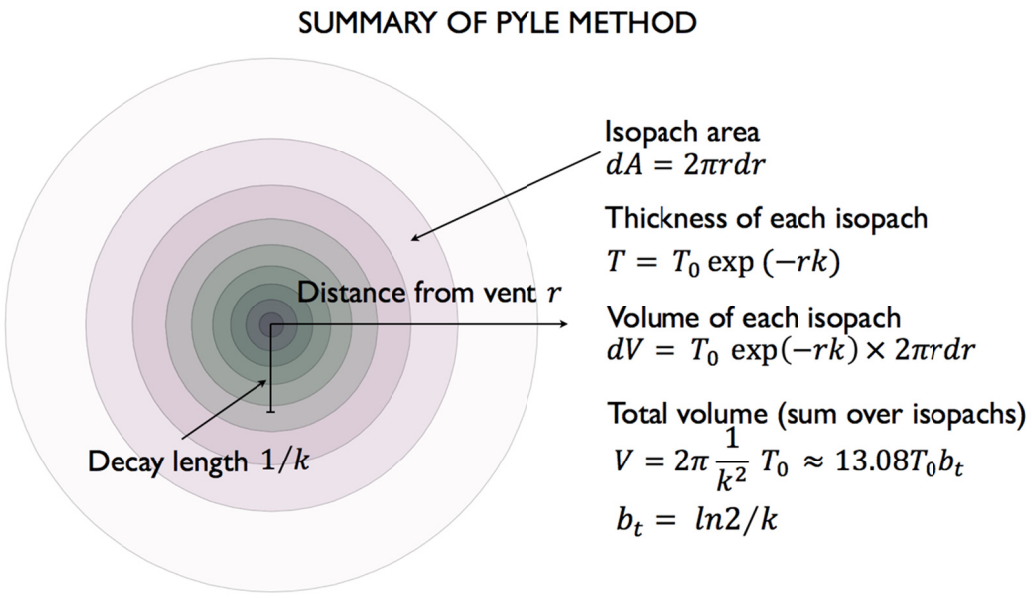

Figure 3-1 Summary of Pyle method (from Pyle, 1989a). For a given distance from the vent r, each circular isopach area will have an area of $dA = 2\pi dr$. If we apply an exponential decay equation, the thickness T at the distance r depends on the thickness at the source (T_0) and the decay length ($1/k$), which characterises the distance over which the thickness decreases by a factor of e. The volume of ashfall in each isopach is the thickness at that distance, multiplied by the area of each isopach. The total volume is obtained by summing (integrating) over all isopachs at all distances. The decay length in the Pyle method is expressed in terms of half-time decay length b_t, which is the distance over which the thickness of the tephra sheet decays by half. b_t is related to the decay length simply by a factor of ln(2) arising from using natural logs or logs of base 2.

Despite wide application of the exponential thinning decay method, tephra fall deposits have been shown to display thickness variations that are more complex than simple exponential

thinning (Froggatt, 1982; Fierstein and Nathenson, 1992; Hildreth and Drake, 1992; Scasso et al., 1994). Rose (1993) argued that fine distal ash settlement differs from that of larger particles, thus volume calculations of some tephra deposits substantially underestimate the true values. Similarly, Bonadonna et al. (1998) and Bonadonna and Phillips (2003) noticed that major changes in thinning rates occur as the particle size decreases. This has been explained as a consequence of the changes of settling behaviours that occur when the particles decrease from high (> 500) to low (< 500) Reynolds numbers (Sparks et al., 1992). The Reynolds number is a dimensionless number that quantifies the relative importance of inertial and viscous forces for given flow conditions. It is expressed as

$$R = \frac{T\rho L}{\eta}$$

where T is terminal velocity, ρ and η the density and the viscosity, respectively, of the medium, and L the length of the particle. Terminal velocity T is reached when the drag force is equal to the gravitational force acting on the particle, so that T is in general a function of particle density and size as well as fluid density and viscosity. Fine ash particles have low Reynolds numbers, which means that settling is dominated by the viscosity of the medium in which they are transported, while large particles characterised by high Reynolds number settle in more turbulent behaviour (in which the inertial forces of the fluid flow are dominant). Depending on the density of air, the boundary between low and high Reynolds number for ash particles occurs between ~ 500 to ~ 100 μm, shifting towards the coarser sized particles at higher altitudes due to decreasing air density (Alfano et al., 2011). The motion of fine particles (length <500 μm) is dominated by viscous forces and therefore strongly affected by the currents in the air (Ersoy et al., 2010).

Indeed, Bonadonna et al., (1998) modelled the sedimentation from laterally spreading plumes and found that, beyond ~ 27 km from the vent, particles finer than 2000 μm are better predicted by using a power-law model rather than an exponentially decaying model. The power law function ($y = m\,x^b$) allows the thickness (y) to decrease more slowly as a function of increasing distance (x), thus better describing the thinning rate of low Reynolds numbers particles. The method has been applied by Bonadonna and Houghton (2005) in a study of the volume of ash ejected by the Ruapehu eruption. The authors described a power law model ($T = T_0 \sqrt{A}^{-k}$, cf.

Eq. (**1**)) and demonstrated that, in cases of eruption with a large amount of fine particles the exponential method can underestimate the total volume by a factor of at least two (Bonadonna and Houghton, 2005).

Although these models are typically applied to plinian eruptions, in which ashfall is preserved in proximal areas and composed of lapilli and coarse ash (i.e. Bonadonna et al., 1998; Bonadonna and Houghton, 2005), the majority of volume calculations of co-ignimbrite ashfall have been made with the same methods. For example, the Campanian Ignimbrite (Pyle et al., 2006), the Minoan eruption (Pyle, 1989b), the 26.5 ka Oruanui eruption in New Zealand (Wilson, 2001), and the 1815 eruption of Tambora, Indonesia (Self et al., 1984) have been assessed with the Pyle (1989a) method. An alternative approach has been proposed by Perrotta and Scarpati (2003), who applied the Pyle (1989a) calculation to the Campanian Ignimbrite, but determined the areas of each isopach by measuring the areas enclosed within thickness contour lines, which were manually traced with drawing software. This avoided approximating the real shape with a simplified (circular of elliptical) shape. Yet, co-ignimbrite ashfall at much greater distances from the vent, and ashfall deposits are predominantly composed of fine and very fine particles (cf. **Chapter one**).

The extreme case of the YTT introduces a high degree of uncertainty when discussing its co-ignimbrite volume with these methods. Rose and Chesner (1987) proposed a method explained in Rose et al. (1973), which plots the isopach thickness *vs.* the area within the isopach. The equation to calculate the volume was $V = \int A\,(t)dt$, where V = volume of ash, A = area covered by a given thickness of ash, t = the ash blanket thickness. They obtained a minimum volume of ~ 840 km^3 Dense Rock Equivalent (DRE) (Rose and Chesner, 1987). The second and most recent attempt to calculate the volume of the YTT ashfall has been presented by Matthews et al. (2012). These authors presented a simulation to calculate the atmospheric dispersion and the thickness of the tephra (HAZMAP model from Macedonio et al., 2005). They obtained a total volume between 1500 and 1900 km^3 DRE (Matthews et al., 2012). The detailed explanation of this method is provided in Macedonio et al., (2005).

3.3 Study methods

The particle sizes and thickness data used for this study are listed in Table 3-1 and Table 3-2. Firstly, five continental ash samples collected during the 2009 and 2010 fieldwork were analysed for bulk particle-size distribution (Table 3-1). This was done in order to characterise the particle size of YTT distal deposits. Particle-size distributions were measured using a Malvern Instruments Mastersizer 2000 (**§1.3** for description of the Malvern preparation and methods). Secondly, seven marine cores presenting two distinct coarse and fine grain units within the core (Table 3-1) were plotted on a size-*vs*.-distance graph, to study the distribution of coarse and fine particles in relation to the distance from the caldera. Thirdly, thicknesses at each location were retrieved from published work, my own fieldwork and personal communications from colleagues (Table 3-2). A database was prepared, showing the geographical coordinates and ash thickness for each data point. If the original work did not differentiate between primary and reworked units the point was excluded from the database. For this reason the thickness database of this chapter is much smaller than the geochemistry database presented in **Chapter four**.

Table 3-1 YTT sites used for particle-size analyses

Sample ID	Latitude (degrees N)	Longitude (degrees E)	Mean diameter (wt%µm)		Reference
Terrestrial					
Bori	19.626	74.633	51		This study
Jwalapuram	15.320	78.134	70		This study
Morgaon	18.305	74.330	64.50		This study
Son Valley	24.544	82.231	62.50		This study
Tejpur	21.892	73.487	62		This study
Marine			*Fine*	*Coarse*	
RC14-37	1.643	89.927	62	125	Ninkovich et al. (1978b)
28-KL	4.701	84.967	22	49.19	Kudrass (personal communication)
42-KL	9.925	84.812	15.63	55	Kudrass (personal communication)
45-KL	11.571	86.951	20.1	55.5	Kudrass (personal communication)
47-KL	11.831	88.851	31	88.39	Kudrass (personal communication)
51-KL	12.658	87.547	22.1	62.5	Kudrass (personal communication)
115-KL	17.7163	89.493	44	63	Kudrass (personal communication)

Table 3-2 Marine and terrestrial YTT cores reporting primary ash thickness. T= terrestrial site

Sample ID	Latitude (N)	Longitude (E)	Primary Thickness (cm)	Reference
CR-02	-3	82.25	8	Pattan et al. 1999
CR-05	-3	88	13	Pattan et al. 1999
NR-1	-9.93	77.7	10	Pattan et al. 1999
NR-21	-11.5	78.7	10	Pattan et al. 1999
NR-35	-11.93	78.483	12	Pattan et al. 1999
NR-54	-7	78.483	5	Pattan et al. 1999
SK-226	-13.3	75.483	8	Pattan et al. 1999
SS-657	-14	76	8	Pattan et al. 1999
MD972151	8.728	109.869	2	Song et al. 2000
SO90-93KL	23.588	64.216	3	Schulz et al. 2002
SO90-94KL	22.488	65.649	4	Schulz et al. 2002
SO93-115KL	18.075	89.380	6	Schulz et al. 2002
SO93-22KL	0.332	83.355	10	Gasparotto et al. 2000/ Kudrass (personal communication)
SO93-9KL	2.927	80.388	4	Gasparotto et al. 2000/ Kudrass (personal communication)
SO93-45KL	11.571	86.951	11	Gasparotto et al. 2000/ Kudrass (personal communication)
SO93-47KL	11.831	88.851	10	Gasparotto et al. 2000/ Kudrass (personal communication)
SO93-51KL	12.658	87.547	20	Gasparotto et al. 2000/ Kudrass (personal communication)
SO93-119KL	17.095	87.7183	0	Gasparotto et al. 2000/ Kudrass (personal communication)
SO93-115KL	17.716	89.493	6	Gasparotto et al. 2000/ Kudrass (personal communication)
SO93-124KL	19.814	90.000	15	Gasparotto et al. 2000/ Kudrass (personal communication)
SO93-126KL	19.823	90.441	2	Gasparotto et al. 2000/ Kudrass (personal communication)
SO93-28KL	4.701	84.967	12	Gasparotto et al. 2000/ Kudrass (personal communication)
SO93-29KL	5.5352	84.072	7	Gasparotto et al. 2000/ Kudrass (personal communication)
SO93-1KL	7.858	79.130	1	Gasparotto et al. 2000/ Kudrass (personal communication)
SO93-42KL	9.925	84.812	10	Gasparotto et al. 2000/ Kudrass (personal communication)
ODP758(layer A)	5.384	90.361	34	Dehn et al. 1991
MD01-2393	10.502	110.061	4	Liu et al. 2006
17962-4	7.181	112.081	3.5	Bühring et al. 2000
17961-2	8.506	112.331	2.5	Bühring et al. 2000
RC17-145	6.702	96.647	4	(Ninkovich et al., 1978a; 1978b; 1979)
V29-14	6.857	86.225	7	(Ninkovich et al., 1978a; 1978b; 1979)
V19-176	7.071	76.754	2	(Ninkovich et al., 1978a; 1978b; 1979)
RC17-128	3.078	80.135	9	(Ninkovich et al., 1978a; 1978b; 1979)
V29-31	3.264	78.018	3	(Ninkovich et al., 1978a; 1978b; 1979)
V19-175	3.896	80.520	11	(Ninkovich et al., 1978a; 1978b; 1979)
RC17-132	1.080	85.083	2	(Ninkovich et al., 1978a; 1978b; 1979)
RC14-37	1.643	89.927	15	(Ninkovich et al., 1978a; 1978b; 1979)
V29-15	11.982	88.678	3	(Ninkovich et al., 1978a; 1978b; 1979)

RC12-340	12.880	90.278	12	(Ninkovich et al., 1978a; 1978b; 1979)
RC12-341	13.266	89.586	11	(Ninkovich et al., 1978a; 1978b; 1979)
V29-23	4.356	79.513	9	(Ninkovich et al., 1978a; 1978b; 1979)
V29-24	4.737	79.028	10	(Ninkovich et al., 1978a; 1978b; 1979)
RC12-343	14.960	90.850	8	(Ninkovich et al., 1978a; 1978b; 1979)
SO93-126KL	19.973	90.033	2	Kudrass et al. 2001
1143-A	9.359	113.290	2	Liang et al. 2001
JWP3 (T)	15.320	78.134	4	Petraglia et al 2007
Serdang (T)	3.0136	101.709	85	Chesner et al. 1991
Son Valley (T)	24.544	82.231	5	This work

Two volume-calculation techniques are developed. The first is based on an exponential dependence between thickness and distance from the vent (Pyle, 1989). Isopach areas (areas of the same thickness) were extrapolated and plotted against the thicknesses in a ln (thickness) vs. (isopach area)$^{1/2}$ plot (Figure 3-2). The total volume of an exponentially thinning tephra sheet is calculated with Eq. (2). The parameters T_0 (maximum thickness at the vent), b_t and k are extracted from Figure 3-2. T_0 is the first number in the equation describing the exponential decay fit (Figure 3-2), k is the slope on the ln (thickness) - (isopach area)$^{1/2}$ plot and the rate of thinning is calculated with the formula $b_t = ln2/k$ (Figure 3-1). The extrapolated parameters T_0 and b_t and the resulting volume are listed in Table 3-3.

Table 3-3 Minimum and maximum volume of ash-fall estimated assuming exponential thinning of the tephra sheet. Dense rock equivalent values are obtained from bulk volume multiplied by a factor of 0.5 (Rose and Chesner, 1987).

	Minimum	**Maximum**
Area (km^2)	13×10^6 (polygon)	24×10^6 (rectangle)
T_0 (cm)	106	223
b_t (km)	391	614
Volume (km^3 DRE)	1208	5000

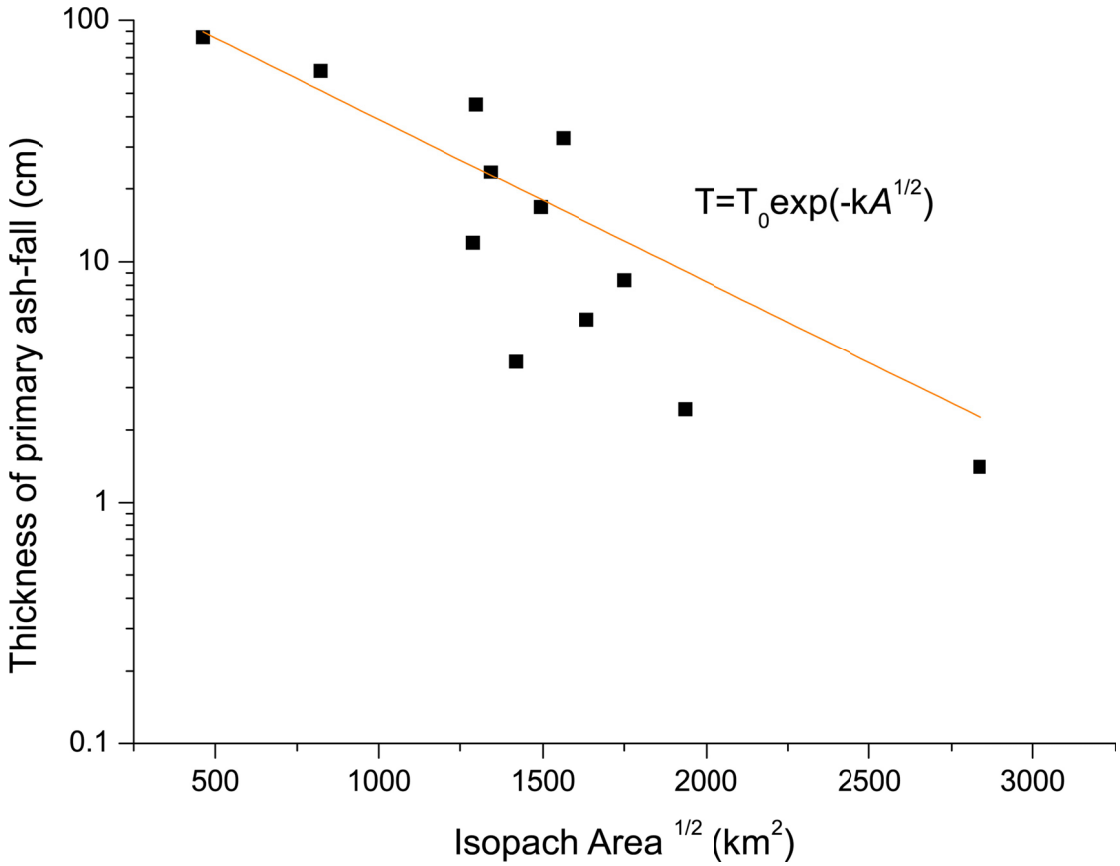

Figure 3-2 Ln (thickness) - isopach area ½ plot using the Pyle (1989a) method. The isopach areas have been calculated using kriging statistical approximation. The method calculates a statistical surface from a set of input points assigned by the author. The thickness surface is calculated using 55 primary ashfall thicknesses reported in the literature (Table 3-4). The twelve data points shown are the twelve isopachs that result from the 55 data points.

Isopach areas were extrapolated using a kriging technique in Geographical Information System (GIS). Kriging is an interpolation technique based on spatial autocorrelation (things that are close to one another are more alike than those further away from each other). The kriging semivariogram shows that towards 342 degrees N-NW the majority of the data have a medium spatial auto-correlation. The model therefore deforms isopachs in the N-NW direction. The resulting isopach map is shown in Figure 3-3. Several data changed not only with the distance, but also with the direction (anisotropy). Wind is the typical cause of anisotropy within a set of data points. An anisotropy correction was therefore applied to the model. Notably, the interpolation was not able to define closed isopachs (Figure 3-3). This arises from there being no data points towards the Southeast of the vent and so insufficient data to extrapolate the isopachs in this region.

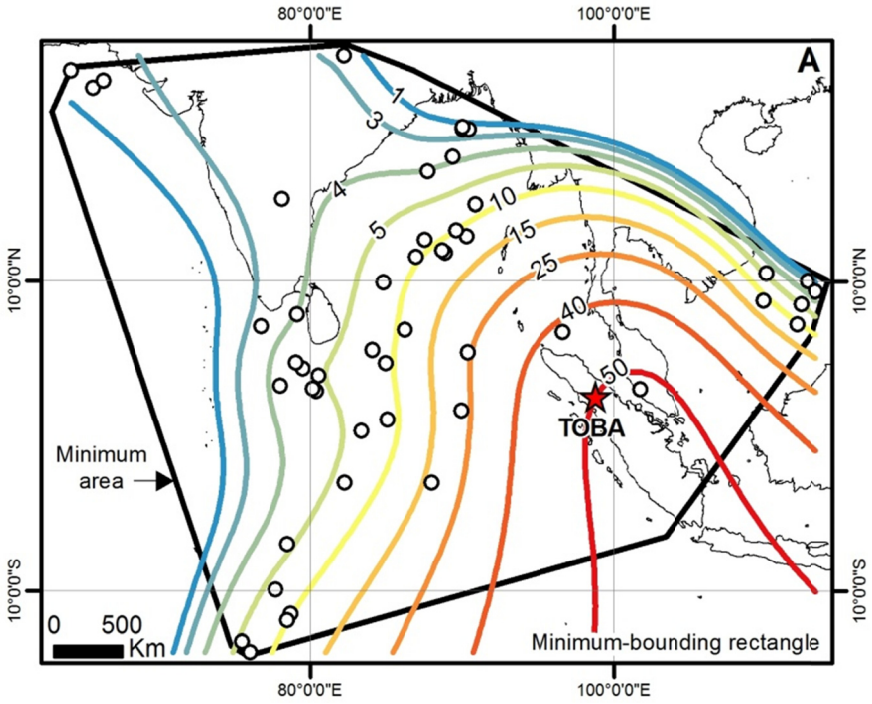

Figure 3-3 Isopach map of the YTT thickness. The absence of cores in the southeaster part of Sumatra precludes fitting a precise shape for the thickness distribution. The minimum area includes only the area with measurements, while the maximum area is defined as the 'minimum-bounding rectangle', which is a calculated surface based on the minimum rectangular extent definable with the available data.

The second technique applies a voronoi tessellation, a well-known method of spatial analysis that is defined as the partitioning of the plane such that, for any set of distinct data points, the cell associated with a particular data point contains all spatial locations closest to that point (Gowda et al., 1983). The tephra thickness data were transformed in voronoi cells with an algorithm based on Delaunay triangulation. The total thickness volume was calculated by summing the average thickness for the weighted area of each Voronoi cell ($V = \Sigma\ Polygon_{area} \times Polygon_{averaged\ thickness}$). Both the volume techniques were calculated using two areas: a smaller polygonal area (minimum area), defined by the extent of the available field data only; and a larger rectangular area (maximum area) determined by the statistical calculation itself (Figure 3-3). GIS names the maximum area the "minimum-bounding rectangle", since it represents the minimum rectangular area that can bound all the data. The polygonal area is 13×10^6 km^2, while the rectangular area is 24×10^6 km^3. Finally, I also applied a crude Area × average thickness calculation, to assess the minimum volume ejected.

3.4 Results

3.4.1 Size characteristics of distal fallout

Bulk particle-size analyses indicate that the YTT tephra is texturally fine sand, with a unimodal distribution. All particles at distal localities in the selected cores are <1000 μm in diameter, including significant fractions of fine (< 63 μm) and very-fine (< 32 μm) ash (Figure 3-4).

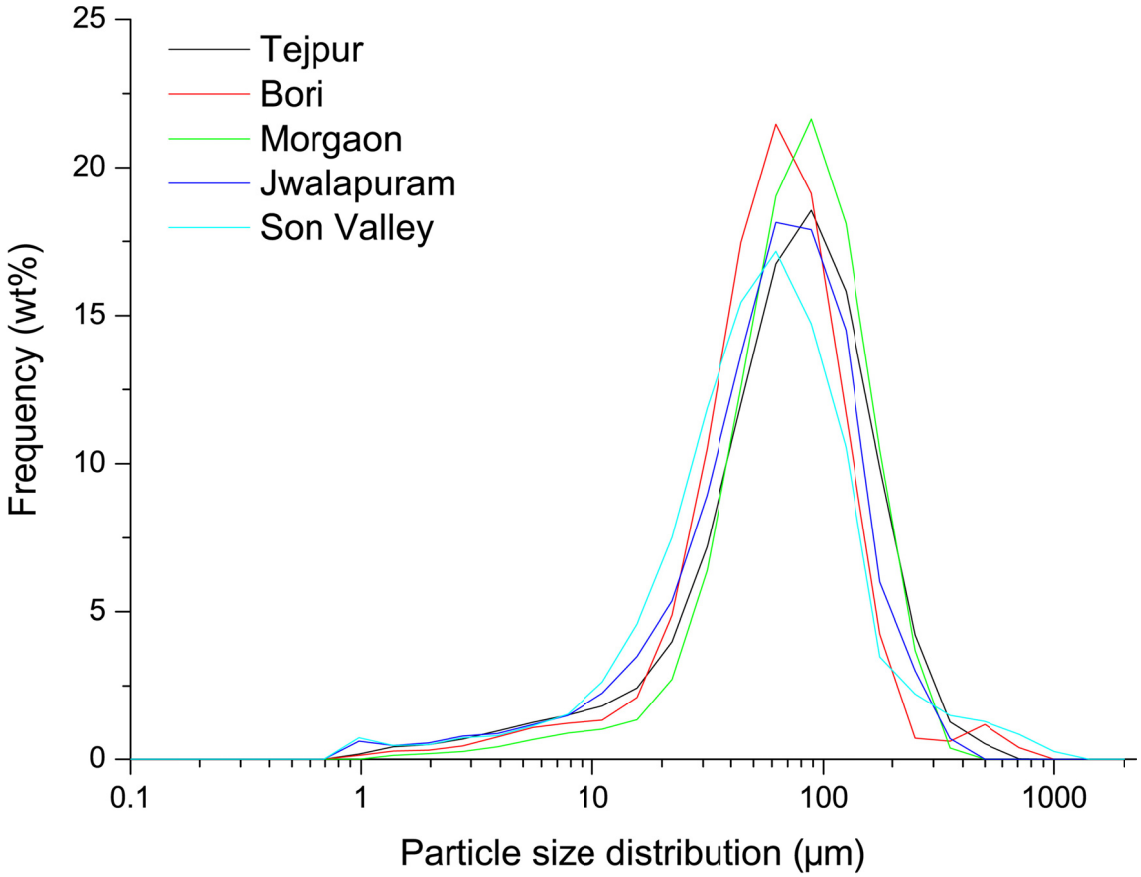

Figure 3-4 Particle-size composition of YTT ash fallout from five terrestrial sites in India. The mean particle size is between 62 and 88 μm. The right skewness of the distribution indicates a long tail of finest ash < 32 μm. The sharp cut off at 1000 μm shows that the YTT terrestrial distal deposits all fall within the category of low Reynolds numbers particles. Tejpur sample provided by Raj (Raj, 2007)

Plots A and B in Figure 3-6 compare the coarse and fine grain-sizes of the seven marine cores in relation to the distance from vent. The coarse layers show exponential decay with distance from the vent, with regression coefficient (R^2) of = 0.6. By contrast, the fine particles from the upper ash units show a weak exponential decay as a function of distance (R^2= 0.4).

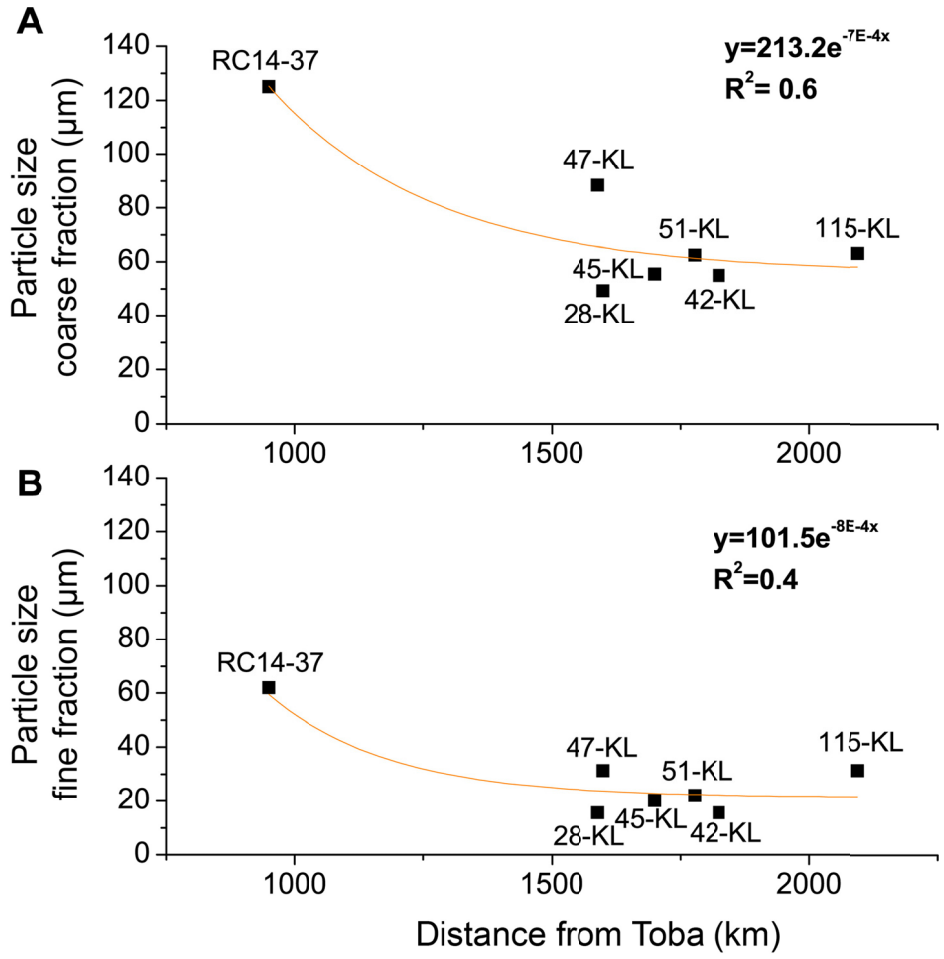

Figure 3-5 Plots of the coarsest (A) and finest (B) average particle sizes (volume %) vs. distance. The exponential equation in A) is evidence for a high correlation between coarse ash and distance (R^2= 0.6), while the equation in B) demonstrates a weaker correlation (R^2= 0.4) between finest particles vs. distance travelled. Samples 115-KL in graph B) also suggest that beyond ~ 2000 km a threshold occurs, over which the finest particles, characterised by low Reynolds numbers, are governed by different drag forces and settling behaviour.

3.4.2 Thickness variations and volume

In order to study the relation between the ash thickness and the distance from the vent, all the available marine and terrestrial YTT reporting primary ash were plotted against the distance from the caldera (Figure 3-6). Only the ash deposits within 1000 km from the vent show exponential thinning, while the majority of the distal tephra thicknesses are uncorrelated with distance. Figure 3-7shows the two volume calculations of this study and compare them with the model of Matthews et al. (2012). The thickness $T_0$was extrapolated using the log (T) vs. log (Area^{½}) plot (Figure 3-2). The total volume calculated with Eq. (2) resulted in ~ 1200 km^3 DRE and 5000 km^3 DRE, for the polygonal and rectangular area respectively (Figure 3-7a). The volume calculated on

the smaller area is in accordance with the model presented by Matthews et al. (2012), which yielded a volume of 1500 km^3.

The voronoi technique (Figure 3-7b) indicates a new ash volume between 770 km^3 DRE and ~ 2000 km^3 DRE. This estimate is consistent with both Rose and Chesner's original estimate of 800 km^3 minimum volume (Rose and Chesner, 1987), and the more recent estimate by Matthews et al. (2012) (Figure 3-7c).

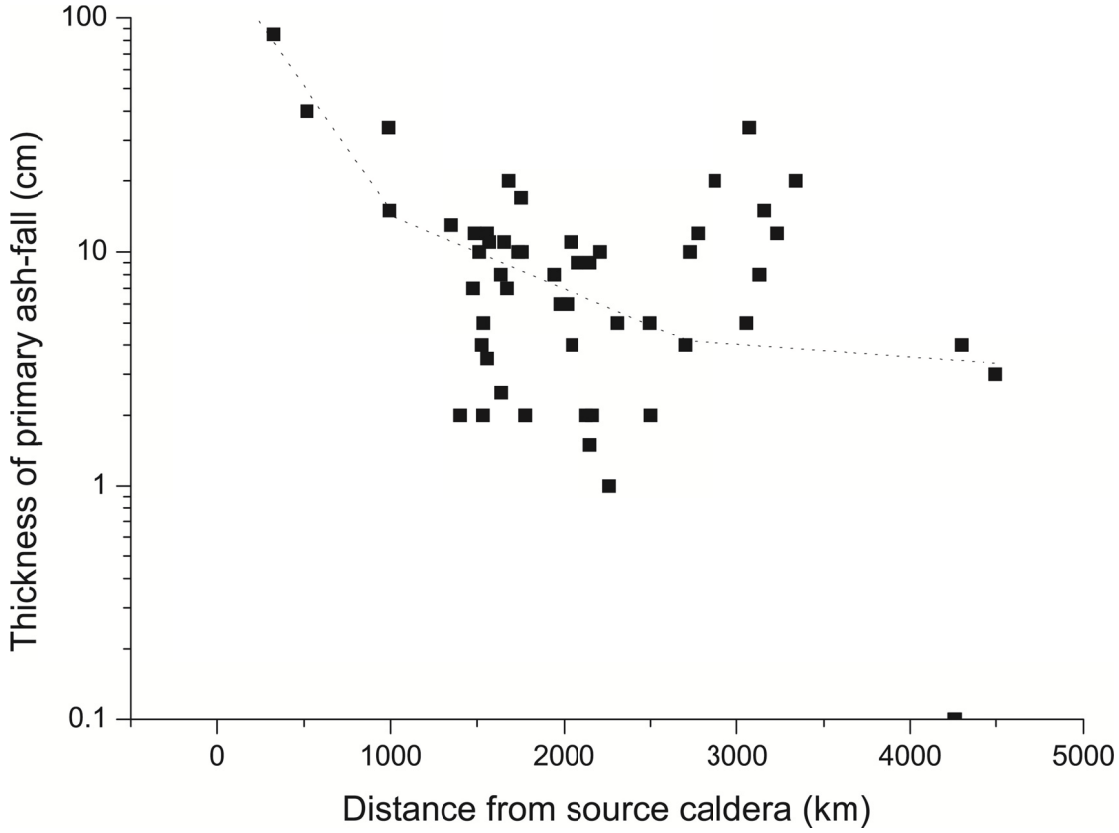

Figure 3-6 Thickness versus distance for terrestrial and deep-sea tephra layers. Reworked thicknesses and bioturbated layers (when indicated) were not included in the volume calculation (Table 3-2). The dashed black line shows the generalised model for thickness variations in tephra fall deposit with segmentation into three domains as described by Bonadonna et al. (1998), where the proximal segment is formed from deposition of high Reynolds number particles, and the distal segment is formed from deposition of low Reynolds number particles (while the transitional region has a mixture of the two particle populations). In the case of Toba, the proximal sites are at 390 km from the source.

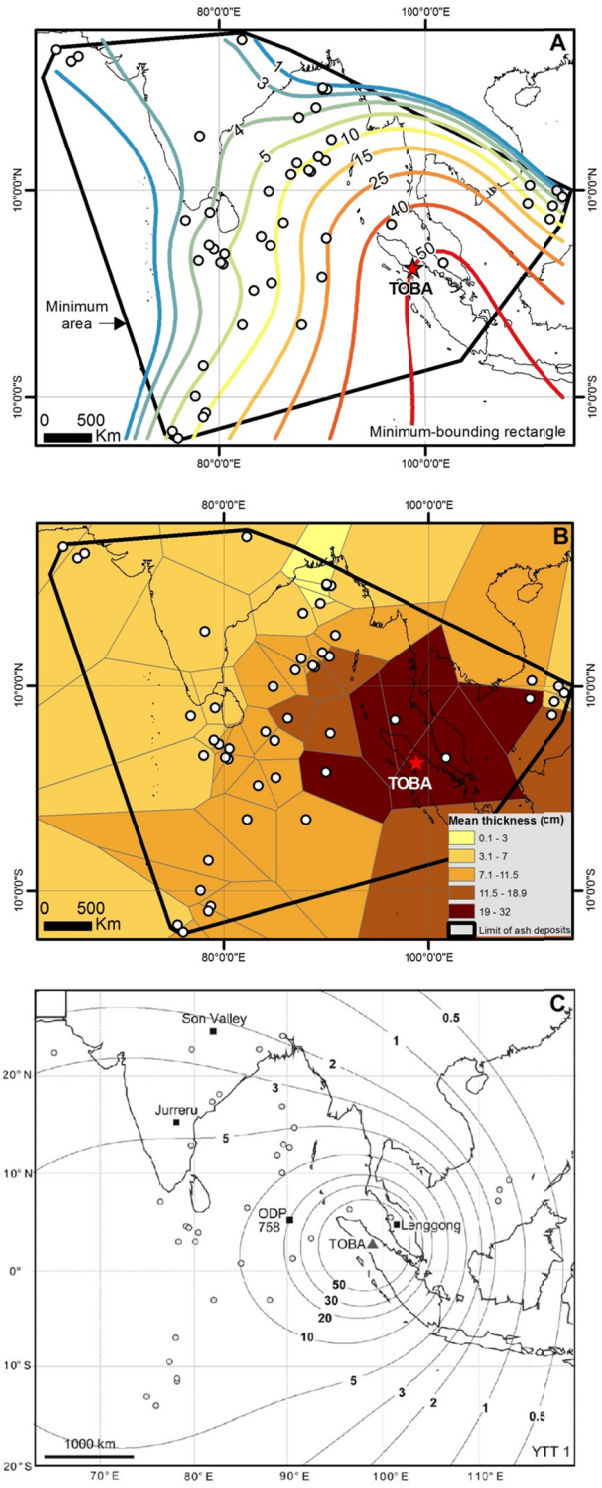

Figure 3-7 Thickness map obtained using (A) exponential decay of thickness (expressed in cm intervals) and (B) Voronoi tessellation. Average thicknesses values were calculated on the basis of the single thickness value, weighted by the area of each voronoi cell. (C) The isopach map in Matthews et al. (2012).

3.5 Discussion

3.5.1 Distribution of YTT co-ignimbrite ash as a function of particle size

Figure 3-4 shows that the majority of the YTT distal deposits are composed of fine to very fine ash. Figure 3-5 shows that the finer mode shows no variation in diameter with distance from source. Below 100 μm, a particle's terminal velocity depends highly on size of the particle and viscosity of the medium (Rose, 1993). In fact terminal velocity in this viscous-dominated regime depends on the square of the particle size, meaning smaller particles fall much more slowly (Wilson and Huang, 1979; Ersoy et al. 2006). In consequence, they spend more time suspended in the atmosphere and therefore have more time to be influenced by the complex currents in the atmosphere (Delmelle et al., 2005), which will increase the anisotropic nature of their distribution.

Although the closest marine core (ODP) is indeed negatively correlated with distance (all cores further away have a lower thickness) all the other marine cores, all lying further than 1000 km from the source, show no correlation with distance. Clearly, a single point is not enough to determine whether there is effectively a correlation, and certainly not enough to determine the nature of this correlation (e.g. exponential *vs.* power law). The absence of a clear relationship between distance and thickness, particularly at large distances, is important and, in addition to the plausible argument given above, based on the finer ash's being dominated by viscous flow, other authors have speculated on the mechanisms that produce an increasing anisotropic distribution with distance from the source.

Sparks and Huang (1980) interpreted this as evidence of two volcanic clouds (cf. **Chapter one**, Figure 1-4). They suggested that in proximal areas, both the fine and the coarse mode arose from the development of a Plinian column, which deposited both coarse and fine ash from a single-column developed around the vent. The distal deposits were, rather, generated in the co-ignimbrite cloud, much finer and able to be transported further away. Another explanation might lie in the wind action upon the co-ignimbrite cloud. Both proximal and distal deposits could have been generated in the co-ignimbrite cloud, but at major distance the local winds break up the co-

ignimbrite cloud and spread fine in different directions, generating the anisotropic effect observed in the database.

3.5.2 Wind patterns

Figure 3-6 shows that at proximal sites, the thickness decays with increasing distance from the vent, whereas beyond ~ 1000 km the thickness shows no correlation. The isopach areas used to calculate the total volume with the Pyle formula (Eq. (2)) do not resemble an elliptical or circular shape, because of the complex wind systems that affected the distribution of the tephra, and isopachs in ultra-distal deposits could not be constructed (Figure 3-3). Outcrops in ultra-distal areas (> 2000 km) are in fact too scarce to produce a robust statistical approximation with kriging (Rose and Durant, 2009).

Overall, the data suggest that the exponential model, which considers a homogeneous wind profile, is inadequate to determination of ash dispersal in ultra-regions when there are complex wind patterns present. A recent study used a three-dimensional simulation to determine the Campanian Ignimbrite tephra dispersal (Costa et al., 2012). The study was based on a set of fully time-dependent meteorological fields and a range of parameters such as erupted mass, mass eruption rate, column height, and total grain size distribution extrapolated from tephra cores in ultra-distal regions (up to 2500 km from the source). The approach was different from that of the study of Matthews et al. (2012): the Costa et al. (2012) simulation uses sets of different wind directions and climate conditions to describe the different ash thickness patterns observed in the real data. Instead Matthews et al. (2012) applied two static wind directions (N-NW and E wind) to describe the entire thickness distribution. The study finds that distal dispersal of co-ignimbrite ashfall cannot be modelled using isopach-based approximations. The simulation indicated 250–300 km^3 of total volume of tephra for the Campanian Ignimbrite, two orders of magnitude larger than the previous estimation suggested in Pyle et al. (2006).

3.5.3 Validity of volume models applied to the YTT

An accurate estimation of tephra volumes from deposit thinning in ultra-distal regions with traditional calculation is almost impossible. Given that the ultra-distal deposits are the chief

constituents of the co-ignimbrite ashfall (Figure 3-4), and exponential decay models fit neither the particle size nor the thickness distributions of ultra-distal ashfall deposits (Figure 3-5, Figure 3-6), it follows that the most important parameter to calculate the volume of the YTT co-ignimbrite ashfall is poorly constrained. In the absence of a better understanding of how much ultra-distal ash was ejected, any volume estimate will to have large error bands. This is clear in the results presented in Table 3-4: all the calculations have a large degree of uncertainty. The models can provide a good approximation for the more proximal deposits decaying with an exponential thickness, but they cannot describe the distal and ultra-distal thickness. This indicates two major conclusions: 1) at present, no model can provide better than an order-of-magnitude estimate of the tephra fallout volume; 2) from the foregoing conclusion, it seems unnecessary to apply exponential calculations or standard wind simulations. This is because they cannot both account for the fundamental, distinguishing features of the YTT ashfall: there is not a unique wind pattern, nor is there an exponential decline of the tephra thickness with distance.

Since all the methods presented both in this chapter and the literature are only crude estimations of the minimum volume, the choice of the voronoi tessellation appears the more suitable to constrain a simplified calculation of the volume of the ashfall. This is because it is more straightforward than both the exponential method and the computer simulation of Matthews et al. (2012). The values (770 –2000 km^3) overlap with the value of 800 km^3 suggested by Rose and Chesner (1987) and the most recent model by Matthews et al. (2012). Nevertheless, it is important to emphasise that the technique is not a model of tephra dispersal, but rather a statistical calculation that weights the individual samples. The results should therefore be interpreted considering some limits of the database, including the scarcity of data points and uneven data-point distribution. For example, Malaysian sites preserve an average thickness between 18 and 25 cm thick of the YTT, but this is potentially biased by inclusion of the Serdang ash (Stauffer et al., 1980), near Kuala Lumpur (Malaysia), reported to be 85 cm thick. Similarly, the absence of thickness information between Malaysia and the South China Sea influences the reliability of the thickness approximation of the inland values in the eastern sites. Another issue with the database is the possible overestimation of ash thickness, particularly in terrestrial sites subjected to significant post-depositional reworking.

In addition, the voronoi tessellation can be executed in GIS only within a projected coordinate system, thus introducing an area error when transforming the sphericity of the Earth to a flat plane. The error increases with the increase of the area, and this could account for overestimation of the rectangular-area volume. Finally, the polygonal-area volume obtained with the voronoi tessellation (770 km^3) is almost half the value estimated by Matthews et al. (2012). However, these authors reported an overestimation of the modelled thicknesses of between 0.2 and 5 times the observed data that could account for these differences. Table 3-4 summarises the range of published measurements, together with this study estimates of the total erupted ash (dense rock equivalent) volume. In view of the results discussed above, all the calculations presented and discussed in this work should be used only as indication of minimum volume.

Table 3-4 Comparison of volume approximation models.

Volume calculation technique	Volume km^3 (DRE) (polygonal area)	Volume km^3 (DRE) (rectangular area)
Exponential decay	1200	5000
Voronoi	770	2000
Simple approximation (Total Area × 10 cm average thickness)	650	1200
Simulation (Matthews et al., 2012)	1500	1900
Exponential (Rose and Chesner, 1987)	800	/

3.6 Conclusion

Since the end of the 1980s, several YTT ash deposits have been discovered in the Asian continent. A re-analysis of the YTT tephra deposits and an update of the current data were therefore timely.

From the particle-size distributions of seven marine cores it is observed that the coarse mode decreases in median diameter with distance from the source, whereas the finer mode shows no variation. This demonstrates that the characteristics of the fine particles strongly influenced the dispersal patterns and accumulation of the YTT ashfall deposits. Moreover, beyond ~ 1000 km, neither coarse nor fine particles are well characterised by an exponentially thinning model. This is likely due to winds having made the distribution highly anisotropic and introduced multiple directions of distribution.

Particle-size behaviour is reflected in the thinning rate of the ash sheet. Ashfall deposits beyond 1000 km from the vent show no exponential thinning decay in relation to the distance. This suggests that volume calculations based on exponential decay of thickness cannot be applied to the YTT. Moreover, the isopach map, necessary to application of the exponential method, cannot be properly traced, because of lack of data in extreme distal areas and because of the complex wind systems affecting the distribution of the tephra. It follows that volume calculations based on single wind directions (i.e. exponential and power-law models) cannot properly account for the YTT dispersal and volume, and that any volume estimation based on isopachs should be avoided.

The most reliable statistical interpolation to assess a simplified value of the minimal volume of ash ejected is the voronoi tessellation, which indicates a total volume ejected between 770 km^3 (DRE) and 2000 km^3 (DRE). These data correspond with the first estimates provided by Rose and Chesner (1987) and the most recent values provided by Matthews et al. (2012). In order to provide an accurate approximation of the total volume of ash ejected during the YTT eruption, more complex simulations accounting for the issues identified above should be proposed. An example is the recent three-dimensional simulation applied to the Campanian Ignimbrite distal deposits. A foreseen issue is that the YTT database is much less comprehensive than that for the Campanian Ignimbrite, but larger in terms of aerial distribution (the Campanian Ignimbrite tephra have been recovered at a maximum distance of 2500 km from the source, while the YTT ashfall mantle extend to *ca*. 4000 km).

It is necessary to investigate further the presence of YTT ash in marine sediment cores beyond southern Sumatra. At present the complete lack of data does not support the creation of a statistical surface correctly describing the YTT ashfall thickness. Several ODP sites in the southern and eastern part of Sumatra report the occurrence of Late Pleistocene ash layers (ODP 115 in the Indian Ocean south of Sumatra and ODP leg 117 in the southern part of the China Sea). New geochemical investigation of these cores might provide the data points necessary to establish the southerly distribution of the YTT ashfall sheet.

The next chapter analyses in detail the chemical features of 72 established YTT marine and continental sites. Geochemical fingerprinting represents the bridge between studying the YTT as

a volcanic entity and as sediment, since the geochemical composition of the glass needs to be assessed before proceeding to correlate tephra over greater distances.

Chapter 4. Geochemical patterns in proximal and distal Toba glass

Based on Gatti et al. (submitted paper)

Abstract

This chapter will focus on its *chemical* properties, synthesising all readily available geochemical data on glass compositions of the YTT. The study includes 69 analyses drawn from the literature and three new analyses. The dataset shows considerable chemical variation. Three principal sources of variation were identified: (i) compositional zonation of the magma reservoir (ii) post-depositional alteration, and (iii) methodological biases. The principal findings are that: (i) the YTT glass geochemistry at a given site strongly reflects the stage of the eruption that yielded the sample (ii) post-depositional glass alteration in marine environments is related to site-specific pore water chemistry (iii) all the samples show a minor 'laboratory fingerprint'.

4.1 Introduction

The YTT has been correlated geochemically through marine and continental deposits as far as 4000 km from Sumatra (Schulz et al., 2002). The YTT deposits have been identified and characterised geochemically for over 100 sites in southern and south-eastern Asia (Figure 4-1). Characterisation of major element geochemistry using an electron microprobe provides reliable results when applied to single glass shards (Westgate et al., 1994; Pearce et al., 2008b). The geochemistry of the YTT glass was assessed (Chesner, 1988) and used for distal stratigraphic correlations and dating (e.g. Horn et al., 1993). Westgate et al. (1998) concluded from the geochemical association that all the ash sites on the Indian subcontinent belong to the YTT. However, other studies have argued against this view and have proposed that the YTT is not the exclusive ash-fall distributed in India.

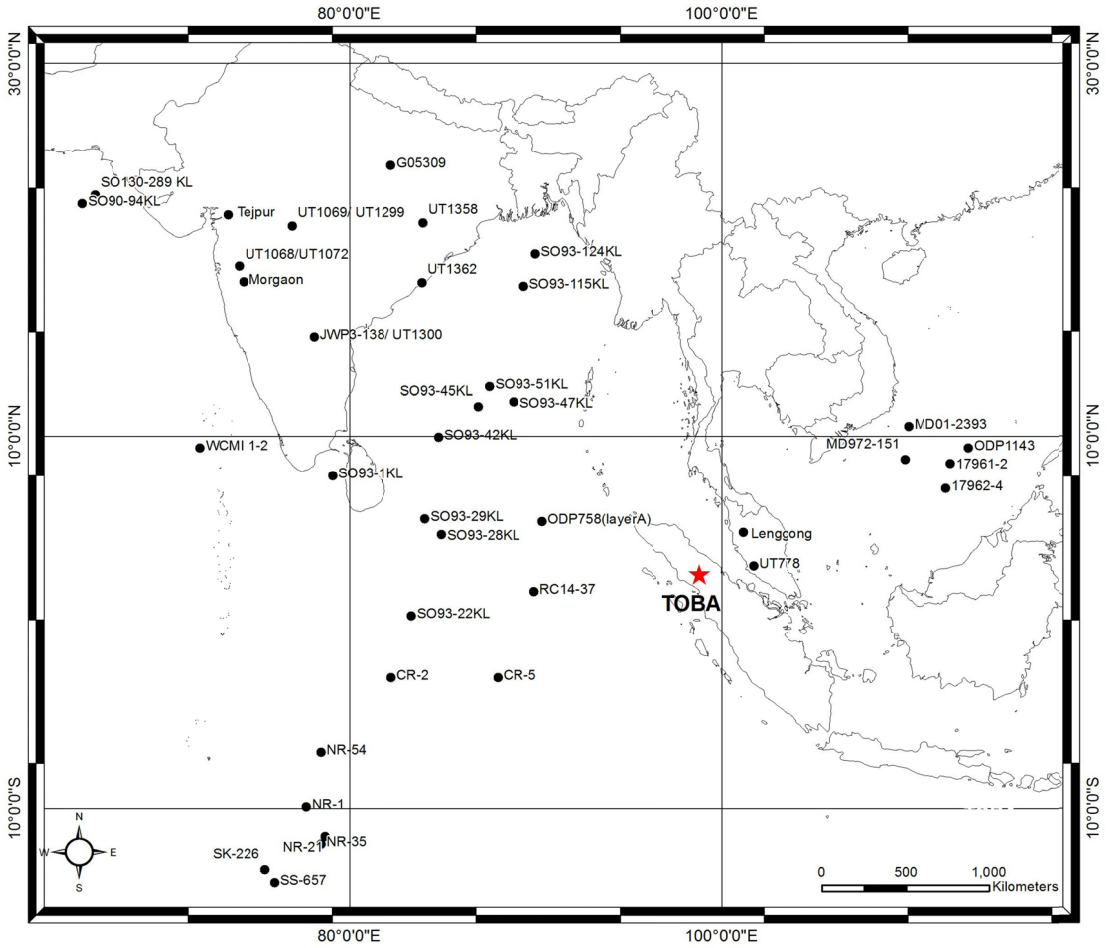

Figure 4-1 Geographical distribution of the YTT. The dots represent YTT sites that have been geochemically fingerprinted (Table 4-2). Note that the geochemical database of the YTT is more detailed than the thickness and particle-size database (**Chapter 3**, Table 3-2). This is because in order to recognise a tephra stratum, geochemical fingerprints are a compulsory procedure, thus every published work on the YTT presents complete major components analyses.

Westaway et al. (2011) obtained a significantly older age for the ash at Morgaon and Bori, in western India (~ 809 ka and ~ 714 ka respectively) and suggested that some tephra deposits in India belong to the Oldest Toba Tuff (OTT, dated 840 ± 30 ka) rather than the YTT. Major element fingerprinting has not resolved this issue since all three of the most recent Toba eruptions are geochemically similar (Smith et al., 2011; Lee et al., 2004). Neither the ash from Morgaon nor that from Bori shows significant major element differences when compared with other ash assigned to the YTT (Shane et al., 1995; Westgate et al., 1998). An approach that could succeed in showing the differences between ash grains is to characterise the YTT geochemical variations. Such variations reflect chemical stratification in the magma reservoir (and thus provide an indication of which eruption generated the ash), and post-depositional alteration. For

example, specific leaching processes, such as hydration (Noble et al., 1967; Cerling et al., 1985; Ghiara and Petti, 1995), or desilication (Wada, 1987; Bakker et al., 1996), give rise to alkali and SiO_2 removal, processes that can perturb K-Ar systematics, resulting in discrepant K-Ar ages (Cerling et al., 1985). Lastly, inter-laboratory reproducibility of chemical analyses should also be assessed in order to quantify possible biases that could result in apparent chemical differences.

Despite the significance that secondary chemical effects can have for the assessment of the distribution and age of the YTT, this issue has hitherto received little attention. The key questions include how much variation exists in distal YTT glass analyses and what the origins are of such variations. To address these questions and to identify pre-eruptive *versus* post-eruptive variability, all readily available YTT glass geochemical data were compared. Specifically, the variations reflecting analytical bias, magmatic differentiation or post-depositional alteration are addressed.

4.2 Geochemistry of the YTT

Ninkovich et al. (1978a) carried out the first characterisation of the Toba tephra from marine cores recovered from the Bay of Bengal. More recently, Chesner, (1998) provided an extensive overview of the YTT 'super eruption' and its occurrence in regional context.

Chesner (1998) described the YTT as sourced from a compositionally zoned silicic magma (Figure 4-2). Compositional zonation typically results from crystal fractionation. Crystallisation begins in the lower parts of the magma chamber, either on the walls or in the magma itself. The first minerals that crystallise (as temperature falls) are ferromagnesian ('mafic') compounds with low silica content, such as olivine and clinopyroxene. As the crystals form, the magma becomes depleted in Fe and Mg, SiO_2 enriched, and less dense. This more 'evolved' magma is buoyant and tends to rise to the roof zone. The continuous re-equilibration between melt and crystals leads to the formation of successive batches of evolved, SiO_2-rich liquids. These stratify at different levels according to their density. The result is a stratified cap of evolved magma, underlain by a pool of more mafic residual magma (Figure 4-2).

The bulk composition of the YTT rocks ranges from rhyolite to rhyodacite. Chesner (1998) classified the rocks as 'high-SiO_2' (> 73% SiO_2) and 'low-SiO_2' (68–72% SiO_2). Three-quarters of the YTT falls within the high-SiO_2 category (Chesner, 1998). Analyses of glass separates (from pumices) indicated that the glass matrix composition is more evolved than the bulk composition, with SiO_2 content typically exceeding 76%. This classifies the YTT glass separates as rhyolite (Marel, 1948). In accordance with Chesner's (1998) hypothesis that the magma chamber is compositionally zoned, the majority of the YTT erupted magma was stored in the upper part of a stratified magma chamber (Figure 4-2).

Recent studies on YTT crystal-hosted glass inclusions suggest pre-eruptive volatile contents of 4.0–5.5 wt% H_2O, < 100 ppm CO_2, < 2000 ppm Cl and < 32 ppm of S (Chesner and Luhr, 2010). The Toba glass compositions are almost eutectic (i.e. minimum melts in the Q-Ab-Or system, Smith et al., 2011), and even where crystallisation extent varies the composition of glasses remains similar (Chesner, 1998).

This chapter will demonstrate that if these glasses are compared on the basis of their elemental ratios rather than with traditional Harker diagrams, the glass geochemistry shows important variations, which reflect the magmatic source and preservation patterns of individual glass shards.

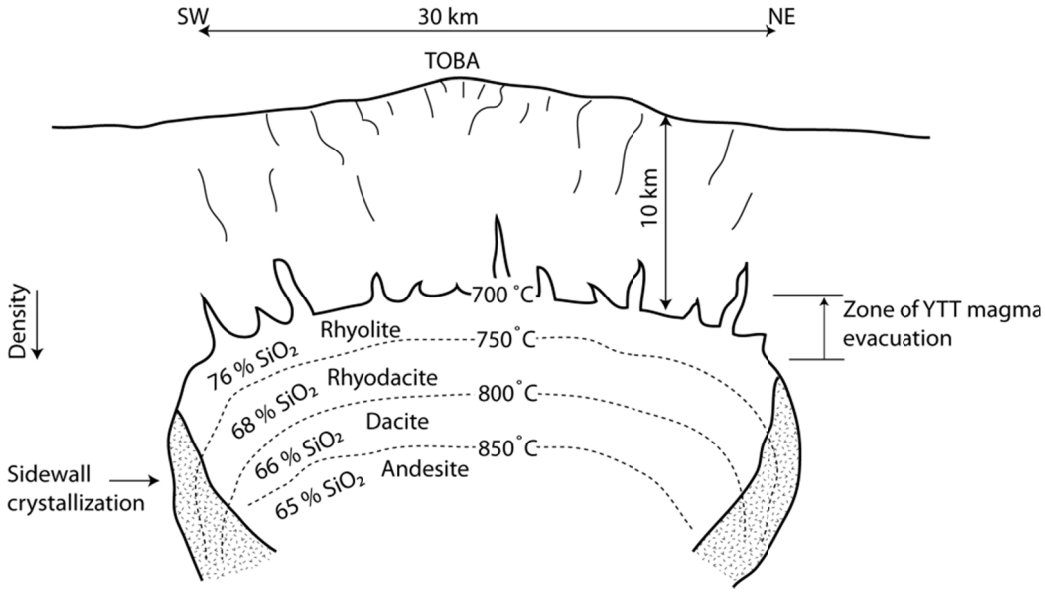

Figure 4-2 Schematic representation of the hypothesised magmatic zonation in the Toba magma chamber. Modified from Chesner, 1998.

4.3 Methods

Seventy-two YTT geochemical analyses were compiled and compared, 69 of which were obtained from the literature (Table 4-2, at the end of the chapter). The sites reviewed are shown in Figure 4-1 and listed in Table 4-2. The geochemistry of three samples of possible YTT ash origin from Morgaon (Figure 4-3a), Bori (Figure 4-3b) and Jwalapuram site 3 (Figure 4-3c), are also shown (Table 4-1). The Morgaon ash has not been geochemically characterised before, although it is the focus of discussion because it has provided an enigmatic date of ~ 800 ka (Mishra et al., 2009; Westaway et al., 2011). Samples were prepared for EPMA analyses, mounted, impregnated, polished and coated with gold (**§ 2.2** for description of EPMA methods).

Figure 4-3 YTT ash in continental environments. Samples from a) Morgaon, b) Bori and c) Jwalapuram were analysed to assess the accuracy and reproducibility of the compositional analyses.

Table 4-1 Samples used as controls in this geochemical study. The geochemical analyses were carried out in the Laboratories of Earth Science at the University of Cambridge. Standard deviations given in brackets. The data were also recalculated to 100% (normalized) for comparative purposes.

wt%	**Morgaon** *Kadhi river*	Morgaon *Normalized*	**Bori** *Kukdi River*	Bori *Normalized*	**JWP3-11S** *Jwalapuram site 3, Jurreru valley*	JWP3-11S *Normalized*
SiO_2	73.9 (1.16)	77.26	73.09 (1.10)	77.31	74.24(1.16)	77.47
Al_2O_3	11.80 (0.29)	12.34	11.57 (0.29)	12.24	11.75(0.29)	12.26
TiO_2	0.04 (0.05)	0.05	0.053(0.05)	0.06	0.05(0.05)	0.05
FeO_{tot}	0.85 (0.34)	0.89	0.84 (0.33)	0.89	0.84 (0.34)	0.88
MnO	0.04(0.08)	0.05	0.05 (0.08)	0.05	0.08 (0.08)	0.08
MgO	0.06 (0.05)	0.07	0.067 (0.05)	0.07	0.05(0.05)	0.05
CaO	0.76 (0.09)	0.79	0.76(0.10)	0.81	0.69 (0.09)	0.73
Na_2O	3.17 (0.2)	3.31	3.127(0.20)	3.31	3.23(0.20)	3.37
K2O	5.01 (0.40)	5.24	4.84(0.36)	5.12	4.90(0.39)	5.11
n	14		14		15	
Total	95.73	100.00	94.54	99.86	95.83	100.00

4.4 Results

4.4.1 Analytical bias

In order to quantify inter-laboratory reproducibility, the variability of SiO_2 and Al_2O_3 concentrations was plotted for identical samples reported in the literature (Table 4-2).

The samples overlap within the usually assumed uncertainty of ± 1 % given from the published sources (Table 4-3). The SiO_2 and Al_2O_3 concentrations for the sample collected on Jwalapuram site 3 (JWP) reported by Petraglia et al. (2007) and re-analysed here, are 0.2% lower than those of the sample analysed by Smith et al. (2001). Indian and Malaysian samples (filled circles in Fig. 4-4) reported by Westgate et al. (1998) show lower Al_2O_3 concentrations (by *ca*. 0.5%) with respect to the same samples analysed by Shane et al. (1995).

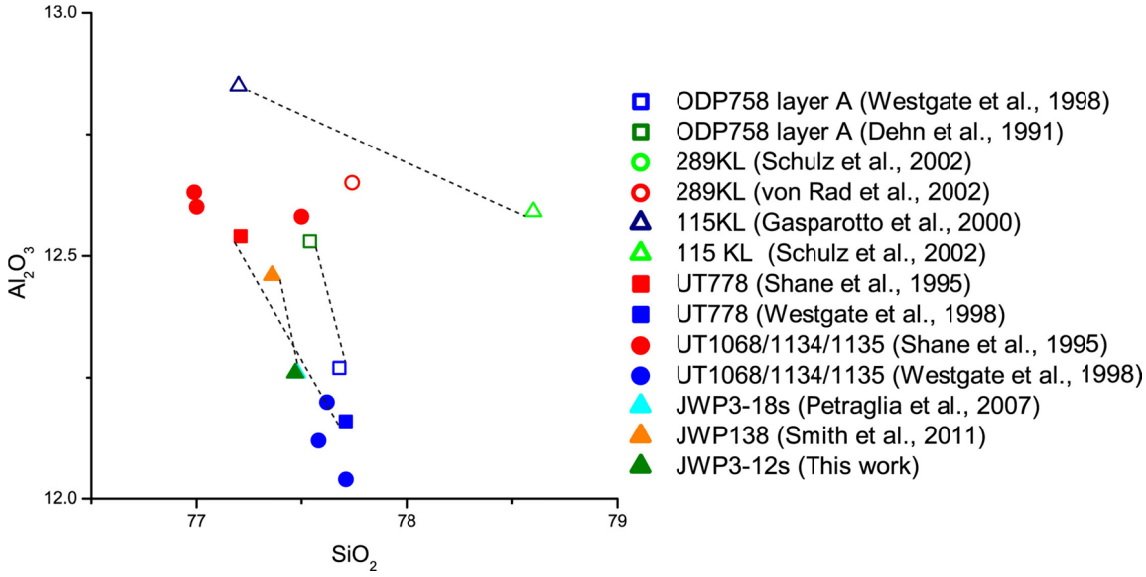

Figure 4-4 Inter-laboratory reproducibility. The graph shows four pairs and one triplet of samples analysed in several laboratories; pairs are highlighted by a dashed line joining the same symbols, colour-coded by laboratory. The samples overlap within the stated uncertainty of 1%.

4.4.2 Magmatic differentiation

Magmatic differentiation can be distinguished using elements that are immobile during secondary alteration processes (Floyd and Winchester, 1978). Immobile elements include TiO_2, Zr, Y, Nb and Al_2O_3. Characterised by insolubility in hydrous fluids at low temperatures, immobile elements are not prone to mobilisation during recrystallisation. They therefore provide

a reliable indicator of magmatic composition. In this case FeO, TiO_2 and Al_2O_3 were selected for distinguishing magmatic differentiation. Al is incorporated in feldspars and garnet, while Ti is incorporated in ilmenite and rutile. Since both Al and Ti are immobile, their ratio is set during fractional crystallisation and not subsequently modified by secondary alteration. FeO is a characteristic mafic element incorporated in olivine, thus the FeO/TiO_2 ratio provides a robust indication of the variation of mafic content in the magma.

Figure 4-5 shows the FeO/TiO_2 *v.* Al_2O_3/TiO_2 ratios extracted from YTT glasses from proximal and distal tephra deposits. The graph shows linear correlation (R= 0.93) between the FeO/TiO_2 and Al_2O_3/TiO_2 ratios, and an order of magnitude variation in the matrix composition of the glasses.

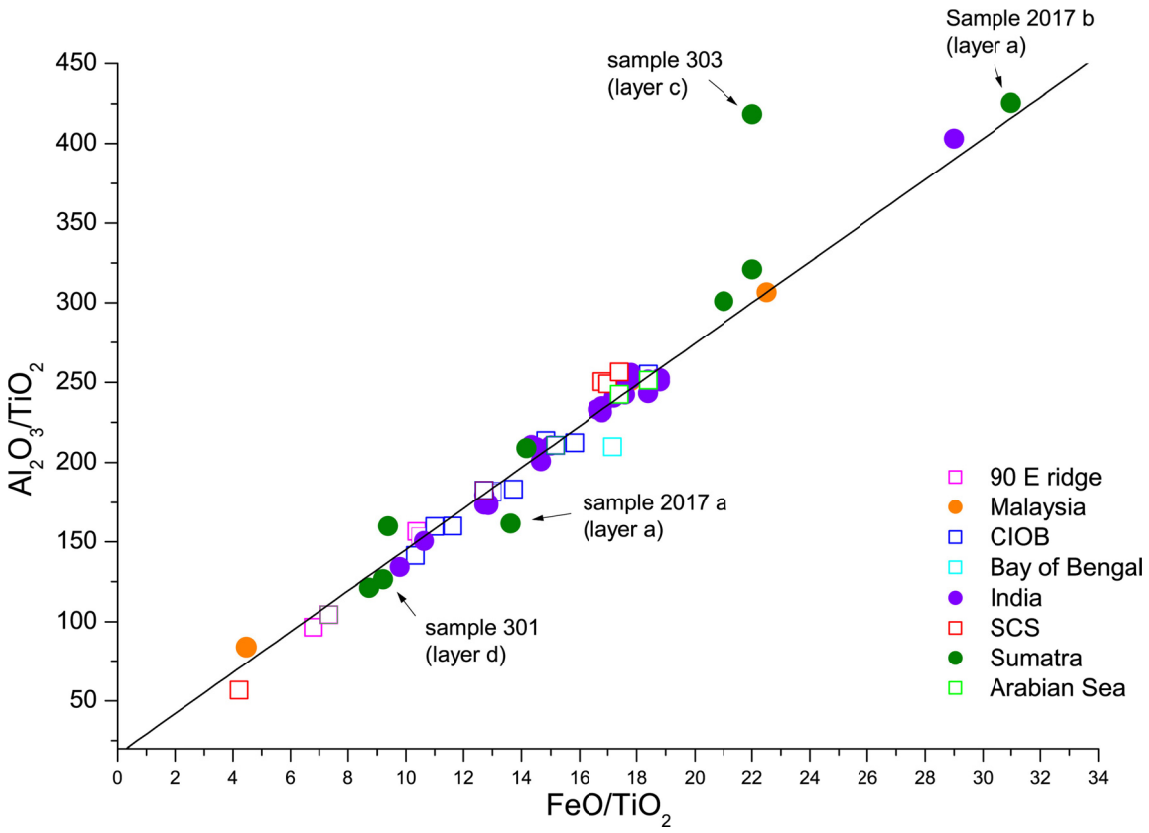

Figure 4-5 Immobile element ratios of YTT glasses from distal ash and proximal pumices deposits in Sumatra. The differences are substantial and unrelated to range or bearing of sites from Toba. The Bay of Bengal ash samples of Gasparotto et al. (2000) are not plotted, because no TiO_2 concentrations were reported.

Because the YTT was sourced from a zoned magma chamber, it is possible to test whether the variations are correlated with the stratification of the pre-eruptive magma. This hypothesis was

tested by locating analogues for three glasses collected from a pyroclastic unit in Sumatra (Figure 4-6) on Figure 4-5 (samples 301, 307 and 2017, Beddoe-Stephens et al., 1983). Sample 301, from the stratigraphically lowermost layer (Figure 4-6), plots at the lower left in Figure 4-5. Sample 2017b, from the uppermost unit (Figure 4-6), plots at the uppermost right in Figure 4-5. This suggests that the chemical composition of the YTT glass in distal deposits varies according to the time a given portion of tephra was erupted at the source. As expected for a diagram showing only immobile elements, there is no clear distinction between marine and continental ash. Note that the 18 oceanic core samples from Gasparotto et al. (2000) are not shown because these authors did not report TiO_2 concentrations.

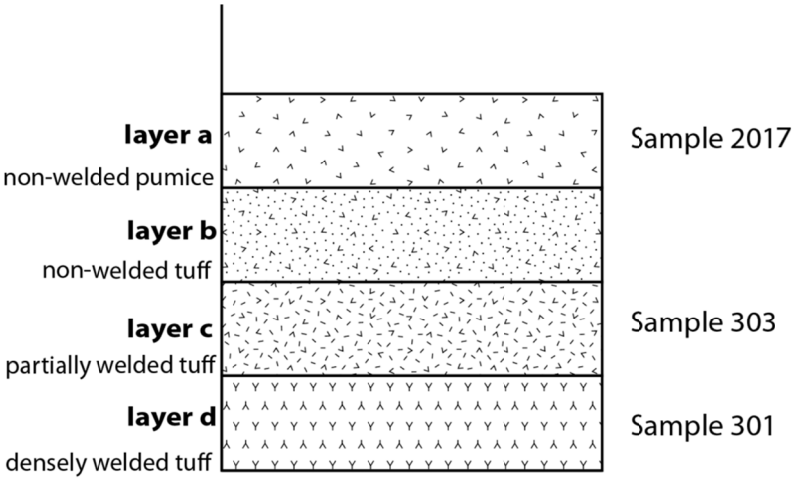

Figure 4-6 Stratigraphy of proximal YTT deposits in Sumatra (Beddoe-Stephens et al., 1983).

4.4.3 Post-depositional alteration

Ash units can be preserved in different types of marine and continental settings. The ash features vary according to the receiving environment (i.e. deep marine or carbonate platform; lacustrine or deltaic) and the sedimentological processes involved in the reworking (turbidites, floods, wind etc; see **chapter six**). When deposited in terrestrial environments, the ash can accumulate in tephra sequences that can reach 10 m or more in thickness (Figure 1-11, Figure 5-3, Figure 6-3). Such accumulations can result either from erosion of non-welded pyroclastic flow deposits in catchment areas, or from remobilisation of local fallout deposits from surrounding hillslopes (Kataoka et al., 2009). In the case of marine deposition, turbidites and bioturbation can disperse the ash layer, resulting in the creation of a gradual unit of volcanic material mixed with the

autochthonous sediments (Thompson et al., 1986). This implies that the ash grains, once deposited, are exposed to the action of water (meteoric or marine), sediments, organisms, bacteria and vegetations (Fanning and Schink, 1969). Mobile elements such as alkali and silica oxides are sensitive to temperature and water chemistry (Perez, 2009). They are therefore a good indicator of the influence of the receiving environment on the chemistry of the glasses.

Figure 4-7 shows the Na_2O/K_2O ratio (an indicator of diagenesis and of aqueous leaching) as a function of the FeO/Al_2O_3 (Fig. 4-7a) and SiO_2/Al_2O_3 (Fig. 4-7b) ratios. Most ash samples recovered from marine basins plot to the left of the diagram, distinct from the continental sites. Exceptions are the Sumatra samples, which show ~ 20% lower Na_2O/K_2O than the rest of the YTT samples; and Central Indian Ocean Basin (CIOB) samples. The latter are notably enriched in Na_2O over K_2O. Samples from the South China Sea (SCS) and the Arabian Sea have silica content similar to that of the samples from continental sites (Fig. 4-7b), and differ from that of the other marine samples. Indian samples from Westgate et al. (1998) have a ~ 4% higher SiO_2/Al_2O_3 with respect to the rest of the continental samples (Fig. 4-7b).

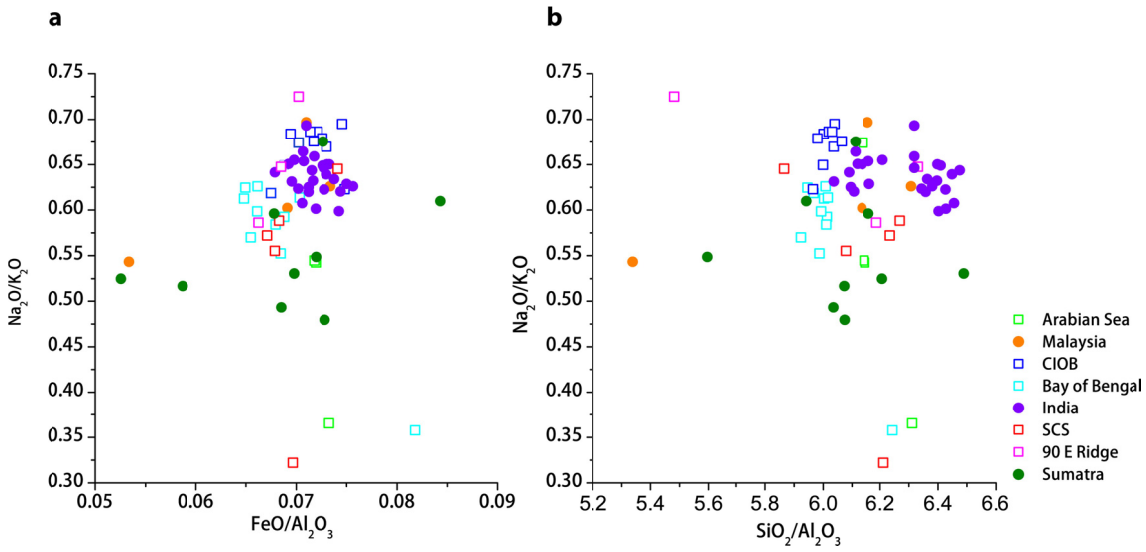

Figure 4-7 Comparison of distal ash elemental ratios, grouped according to location. (a) Na_2O/Ka_2O vs. FeO/Al_2O_3. The abscissa is the ratio of two immobile elements, which records the original composition of the magmatic source. In this diagram, alteration causes a vertical shift of data points. (b) Na_2O/Ka_2O ratio vs. SiO_2/Al_2O_3. For the abscissa we did not plot the silica concentration, but rather its ratio to alumina, so as to reduce the effect of inter-laboratory bias (Figure 4-4).

4.5 Discussion

4.5.1 Analytical bias

Analyses of the same glass samples performed in several laboratories show minimal offsets of 0.5-1% that are due to inter-laboratory shifts, possibly owing to different techniques applied, instrumentation, chemical and rock standards used. For example, the geochemistry of the sample from JWP site 3 (India) analysed in this work is similar to the data presented by Petraglia et al. (2007), collected from the same stratigraphic section. However, both are *ca.* 0.3% lower in Al_2O_3 than the sample characterised by Smith et al. (2011), analysed in another laboratory. The analyses from this research and from Petraglia et al. (2007) were conducted in the same laboratory with the same instrument. Similarly, there is a 1% difference in the SiO_2/Al_2O_3 ratio of the Indian samples from Westgate et al. (1998) as compared with the same Indian samples reported by (Shane et al., 1995). This could also account for the post-depositional shift in SiO_2/Al_2O_3 ratios shown by the samples from Westgate et al. (1998) in Fig. 4-7b. Such discrepancies are probably related to analytical bias and/or to large sample heterogeneity. These results suggest that geochemical analyses of the YTT in this database are affected by a systematic inter-laboratory uncertainty of *ca.* ± 1%. These variations do not mask the broad characterisation of the YTT, nor the magmatic differentiation shown in Figure 4-5. This is because the inter-laboratory error is smaller than the variations related to the magma chemistry. However, they do suggest that any study endeavouring to reveal very subtle geochemical variability should be based on analyses from a single laboratory, performed in a short period under stable instrumental conditions (Kuehn et al., 2011).

4.5.2 Pre-eruptive magmatic differentiation

Since immobile elements reflect the initial magma composition, the origin of the wide and tightly correlated variation between FeO/TiO_2 and Al_2O_3/TiO_2 shown in Figure 4-5 is likely to be a primary magmatic process. The trend in FeO/TiO_2 may reflect a progressive tapping of deeper, less evolved magma during the eruption. However, the increase in Al is more difficult to explain in such a scenario. The simplest way to produce the observed correlation is fractional crystallisation. Low Ti reflects crystallization of Fe-Ti oxides: the process depletes the melt in Ti

and Fe to form Ti-rich minerals, such as ilmenite, biotite or hastingsite. The diagram therefore shows the strong control of fractional crystallization on the YTT glass geochemistry.

It is also noted that low values of FeO/TiO_2 broadly correspond to ash ejected during the initial phases of the eruption, while high FeO/TiO_2 values are found in the ash ejected during the final phases (Figure 4-5). The changes in FeO/TiO_2 thus also reflect the compositional zonation of the magmatic chamber that arises through fractional crystallisation.

4.5.2.1 YTT *versus* OTT

The large YTT database allows comparison of a substantial number of YTT samples. OTT studies are rarer. Due to the debate on the age of the Morgaon ash, a comparison of the immobile elements of samples attributed beyond doubt to the OTT (~ 800 ka) and YTT (~ 73 ka) is presented (Figure 4-8). All the samples overlap. The pattern suggests that the Toba super-eruptions are similar in terms of both chamber dynamics and pre-eruptive differentiation processes.

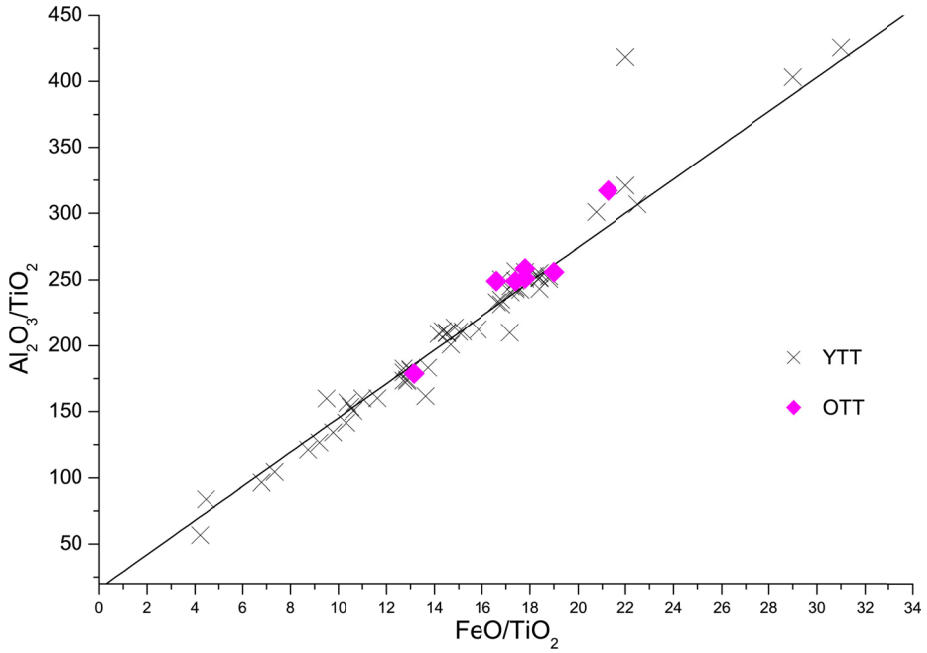

Figure 4-8 Immobile element ratios for YTT *versus* OTT. The YTT samples from figure 4-5 are shown as crosses, while the eight undoubted OTT samples are shown as filled symbols. The OTT samples resemble the YTT glasses. The graph clearly shows that major elements cannot discriminate between OTT and YTT. OTT samples from: Dehn et al. (1991) (90° E Ridge), Lee et al. (2004) (SCS), Liang et al. 2001 (SCS), Pattan et al. (2010) (CIOB), Smith et al. (2011) (90° E ridge).

The K concentrations of Morgaon ash reported by Westaway et al. (2011) are compatible with the typical K_2O concentrations of the YTT; therefore, the possibility of an older K-Ar age due to a massive (>90 %), very recent K depletion is excluded. The ratios of the Morgaon ash are higher in FeO/TiO_2 than the average YTT ash found in India. They are similar to YTT glass samples from Sumatra (Chesner, 1998), but also to the OTT sample 17957 from the South China Sea (Lee et al., 2004, Figure 4-8). Taking into account that the immobile major elements cannot distinguish between OTT and YTT, the hypothesis that Morgaon ash is sourced from the OTT eruption cannot be excluded by the present data.

4.5.3 Post-depositional alteration and definition of geochemical provinces

To investigate secondary element mobilisation, the mobile elements (alkalis) sensitive to secondary alteration were compared. The SiO_2/Al_2O_3 ratio takes into account the secondary mobilisation of Si by leaching, while minimising the influence of primary Si variation (e.g. due to magma reservoir zonation, **§ 4.5.2**). However, as Al is also enriched in the residual magma, the SiO_2/Al_2O_3 ratio is much more sensitive to secondary leaching than to primary magmatic processes.

Samples from the Arabian Sea and Bay of Bengal presented in Schulz et al. (1998) and sample MD97-2151 from the South China Sea (Song et al., 2000; see Table 4-3) present distinctive lower alkali ratios coupled with high Si. This places the samples in the lowermost part of the graph (Fig. 4-7b). However, the raw data (Table 4-3) show that the low alkali ratio is due to a significant low amount of Na (1.69 wt%), combined with unusually high Si content (79 wt%). It is possible that the analyses performed by these authors resulted in Na loss and migration of the latter into Si. The phenomenon is common when analysing tephra with EPMA and it can be avoided using few simple procedures (Kuehn et al., 2011).

On the other hand, the samples from Sumatra have Na/K ratios ~ 20% lower than those of the rest of the analysed samples (Fig. 4-7). The samples from Sumatra are not tephra, but welded tuff and pumices. The exposure of the welded rocks to tropical weathering, coupled with differences between welded rock and tephra, can explain the differences between the Sumatra samples and the rest of the database.

It is difficult to speculate on the observed post-depositional weathering trends and relate them unmistakeably to specific environments of deposition (i.e. deep marine ocean, continental etc.), since several samples (i.e. the Nineties Ridge tephra) follow none of these categories. However, broadly, the Bay of Bengal tephra show 7–8% lower Na/K ratio and ~ 3% lower SiO_2/Al_2O_3 ratio with respect to those from continental sites; the CIOB presents SiO_2/Al_2O_3 loss (~ 3%); the SCS and the Arabian Sea data show a lower Na/K ratio (~ 7%) compared to the continental sites, but have SiO_2/Al_2O_3 ratios similar to ash deposited in subaerial environments. Site-specific pore water chemistry could account for the evidenced desilication and alkali loss. Data from the Ocean Drilling Project show that the silica content of the interstitial water of the ODP1143 core (2771 water depth, see Table 4-2), in the South China Sea is between 100 to 900 times higher than the silica in the ODP 116-718 core, from the Central Indian Ocean (4730 m water depth). Alkalinity is also higher in the South China Sea (10.1 mM *versus* 5.13 mM of the Indian Ocean), while salinity appears similar for both the interstitial water. The ODP website reports only one drilled core in the Bay of Bengal, the DSDP 22-218, in the lower part of the fan. Data regarding specific elements are not available; however the reported salinity of the Bay of Bengal interstitial water is averagely 2% lower than the South China and Indian Ocean water.

Furthermore, differences in individual ion concentrations (e.g. Si, Na^+, K^+) could account for the differences showed in Fig. 7-8. For example, alkali migration is a common feature in ash buried in marine environments (Shikazono et al., 2005), and several marines sites (i.e. Bay of Bengal, South China Sea, Arabian Sea) show a 7–8% lower Na/K ratio. However, the sites from the Central Indian Ocean have higher level of alkali, similar to continental sites. The CIOB ash might have been naturally enriched in alkali. Another possibility is that the CIOB ash was lower in alkali concentration and this might have inhibited the hydrogen exchange necessary to induce significant alkali migration (Cerling et al., 1985).

From the discussion above, it appears that secondary alteration can influence the alkali and silica concentrations in the rhyolitic glass. Marine deposits from the Bay of Bengal overall show ~ 8% lower Na/K and ~ 3–4% lower SiO_2/Al_2O_3 ratios than continental sites. The South China Sea tephra show a similar alkali loss, but have SiO_2/Al_2O_3 ratios similar to the continental sites. The

Central Indian Ocean ash show silica loss of ~3-4% with respect to the continental samples, but does not show alkali loss similar to the other marine sites.

4.6 Conclusion

The samples analysed at several laboratories reveal a baseline inter-laboratory variability of ± 1 %. Although these variations do not influence the characterisation of the YTT fingerprints, these internal differences should be taken into account when using chemical fingerprints for analytical studies that require a resolution higher than 1 %.

Major differences are found when comparing immobile elements ratios (FeO/TiO_2 and Al_2O_3/TiO_2). Glass varies from higher-TiO_2 rhyolite (FeO/TiO_2 ratio between 0.1 and 10), to lower-TiO_2 rhyolite (FeO/TiO_2 >22). The ratios indicate the stages of magma fractional crystallisation. Crudely, the enrichment in FeO/TiO_2 also reflects the magma drawdown depth vs. time of the eruption: the first phase of the eruption ejected the most evolved magma, situated in the upper part of the chamber. This is consistent with fractional crystallization driving the process of zonation of the YTT magma reservoir.

The mobile (Na, K and Si) *versus* immobile (Fe and Al) element plots showed as differences relate to site-specific water pore chemistry, namely Si-enrichment, and individual ion concentrations can influence the content of alkali and silica of the marine tephra, with variations that range from 7-8% for alkali and 3-4 % for silica.

Geochemical fingerprinting is an important tool which allows the YTT distal deposits to be used as chronological markers. Once the ash has been identified, the tephra deposits need to be analysed in their stratigraphic context, to establish their value as a stratigraphic marker. Sedimentological and stratigraphic features of the tephra deposits thus need to be carefully interpreted in order to understand the path and mechanisms that lead to the deposition and preservation of the ash. The following chapters (**five and six**) deal with the assessment and understanding of such mechanisms, using YTT tephra layers in two distinct environmental settings.

Table 4-2 Literature data used for geochemical comparison. Locations listed here are reported in Figure 4-1; w.d. = water depth. In case of multiple sampling from the same core (i.e. Gasparotto et al., 2000) the lowest sample was used. FeO_{tot} values from Chesner (1998) and Pattan et al. (2001) calculated from Fe_2O_3.

Sample	Location	Environment	Reference
MD01-2393	South China Sea	Submarine/continental slope (1230 m w.d.)	Liu et al., (2006)
MD97-2151	South China Sea/ south-eastern Vietnam	Submarine/shallow shelf (Wan–An Shallow, 1550 m w.d.)	Song et al. (2000); Chen et al. (2000)
17961–2	South China Sea	Submarine/ carbonate platform with hemipelagic sediment drape (1968 m w.d.)	Bühring et al. (2000)
17962–4	South China Sea	Submarine/ carbonate platform with hemipelagic sediment drape (1969 m w.d.)	Bühring et al. (2000)
ODP1143 (layer A)	South China Sea	Submarine/unspecified (2782 m w.d.)	Liang et al. (2001)
ODP758 (layer A)	Southern Bay of Bengal/90east Ridge	Submarine/deep water/ on an echelon block 1000 m above the Bengal fan (2924 m w.d.)	Dehn et al. (1991)
SO130-289KL	Northern Arabian Sea/Pakistan margin	Submarine/continental slope off the Indus delta/oxygen minimum zone (571 m w.d.)	Schulz et al. (2002),Von Rad et al. (2002)
UT1069	Indian subcontinent/Narmada valley	Subaerial/fluvial/ semi-arid	Shane et al. (1995)
Kota Tampan	Malaysia	Subaerial/palaeofluvial/tropical humid	Ninkovich et al. (1978a)
ID 680	Toba, Siguragura (glass fraction)	Subaerial/volcanic caldera/tropical humid	Ninkovich et al. (1978a, 1979)
RC14-37	Southern Bay of Bengal/90east Ridge	Submarine/deep sea	Ninkovich et al. (1978a, 1979)
94A5-G	Toba (glass fraction from pumice)	Subaerial/volcanic caldera/tropical humid	Chesner (1998)

63A1-G	Toba (glass fraction from pumice)	Subaerial/volcanic caldera/tropical humid	Chesner (1998)
R301(M)	Toba, Haranggaol (glass matrix from welded tuff)	Subaerial/volcanic caldera/tropical humid	Beddoe-Stephens et al. (1983)
R303(M)	Toba, Haranggaol (glass matrix from unwelded tuff)	Subaerial/volcanic caldera/tropical humid	Beddoe-Stephens et al. (1983)
2017(M)-1	Toba (glass matrix from unwelded pumice)	Subaerial/volcanic caldera/tropical humid	Beddoe-Stephens et al. (1983)
2017(M)-2	Toba (glass matrix from unwelded pumice)	Subaerial/volcanic caldera/tropical humid	Beddoe-Stephens et al. (1983)
SO90-94KL	Northern Arabian sea/ Indus fan	Submarine/ unspecified (2109 m w.d.)	Schulz et al. (2002)
SO93-115KL	Middle Bengal Fan	Submarine/unspecified	Schulz et al. (2002)
UT1068	Kukdi River W.India	Subaerial/fluvial/semi-arid	Shane et al. (1995)
UT788	Serdang, Malaysia	Subaerial/lacustrine/tropical humid	Shane et al. (1995)
CR-02	Central Indian Basin	Submarine/deep ocean/ abyssal siliceous oozes (4900 m w.d.)	Pattan et al. (1999)
CR-05	Central Indian Basin	Submarine/deep ocean/ abyssal siliceous oozes (4300 m w.d.)	Pattan et al. (1999)
NR-1	Central Indian Basin	Submarine/deep ocean/ abyssal siliceous oozes (5250 m w.d.)	Pattan et al. (1999)
NR-21	Central Indian Basin	Submarine/deep ocean/ abyssal siliceous oozes (5325 w.d.)	Pattan et al. (1999)
NR-35	Central Indian Basin	Submarine/deep ocean/ abyssal siliceous oozes (5450 m w.d.)	Pattan et al. (1999)
NR-54	Central Indian Basin	Submarine/deep ocean/ abyssal siliceous oozes (5200 m w.d.)	Pattan et al. (1999)

SK-226	Central Indian Basin	Submarine/deep ocean/ abyssal siliceous oozes (5270 m w.d.)	Pattan et al. (1999)
SS-657	Central Indian Basin	Submarine/deep ocean/ abyssal siliceous oozes (5050 m w.d.)	Pattan et al. (1999)
WCM-1	Western Continental Margin of India/Arabian Ocean	Submarine/ (2300 m w.d)	Pattan et al. (2001)
WCM-2	Western Continental Margin of India/Arabian Ocean	Submarine/ (2300 m w.d)	Pattan et al. (2001)
1KL 395	Bay of Bengal	Submarine/continental slope/ hemipelagic (395 cm from the top of the piston core.)	Gasparotto et al. (2000)
22KL 104	Bay of Bengal	Submarine/foot of seamount in fan area/pelagic (104 cm from the top of the piston core.)	Gasparotto et al. (2000)
22KL 719.5	Bay of Bengal	Submarine/foot of seamount in fan area/pelagic (718 cm from the top of the piston core.)	Gasparotto et al. (2000)
28KL 227	Bay of Bengal	Submarine/floor of seamount in fan area/pelagic (227 cm from the top of the piston core)	Gasparotto et al. (2000)
29KL 170	Bay of Bengal	Submarine/turbidite plain/hemipelagic (170 cm from the top of the piston core)	Gasparotto et al. (2000)
29KL 173	Bay of Bengal	Submarine/ turbidite plain/hemipelagic (169 cm from the top of the piston core	Gasparotto et al. (2000)
29KL 176	Bay of Bengal	Submarine/ turbidite plain/hemipelagic (169 cm from the top of the piston core.)	Gasparotto et al. (2000)
42KL	Bay of Bengal	Submarine/mud waves above plain level/hemipelagic (267 cm from the top of the piston core	Gasparotto et al. (2000)

45KL	Bay of Bengal	Submarine/channel levee/turbidite (1067 cm from the top of the piston core.)	Gasparotto et al. (2000)
45KL 1075–1078	Bay of Bengal	Submarine/ channel levee/turbidite (1075 cm from the top of the piston core.)	Gasparotto et al. (2000)
47KL 151.5–154	Bay of Bengal	Submarine/trapped levee in old channel/hemipelagic with turbidite (152 cm from the top of the piston core)	Gasparotto et al. (2000)
47KL 161–162	Bay of Bengal	Submarine/ trapped levee in old channel/ hemipelagic with turbidite (161 cm from the top of the piston core)	Gasparotto et al. (2000)
51KL 721–723	Bay of Bengal	Submarine/marginal levee of active channel/turbidite (721cm from the top of the piston core)	Gasparotto et al. (2000)
51KL 729–732	Bay of Bengal	Submarine/marginal levee of active channel/turbidite (729 cm from the top of the piston core)	Gasparotto et al. (2000)
51KL 738–741	Bay of Bengal	Submarine/marginal levee of active channel /turbidite (738cm from the top of the piston core)	Gasparotto et al. (2000)
115KL 391–393	Bay of Bengal	Submarine/middle fan, distant to channel/ hemipelagic (398 cm from the top of the piston core)	Gasparotto et al. (2000)
115KL 397–399	Bay of Bengal	Submarine/middle fan, distant to channel/ hemipelagic (389 cm from the top of the piston core)	Gasparotto et al. (2000)
124KL 454–456	Bay of Bengal	Submarine/upper fan/ hemipelagic (454 cm from the top of the piston core)	Gasparotto et al. (2000)
NP4, NP6, NP7 & NP8	Sumatra	Subaerial/ volcanic caldera/ tropical humid	Smith et al. (2011)
NP5	Lenggong, Malaysia	Subaerial/fluvial/tropical humid	Smith et al. (2011)

JWP138	Jwalapuram, India	Subaerial/ palaeolacustrine/arid	Smith et al. (2011)
G05309 & GOC1	Son Valley, India	Subaerial/fluvial/semi-arid	Smith et al. (2011)
JWP3-18s	Jwalapuram, India	Subaerial/ palaeolacustrine/arid	Petraglia et al. (2007)
UT1069	Indian subcontinent	Subaerial/fluvial/ semi-arid	Westgate et al. (1998)
UT1070	Indian subcontinent	Subaerial/fluvial/semi-arid	Westgate et al. (1998)
UT1299	Indian subcontinent	Subaerial/fluvial/ semi-arid	Westgate et al. (1998)
UT1359	Indian subcontinent	Subaerial/fluvial/ semi-arid	Westgate et al. (1998)
UT1358	Indian subcontinent	Subaerial/fluvial/ semi-arid	Westgate et al. (1998)
UT1300	Indian subcontinent	Subaerial/fluvial/ semi-arid	Westgate et al. (1998)
UT1361	Indian subcontinent	Subaerial/fluvial/ semi-arid	Westgate et al. (1998)
UT1362	Indian subcontinent	Subaerial/fluvial/ semi-arid	Westgate et al. (1998)
UT1071	Indian subcontinent	Subaerial/fluvial/ semi-arid	Westgate et al. (1998)
UT1072	Indian subcontinent	Subaerial/fluvial/ semi-arid	Westgate et al. (1998)
UT1134	Indian subcontinent	Subaerial/fluvial/ semi-arid	Westgate et al. (1998)
UT1135	Indian subcontinent	Subaerial/fluvial/ semi-arid	Westgate et al. (1998)
UT1068	Indian subcontinent	Subaerial/fluvial/ semi-arid	Westgate et al. (1998)
Bukit Sapi	Lenggong, Malaysia	Subaerial/fluvial/tropical humid	This thesis
Kampung Luat 2	Lenggong, Malaysia	Subaerial/fluvial/tropical humid	This thesis
Kampung Luat 3	Lenggong, Malaysia	Subaerial/fluvial/tropical humid	This thesis
Bori	Western India	Subaerial/fluvial/semi-arid	This thesis
JWP-3	Southern India	Subaerial/ palaeolacustrine/arid	This thesis
Morgaon	Western India	Subaerial/fluvial/semi-arid	This thesis

Table 4-3. Major element compositions (on volatile-free basis) of glass shards from selected literature data. Values represent average; all data were recalculated to 100% for comparative purposes. FeO*, all Fe as FeO. Available original totals are reported in red.

Sample	Location	Reference	SiO_2	Al_2O_3	TiO_2	FeO*	MnO	MgO	CaO	Na_2O	K_2O
SO130-289KL	Arabian Sea	Schulz et al. (2002)	77.74	12.65	0.06	0.91	0.07	0.06	0.72	2.74	5.05
SO90-94KL	Arabian Sea	Schulz et al. (2002)	79.27	12.56	0.05	0.92	0.08	0.05	0.74	1.69	4.62
SO130-289KL	Arabian Sea	von Rad (2002)	77.74	12.65	0.05	0.91	0.07	0.06	0.72	2.75	5.04
SO130-289KL	Arabian Sea	von Rad (2002)	74.46	12.12	0.05	0.87	0.07	0.06	0.69	2.63	4.83
WCMI	Arabian Sea/ Western Continental Margin	Pattan et al., (2001)	76.94	12.53	0.12	0.88	0.12	-	0.83	3.40	5.04
1KL 395	Bay of Bengal	Gasparotto et al. (2000)	76.89	12.81	-	0.83	-	0.1	0.79	3.26	5.32
28KL 227	Bay of Bengal	Gasparotto et al. (2000)	76.99	12.86	-	0.88	-	0.12	0.82	2.96	5.36
29KL 176	Bay of Bengal	Gasparotto et al. (2000)	76.9	12.79	-	0.88	-	0.1	0.81	3.17	5.35
42KL	Bay of Bengal	Gasparotto et al. (2000)	76.89	12.98	-	0.85	-	0.07	0.82	3.05	5.35
45KL 1075–1078	Bay of Bengal	Gasparotto et al. (2000)	76.94	12.94	-	0.84	-	0.11	0.78	3.23	5.17
47KL 161–162	Bay of Bengal	Gasparotto et al. (2000)	76.91	12.89	-	0.87	-	0.1	0.78	3.23	5.22
51KL 738–741	Bay of Bengal	Gasparotto et al. (2000)	77.06	12.86	-	0.85	-	0.09	0.77	3.13	5.23
115KL 397–399	Bay of Bengal	Gasparotto et al. (2000)	77.2	12.85	-	0.85	-	0.07	0.72	3.2	5.11
124KL 454–456	Bay of Bengal	Gasparotto et al. (2000)	77.01	12.8	-	0.9	-	0.11	0.75	3.21	5.23
22KL 719.5	Bay of Bengal	Gasparotto et al. (2000)	77	12.81	-	0.87	-	0.07	0.77	3.13	5.36
SO93-115KL	Bengal Fan (Middle)	Schulz et al. (2002)	78.6	12.59	0.06	1.03	0.06	0.06	0.76	1.8	5.03
CR-02	Central Indian Basin	Pattan et al., (1999)	76.53	12.83	0.07	0.96	0.08	0.04	0.82	3.27	5.25
CR-05	Central Indian Basin	Pattan et al., (1999)	76.73	12.79	0.08	0.88	0.06	0.04	0.76	3.34	5.14
NR-1	Central Indian Basin	Pattan et al., (1999)	76.9	12.74	0.09	0.93	0.07	0.05	0.79	3.41	5.09

Sample	Location	Reference	SiO_2	Al_2O_3	TiO_2	FeO*	MnO	MgO	CaO	Na_2O	K_2O
NR-21	Central Indian Basin	Pattan et al., (1999)	76.94	12.82	0.06	0.89	0.06	0.05	0.78	3.42	5
NR-35	Central Indian Basin	Pattan et al., (1999)	76.95	12.69	0.07	0.91	0.05	0.05	0.76	3.44	5.09
NR-54	Central Indian Basin	Pattan et al., (1999)	76.94	12.74	0.06	0.95	0.08	0.04	0.78	3.46	4.98
SK-226	Central Indian Basin	Pattan et al., (1999)	76.81	12.76	0.05	0.92	0.05	0.05	0.8	3.48	5.07
SS-657	Central Indian Basin	Pattan et al., (1999)	76.89	12.75	0.07	0.91	0.05	0.06	0.79	3.46	5.04
JWP3-18s	India (Jwalapuram)	Petraglia et al. (2007)	77.48	12.26	0.06	0.87	0.08	0.06	0.80	3.44	4.96
JWP3-18s	India (Jwalapuram)	Petraglia et al. (2007)	73.59	11.65	0.05	0.831	0.08	0.05	0.76	3.27	4.71
UT1068	India	Shane et al. (1995)	77	12.6	0.05	0.89	0.07	0.06	0.76	3.35	5.04
UT1069	India	Shane et al. (1995)	77.15	12.67	0.06	0.86	0.08	0.06	0.78	3.26	5.08
UT1134	India	Shane et al. (1995)	77.5	12.58	0.07	0.89	0.07	0.06	0.79	3.29	5.03
UT1135	India	Shane et al. (1995)	76.99	12.63	0.06	0.9	0.07	0.06	0.77	3.22	5.15
UT1136	India	Shane et al. (1995)	77.26	12.59	0.05	0.92	0.06	0.05	0.74	3.22	4.95
UT1137	India	Shane et al. (1995)	77.12	12.63	0.05	0.94	0.06	0.05	0.80	3.14	5.06
UT1138	India	Shane et al. (1995)	77.22	12.53	0.05	0.94	0.06	0.05	0.73	3.18	5.06
JWP138	India	Smith et al. (2011)	77.36	12.46	0.05	0.87	0.07	0.06	0.75	3.25	4.96
G05309 & GOC1	India	Smith et al. (2011)	76.92	12.57	0.06	0.87	0.07	0.05	0.78	3.36	5.16
UT1069	India	Westgate et al. (1998)	77.78	12.26	0.05	0.86	0.05	0.04	0.8	3.08	4.94
UT1070	India	Westgate et al. (1998)	77.63	12.21	0.05	0.87	0.06	0.06	0.8	3.13	5.05
UT1299	India	Westgate et al. (1998)	77.81	12.02	0.05	0.86	0.03	0.05	0.75	3.24	5.03
UT1359	India	Westgate et al. (1998)	77.76	12.06	0.06	0.88	0.06	0.05	0.76	3.21	5.02
UT1358	India	Westgate et al. (1998)	77.76	12.1	0.03	0.87	0.06	0.05	0.8	3.08	5.12

Sample	Location	Reference	SiO_2	Al_2O_3	TiO_2	FeO*	MnO	MgO	CaO	Na_2O	K_2O
UT1300	India	Westgate et al. (1998)	77.68	12.12	0.05	0.88	0.05	0.06	0.83	3.22	4.96
UT1361	India	Westgate et al. (1998)	77.69	12.09	0.09	0.88	0.05	0.06	0.82	3.14	5.04
UT1362	India	Westgate et al. (1998)	77.67	12.14	0.07	0.89	0.06	0.05	0.75	3.24	4.98
UT1071	India	Westgate et al. (1998)	77.64	12.14	0.05	0.87	0.05	0.04	0.77	3.22	5.09
UT1072	India	Westgate et al. (1998)	77.57	12.16	0.05	0.92	0.07	0.05	0.83	3.17	5.06
UT1134	India	Westgate et al. (1998)	77.58	12.12	0.07	0.9	0.06	0.06	0.78	3.1	5.18
UT1135	India	Westgate et al. (1998)	77.71	12.04	0.08	0.85	0.07	0.05	0.74	3.14	5.17
UT1068	India	Westgate et al. (1998)	77.62	12.2	0.07	0.9	0.07	0.05	0.79	3.17	5
Kampung Luat 2	Malaysia (Lenggong)	Gatti et al. (2012)	77.39	12.27	0.04	0.90	0.08	0.07	0.78	3.27	5.22
Kampung Luat 2	Malaysia (Lenggong)	Gatti et al. (2012)	74.62	11.83	0.04	0.87	0.08	0.07	0.75	3.15	5.03
UM6315	Malaysia (Kota Tampan), glass shard fraction	Ninkovich et al. (1978a)	76.09	14.25	0.17	0.84[1]	0.05	0.10	1.05	2.62	4.82
UM6315	Malaysia (Kota Tampan), glass shard fraction	Ninkovich et al. (1978a)	72.6	13.6	0.16	0.75[2] / 0.05[3]	0.05	0.1	1.00	2.50	4.60
UT778	Malaysia (Serdang)	Shane et al. (1995)	77.21	12.54	0.05	0.89	0.08	0.06	0.72	3.4	4.88
NP5	Malaysia (Lenggong)	Smith et al., (2011)	77.24	12.59	0.06	0.87	0.07	0.06	0.77	3.09	5.13
ODP758	Nineties ridge	Dehn et al. (1991).	77.54	12.53	0.08	0.83	-	0.05	0.80	3.02	5.15
UT1363-ODP758	Nineties ridge	Westgate et al. (1998)	77.68	12.27	0.08	0.84	0.08	0.05	0.79	3.16	4.88
RC14-37	Nineties ridge	Ninkovich et al. (1978a)	74.17	13.53	0.14	1.03[1]	0.07	0.26	1.70	3.82	5.27
RC14-37	Nineties ridge	Ninkovich et al. (1978a)	71.80	13.10	0.14	0.15[2] / 0.85[3]	0.07	0.25	1.65	3.70	5.10
17961–2	South China Sea	Bühring et al. (2000)	78.04	12.45	0.05	0.85	0.07	0.06	0.76	2.86	4.86
17962–4	South China Sea	Bühring et al. (2000)	78.05	12.52	0.05	0.84	0.07	0.06	0.77	2.78	4.86

Sample	Location	Reference	SiO_2	Al_2O_3	TiO_2	FeO*	MnO	MgO	CaO	Na_2O	K_2O
ODP1143	South China Sea	Liang et al. (2001)	77.93	12.82	0.05	0.87	0.1	0.02	0.76	2.66	4.79
MD01-2393	South China Sea	Liu et al. (2006)	76.78	13.09	0.23	0.97	0.25	0.87	0.8	2.75	4.26
MD97-2151	South China Sea	Song et al. (2000)	79.38	12.78	0.07	0.89	0.06	0.04	0.75	1.47	4.56
R301	Toba (matrix glass)	Beddoe-Stephens et al. (1983)	77.36	12.66	0.10	0.92	0.07	0.02	0.66	3.31	4.90
R301	Toba (matrix glass)	Beddoe-Stephens et al. (1983)	74.32	12.16	0.10	0.88	0.07	0.02	0.63	3.18	4.71
R303	Toba (matrix glass)	Beddoe-Stephens et al. (1983)	77.88	12.55	0.03	0.66	0.06	0.01	0.79	2.76	5.26
R303	Toba (matrix glass)	Beddoe-Stephens et al. (1983)	74.32	11.98	0.03	0.63	0.06	0.01	0.75	2.63	5.02
2017_a	Toba (matrix glass)	Beddoe-Stephens et al. (1983)	77.49	12.84	0.04	0.88	0.05	0.07	0.63	2.64	5.35
2017_a	Toba (matrix glass)	Beddoe-Stephens et al. (1983)	74.72	12.38	0.04	0.85	0.05	0.07	0.61	2.55	5.16
2017_b	Toba (matrix glass)	Beddoe-Stephens et al. (1983)	77.57	12.77	0.03	0.93	0.04	0.05	0.52	2.62	5.46
2017_b	Toba (matrix glass)	Beddoe-Stephens et al. (1983)	74.89	12.33	0.03	0.9	0.04	0.05	0.5	2.53	5.27
63A1-G	Toba (glass from pumice)	Chesner (1998)	76.83	12.93	0.08	1.09	0.07	0.18	0.94	2.94	4.82
94A5-G	Toba (glass from pumice)	Chesner (1998)	78.12	12.04	0.04	0.84	0.06	0.15	0.62	2.79	5.26
6A2-G	Toba (glass from pumice)	Chesner, (1998)	77.6	12.78	0.08	0.75	0.06	0.20	0.80	2.6	5.03
Id 680	Toba (Si Gura Gura), glass shard fraction	Ninkovich et al. (1978a)	74.65	13.34	0.11	0.96[1]	0.06	0.36	2.27	2.89	5.27
Id 680	Toba (Si Gura Gura), glass shard fraction	Ninkovich et al. (1978a)	72.20	12.90	0.11	0.30[2] / 0.70[3]	0.06	0.35	2.20	2.80	5.10
NP4, NP6, NP7 & NP8	Toba	Smith et al., (2011)	77.24	12.54	0.06	0.85	0.07	0.05	0.78	3.1	5.2

[1] Values from Ninkovich et al. (1978a and 1979) were reported as Fe_2O_3 and FeO. It is inappropriate to simply add or subtract FeO mass % and Fe_2O_3 mass % to obtain the FeO_{tot}. In order to calculate the FeO_{tot} I applied the formula $\sum$ FeO= FeO+(Fe_2O_3 ÷ 1.11).[2] Fe_2O_3; [3] FeO.

Chapter 5. Stratigraphic significance of the YTT layer in the Son valley

Based on Gatti et al. (2011)

Abstract

The Middle Son Valley was the first site on the Indian subcontinent of reported discovery of YTT deposits. Although distal ash has been studied since the 1980s, its stratigraphy and the mechanisms involved in its transport and deposition have not been previously assessed. This chapter reports on the stratigraphy of the YTT ash layers in alluvial deposits of the Middle Son Valley, in order to reconstruct the taphonomy of the tephra deposits and the dynamics of their deposition. The YTT occurrences in the Middle Son Valley are shown to be unreliable as chronostratigraphic markers for millennial scale palaeoenvironmental reconstruction.

5.1 Introduction

The Middle Son Valley (Madhya Pradesh, North Central India) is the first locality in India from which findings of YTT were reported (Williams and Royce, 1982). Initially these sites were investigated for the abundance of Middle Palaeolithic archaeological assemblages (Acharyya and Basu, 1993). However, since the 1980s they have become the focus of palaeoenvironmental studies for understanding the immediate and longer-term impacts of the YTT super-eruption on climate and humans (Basu et al., 1987; Bobe et al., 2002).

To improve understanding of the extent and severity of the environmental impacts of the YTT eruption, it is critical to determine how long it took for the ash to be re-deposited and consolidated on the landscape. The longer the ash remained mobile in the environment, the more severe the impact on vegetation and associated ecosystems would have been (Fritz, 1980; Collins and Dunne, 1986).

Tephra successions, if suitably preserved, can be used as chronostratigraphic markers. The YTT stratum in the Middle Son Valley, in particular, has been repeatedly used as a marker horizon in archaeological investigations (Williams and Royce, 1982; Jones and Pal, 2005). For example, using artefacts in secondary contexts, Jones and Pal (2009) observed a change in lithic technology

between the tools below and above the ash, and proposed a shift in hominid behaviour during the Upper Pleistocene. This suggested that the Toba eruption contributed to such changes. Furthermore, recent studies by Jones (2010) and Jones (2012) used the YTT layer at two localities in the Son Valley, Ghoghara and Khunteli, to investigate the link between Toba ash, environmental disruption and hominid evolution. They proposed that the depositional regime in the Middle Son valley changed following the ash-fall, and this could have affected hominid population dynamics in the area.

Despite the frequent use of the Son Valley YTT stratum for archaeological and geological studies, its reliability as a stratigraphic marker has been given limited consideration. The aim of this chapter is to contextualise the distal YTT stratum of the Middle Son Valley through a study of the stratigraphy of the volcaniclastic sequences, in order to provide textural and structural details of the tephra units. This chapter presents a series of stratigraphic sections containing YTT tephra located between the Rehi River and the site of Khunteli (Figure 5-1), exposed in the modern riverside cliffs.

The characteristics of the preserved ash lead to an interpretation of the river activity before and after the eruption. This, together with the field evidence of their sedimentary context, suggests that the YTT deposits of the Son Valley area might not provide a reliable chronostratigraphic marker in the region for long-term palaeoenvironmental reconstructions and archaeological correlations. An exception is the site of Ghoghara.

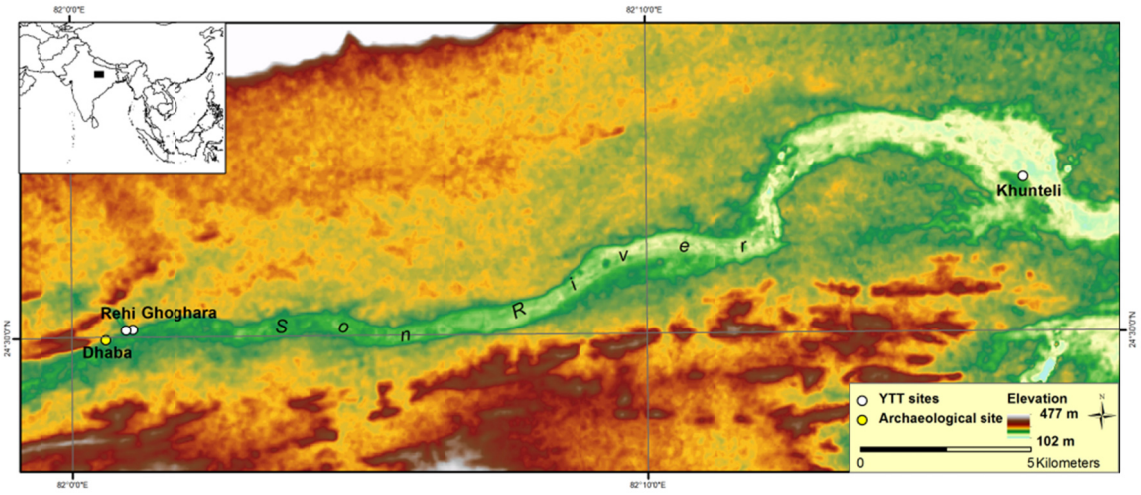

Figure 5-1 Location of the tephra sites in the Son Valley. The yellow dots on the map represent the logged sites presented in this work. DEM from ASTER GDEM (ASTER GDEM is a product of METI and NASA).

5.2 Study Area

The Middle Son Valley lies 100 km south of Allahabad and 130 km southwest of Varanasi, in north central India (24° 7' N, 80°/83° 50' E, Figure 5-1). The regional climate is sub-tropical, characterised by hot humid summers (April-September, temperatures > 40 °C), and cooler winters (October-March) with low precipitation. Affected by the summer monsoon from June to September, the topography and geomorphology of the hills and valleys reflect the intense summer runoff, which has deeply incised the river terraces.

The Son (784 km long) is one of the longest rivers of India and the longest of the southern tributaries feeding into the River Ganges. It flows, as does the Narmada River, along the line of a major E-W tectonic lineament, the Narmada fault (Williams and Royce, 1982). Originating in Madhya Pradesh, the Son flows north-northwest and cuts through Middle Proterozoic limestone and shale bedrock of the Vindhyan Super-Group (Singh, 1980) and Middle-Pleistocene and Holocene alluvial plains (Banerjee and Jeevankumar, 2007), before turning eastwards to encounter Middle Proterozoic sandstone of the Kaimur Range (Morad et al., 1991). The modern channel has incised the metamorphic bedrock to a depth of about 30-35 m, forming deposits dominated by sand (Bhattacharyya and Morad, 1993). Throughout its history, the passage of the Son river has been strongly influenced by climatic factors (reflected in changes in its flood-plain

deposition and channel down cutting), since the river is constrained laterally by its geological setting (Sharma and Clark, 1983; McMenamin et al., 1983).

The area of study includes river-cut cliffs in the alluvial zone between the confluence of the Rehi and Son rivers and Khunteli (or Khuteli) (Figure 5-1). The reported YTT deposits (Acharyya and Basu, 1993; Jones and Pal, 2005) comprise a discontinuous tephra bed covering an area of ~ 90 km^2 ranging in thickness from 20 cm to 3–4 m. Between Rehi and Ghoghara (first described by Williams and Royce in 1982), lateral variations within the ash deposits are minimal, and the ash unit appears repeatedly at a height between 4 and 6 m above the present river bed in cliff exposures. The Son river alluvial basin includes terraced surfaces flanked by floodplains, and point-bar and alluvial fan deposits. The main river channel is bounded by a series of Middle and Late-Pleistocene and Early-Holocene 10 to 30 m thick terraces, and deeply-incised seasonal channels known as '*nalas*'. The terrace incised by the modern Son has been intensively studied because of the presence of the YTT marker interstratified in the preserved fluvial sequence, as well as the coincidence of Middle Palaeolithic and Neolithic artefacts recovered from the sediments below and above the ash (Williams and Royce, 1982; Sharma and Clark, 1983; Williams and Royce, 1983; Jones and Pal, 2005; Jones and Pal, 2009; Haslam et al., 2010). The geological context of the terrace is unclear, mainly due to the absence of dates and robust stratigraphic correlation (Mandal, 1983).

The first study of the geomorphological succession and alluvial sequences of the Middle Son Valley was carried out by Williams and Royce (1983). A detailed geological survey was undertaken after the discovery, in the 1970s, of 334 localities yielding archaeological artefacts ranging from the Lower Palaeolithic to Neolithic periods (Sharma, 1980: 88-115). The Son Valley alluvial sequence has been subdivided into four formations (Table 5-1). In chronological order (oldest to youngest) they are: the *Sihawal Formation, Patpara Formation, Baghor Formation and Khetaunhi Formation* (Williams and Royce, 1982; Williams and Royce, 1983; Williams and Clarke, 1995; Williams et al., 2006). Several models have been proposed for the geomorphological evolution of the alluvial plain of the Middle Son Valley ranging from the early Pleistocene to the late Holocene (Williams and Royce, 1982, 1983; Williams and Clarke, 1995; Williams et al., 2006).

In their initial geomorphological model, Williams and Royce (1983) proposed that the aggradations of the floodplain started with the accumulation of non-fluvial colluvium (the *Sihawal Formation*), ~ 100 ka ago, followed by the aggradation of *Patpara* (~ 30 ka ago). During this period the river shifted to a low sinuosity bed-load regime and created a + 25 m high terrace. Following this phase of aggradation and incision, the river accumulated the sediments ascribed to the *Baghor Coarse* member, dated ~ 18 ka, maintaining the same style it had during the accumulation of Patpara. A drastic change has been suggested during the accumulation of the Baghor Fine member, (dated ~ 13 ka), during which the Son moved to a narrow, deep suspended load-dominated regime.

More recently, Williams et al., (2006) introduced a new unit between the deposition of the *Sihawal* and *Patpara* called the *Khunteli Formation*, dated ~ 58 ka (Table 5-1). The introduction of this new formation led to a new geomorphological model (Williams et al., 2006). In this model the authors suggest five major phases of aggradation at ~ 90 ka, ~ 73 ka, 58-45 ka, 39-16 ka, and 5.5-3.5 ka. These periods corresponded, respectively, to the deposition of *Sihawal*, *Khunteli*, *Patpara*, *Baghor* and *Khetaunhi Formations*. The phases of aggradation were said to correspond broadly to phases of colder and a drier climate, with weakened summer monsoon regimes, while river incisions corresponded to periods characterised by strong summer monsoons and high river-discharges (Gibling et al., 2008).

Table 5-1 Quaternary alluvial stratigraphy of the Middle Son Valley.

Formation	Type-section	Description	Chronology	Reference
Khetaunhi	1 km upstream from the Rehi-Son confluence, on the right hand side of the river.	Alluvial sands and clays	**5,305 -3,215 yr BP** by ^{14}C on shell and charcoal (Williams and Clarke, 1984); **6.3 – 3.2 ka** calibrated radiocarbon (Pal et al., 2005)	Williams and Royce, 1982; Williams and Royce, 1983; Williams and Clarke, 1984; Williams et al., 2006.
Baghor	South side of the Baghor village	Two-member formation: coarse unit (*Baghor Coarse*), characterised by large-scale sandwaves and a finer upper member (*Baghor Fine*) made of overbank fine sands and silts	Baghor *Coarse*: ~ **24– ~ 39 ka** ; Baghor Fine: **~** 19 ka (Pal et al., 2005; Williams et al., 2006)	Williams and Royce, 1982; Williams and Royce, 1983; Williams and Clarke, 1984 Williams et al., 2006.
Patpara	The archaeological site of Patpara, near the Patpara village	Alluvial sands, clays and gravels with clasts in the range from sand to cobbles	**100 – 30 ka** (Williams and Royce, 1983); ~ 58 ka (Williams et al., 2006).	Williams and Royce, 1982; Williams and Royce, 1983; Williams and Clarke, 1984; Williams et al., 2006.
Khunteli	On the right hand bank of the Son, near the village of Khunteli, and on the left bank of the river Son near its confluence with the Rehi river	Basal unit of unconsolidated medium sand, a discontinuous bed of volcanic ash, cross-bedded and planar-bedded medium and coarse sands and fine gravels; an upper unit of carbonate cemented gravels	~ **74 ka** (Williams et al., 2006)	Williams et al., 2006.
Sihawal	Village of Sihawal, 1 km east of the archaeological site of Sihawal	Non-fluvial clayey gravels and gravelly clays	**~ 100 – 90 ka** (Williams et al., 2006); **~ 130 – 137 ka** (Haslam et al., 2011)	Williams and Royce, 1982; Williams and Royce, 1983; Williams and Clarke, 1984; Williams et al., 2006.

5.3 Methods

The aim of this chapter was to assess the validity of the tephra as a stratigraphic marker. In an attempt to correlate the tephra layer across sections, 30 km of the river bank exposures were surveyed, logged and sampled (see **§2.1**). Serial photographs of cliff sections were taken from boat and bank traverses, and photomosaics were constructed to aid the contextualisation of the YTT layer in the stratigraphy. The modern topography was surveyed using a Total Station (Zeiss Elta R55 EDM). The 600 points obtained were interpolated using the software Surfer 3.0 and ArcMap (Figure 5-2) that provided a further means of investigating the distribution of the tephra.

Nine sections exposing volcaniclastic sediments were discovered and surveyed during the 2009 fieldwork (Table 5-2). Six sections were logged and their sedimentological structures described in terms of depositional facies (Table 5-2). Two of these sites, GG1 and KH, have been previously described (Williams and Royce, 1982; Jones and Pal, 2005; Williams et al., 2006; Jones and Pal, 2009; Jones, 2010). The six sites were selected on the basis of their exposure, ash characteristics, sediment structures and spatial distribution (Table 5-2).

In order to isolate the depositional environments in which the tephra was identified, the sediments have been assigned facies and floodplain associations using the codes proposed by Nanson and Croke (1992) and Miall (1996), respectively. The major facies assemblages and the depositional settings prevailing at the time of the ash deposition were identified. This led to a geomorphological model for the dynamic activity of the river during the critical period of interest.

Table 5-2 List of the sites investigated during the 2009 field campaign.

Type	Site	Locality	Coordinates		Lit.	Thickness primary ash (cm)	Thickness secondary ash (m)	Selection criteria
PRIMARY +SECONDARY ASH	RH1	Rehi	24°30′9″N	82° 0′ 56″E	N/A	5	1.6	Western site
	GG1	Ghoghara cliffs (Main Site)	24°30′7″N	82° 1′ 2″ E	Williams and Royce, 1982	5	1.5	Main ash site, firstly discovered
	GG1.b	Ghoghara cliffs (gully)	24°30′7.5″N	82°1′2.99″E	N/A	2-5	1.05	Sediment structures
	GG2	Ghoghara cliffs	24°30′10″N	82° 1′ 8″E	N/A	0.1 (disturbed lenses only)	0.90	/
	GG3	Ghoghara cliffs	24°30′8″N	82° 1′ 9″E	N/A	0.45 (disturbed)	1.4	/
	GG4	Ghoghara cliffs	24°30′7″N	82° 1′ 11″E	N/A	0.1-0.4	2.28	Eastern site
	GG5	Ghoghara cliffs	24°30′14″N	82°1′20.6″E	N/A	disturbed lenses only	~ 1	/
SECONDARY ASH ONLY	RH2	Rehi confluence	24°30′6″N	82° 0′ 55″E	N/A	/	1.3	Western secondary only site
	KH	Khunteli	24°32′28″N	82°16′ 33″E	Acharyya and Basu, 1993	/	2.2	Situated on the right side of the river

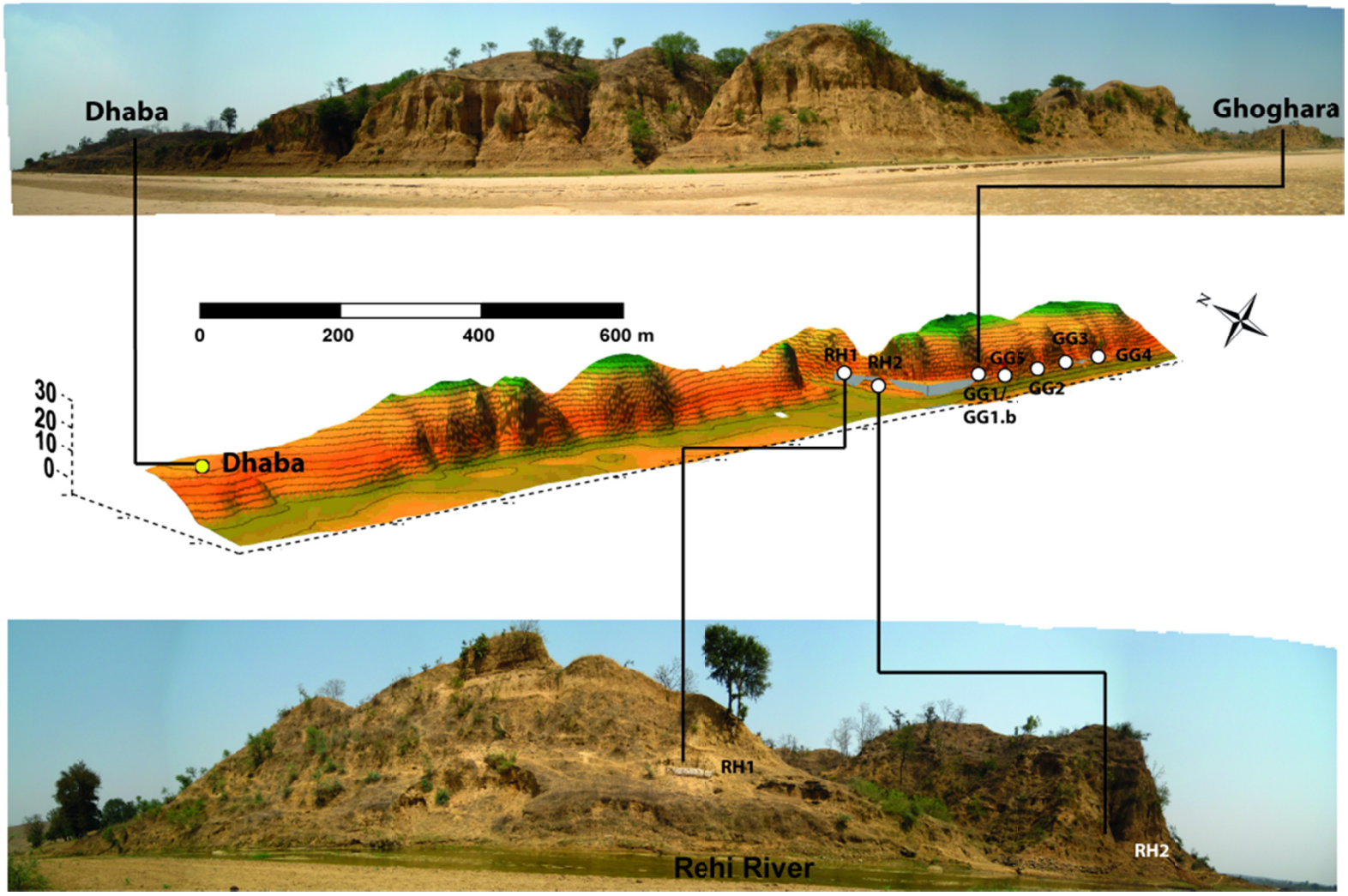

Figure 5-2 Sites and position of YTT ash at Ghoghara. The topographic profile was derived from a survey carried out with a Zeiss Elta R55 EDM total station. The photomosaic shows the morphology of the riverside cliffs and the position of the ash sites Rehi 1 (RH1) and Rehi 2 (RH2).

5.3.1 Criteria for discriminating primary ash fallout and reworked tephra deposits

For this work, sites were selected that represented primary and/or reworked ash, and considered textural, sedimentological and stratigraphical characteristics of the ash and its associated sediments. Primary (unreworked) ash-fall is characterised by: i) its whiteness (Munsell code 7.5YR or 10 YR 8/1 or 8/2); ii) thickness ranging between 4–5 cm; iii) sharp lower contact with siliciclastic sediments; and iv) homogeneous texture. Secondary (reworked) ash deposits are characterised by: i) either massive or with post-depositional structures (cross-bedding, root casts, bioturbation); ii) discontinuous/mixed contacts with units above/below, and iii) geomorphological features indicating displaced facies (including blocks of ash within older sediments, traces of slumping, etc). Further details on the differences between primary and secondary ash can be found in **Chapter six** (Table 6-4).

5.4 Tephrostratigraphy

5.4.1 Primary and secondary ash sites

The sites lie within an area between the Rehi-Son confluence and the cliff on the northern bank of the Son river (Figure 5-2).

Excavations here demonstrated that the sites in which primary ash was identified all present a similar stratigraphic sequence (Figure 5-3). The sections include 2–8 m of cross-bedded brownish medium sand (*Facies Scp*), a 5 cm clay bed (*Facies Cl*) at the base of the sections and 1-3 m of micaceous coarse silt (*Facies Smc*) enriched in calcrete on the top of the sequence, capped with soil (*Facies P*). The ash horizon can be distinguished within all the studied sections, but only three provide important tephrostratigraphic markers: sections RH1, GG1 and GG4. These horizons consist of a 2–8 cm thick stratum of primary ash (*Facies PA*), the base of which is always sharp on the underlying clay, and 1-2 m thick unit of reworked ash (*Facies SA*) gradationally overlying *Facies PA*.

The primary ash is characteristically powdery in texture, comprises finer grains and is white (10YR or 7.5YR 8/1 and 8/2). The secondary ash is texturally coarser, darker (10 YR 8/3 or 7/1)

and appears in massive beds with no apparent internal depositional structures. The ash sequence gradually coarsens upwards and the contact between the secondary ash and the siliciclastic silt is indistinct.

Table 5-3 Lithofacies codes and description, association and interpretation (after Miall , 1996).

Lithofacies	Code	Colour	Description	Architectural Element	Stratigraphic position	Type-section
Palaeosol	P	7.5 YR 7/4	Pedogenetically altered, oxidised sediment enriched in calcretes+ and roots.	Distal/abandoned	Above ash	Everywhere
Micaceous massive silty sand with calcretes	Smc	10 YR 6/6	Massive unit of heterogeneous sand mixed with micas and silt. Calcrete nodules and roots.		Above ash	Everywhere
Secondary ash	SA	10 YR 8/3, 7/1,7/3, 7/4	Volcaniclastic silt, mixed with sand; usually finely laminated, coarsening upward.		Above ash	Everywhere
Primary ash	PA	10 YR 8/1	Very fine ash, compact and without fluvial structures.		Ash	RH1, GG1.a, GG1.b, GG4
Coarse Clay with roots/calcretes/sand	Csc	10 YR 4/3	Massive clay mixed with sand or silt, enriched in calcrete nodules and roots.	Overbank	Below ash	RH2
Massive coarse clay with mudcracks	Cm	10 YR 4/3	Massive clay.		Below ash	RH2
Laminated fine clay	Cl	10 YR 7/4, 5/4	Clay mixed with sand, presenting fine horizontal lamination		Below ash	RH1, GG1,GG1.b, GG4, KH
Cross-bedded pebbly sand	Scp	7.5 YR 6/4 10YR 6/3, 6/6	Poorly sorted planar cross-bedded medium to find sand; horizontal laminations, imbricates pebbles, shale grains.	Lateral accretion	Below ash, near the present channel bed	RH1, GG1,GG1.b, GG4, KH

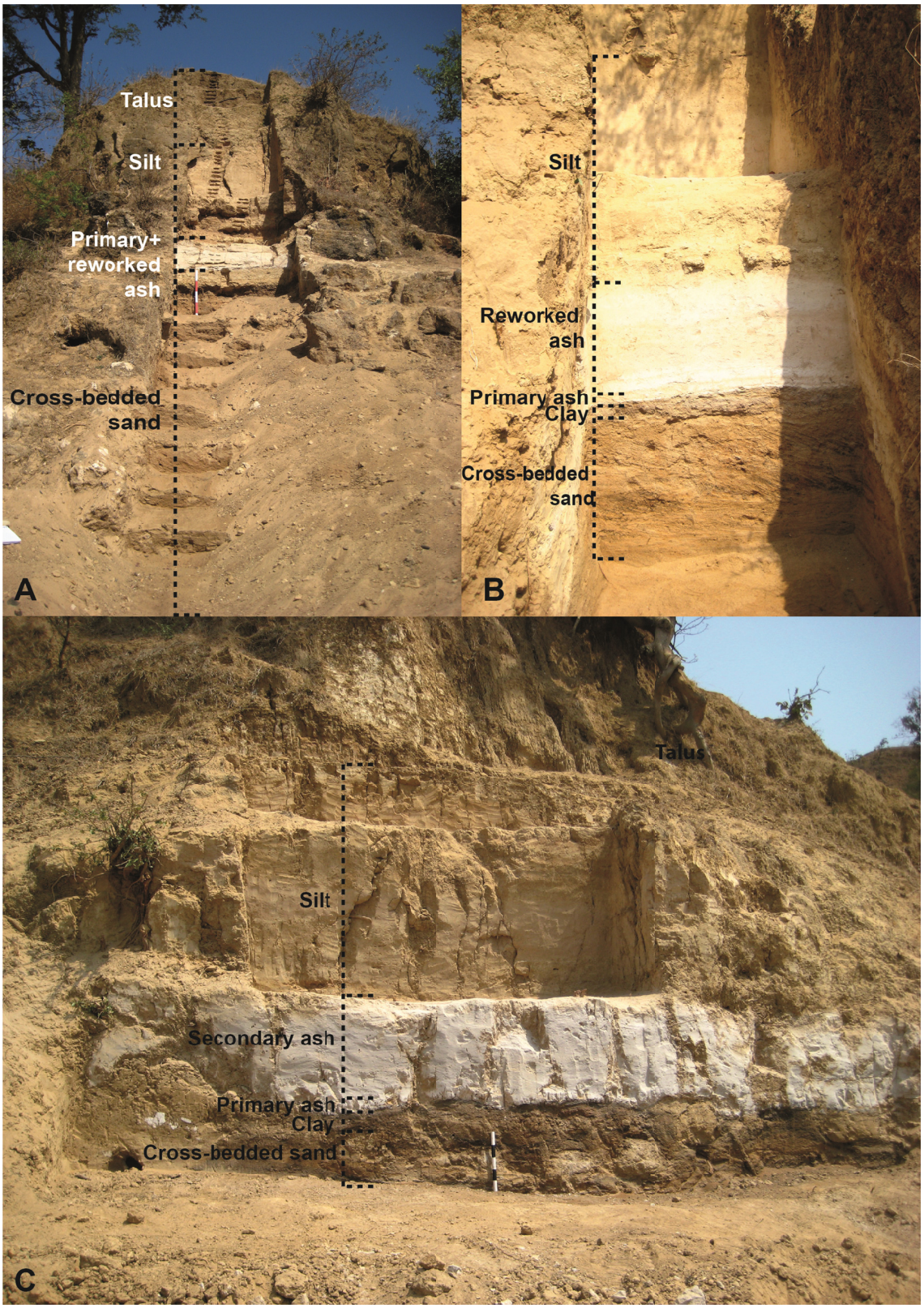

Figure 5-3 The principal ash sites of the Rehi-Ghoghara location: A) Ghoghara 1 (GG1); B) Ghoghara 4 (GG4) and C) Rehi 1 (RH1).

5.4.2 Sites showing only reworked ash

The two sequences that presented reworked ash show particular stratigraphic characteristics (Figure 5-4). The RH2 section (Figure 5-4a) is composed of dark brown carbonate cemented clay (*Facies Cm*); lenses of gravel, in which a mixture of fine sand is also observed within the clay, the latter becoming coarser and carbonate-rich towards the top (*Facies Csc and P*). The reworked ash (~ 1.3 m thick) is intermixed with the same micaceous silt that overlies the other sequences (*Facies Smc*). The Munsell colour of the secondary ash of RH2 is 7.5YR 7/4 (pink). Compared with the primary and secondary sequence, it appears that RH2 represents only the final part of the volcaniclastic reworked units. Again, no sedimentary structures are recognised within the ash unit. KH (Figure 5-4b) is stratigraphically similar to section GG1, since it exposes the same cross-bedded sand seen at the base of the section (~ 8 m thick). The cross-bedded sand alternates with fine bands of clayey silt, 2-3 cm thick: 11 m above the river bed, the cross-bedded medium sand unit is capped by a fine stratified sand unit and a thick carbonate band. A thin ash layer overlies the latter, 1-cm thick and mixed with clay. The secondary ash unit at KH appears sedimentologically similar to a 2-m lens of volcaniclastic material mixed with clay and laminated sand. The unit is yellowish brown in colour (10 YR 5/4). Although fine laminations appear within the lower sand units and the clay, their origin is uncertain.

Figure 5-4 Sites containing secondary ash only. A) Rehi 2 (RH2), nearby the primary ash site of Rehi 1 (RH1) and B) Khunteli (KH), 30 km downstream from Ghoghara, on the Son's south bank. The tephra layer is only visible at the top end of the section, and is substantially reworked.

5.4.3 Tephra sedimentological structures and geometry

The majority of the tephra deposits in the Son valley show no evidence of sedimentological structures in the upper reworked tephra layers. The exception is site GG1.b, in a gully near the Ghoghara main section. This site (Figure 5-5) exposes ~ 8 cm basal ash, revealing a 'primary' ash layer that can itself be subdivided into four sub-units: 1) ash 1, in direct contact with the clay unit; it is 1.5 cm thick, white (7.5YR 8/1), powdery; 2) ash 2, on the top of ash 1, divided by a sharp darker contact; it is 2.5 cm thick, pinkish white (7.5YR 8/2,); 3) ash 3, located on the top of ash 2; it is a 1 cm thick lens of darker ash, including medium sand grains impurities; 4) ash 4, ~ 3 cm of white (5YR 8/1) powdery ash, visually very similar to ash 2. Ash 4 is overlain by a heavily bioturbated palaeosurface, ca. 1 mm thick. The palaeosurface is sharply overlain by 1.5 m thick reworked ash deposits.

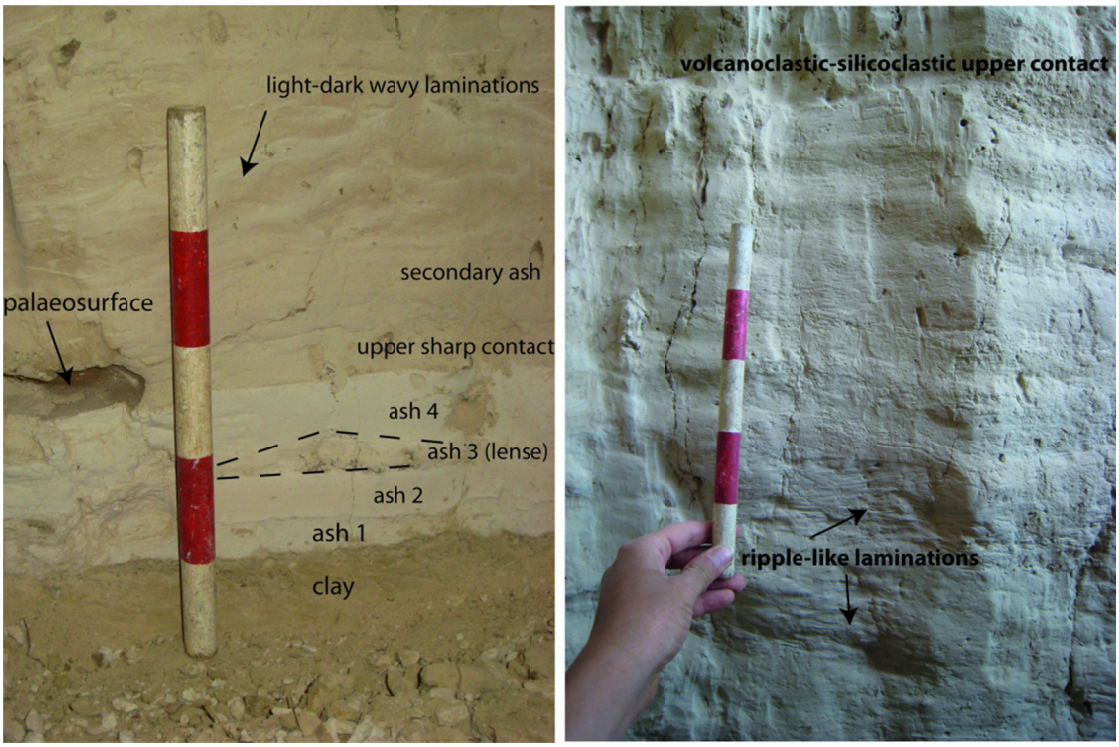

Figure 5-5 Primary ash layer and reworked sequence in GG1.b.

The unit is characterised by several sedimentary structures (Figure 5-5): ~ 1-2 mm thick ripple-like laminations, grouped in cm-thick bands, repeated cyclically every 10 cm; light-dark wavy bands, 1 to 3 mm thick, and thicker parallel bands. The volcaniclastic component gradually

decreases towards the top of the sequence. No traces of post-depositional disturbance (i.e. slumped blocks, roots, rhyzoliths, or carbonate nodules) are found within the ash.

5.5 Discussion

Although the ash at sites GG1 and KH have been studied since the 1980s, examination of the taphonomy of the ash units has been minimal (Williams et al., 1996, Jones, 2007; Williams et al., 2009). To date, the ash of GG1 has been described as 'well preserved' and '80 cm relatively pure' (Jones and Pal, 2005), 'compact' (Jones, 2010), 'discontinuous bed of pure volcanic ash up to 1.5 m thick' (Williams et al., 2006), and 'laterally discontinuous unit of volcanic ash up to 4 m thick' (Williams and Royce, 1983). The reworked ash has received less attention, being described only by Williams et al. (2009) as 'completely cemented with carbonate from 3.45 to 3.83 cm above the base of the ash' in the Ghoghara section, while 'the upper 70 cm of the ash is reworked' in Khunteli (Williams et al., 2009).

The facies reconstruction (Table 5-3) allows discussion of the stratigraphical characteristics of the YTT in their sedimentary context, thus demonstrating how ash facies associations can unravel the dynamics of a river depositing, redepositing and preserving the tephra (Macklin et al., 2002; Lewin et al., 2005; Bridgland and Westaway, 2008). These features should be considered carefully if a tephra layer is to be used as a chronostratigraphic marker.

5.5.1 The local environment pre- and post-deposition of the YTT in the Middle Son Valley

The lithofacies assemblages identified represent specific styles and sub-environments of deposition within the river catchment. Figure 5-6 shows the stratigraphic units of the six type-sections, the corresponding facies and their lithofacies association.

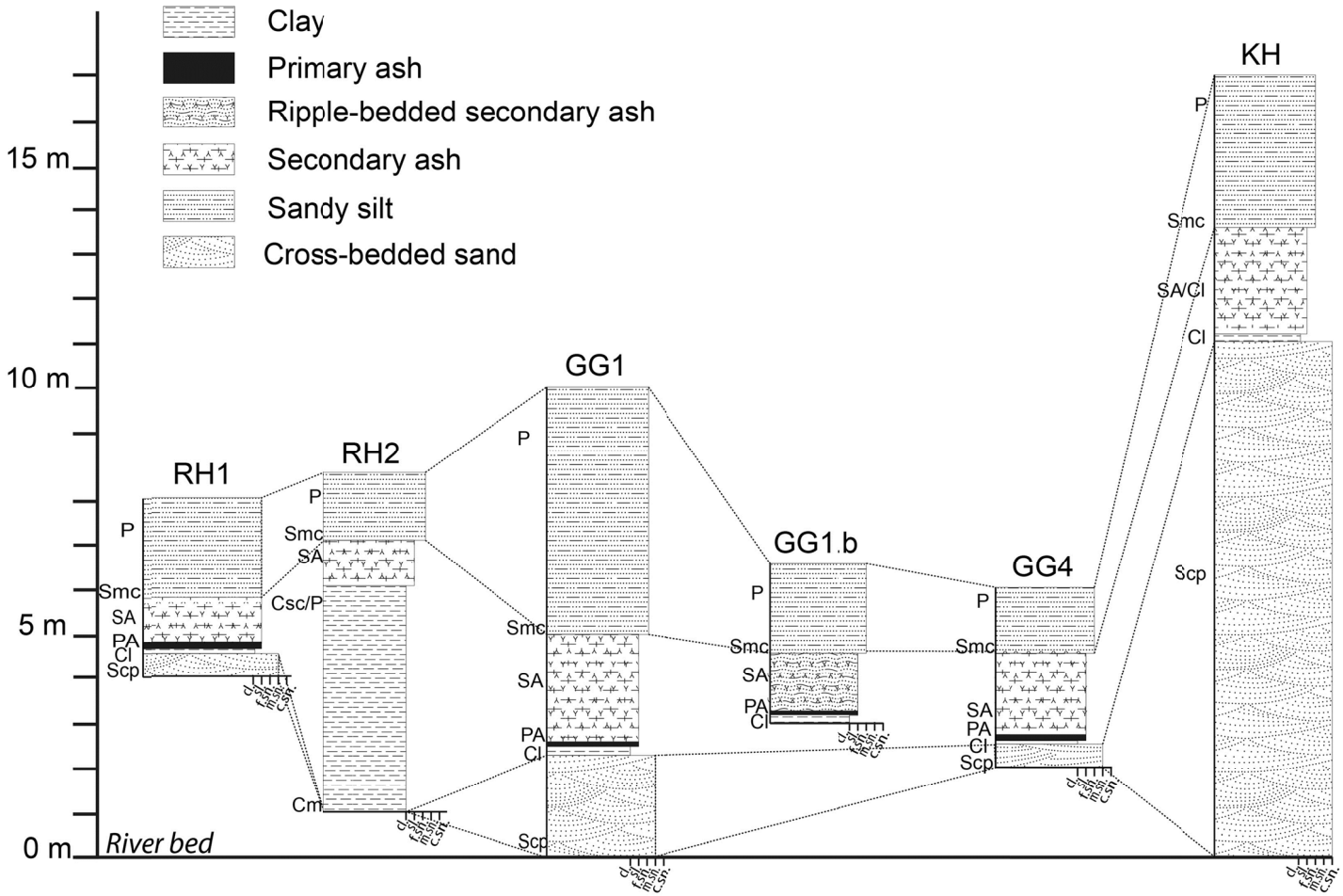

Figure 5-6 Tephra type-section logs. The facies association between Rehi and Khunteli offers an insight into the morphology and activity of the river around 74 ka ago. The YTT sequence around this area is remarkably similar, suggesting the requirement of particular environmental niches for the preservation of the primary volcanic ash fallout horizon (Stollhofen et al., 2008).

The sedimentary structures within this facies (cross-lamination, imbrication, poor sorting) indicate that the sand was deposited on a point-bar or counterpoint-bar (cf. Miall facies code, Miall, 1996). The medium grained, cross-bedded sand observed at all the sites at the base of the succession (except RH2 and GG1.b) suggests proximity to the active channel. These characteristics indicate a large-scale depositional environment of lateral accretion from the main river channel, similar to the bar accretions observed in the Narmada river, Gujarat (Khadkikar, 2003). The river eroded on one side of the channel and deposited its finer sediments on the other side, creating point-bars and shallow-water deposits.

Facies Cl suggests a distal, shallow-water, low-energy environment. This is consistent with the presence of very fine, powdery volcanic ash overlying this clay. Both *Facies PA* and *SA* also suggest a low energy aquatic environment, favourable to preservation of the deposits. The facies association characteristics suggest an overbank environment, established prior to ash deposition. Facies *Smc* and *P* are characterised by coarser silt, pervasive pedogenic features and carbonate nodules. The presence of carbonate nodules and roots clearly indicates a cessation of fluvial activity, and the facies association may represent an abandoned terrace surface, or distal deposits that the river was unable to reach even during floods (Simonsen and Toft, 2006).

These multi-facies associations indicate a fluvial floodplain setting consisting of ephemeral ponds and oxbow lakes isolated from the main channel through point-bars and floodplain surfaces, where the ash could be preserved. This is consistent with microanalyses of the tephra units in the Ghoghara and Khunteli sections conducted by Jones (2010), which highlighted a distinct difference between the particle-size distribution of the primary ash (~ 60 μm) and the upper secondary ash layer (> 125μm), thus suggesting the primary ash was deposited into an aquatic environment. Figure 5-7 shows the lateral accretion and deposition on the point-bar of coarse sediments (gravel-size), the deposition of medium sediments in the near-channel overbank environment (medium and fine sand-size), and the accumulation of fine sediments in the distal overbank areas (silt and clay).

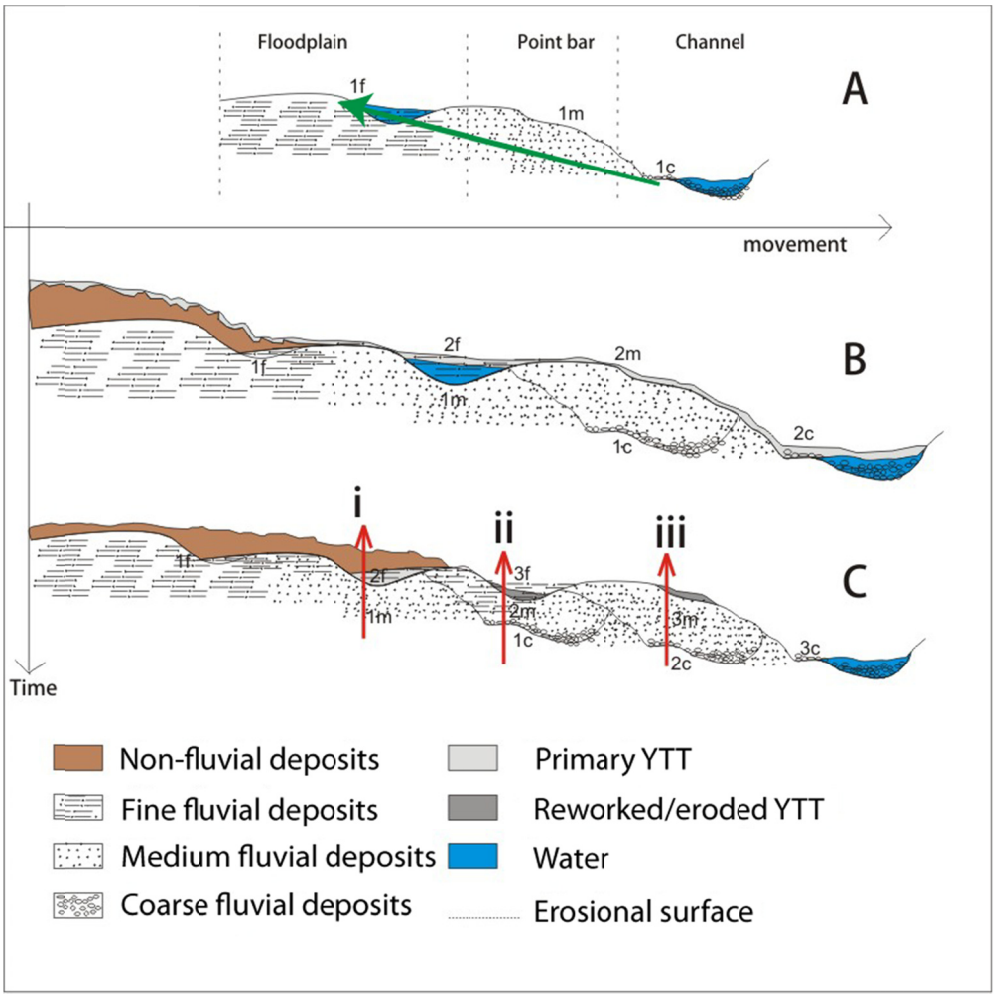

Figure 5-7 a) Generalised macroscale model of a point-bar-channel in a low-to-medium sinuosity river; the main active channel is shown on the right; lateral accretion deposits are shown on the flanks of the point-bar; overbank deposits fill a shallow-lake at left of the point-bar, in the floodplain; the green arrow indicates the lateral aggradation of the river; b) hypothetical river geomorphology at the moment of the ash-fallout; c) late-stage evolution of the ash deposits, with the ash incorporated in a fluvial system reaching a new equilibrium. c= coarse fluvial sediments; m=medium fluvial sediments; f= fine fluvial sediments. Cases i), ii) and iii) indicate three possible scenarios. Case i) is the case of distal floodplain, with the ash deposited in a low-energy environment, where the water can reach the ash only during seasonal floods, bringing only the finer sediments. In this case primary ash is preserved beneath a gradual accumulation of fine reworked ash. Case ii) represents the case of ash preserved in a relatively protected location, but exposed to reworking. In this case the primary ash might have been preserved in its original context, but the upper contact might have been partially eroded and redeposited after. Case iii) represents the ash exposed in a secondary-deposition site. Ash reached the site from upstream, subsequent to the river action. In this case the YTT will show strong signs of reworking and will not be preserved as primary deposit.

As a result of the lateral accretion-aggradation style in this area, the river deposits its sediments laterally and not vertically (Figure 5-7a: note the arrow indicating the preferential aggradation direction). In such a setting, following the eruption, primary ash would have been preserved only in protected low-energy niches that were rapidly buried by later sediments. The remaining ash, especially if left exposed at the surface, would have been rapidly eroded to be re-deposited downstream or in lateral channels (Németh and Cronin, 2007). The progression from lateral accretion to overbank to abandoned terrace environments apparent in the Ghoghara section suggests a gradual shift in the river morphology. This change in depositional style is reflected in changes in the grain size of the deposits (from medium sand to silt) that are typical of fining-upward fluvial sequences: the river fills the channel and its active bed shifted laterally further south.

5.5.2 YTT deposits in the Middle Son Valley as a chronostratigraphic marker?

Several attempts have been made to place the YTT within the broader alluvial stratigraphy of the Son Valley, in order to reconcile the history of the alluvial plain with the archaeological artefacts. Review of the literature leaves the exact stratigraphic position of the YTT bed in relation to the Quaternary formations unclear. The YTT has been placed within the *Baghor Coarse Member* (Williams and Royce, 1982; Basu et al. 1987; Acharyya and Basu, 1993), beneath the *Baghor Coarse Member* (Williams and Clarke, 1995), at the junction between the *Patpara Formation* and in the *Baghor Coarse Member* (Jones and Pal, 2005; Jones, 2010). More recently it has been proposed that the tephra lies between a newly described *Khunteli Formation*, dated to 73 ka, and the *Patpara Formation*, with an age of 56 ka assigned to the latter (Williams et al., 2006).

Here it is suggested that these inconsistencies are related to the assumption that the tephra bed always occurs in its correct (i.e. primary) stratigraphic position and the lack of dates in direct association with the tephra sediments. Furthermore, the geomorphological model indicates that river aggradation has tended to create a lateral discontinuity that disturbs the vertical accumulation; therefore assigning the ash to a specific vertical unit could be misleading.

5.5.3 Reliability of the YTT as palaeoenvironmental marker

A more recent study (Williams et al., 2009) also focused on the Rehi and Khunteli sections, in an attempt to gain insights into the environmental impacts of the YTT eruption. In this work, carbon and oxygen isotopic ratios were measured in calcareous nodules and root casts found below, within and above the ash sampled from the GG1 and KH sites. The results suggested replacement of C_3 forest that had thrived prior to the YTT fallout by C_4-dominated grasslands or wooded grasslands afterwards. They concluded that the YTT eruption led to these changes. Similarly, Jones (2010) considered the silt-dominated facies overlying the ash a sign of abrupt climatic change immediately after the eruption.

While the time-frame and pace of aggradation of the post-tephra units, together with the time of restabilisation of the system, cannot be determined only using stratigraphy, it is also notable that there is no evidence that the units overlying the ash were deposited immediately after the eruption. The model proposed here implies that the river deposits at Ghoghara and Khunteli were exposed to erosion and reworking, such that the stratigraphy of the ash deposits could result from incision, lateral erosion and redeposition on a timescale of weeks to decades (i.e. Lawrence and Ripple, 2000; Todesco, 2004; Zobel and Antos, 2007), to centuries (i.e. Telford et al., 2004), to millennia (i.e. Lotter et al., 1995). The silt-dominated facies overlying the ash is widespread on the top of all the Middle, Late Pleistocene and early Holocene terraces.

The post-Toba floodplain silt facies could indicate either that the dynamics of the river channel changed substantially following the eruption (suggesting a strong post-Toba environmental and climatic effect), or that the coarse/medium sand above the ash layer is no longer preserved. The latter could indicate by contrast a migrating channel and change in facies, suggesting a major geomorphological impact on the river rather than eruption-related climatic changes.

The major problem in tackling the palaeoenvironmental impact of the Toba super-eruption is that existing methods of palaeoenvironmental reconstructions lack the analytical precision needed to answer the time-scale issue (Williams, 2012b). Moreover the sedimentation rate in fluvial environments lack the temporal resolution needed to address questions regarding climate change after the YTT eruption (Paredes et al., 2007). The Ghoghara site GG1.b, at which fine

stratification indicates a slow sedimentation rate, appears to be the one locality suitable for chronology-critical work.

5.5.4 Reliability of the YTT as an archaeological marker

Archaeological studies (Jones and Pal, 2005; Jones, 2007; Jones and Pal, 2009) have attempted to establish associations between the ash and the Palaeolithic artefacts in the Middle Son Valley deposits.

It is noted that artefacts have not been recovered from stratigraphic units that show clear evidence of YTT primary ash and the time at which evidence of human populations reappeared may be in the order of millennia (given the uncertainty of the dating methods previously employed, see Jones and Pal, 2009). It has been demonstrated that the evidence of reworking at many of the Middle Son Valley sites, suggesting that the chronological relationship between the artefacts and the YTT strata in the Son Valley is insufficient to allow a robust connection between the eruption and its human impact. The palaeogeomorphology of the area suggests that new archaeological sites in association with primary YTT horizons might be found closer to the interior of the fluvial plain, towards the Rehi River.

5.6 Conclusion

The lithofacies associations from the Rehi-Ghoghara-Khunteli sites presented here have revealed an environment conducive to the preservation of primary ash fallout. Nevertheless, the YTT ash was preserved only in selected geomorphic environments that offered protection to the unconsolidated volcanic particles. This environment was a low energy, shallow-water depression near the main river channel. Before the YTT fallout, the Son River had adopted the characteristics of a sand-dominated, medium-sinuosity and low-gradient river, with laterally stable single channel, seasonal floods, floodplains and point-bars. The fining-upwards sequence (reflected in the shift from lateral accretion to overbank and distal channel) could represent the gradual filling of the river-bed due to meander migration.

The stratigraphic context of ash deposits in the Middle Son valley is rarely of the quality required to provide a well-defined chronostratigraphic marker horizon. The ash units often show

abundant evidence of reworking, with an upper boundary in gradational contact with the overlying silts. Out of 30 km of river bank surveyed (on either side of the river), only one localised occurrence where the ash could be considered 'primary' in context was found, and neither of the ash locations corresponded to a co-location of archaeological artefact assemblages. It is therefore critical that sampling for dating and palaeoenvironmental reconstructions take full account of the sedimentation style and morphology of the river and the associated evolution of the local landscape over the period.

The next chapter focuses on this issue, using particle size analyses, magnetic susceptibility and scanning electron microscope images to analyse the mechanisms of accumulation and preservation of reworked deposits in Malaysia, ~ 390 km from the vent. The micro-scale analyses allow further exploration of the mechanisms theorised in this chapter, revealing site-specific processes that radically modify the stratigraphy of the tephra beds and have primary control of the ash characteristics.

Chapter 6. Depositional processes and sedimentology of YTT deposits in the Lenggong Valley, Malaysia

Based on Gatti et al. (2012).

Abstract

Chapter six builds on the discussion of chapter five, analysing in detail the characteristics of reworked tephra and reconstructing the mechanism of deposition and accumulation of distal deposits. It will show that the taphonomy of the tephra can be interpreted in terms of environment of deposition and mechanisms of reworking, and that these factors are fundamental to assessment of the relevance of the ash to chronostratigraphic and palaeoenvironmental reconstructions.

The chapter presents a study of the characteristics and depositional processes of four newly discovered deposits of the YTT in the Lenggong valley, Malaysia. It focuses, in particular, on site stratigraphy, sample particle-size distributions, magnetic susceptibility and mineralogical associations. Reworked tephra display variable sedimentological characteristics: polymodal and unimodal, very fine to coarse grained distributions, variable percentages of ash ranging from 70–99% in the main size fraction (63-125 μm). It is found that particle-size distributions from this study are similar to those of published analyses for primary YTT deposits, demonstrating that particle size alone cannot distinguish primary from secondary tephra deposits. The reworked YTT tephra from Malaysia are associated with fluvial and colluvial transport and deposition. Three volcaniclastic facies have been identified corresponding to flood-flow, mudflow and slumping sedimentation. The evidence suggests that the ash accumulated rapidly, over a period of a few days to months, and was quickly buried. In this valley, the ideal site for palaeoenvironmental reconstructions is Kampung Luat *3*, where ash accumulated on a vegetated floodplain and at least two distinct phases of sedimentation are represented. Despite the rapid accumulation, these sites are not well suited to palaeoenvironmental study of the YTT impacts. This has wider implications for palaeoenvironmental reconstruction based on reworked tephra sequences.

6.1 Introduction

Distal tephra deposits can be used to correlate a wide variety of palaeorecords over ranges of up to thousands of kilometres (Sarna-Wojcicki et al., 1985). Tephrostratigraphy and tephrochronology, including the study of microtephra, therefore represent an important complement to palaeoenvironmental (ie. Zanchetta et al., 2011; Narcisi and Vezzoli, 1999; Froese et al., 2006; di

Rita et al. 2009) and archaeological reconstructions (Petraglia et al., 2007; Petraglia et al. 2009; cf. **Chapters four and five**) because they are capable of providing easily-identified, isochronous markers (Sarna-Wojcicki and Davis, 1991; Alloway et al., 2007; Lowe, 2011; Davies et al., 2012). However, before being used in this way, their integrity should be carefully assessed. Only primary deposits (i.e. *in situ* ashfall deposits) should be used for chronological reconstructions, since only ash immediately deposited after the eruption can guarantee temporal continuity between the strata. Distinguishing primary from secondary deposits (i.e. those arising from reworking of primary ash materials) is therefore a fundamental step prior to assuming that encasing sediments represent pre- and post-eruptive periods.

To this end several solutions have been proposed. For example, Morley and Woodward (2011) used micromorphology to distinguish between primary and secondary deposits. Using a combination of grain counting and micro-scale structures, they suggested that the higher content of ash grains, the absence of fluid reworking and vertical structures, together assisted in determining whether or not the ash was in primary context. Jones (2010) studied the particle-size distributions of primary and reworked ash units at Jwalapuram in India. She noticed that the lowermost primary ash was finer-grained than all other ash samples, and suggested that such a particularly fine-grained composition resulted from sorting of the ash fallout during gentle redeposition into an aquatic environment. Generally, in the majority of studies the differences between primary and secondary ash are assessed through a combination of micro-scale and macro-scale semi-quantitative observations, adapted to each case.

While reworked deposits may not provide reliable temporal markers, they can still be valuable in palaeoenvironmental studies, such as in the investigation of the environmental impact of ash fallout on the receiving environment. Proxies including pollen, phytoliths, benthic organisms and geochemical traces from sediments have been used in assessing post-eruptive environmental changes (Schulz et al., 1998; Margari et al., 2007; Williams et al., 2009; Haslam et al., 2010). However, before reworked tephra deposits can be used in palaeoenvironmental studies, it is vital to understand and reconstruct their depositional history and transport pathways.

Traditional environmental records provided by geochemical and palaeontological proxies are usually extracted from high-resolution sedimentary sequences that have established temporal records, such as lake beds, varve and loess (Lowe and Walker, 1984). In the case of tephrostratigraphical sections, the resolution of sediments deposited is too low to be distinguished temporally (Williams, 2012b). The question is therefore whether environmental proxies can reliably record environmental changes that occurred during and after the ashfall event. The first step in addressing this question is to understand the depositional pathway that resulted in the formation of the tephra unit, in order to select the best site for palaeoenvironmental reconstruction. Errors can arise where gaps occur in the episodes of accumulation as a consequence of non-deposition, local erosion and/or low sediment yields. The high variability of the sedimentological characteristics of the reworked tephra — even when the ash is deposited in the same environment — can further complicate the reconstruction of the reworking processes (Davies et al., 2007; Pyne-O'Donnell, 2011; Davies et al., 2012).

This chapter focuses on these two issues, an attempt to distinguish between primary and secondary ash and an assessment of the mechanisms of tephra reworking. For this purpose, the research analyses four newly discovered Younger Toba Tuff (YTT) tephra exposures at Lenggong, in Malaysia (Figure 6-2), in addition to presenting new geochemical data on the glass shards that confirm that the tephra corresponds to the YTT. The aims are: a) to determine whether it is possible, using the methods presented, to distinguish between primary and secondary ash and b) to determine the most suitable site in the Lenggong valley for future palaeoenvironmental reconstruction.

6.2 Study Area

The Lenggong valley (Figure 6-2) lies in the Perak district of north Peninsular Malaysia, 350 km from the Toba caldera. It is well known as a site of YTT tephra deposits (Scrivenor, 1930; Ninkovich et al., 1978a; Stauffer et al., 1980; Chesner et al., 1991; Mokhtar, 2009; Smith et al., 2011; Matthews et al., 2012). The most studied YTT site in the valley is Kota Tampan, where the ash has been used as an isochronous marker in assessing the age of the sediments and their associated stone tools. Here a ^{14}C date of ~ 35 ka was obtained for the sediments immediately

underlying the ash, the latter including the Tampan Palaeolithic tools (Stauffer, 1973). Later, Ninkovich (1978a) characterised the ash by geochemical fingerprinting, confirming it to be the YTT, and thus reinterpreted the age of the Tampanian tools to ~ 75 ka. Although the Lenggong valley tephra have been geochemically characterised and identified as YTT (e.g. Mokhtar, 2009; Smith et al. 2011; Matthews et al. 2012), to the authors' knowledge no accurate stratigraphic study has been carried out on the nature and geological significance of the Lenggong tephra. Nor is it known whether the YTT ash at Kota Tampan is a primary or reworked deposit.

The Perak River (North-Western Malaysia, Figure 6-1, Figure 6-2) rises in the northern Perak-Kelantan-Thailand border area (Morgan, 1973). The river is ~ 400 km long and is associated with a gently northeast to southwest sloping terrain (Figure 6-1). Beyond the artificial lake of Kampong Kuala Benderok and the Temenggor dam, the Perak river has a relatively constant gradient of ~ 0.8 m km^{-1}. The Lenggong valley is ~ 40 km long and ~ 4–2 km wide, constrained between the deeply dissected slopes in the Main Range Granite, a post-Triassic acid pluton (Stauffer, 1972), through which the river has incised. The overlying Quaternary sequences of south Perak comprise four alluvial deposits that characterise the inland valley fill (Walker, 1956; Stauffer, 1972): in ascending chronological order they are the Boulder beds, the Old Alluvium (Middle Pleistocene), the Young Alluvium (from the last interglacial to present) and Organic mud and peat (Holocene).

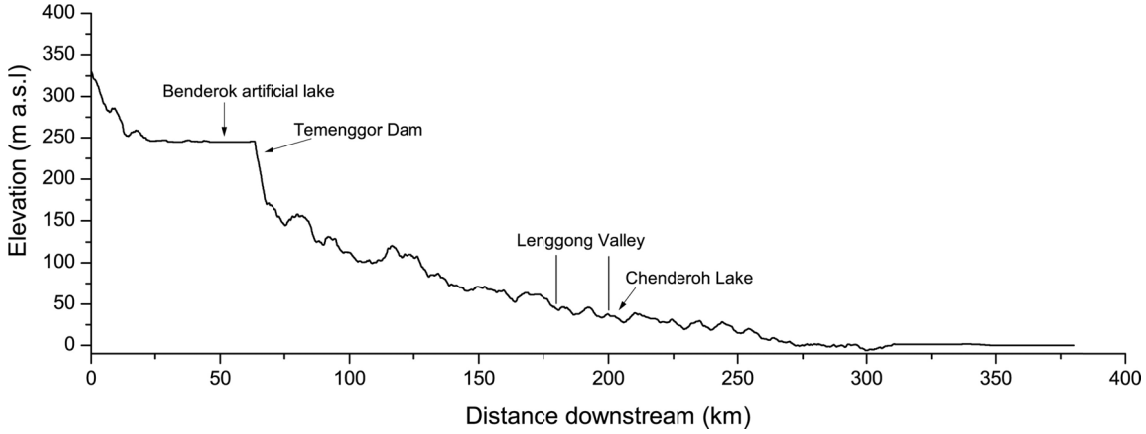

Figure 6-1 Longitudinal profile of the Perak River. Key localities are indicated and correspond to the sites in Figure 6-2. Profiles extrapolated from ASTER DEM (ASTER GDEM is a product of METI and NASA).

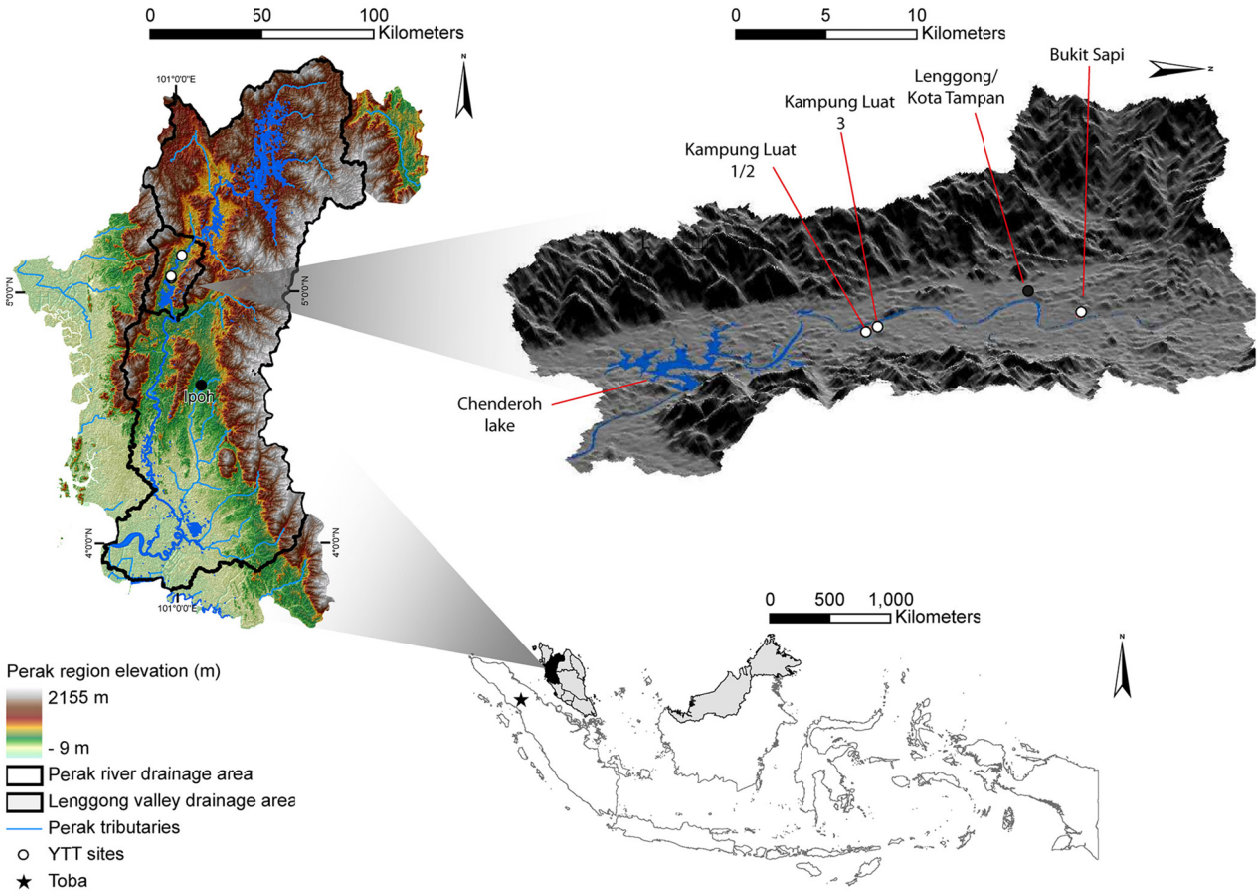

Figure 6-2 Map of the Perak river region, northwest Peninsular Malaysia. The Perak region is bounded at north by the Thailand border and Kedah County, east by the Malaysian counties of Kelantan and Pahang, west by the Malaccan Strait, and south by the Selangor region. The Lenggong valley is geomorphologically composed by the dissected hill slopes of the Main range Granite (Stauffer et al., 1972) and the alluvial Quaternary sediments of the Perak floodplain. Mt. Toba is ~ 350 km from the Lenggong valley. ASTER DEM of the region obtained from GDEM (ASTER GDEM is a product of METI and NASA).

6.2.1 Geomorphological setting

Four sites were investigated in 2010 (cf. **Chapter two**, Table 2-1). They lie near the village of Lenggong (5° 7' 42.52'' N, 100° 59' 34.35'' E), 60 km north from the capital of Perak Ipoh. The terrain is mostly covered by rainforest (Figure 6-3).

The Kampung Luat sites lie near the main channel of the Perak river. Sites Kampung Luat 1 and Kampung Luat 2 (KgL1 and KgL2) lie, respectively, on the eastern bank of the river, 289 m and 212 m from the main channel, at 69 and 68 m a.s.l., 4 and 3 m above the main channel, now at the margins of an artificial lake (Figure 6-3a/b). The base of the ash was obscured, and the top truncated by modern soil.

Kampung Luat 3 (KgL3) lies on a well-preserved fluvial terrace to the right of the main channel. The ash is preserved at an altitude of 71 m a.s.l., 115 m from the main channel and at 11 m above the Perak river bed. The ash units lie at the top of the fluvial terrace, exposed during a quarry excavation (Figure 6-3c). No deposits overlie the tephra at this site, the surface of the ash being colonised by dense rainforest vegetation. The unit exposed at Bukit Sapi (BTS) occurs at an altitude of 79 m a.s.l. The site is 4.70 m away from the main channel, 14 m above the river bed. This site is part of a small tributary stream valley incised into the north-western side of the Perak river valley. Neither the bottom nor top of the sequence could be seen because of the vegetation cover (Figure 6-3).

Figure 6-3 YTT sites in the Lenggong valley. a) Kampung Luat 1 (KgL1); b) Kampung Luat 2 (KgL2); c) Kampung Luat 3 (KgL3); d) Bukit Sapi (BTS).

6.3 Methods

Ash samples were collected at different intervals, depending on the structures and type of sediments occurring within the sequences (**§ 2.1)**. Facies interpretations are based on the depositional models of Nakayama and Yoshikawa (1997) and Kataoka (2005). Geochemical, particle-size and magnetic susceptibility analyses were executed following the protocols summarised in **§ 2.2.1**, **§ 2.2.3** and **§2.2.4**, respectively. Additionally, single grains were subsampled using 1% of sieved fractions (< 32 μm, 63–125 μm, 125–250 μm, 250–500 μm; 500–1000 μm), mounted on glass slides with glycerine and visually counted. Grains were classified as glass shards if they presented at least three tephra-like morphological features: crossed-polar full extinction, the presence of bubble walls/cuspid shape, an absence of refraction, sharp edges and absence of preferential crystallographic directions. Siliciclastic grains mainly comprised mica, quartz grains and undifferentiated clay mineral aggregates. Rare zircon and tourmaline were also present.

6.4 Results

6.4.1 Geochemistry

Table 6-1 shows the geochemical components of the Lenggong tephra. The fingerprints of the tephra samples confirm the nature and origin of the Lenggong unit as ejecta from the YTT eruption.

The glass analyses of the samples from the Lenggong sites resemble those from the YTT reported in the literature (Figure 6-4a). Minor differences between the new determinations and earlier data can be explained by use of different standards for calibration (as discussed in **Chapter four**, Figure 4-4). Similarly, rare earth element (REE) profiles of the Lenggong ash resemble the YTT REE profile reported in the literature (Figure 6-4). The results indicate relative enrichment in light REE, slight depletion of heavy REE and consistent, distinct negative Eu anomalies (Figure 6-4, Table 6-1).

Table 6-1 Major and REE elements of the Lenggong ash. Standard deviations given in brackets.

wt%	**Bukit Sapi**	**Kampung Luat 2**	**Kampung Luat 3**
SiO_2	74.88 (1.16)	74.62 (1.13)	74.07 (1.16)
TiO_2	0.05 (0.05)	0.04 (0.05)	0.05 (0.05)
Al_2O_3	11.92 (0.29)	11.83 (0.32)	11.83 (0.29)
FeO	0.87 (0.34)	0.87 (0.32)	0.83 (0.34)
MnO	0.06 (0.08)	0.07 (0.08)	0.05 (0.08)
MgO	0.06 (0.06)	0.07 (0.05)	0.06 (0.05)
CaO	0.75 (0.09)	0.75 (0.12)	0.78 (0.09)
Na_2O	2.95 (0.19)	3.15 (0.22)	3.04 (0.20)
K_2O	5.13 (0.41)	5.03 (0.40)	5.07 (0.41)
n	31	32	18
Total	96.67	96.42	95.78

ppm	**Bukit Sapi**	**Kampung Luat 2**	**Kampung Luat 3**
La	18.09 (2.4)	21.38 (6.6)	24.73 (4.1)
Ce	37.76 (4.2)	49.37 (16.2)	50.21 (7.4)
Pr	3.55 (0.5)	4.641 (1.6)	4.7 (0.7)
Nd	12.56 (1.7)	16.85(6.0)	16.53 (3.0)
Sm	2.32 (0.4)	3.69(1.5)	3.42 (0.8)
Eu	0.28 (0.1)	0.29(0.1)	0.32 (0.1)
Gd	2.17 (0.6)	3.12(1.6)	2.98 (0.6)
Tb	0.39 (0.1)	0.63(0.3)	0.58 (0.2)
Dy	2.40 (0.3)	4.077(2.2)	3.67 (0.8)
Ho	0.53 (0.1)	0.95(0.5)	0.88(0.2)
Er	1.60 (0.4)	2.84(1.4)	2.55(0.6)
Tm	0.24 (0.01)	0.49(0.2)	0.44 (0.1)
Yb	2.13 (0.5)	3.88(1.9)	3.29(0.9)
Lu	0.31(0.1)	0.54 (0.2)	0.51 (0.1)
n	15	10	14

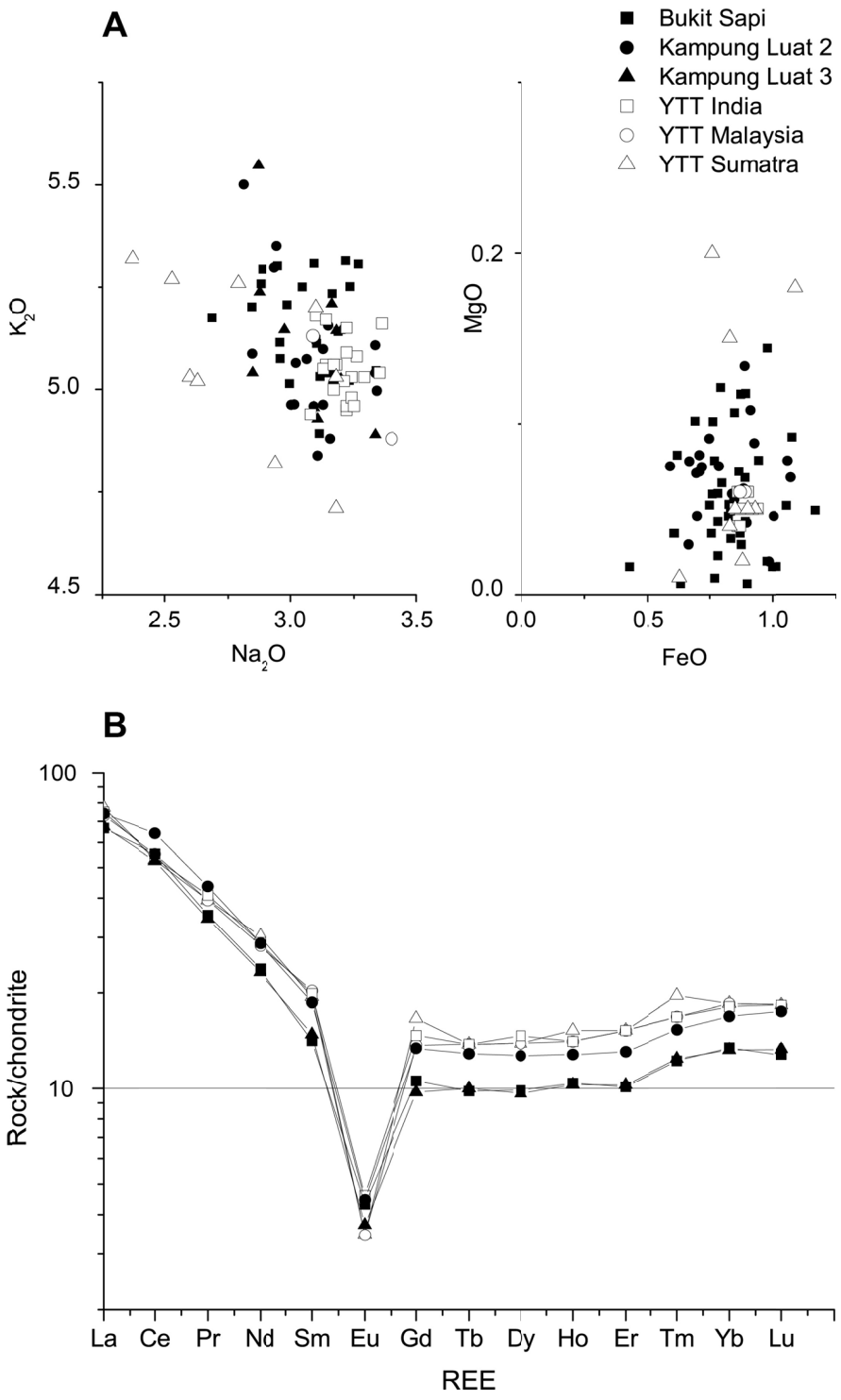

Figure 6-4 A) Major chemical components of the Lenggong ash compared with geochemical fingerprints of identified YTT glass from literature. Data from: Shane et al., 1995, Westgate et al. 1998, Smith et al. 2011 (India); Shane et al. 1995, Smith et al. 2011 (Malaysia); Westgate et al. 1998, Smith et al. 2011, Chesner et al. 1998, Beddoe-Stephens et al. 1983 (Sumatra). It is noteworthy that the three proximal samples collected from the Toba caldera on Sumatra showed values differing slightly from those of distal areas. This could be explained by the sample type, indicated as welded tuff by the authors of the analyses; B) Rare earth elements values for the YTT Lenggong valley ash and the literature reference. Rare elements analyses from Smith et al. (2011)

6.4.2 Stratigraphy

All samples investigated, except for the siliciclastic units at the base of Kampung Luat 3, consist only of tephra.

Kampung Luat 1 and 2 (KgL1, KgL2, 5° 03.360' N, 100° 58.864' E) lie on the opposite side of an artificial lake. Here the sandy tephra units (3.8 and 4.4 m thick, respectively) appear massive, and show few or no sedimentological structures (Figure 6-5a/b). No change in either units or lithology was apparent.

The Kampung Luat 3 sequence (KgL3, 5° 03.833' N, 100° 58.821' E) is 3.7 m thick in total, and consists of a lower, 1.19 m thick siliciclastic unit (mainly clay and quartz), overlain by a 2.36 m thick volcaniclastic sequence of sandy ash with horizontal laminations (Figure 6-5c). The ash unit shows alternating light grey (10 YR 6/2-7/2) and grey (10YR 5/1) laminations. The lower siliciclastic and the upper volcaniclastic sediments are divided by a ~ 20 cm-thick lens, composed of oxidised brownish yellow (10 YR 6/8) sandy ash, and are delimited top and bottom by a 5-7 cm thick dark brown (7.5YR 5/8) very finely wavy laminated reddish clay (Figure 6-6).

A fourth site, Bukit Sapi (BTS, 5° 08.776' N, 101°01.398' E) exposes a 3.7 m thick sequence composed of a massive, light brownish grey (10 YR 4/2) silty and sandy ash (Figure 6-5d). The ash outcrop can be visually subdivided into three ash 'sub-units' separated by sharp contacts: 1) basal silty ash with clay component, ~ 1 m thick, light brownish grey (10 YR 6/2); 2) upper sandy ash, 2.20 m thick, dark greyish brown (10 YR 4/2), covered by soil and vegetation in the top 30 cm; 3), block of massive, compacted fine ash, 50 cm thick, white (10 YR 8/1), sandwiched between sub-units 1) and 2); the block is ~ 1.5 m from the bottom of the section.

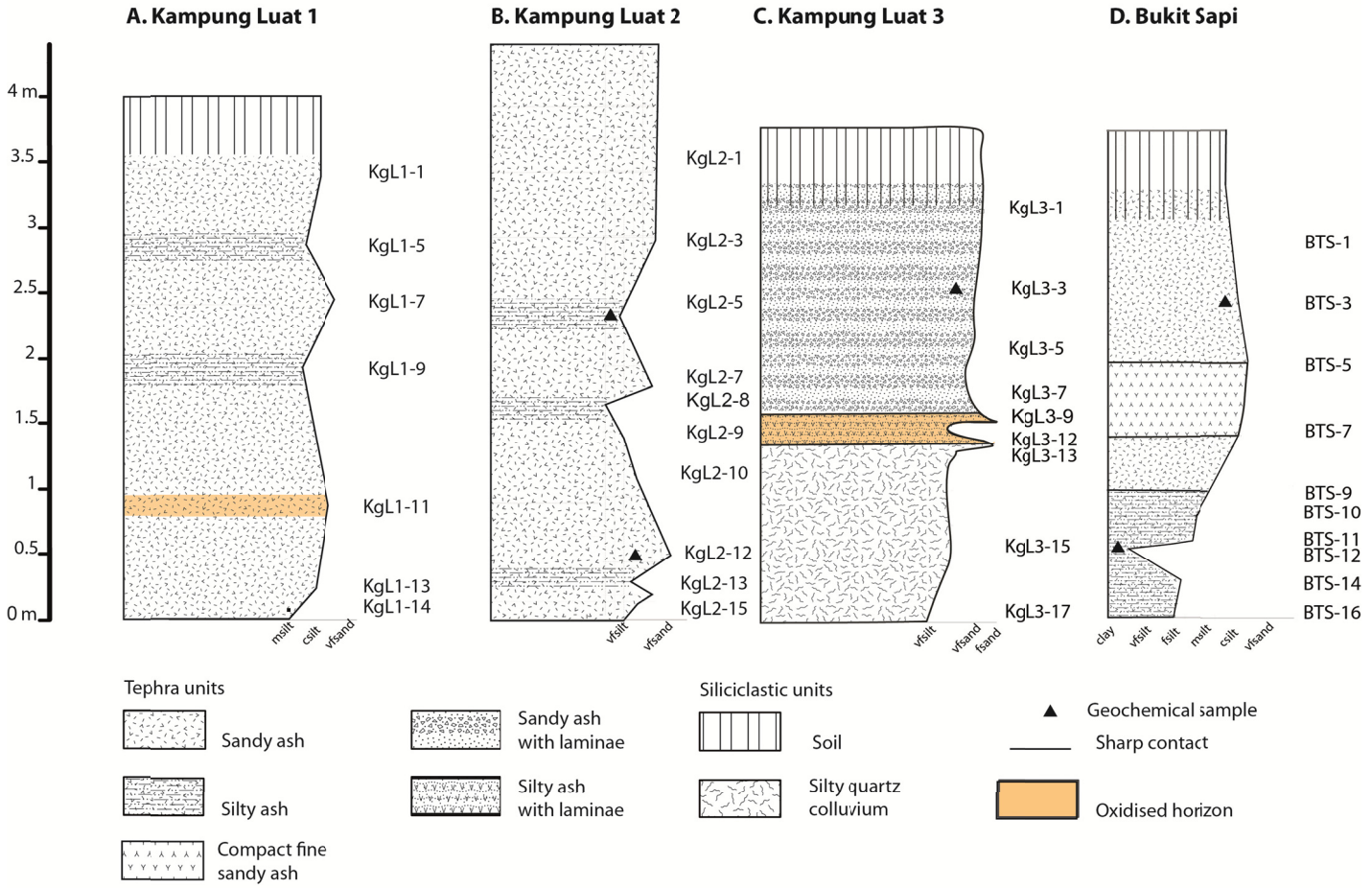

Figure 6-5 Schematic log of the tephra sedimentary sequences at Lenggong valley. The tephra units are the main sedimentological components for all four sequences. Five EMPA analyses have been obtained from the lower and upper units of KgL2, 3 and BTS, and, in conjunction with LA-ICPMS Rare Earth Elements analyses, confirmed the association of the tephra with the Younger Toba Tuff.

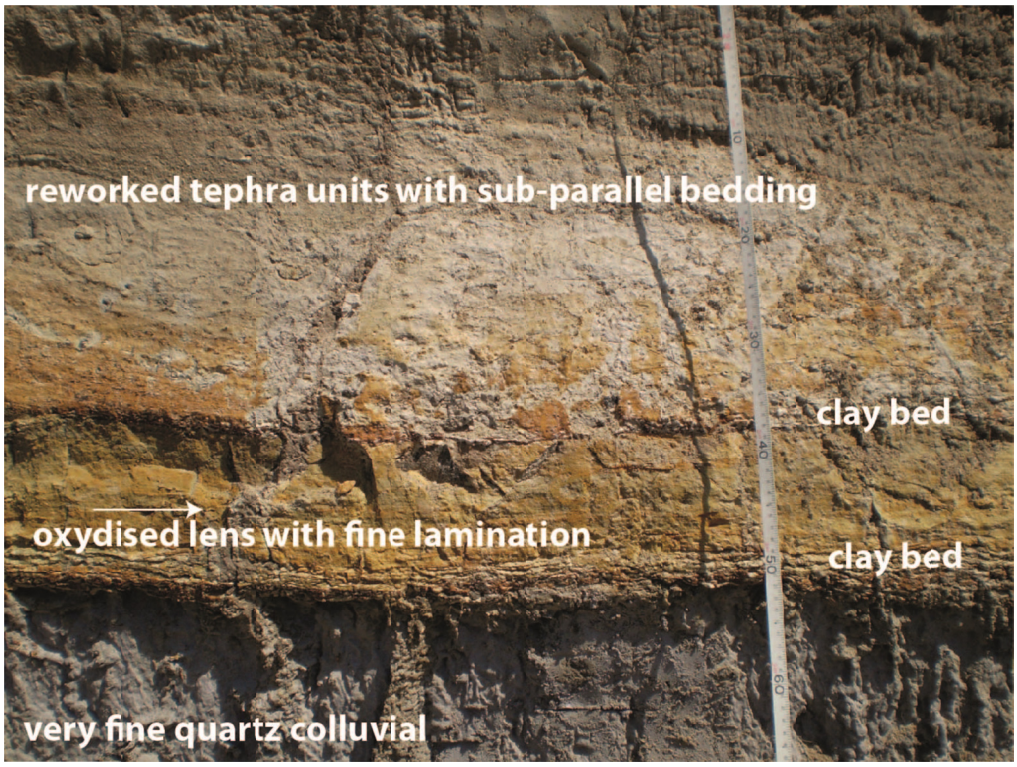

Figure 6-6 Sedimentary features of the oxidised lens at the base of the ash in KgL3. Note the dark red finely laminated clay bands limiting the oxidised lens. The association of iron oxides and clay suggests the development of a soil horizon and extended subaerial exposition of the terrace, before inundation by the river overbank sediments.

6.4.3 Sedimentology

Particle-size distributions for the Lenggong valley samples are provided in Table 6-2. Magnetic susceptibility (MS) and profile-averaged frequency distributions for each site are shown in Figure 6-7. The KgL1 YTT ash shows moderately sorted, unimodal grain-size distributions (Figure 6-7a, Table 6-2). The particle-size distributions indicate a sand-dominated environment (64%), with a minor silt component (34%) and 2% clay. The mean grain-size values range between 57 and 100 μm (very coarse silt - very fine sand).

The ash at KgL2 is poorly to very poorly sorted, mainly unimodal and bimodal (Figure 6-7b, Table 6-2). The analyses indicate high variability through the vertical sequence, with no apparent grading. The sediment at KgL2 is composed of 62% sand, 37% silt and 1% clay, with means clustered at 100 μm (very fine sand, Table 6-2).

Table 6-2 Selected particle size distribution parameters for the Lenggong YTT ash. Grain-size distributions measured on Malvern Mastersizer 2000, data quoted as average of 4 analyses per sample. Mean particle size quoted as geometric mean following method of Blott and Pye (2001). Particle fractions are chosen according to ash grain-size classification divisions.

Sample ID	Mean (μm)	Sorting (μm)	63-125 μm fraction of the total	>250 μm fraction of the total	Distribution	Sorting
KgL3-1	115.9	3.6	29%	28%	Bimodal	Poorly Sorted
KgL3-3	93.13	2.9	47%	14%	Unimodal	Poorly Sorted
KgL3-5	89.64	5.2	28%	29%	Trimodal	Very Poorly Sorted
KgL3-7	77.17	3.5	40%	15%	Unimodal	Poorly Sorted
KgL3-8	178.7	4.2	28%	29%	Bimodal	Very Poorly Sorted
KgL3-9	51.04	3.3	49%	6%	Bimodal	Poorly Sorted
KgL3-11	151.9	2.9	27%	34%	Bimodal	Poorly Sorted
KgL3-12	123.8	5.4	24%	35%	Trimodal	Very Poorly Sorted
KgL3-13	52.68	4.5	38%	12%	Trimodal	Very Poorly Sorted
KgL3-15	59.17	5.0	29%	17%	Trimodal	Very Poorly Sorted
KgL3-17	33.21	4.1	45%	4%	Trimodal	Very Poorly Sorted
KgL2-1	121.2	4.8	25%	37%	Trimodal	Very Poorly Sorted
KgL2-3	110.9	4.3	24%	33%	Unimodal	Very Poorly Sorted
KgL2-5	59.35	5.2	27%	24%	Bimodal	Very Poorly Sorted
KgL2-7	111.3	3.9	27%	30%	Bimodal	Poorly Sorted
KgL2-8	46.96	2.4	65%	0	Unimodal	Poorly Sorted
KgL2-9	65.01	3.7	39%	11%	Unimodal	Poorly Sorted
KgL2-10	81.75	3.9	35%	20%	Bimodal	Poorly Sorted
KgL2-12	155.0	4.2	21%	46%	Unimodal	Very Poorly Sorted
KgL2-13	74.36	4.1	37%	19%	Bimodal	Very Poorly Sorted
KgL2-14	116.5	3.7	29%	30%	Bimodal	Poorly Sorted
KgL2-15	78.29	4.5	31%	22%	Bimodal	Very Poorly Sorted
KgL1-1	83.21	4.3	30%	21%	Unimodal	Very Poorly Sorted
KgL1-3	71.92	3.5	44%	12%	Unimodal	Poorly Sorted
KgL1-5	100.5	3.3	34%	20%	Unimodal	Poorly Sorted
KgL1-7	68.51	3.5	44%	10%	Bimodal	Poorly Sorted
KgL1-11	95.21	3.7	32%	22%	Unimodal	Poorly Sorted
KgL1-13	78.52	3.3	41%	12%	Unimodal	Poorly Sorted
KgL1-14	57.55	3.1	53%	5%	Unimodal	Poorly Sorted
BTS-1	86.15	2.8	45%	5%	Unimodal	Poorly Sorted
BTS-3	109.2	2.6	40%	17%	Unimodal	Poorly Sorted
BTS	127.5	2.5	35%	20%	Unimodal	Poorly Sorted
BTS-7	111.1	3.2	33%	20%	Bimodal	Poorly Sorted
BTS-9	54.72	2.5	69%	0%	Unimodal	Poorly Sorted
BTS-10	41.27	2.5	67%	0%	Unimodal	Poorly Sorted
BTS-11	36.56	6.9	17%	19%	Polymodal	Very Poorly Sorted
BTS-12	8.233	4.8	6%	1%	Bimodal	Very Poorly Sorted
BTS-14	28.84	5.9	13%	15%	Trimodal	Very Poorly Sorted
BTS-16	23.88	3.9	29%	7%	Bimodal	Poorly Sorted

The KgL3 sediments are polymodal, very poorly sorted and show substantial variations in mean particle sizes ranging from 51 to 178 μm (Figure 6-7c, Table 6-2).

The BTS ash particle-size distributions range between 8 -127 μm. The sediments at this site show a higher clay frequency within the lower part of the section (Figure 6-7d). Moreover, this is the only site at which the silt component exceeds that of the sand (51% silt *v.* 47% sand, Table 6-2). Standard deviations indicate poorly to very poorly sorted sediments, with trimodal frequency distributions in the lower part of the section, but a unimodal distribution in the upper part.

The ash at KgL2 and BTS is low in magnetic mineral content. The samples from KgL3, as expected, show a stronger magnetic susceptibility of the oxidised lens ($9.3\ 10^{-8}\ m^3kg^{-1}$), whilst KgL1 shows a weak magnetism at the level of the thin oxidised lens observed in sample KgL1-11 ($6.4\ 10^{-8}\ m^3kg^{-1}$), but also a strong magnetism in sample KgL1-5 ($22.6\ 10^{-8}\ m^3kg^{-1}$, Figure 6-7). All samples reveal an increasing magnetic susceptibility towards the top, arising from contamination by overlying soils.

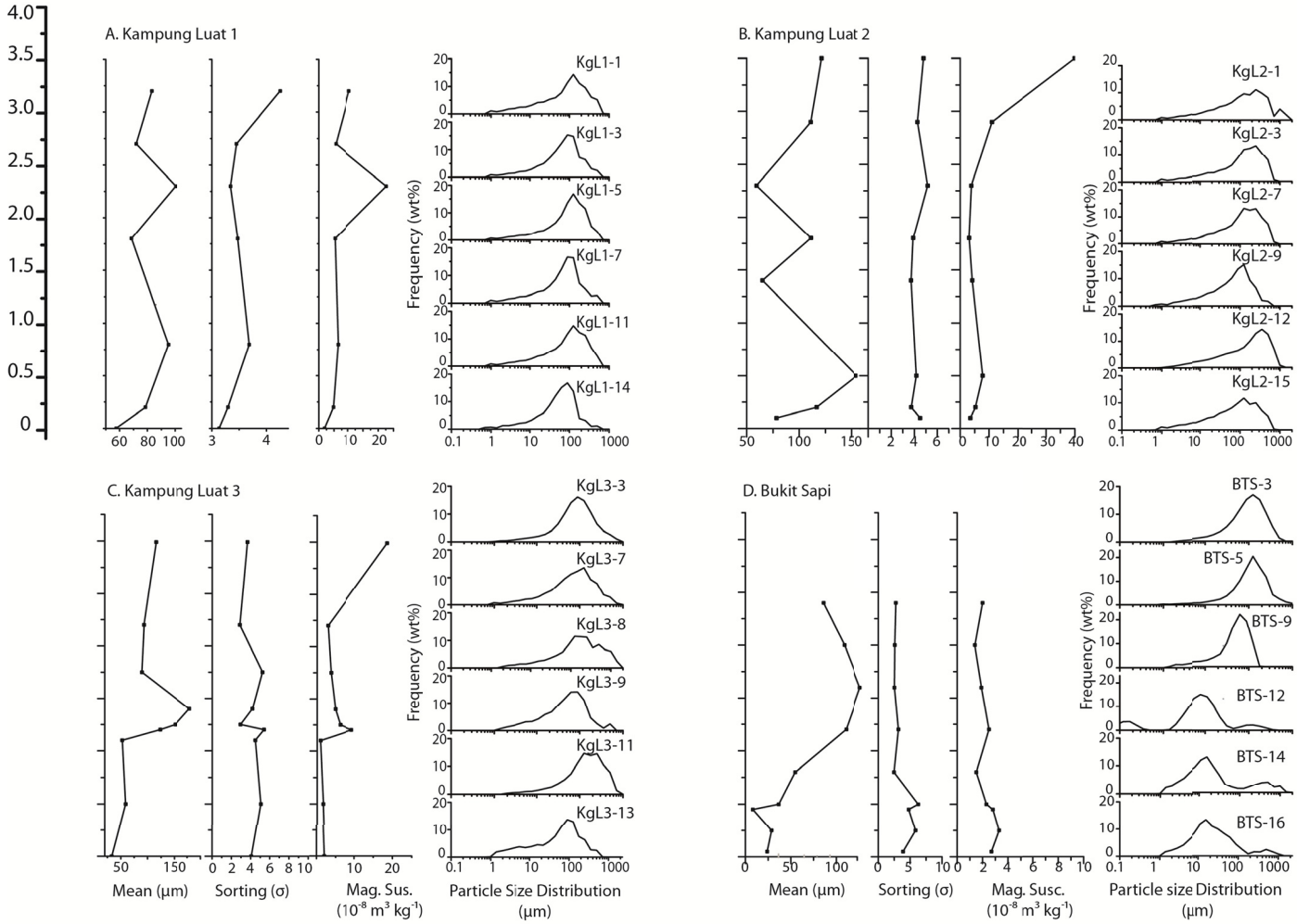

Figure 6-7 A) Sedimentological characteristics of KgL1. The particle-size distributions of KgL1 are skewed towards the coarser grain sizes. B) Sedimentological characteristics of KgL2. C) Sedimentological characteristics of KgL3. The oxidised lens is evident in the MS profile. High MS values towards the top units are probably sign of contamination by the upper soil. D) Sedimentological characteristics of BTS. BTS presents the finer grain sizes (2% clay, 51% silt). This is visible in the particle size distribution, shifted towards finer grain size. It is also in accordance with the geomorphic reconstruction of the site, which indicated that BTS does not belong to the same depositional environment of KgLs but to a small tributary.

Taphonomic heterogeneity of the Lenggong reworked deposits is reflected in their mineralogical associations. In the 63–125 μm interval, considered the dominant size interval for ash, the amount of ash ranges between 59 to 99 % (Table 6-3). In the > 250 μm interval, considered the 'non-ash' fraction, the ash percentages range from 36% to 89% of the total. A few samples did not have substantial coarse fractions (indicated N/A in Table 6-3). The site that includes most ash is KgL1 (Table 6-3), at which mineralogical components in the 63–125 μm fraction also show minor content of quartz, zircon, tourmaline and mica. In contrast to KgL1, the KgL2 samples (particularly those from lower in the section) contain mica flakes, together with a minor quartz and zircon, representing 50 to 90% of the non-ash grains. Modern plant fragments have been identified in KgL2-9. The KgL3 ash is particularly variable: the proportion of ash in the sediments decreases sharply in the middle of the unit, before again increasing towards the top. As expected, the clay hardpans sandwiching the ash lens have low ash content (sample KgL3-12, Table 6-3). Microscopic analyses of the ash grains in the oxidised lens at KgL3 reveal traces of iron oxides on the glass surfaces (Figure 6-8).

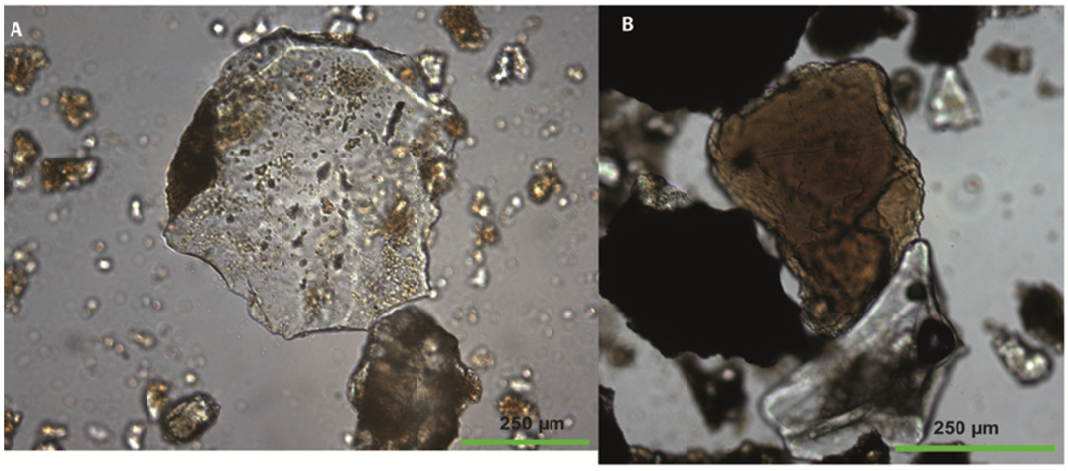

Figure 6-8 A) Oxidised patina on the surface of KgL3 grains and B) Mica flake Kgl2.

6.5 Discussion

The tephra units of the Lenggong valley are geochemically similar to those reported as YTT from other sites (Shane et al., 1995; Westgate et al., 1998; Petraglia et al., 2007; Smith et al. 2011). Since the Lenggong ash was derived from the same eruption, and assuming it was deposited

contemporaneously, any difference between the sites (in thickness, mineralogy, grain size) should reflect post-deposition processes.

Table 6-3 Ash content in the Lenggong valley tephra deposits.

Site	63–125 µm ash fraction	> 250 µm ash fraction
KgL1-3	96%	71%
Kgl1-5	92%	86%
KgL1-7	96%	N/A
KgL1-11	94%	89%
KgL1-13	95%	N/A
KgL1-14	99%	N/A
KgL2-3	77%	87%
KgL2-5	84%	71%
KgL2-8	77%	N/A
KgL2-9	89%	36%
KgL2-12	77%	69%
KgL2-15	74%	78%
KgL3-3	93%	48%
KgL3-5	59%	61%
KgL3-7	78%	58%
KgL3-8	93%	49%
KgL3-11	92%	84%
KgL3-12	22%	10%

6.5.1 Primary and reworked tephra: a reliable method of distinction?

The exposed tephra deposits in the Lenggong valley present general taphonomic characteristics that reveal the reworked nature of the sediments: they are up to ~ 4 m in thickness, include structures such as wavy laminations and they have non-volcanic components that imply mixing with other sedimentary detritus prior to final deposition. No primary ash was found at the sites.

A recent study of the primary ash layer in the Son Valley, India, showed a distinctive difference between the primary ash particle-size distributions - described as well-sorted, unimodal, with mean centred between 63 and 50 µm - and the reworked ash deposits above the primary stratum, characterised by polymodal distributions, poor sorting and presence of coarser particles (Lewis et al., 2012). Figure 6-9 shows a comparison of the particle-size distributions at Jwalapuram site 3 (Jones, 2010), and site KgL1. Jwalapuram exposes 5 cm of primary ash and 2.30 m of overlying reworked material. The plot shows that particle-size distributions of both the primary and reworked material from India and Malaysia are similar. The KgL1 samples are skewed to the right (very fine skewness), unlike the Indian samples. However, all the Indian tephra show a similar

skewness, independent of their being primary or reworked. Skewness may therefore develop through plume dispersion in the atmosphere, rather than provide a diagnostic indicator of primary ash.

The presence of coarser particles should not be taken as an indication of non-volcanic particles (and thus an indication of reworking). Scanning electron microscope images of grains from sample KgL2-1 reveal that the larger grain-size fraction is composed of ash aggregates and not non-volcanic grains (Figure 6-10). Ash particle aggregation is a widely recognised phenomenon in distal tephra deposits, although the process remains only partially understood. It could occur either during atmospheric transport or post- depositionally (Folch et al., 2010).

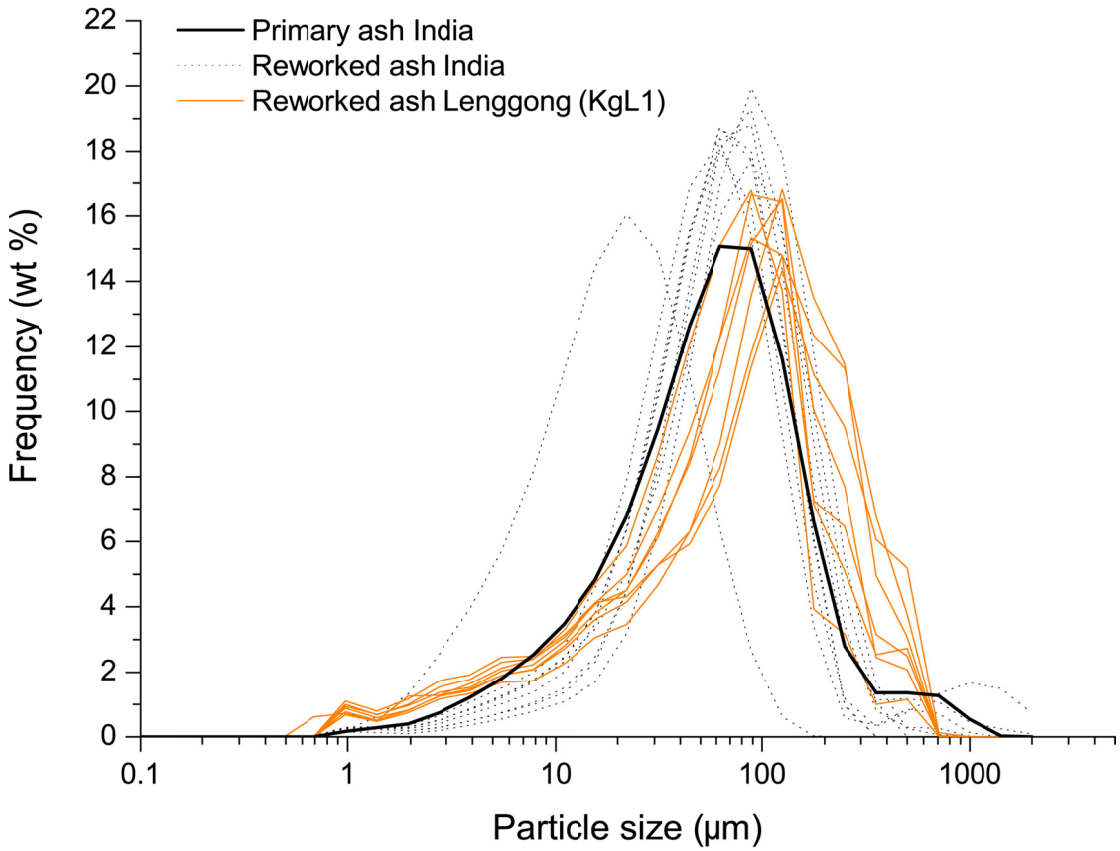

Figure 6-9 Particle-size distributions of the primary ash found at Jwalapuram site 3 and the reworked tephra from the Lenggong valley. The particle-size distributions from the Indian and Malaysian samples are similar. The primary ash sample (in bold) is symmetric and has a finer mean peak than the Malaysian reworked tephra. However, ash aggregation could account for such a discrepancy. Primary ash data from Jones (2010).

In summary, if the primary facies can be seen in the field, features such as moderate sorting, unimodality and high ash content can reliably be applied to support the interpretation (Table 6-4,

McLaren and Bowles, 1985; Klovan, 1966). However, these features cannot exclude the possibility that the ash is reworked: since as shown, secondary ash can be well sorted, fine and unimodal. This implies that where there is not a clearly exposed outcrop (for example in the case of cryptotephra in caves or lake cores) such techniques cannot be considered sufficiently robust to discriminate between the two (cf. also Davies et al., 2007; Morley and Woodward, 2011).

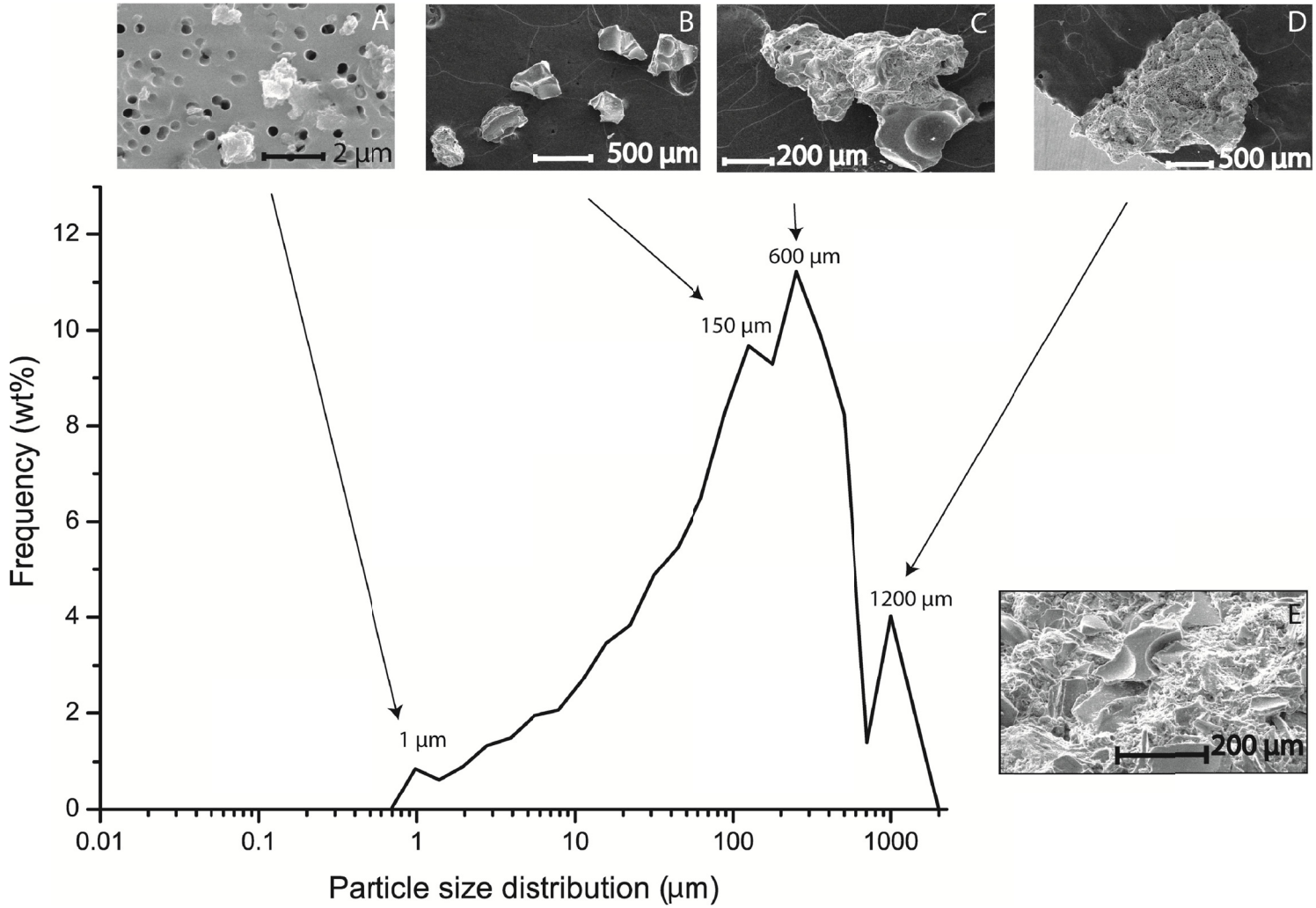

Figure 6-10 Polymodality is a typical characteristic of distal tephra horizons, due to the poor sorting and ash aggregations. Polymodality and unimodality are thus not diagnostic features to distinguish between primary and secondary ash. It is notable that two of three peaks in sample KgL2-1 are composed of ash shards (B) and ash shards aggregates (C, D). Photo E shows a zoom on a 1200 µm aggregate: it is possible to distinguish the cemented silica matrix and the micro glass fragments.

Table 6-4 General characteristics of primary and secondary ash units. The presence of a combination of these features usually distinguishes primary from secondary ash in terrestrial distal deposits where the tephra appear in metre-thick outcrops. The problems occur when the ash is found in sub-millimetre-scale strata, i.e. in cryptotephra or microtephra.

	PRIMARY ASH	SECONDARY ASH
Thickness	Cm-scale (usually 4-10 cm)	Can reach 10+ m
Colour	White looking (10 YR 8/1 and 8/2; 7.5 YR 8/2)	Wide range of grey-toned colours (10 YR 4/2; 10 YR 8/3, 7/3 and 7/4)
Basal contact	Sharp non-erosive	Gradual, erosive, non-erosive
Upper contact	Sharp non-erosive if sealed by non-volcanic sediments; gradual if overloaded by reworked units/ bioturbated	Gradual, erosive, non-erosive
Sedimentary structures	Variable, but usually no trace of vertical grading or water percolation structure; ball and pillows structures can be found at the upper boundary, if the ash was deposited in an aqueous environment	Variable: massive, horizontal stratification, ripple-cross lamination, parallel thin lamination, cross-bedded.
Grain shape	No difference	No difference
Grain-size distributions	Unimodal	Unimodal; polymodal
Lateral persistency	Variable	Consistent and variable
Cementation	Variable	Variable

6.5.1.1 The Kota Tampan YTT layer and archaeological implications

Collings (1938, p. 575) described the ash at Kota Tampan as a "deposit of volcanic tuff overlying a bed of sand and gravel, which itself rests on laterite, [..] probably an old terrace of the Perak River". The ash was reported to be 3 m in thickness, overlying gravel beds from which Palaeolithic implements belonging to 'Tampanian' industry had been recovered (Collings, 1938). Although the ash was not then characterised as primary or secondary, this author's stratigraphic description appears comparable with that at KgL3. He obtained a date of ~ 35 ka for the Tampan Palaeolithic tools, based on ^{14}C dating of wood obtained immediately underlying the ash (Stauffer, 1973). Later the dating of the YTT ash to 75 ka led to a corresponding increase in the age of the Tampanian tools (Ninkovich 1978a). However, comparison with the sequences examined here indicates that the excessive thickness of the Kota Tampan ash provides a strong suggestion of the secondary nature of the deposit. Since there is no record of a basal primary ash unit at this site, the implication is that the Kota Tampan ash could be reworked and deposited at a later date.

6.5.2 Mechanisms of tephra reworking in the Lenggong valley

The reported sedimentary structures and the particle-size distributions consistently suggest fluvial transport as the main process of accumulation and deposition of the distal tephra in the Lenggong valley. The absence of grading argues against tephra fallout as the predominant depositional process (Favalli et al., 2006). All the sequences studied are poorly to very poorly sorted, classified texturally as muddy sand, and sedimentologically classified as coarse silt, very coarse silt or very fine sand (Table 6-2). The deposits of KgL1, KgL2 and BTS are massive, while KgL3 showed horizontal laminations and planar bedding. Modern plant material has been found in all the deposits, particularly in KgL2. The percentage of ash varies in each deposit, although the principal grain-size interval (63-125 μm) contains 71 - 99% ash.

The tephra at KgL3, situated near the main channel, includes marked horizontal laminae and an oxidised ash lens ~ 10 cm thick, sandwiched between two ~ 5 cm thick clay hardpans. The lens is capped by 2.30 m of reworked tephra, sub-horizontally parallel laminated. The basal contact with the non-volcanic unit is non-erosional. The upper deposits at KgL3 are the product of the transport and redeposition of ash remobilised from upstream, probably by a flood flow. Yet, the wavy, laminated clay hardpans indicate deposition from suspension in slack water. Subaerial exposure preceded another phase of flooding and inundation. These characteristics suggest that KgL3 was deposited in a vegetated floodplain or swamp, characterised by seasonal flooding and desiccation (Nakayama and Yoshikawa, 1997). Similar tephra deposits separated by clay hardpans have been identified at Jwalapuram, in India (Petraglia et al., 2007). The deposit shows six clay hardpans through the ash sequence. Petraglia et al. (2007) interpreted the couplets as representing six monsoon cycles, characterised by wet (ash) and dry (clay) periods. KgL3 includes two clay hardpans, suggesting that the lens might represent one rainy season embedded between two dry seasons.

The ash at KgL1 and 2 was deposited in a depression. The particle-size distributions and mineralogical associations indicate a chaotic mixture of silty-sized ash and fine-sand-sized ash (Figure 6-7). This suggests that the two sequences are likely to be derived from slumping sedimentation in a colluvial area (Kataoka, 2005) possibly during a major flood event that remobilised the fall deposits from the surrounding hills. Such volcaniclastic facies might represent

a direct effect of the low liquefaction resistance of volcaniclastic deposits (Nakayama, 2001). Such types of slump deposits have been identified in volcaniclastic sequences in the Pliocene Mushono tephra, in central Japan (Kataoka, 2005).

Notably, although KgL1 and 2 are likely to have been deposited during the same slumping event, they show contrasting sedimentological characteristics. The high mica content at KgL2. (Figure 6-8) could have arisen from site-specific syn- or post-depositional processes. The bedrock underlying the catchment is micaceous granite. The presence of a nearby tributary could therefore have brought allochthonous mica from its local catchment. Alternatively, the KgL2 ash might originally have been closer to the palaeochannel bank, where it could have been more exposed to local bedrock weathering. At this site the lower units appear to be enriched in mica, probably eroded from underlying granites during flood events. Conversely, the mica could also be a primary magmatic component of the YTT tephra, since biotite is a primary product of the YTT bulk material (Chesner, 1998; Smith et al., 2011), and the accumulation of mica flakes in the basal stratum could be related to the density differences between mica (ρ=2900 kg/m^3) and rhyolite glass shards (ρ=2350-2450 kg/m^3). However, mica flakes may behave very differently from glass shards hydrodynamically, and the shape of the grains could be more important than density. This suggests that several site-specific parameters determined the final characteristics of the preserved deposits.

BTS is massive in aspect, similar to KgL2 1 and 2. However, the textural analyses showed that BTS is consistently finer (2% clay) and presents clear alternating subunits of clay-like and silty ash (Figure 6-5, Figure 6-7). Magnetic susceptibility reveals clear differences between lower and upper silt (Figure 6-7d). Massive resedimented units indicate that reworking occurred through hyperconcentrated flows resulting in sudden aggradation of ash (Segschneider et al., 2002; Kataoka, 2003; Manville et al., 2005; Manville et al., 2009a; Manville et al., 2009b). This suggests that BTS is the result of a mudflow (Nakayama and Yoshikawa, 1997) and the changes in particle size between bottom and top could indicate waxing and waning flow. Examples of similar lahar facies have been reported of the Ebisutoge–Fukuda tephra (Kataoka et al., 2009), and Ohta tephra of the Tokai Group (Nakayama and Yoshikawa, 1997), both in central Japan.

6.5.2.1 Time of deposition and implications for the YTT environmental impact debate

Magnetic susceptibility of sediments is an indicator of soil-forming processes in areas containing uniform parent material (Mullins, 1977). The constant values recorded for the samples analysed suggest the tephra accumulated in a short period. Neither the sedimentation rate, nor the total accumulation time for each deposit can be determined in the absence of bracketing ages below and above the units, and such data are not yet available for the Lenggong deposits (neither volcanic nor siliciclastic). Nevertheless, the facies suggest mudflow, slumping and flood flow as the main depositional processes, mechanisms that usually operate on timescales of hours or days (Nammah et al., 1986; Hayes et al., 2002; Mastrolorenzo et al., 2002). The only site that suggests subaerial exposure and a clear depositional hiatus is KgL3. Here a lens of ~ 10 cm of ash was deposited, probably from material in suspension, and sealed between two clay hardpans (Figure 6-6). This site is thus the best candidate for possible palaeoenvironmental studies in the area.

Nevertheless, attention is required when interpreting the palaeoenvironmental signals extracted from reworked tephra. Firstly, the time lag between the primary deposition of the YTT and the flood events is unknown. Therefore, the genesis of the palaeorecords might not be directly related to the eruption impact. Moreover, the records are likely to be influenced by site-specific morphological characteristics. This has been recently considered by Blinkhorn et al. (2012). These authors demonstrated that the oxygen and carbon stable isotope traces extracted from pedogenic carbonate beneath and overlying the YTT in twelve terrestrial deposits at Jwalapuram (see **§2.1** and Figure 2-1) were extremely variable. Such variability appeared directly linked to site-specific features (i.e. topographic height), rather than post-eruptive environmental feedbacks. This recent discovery reinforces the findings of this thesis, demonstrating the strong controls of the receiving environments on the tephra taphonomy. These have profound implications for the wider YTT debate, where conclusions regarding a drastic impact of the ashfall have been reached upon palaeoenvironmental reconstructions from proxies extracted from reworked tephra sequences (e.g. Williams et al., 2009; Haslam et al., 2010). In the light of the process highlighted herein, such conclusions maybe unsafe. In a broader sense the processes identified indicate that environmental techniques must be adapted to reflect the sedimentological and stratigraphical characteristics of the tephra sediments at any particular site.

6.6 Conclusion

Analysis of the stratigraphy and sedimentology of four new YTT localities in the Lenggong valley, Malaysia, have demonstrated that these tephra sequences are associated with fluvial and colluvial transport and deposition. Three volcaniclastic facies have been identified corresponding to flood-flow, mudflow and slumping sedimentation. Both major elements and REE chemical fingerprints confirm that the tephra in these facies corresponds to the YTT eruption

The field stratigraphy, particle mineralogical associations and size distribution of the sediments together indicate that the tephra deposits are reworked. The data suggest that the ash deposition occurred rapidly, on the scale of days or months. Although there are no dates currently available for the Lenggong sediments, further studies should be undertaken in order to assess the absolute age of the floods events and their accumulation rate. KgL3 is the only site at which non-volcanic material is exposed beneath the ash and where the mechanism of deposition allowed the development of an undisturbed ash unit. It should therefore be a good candidate for further studies to establish the detailed depositional chronology. The investigations reported here suggest that other areas of Peninsular Malaysia are likely to host YTT deposits. These include the Singar sub-catchment or the Temengor Lake, which might provide a locus for the testing of the mechanisms of accumulation and preservation outlined here.

Analyses of the mechanism of tephra reworking are particularly important in the case of the YTT, given the wide use of the ash deposits to assess the YTT environmental impact and its possible consequences for human populations. The results highlight the need to address new questions in order to refine the YTT debate, for example: how the rate of accumulation of the reworked ash sequence can be determined. Are there palaeoenvironmental proxies that can be extrapolated from the reworked sequence and with certainty related to the ashfall impact?

On a global scale, the work reported herein demonstrates the importance of producing detailed examinations of tephra units and their sedimentary environments, particularly when the tephra are used for chronological correlation, and where the occurrence of the ashfall could have had strong environmental impacts. This is particularly important in situations where substantial sediment transport and topographic contrasts predominate, as in Malaysia.

A major problem in the application of tephra for chronology and stratigraphy is the differentiation between primary and secondary ash. This chapter has demonstrated that particle-size analyses alone cannot be used in isolation to distinguish the two. This has significant implications when correlation is based on micro-tephra or cryptotephra. A new method is therefore required to differentiate unequivocally between primary and secondary ash facies. Ideally this should be a micro-scale technique that allows us reliably to distinguish the two on the basis of the characteristic features of single grains.

These concluding remarks bring the thesis to the point where it is appropriate to reflect on what has been achieved, and what still remains to be done in the future. **Chapter seven** will therefore discuss the conclusions of this work and the future objectives that flow from the point that this research has reached.

Chapter 7. Conclusions

Albert Einstein, in his Ideas and Opinions, suggested that "A great effort in the enterprise of science goes into constructing 'well-posed problems', that is, to directing and focusing the spotlight of enquiry to those questions that have certain and unambiguous answers" (Einstein, 1954, p. vii). This study does not provide a final answer to the question 'What was the environmental impact of the YTT?'. However, it has clearly demonstrated that the methods previously used to obtain such answers have neglected vital aspects of the YTT characteristics. For instance, previous estimates of the erupted volume of ash have been based on a method that has been here demonstrated to be insufficient to modelling the co-ignimbrite ashfall dispersal. The volume estimates of Rose and Chesner (1987) and that of Matthews et al.(2012) should therefore be considered only as crude approximations and be used cautiously in any further modelling of the eruption.

This thesis has also demonstrated two important tephrostratigraphic principles ignored in the previous literature. Firstly, if ash has been reworked, it should not be used as chronostratigraphic marker. It seems a basic observation, yet the majority of palaeoenvironmental reconstructions at terrestrial sites have been based on unverified sites, where the ash was clearly reworked, or at best of dubious status (i.e. Williams et al., 2009).

Secondly, it shows that the reworking of ash has dramatic consequences on its distribution and taphonomic characteristics, which, in consequence, cannot be related only to the volcanic signal; put simply, a clear understanding of reworking processes is essential. For example, palaeoenvironmental signals extracted from carbonate nodules in the tephra sequences of Jwalapuram (Haslam et al., 2010; Blinkhorn et al., 2012) are of limited application in the absence of an account of the reworking processes that generated the deposits from which the proxies were extracted. Similarly, the standard reconstruction methods such as those used by Jones ([2010], changes in sedimentation patterns, particle size distributions) can be strongly influenced by local transport mechanisms, and it is not clear if they can record the volcanic impact at all.

This work has provided a contribution to the YTT literature, and more significantly, it allows us to redefine the problem and construct well-focused and useful questions for future research. Here, therefore, the concluding chapter synthesises the main points of the thesis (**7.1**), identifies limitations of the studies (**7.2**) proposes new directions for future work (**7.3**), and discusses the broader implications (**7.4**).

7.1 Synthesis

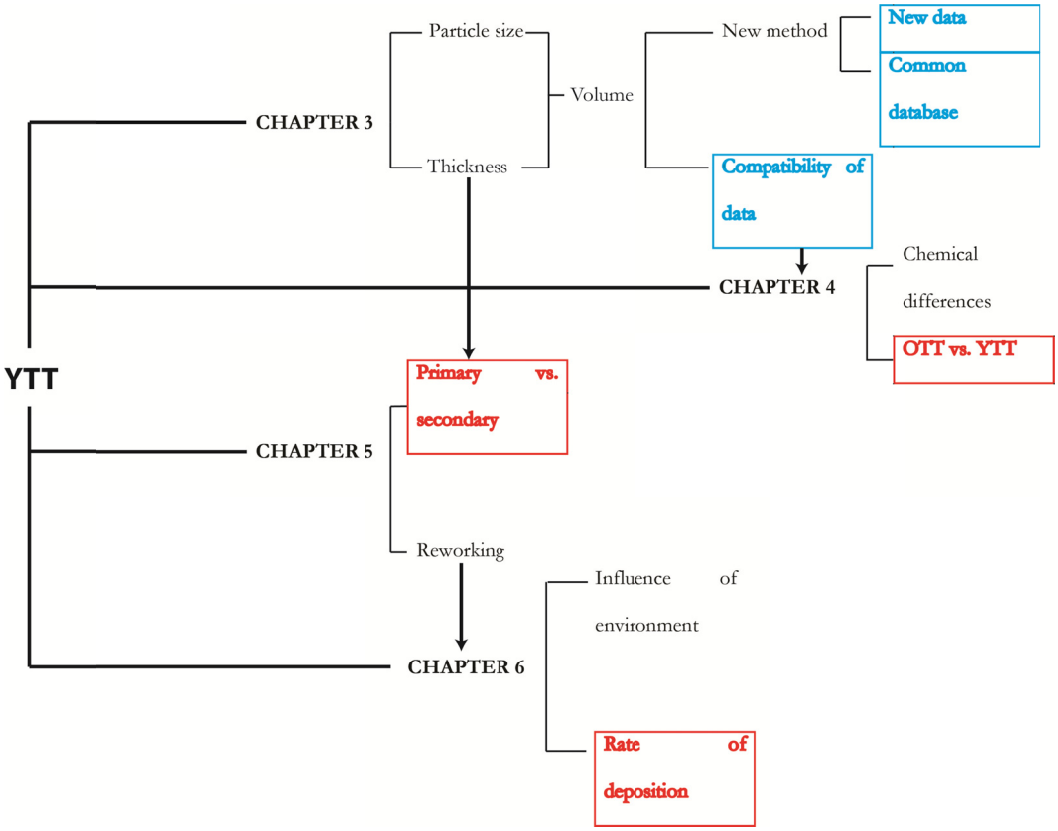

Figure 7-1 Conceptual diagram of the organization of the key chapters of this thesis, highlighting the main issues. Light blue represents broad issues related to the YTT literature, i.e. the lack of substantial data and the incompatibility of the literature reports. The red boxes represent future research topics (discussed in § **7.3**).

The principal difference between the YTT and any other known eruption is the extreme distance reached by the ashfall (more than 4000 km from the source) and the exceptional thickness of preserved ash deposits. **Chapter three** introduced a meta-analysis of the primary thickness and particle sizes of known YTT sites. The data revealed that the YTT deposits are largely composed of fine and very fine particles, and that neither the particle-sizes nor the thickness of the deposits

decrease in relation to the distance from the vent. It is also noted that reported data were often incomplete and inconsistent, which limited the scope of broader analysis.

Arguably the most widely described characteristics of the YTT that have been reported are the geochemical fingerprints of the tephra in each location. **Chapter four** compiled these data and tested the robustness and comparability of analyses from different authors, discovering inter-laboratory biases. Importantly, it showed that comparison of immobile elements provides evidence of significant chemical variation. This novel analysis showed how the YTT ash carries the stamp of compositional zonation established in the magma reservoir at the time of the eruption. The chapter also attempted to resolve the issue of the ash of Morgaon, India, dated as OTT but geochemically similar to the YTT. Analyses of the ratios of major elements were unable to resolve the issue, demonstrating that the OTT and YTT major elements are fundamentally identical.

Chapter five presented the case of another important Indian YTT layer, moving from analysis of the YTT at the scale of individual particles to the YTT as thick tephra deposits. The fundamental issue of differentiation between primary and secondary ash was addressed by developing the tephrostratigraphy of the Son Valley. This also demonstrated the necessity of discriminating between tephra transport mechanisms (in this case, fluvial).

Finally **Chapter six** used the tephra deposits, in this case the secondary ash deposits in the Lenggong valley, Malaysia, to reveal tephra reworking mechanisms. The study showed that the accumulation of tephra occurred reasonably rapidly, probably on the timescale of decades, strongly influenced by proximity to flowing water and local landscape features. A detailed analysis of particle size distributions and allochthonous components showed that these characteristics are not diagnostic of the source of the ash. This chapter further highlighted the need for future work to assess the relative rate and timescale of tephra accumulation.

7.2 Limitations of the research

In addition to the substantial progress outlined above, the research has clearly demonstrated the limitations of current geochemical and sedimentological methods. It highlights three important questions that remain unresolved.

Can we reliably distinguish primary and secondary ash? A key challenge is to develop a quantitative method to distinguish primary and secondary ash in the lab. Current practice is to use a suite of characteristics – such as colour, particle size, presence of allochthonous components, thickness and nature of the contact boundaries – to distinguish the two, but the approach is fundamentally qualitative. These analyses, the most detailed to date, were unable to identify characteristics that reliably distinguish the source of the ash. Estimating primary tephra thickness is also subjective, since the upper boundary between primary and the secondary ash is often poorly defined.

Can we estimate the rate of accumulation of reworked tephra? Poor temporal resolution of the tephra sequence leaves substantial uncertainty in estimating the timeframe of secondary ash deposition. This is crucial in considering the potential environmental impact of the ashfall, since the time taken for the system to re-establish its pre-eruption equilibrium is an important indicator of damage to the receiving environment.

Can we determine the difference between OTT and YTT tephra? Current methods are unable to distinguish between OTT and YTT composition, and recent findings of OTT products some 1000 km from the eruption site now suggest that OTT could have been of similar magnitude to the YTT. The Morgaon ash has now been dated to ~ 800 ka, raising the question whether OTT deposits are present in India. This brings new importance to this geochemical issue, as it has implications for our understanding of early human migration patterns.

7.3 Future research

The progress towards improved tephrostratigraphy presented in this thesis can be used as a springboard for future research to address the unresolved questions presented above. These might include:

Assessment of quantitative differences between primary and secondary ash by establishing diagenetic features on the surfaces of individual grains. Weathering of volcanic ash begins immediately after sedimentation; the extent of alteration depends on specific conditions including exposure to meteoric water and the depth of burial. Although I have demonstrated that rhyolitic ash is resistant to alteration (**Chapter four**), high-resolution IR-spectra on rhyolitic glasses from Kamchatka, Russia, showed a modest development of opal during different lithogenic stages (Kuznetsova et al., 2009). The presence of such secondary products could be used as a diagnostic indicator of primary vs. secondary ash. However, clay mineral analyses previously performed on YTT ash (the author, unpublished data) showed that clay minerals are difficult to detect when associated with a large amount of ash. Crystal fractions < 1 μm, must be used and special care is needed when detecting the opal by x-ray diffraction, since even a small quantity of glass shards can deflect the x-rays.

Use of fallout and/or lithogenic radionuclides to assess ash sedimentation rates. Medium-term (101–102 years) rates of overbank sedimentation on river floodplains have been successfully measured using the fallout radionuclides ^{137}Cs and excess ^{210}Pb. The YTT is too old for the use of these indicators, but the ratio between radionuclides ^{26}Al and ^{10}Be (half-life of 7.30 × 105 and 1.5 × 106 years respectively (Balco et al., 2005)) might be used instead. The Al/Be ratio varies with the duration of burial and these elements are incorporated in quartz grains accumulated with the tephra. Thus the ratio might indicate the time between burial of the primary ash and the accumulation of secondary ash (Pelletier et al., 2008).

Alternative geochemical techniques to distinguish between OTT and YTT. Analysis of welded tuffs belonging to the OTT in Sumatra suggested that the rare elements Ba, Sr and Rb might discriminate between OTT and YTT (Chesner, 1998). Until the discovery of OTT tephra in the South China Sea, it was assumed to be a minor eruption, and thus OTT distal ash has been characterised only in terms of major components, and rare elements analyses are not presently available. The first step therefore would be to analyse the rare element composition of known OTT samples, such as the OTT recovered from site 578 or 1143A of the Ocean Drilling Programme, two marine cores that reported all three of the Toba ash layers. If these rare elements cannot be used to distinguish between the two, another approach might be to analyse the light

rare earth element (LREE) composition of accessory minerals present in the tephra such as apatite or allanite. Allanite in particular is LREE-rich, and previous analyses showed that the YTT allanite is higher in such elements than is the OTT allanite (Chesner and Ettlinger, 1989; Chesner, 1998). These accessory minerals are however infrequently found in distal tephra deposits.

7.4 Broader implications

This work has demonstrated several stratigraphic misconceptions and identified new approaches to enhance volcanological understanding. It has also highlighted several remaining issues in YTT research, and important ways in which to address them. This research has focused on the YTT eruption, an exceptional event in the Earth's recent history, but it has broader implications.

Volcanology. The problem of complex settling behaviours of small particles has important implications for recent ash cloud monitoring for aviation hazards, as seen after the 2010 eruptions of Eyjafjallajökull. Jet engines can be severely damaged by volcanic ash and it is therefore important to understand the complex dynamics between the volcanic cloud, particle behaviour and atmospheric transport. Similarly, the phenomenon of ash aggregation seen in the survey sites in Malaysia has recently been discovered in some ashfall deposits from the 1981 eruption of Mount St. Helens (Durant et al., 2009). It is now believed that ash aggregates play an important role in controlling ash dispersal and sedimentation, although the processes by which they form remain uncertain.

Climatology. Distinguishing primary from secondary ash is especially important in the case of cryptotephra or in cases where the geological section does not allow separation of the two. This might prove extremely useful in climatic reconstructions. For example, cryptotephra recovered from marine and lacustrine cores in Scotland and the North Sea, if correctly dated, could significantly improve the chronology of Holocene climatic oscillations, with implications for the role of climatic changes in shaping the development of European communities.

Geochemistry. Chapter 4 has shown how rhyolitic ash releases elements into the receiving environment. Many of the elements which can leach from the ash (Al, Fe, Na, K) are included in drinking water guidelines due to their toxicity, and may constitute potential hazards to the

environment and human health. The environmental geochemistry of ancient volcanic ash could therefore help us to evaluate water supply systems affected by ash leaching after, for example, a strong rain event (cf. Crowley et al., 1994).

Geoarchaeology. The YTT is an important marker in Archaeological studies, partly because the eruption coincided approximately with the spread of modern humans out of Africa and across Asia (James and Petraglia, 2005; Petraglia et al., 2009; Armitage et al., 2011). When stone tools of the "Tampanian Men" were found in Kota Tampan, Malaysia, at the beginning of the 1960s, the sediments associated with these archaeological artefacts were radiocarbon dated at ~ 35 ka BP. Once it was discovered that the ash above those sediments was YTT, the age of the stone tools was revised to ~ 74 ka. If the Kota Tampan ash proves to be the product of reworking, it could cast doubt on the older age attributed to the artefacts. This has major implications not only for Malaysian archaeology, but also for studies tracing the migration of modern humans from Malaysia to Australasia. Revising our understanding of the YTT marker, and the broader implications this might have for those archaeological theories which rely upon it, suggests creating a new mindset within the discipline of Geoarchaeology.

Multidisciplinary Sciences. Michael Petraglia, in the Quaternary International special volume "*The Toba Volcanic Super-eruption of 74,000 Years Ago: Climate Change, Environments, and Evolving Humans*", concluded the introductory preface by saying "This work indicates the need for substantial further research on the Toba super-eruption and its impact. Clearly, the most profitable way forward is to form interdisciplinary collaborations among volcanologists, climate modellers, plant scientists, mammalian palaeontologists, geneticists, palaeoanthropologists, and archaeologists." (Petraglia et al., 2012, p.3).

The term "multidisciplinary" is often misinterpreted; we should not simply mean the use of findings from overlapping disciplines to explain a question — this is merely collecting evidence to test a theory. Rather, the term should conjure images of the search for solutions from other disparate fields of endeavour, looking for alternative points of view, trying to resolve questions that our discipline has posed using tools gathered from other branches of learning, maybe far away from our own field of knowledge. This returns us to the thoughts of Einstein: analyses and

argument often result in modification, refinement, alteration and restatement of questions. We may here have an answer to our original question, but much more interesting is now the illuminated path ahead.

Chapter 8. References

Acharyya, S. K., and Basu, P. K. 1993. Toba Ash on the Indian Subcontinent and Its Implications for Correlation of Late Pleistocene Alluvium. Quaternary Research 40 (1): 10-19.

Aldiss, D. T., and Ghazali, S. A. 1984. The regional geology and evolution of the Toba volcano-tectonic depression, Indonesia. Journal of the Geological Society 141 (3): 487-500.

Alfano, F., Bonadonna, C., Delmelle, P., and Costantini, L. 2011. Insights on tephra settling velocity from morphological observations. Journal of Volcanology and Geothermal Research 208 (3-4): 86-98.

Alloway, B. V., Larsen, G., Lowe, D. J., Shane, P. A. R., Westgate, J. A. 2007. Quaternary Stratigraphy, Tephrochronology. In: A. E. Scott (Editor-in-Chief), Encyclopedia of Quaternary Science, Elsevier, Oxford, pp. 2869-2898.

Ambrose, S. H. 1998. Late Pleistocene human population bottlenecks, volcanic winter, and differentiation of modern humans. Journal of Human Evolution 34 (6): 623-651.

Ambrose, S. H. 2003. Did the super-eruption of Toba cause a human population bottleneck? Reply to Gathorne-Hardy and Harcourt-Smith. Journal of Human Evolution 45 (3): 231.

Andrews, B. J., and Manga, M. 2012. Experimental study of turbulence, sedimentation, and coignimbrite mass partitioning in dilute pyroclastic density currents. Journal of Volcanology and Geothermal Research 225-226 (0): 30-44.

Armitage, S.J., Jasim, S.A., Marks, A.E., Parker, A.G., Usik, V.I., Uerpmann, H.-P. 2011. The Southern Route Out of Africa: Evidence for an Early Expansion of Modern Humans into Arabia. Science 331(6016): 453–456.

Bachmann, O., and Bergantz, G. W. 2008. Deciphering magma chamber dynamics from styles of compositional zoning in large silicic ash flow sheets. *In* "Reviews in Mineralogy and Geochemistry." pp. 651-674.

Baines, P. G., and Sparks, R. S. J. 2005. Dynamics of giant volcanic ash clouds from supervolcanic eruptions. Geophys. Res. Lett. 32 (24): L24808.

Bakker, L., Lowe, D. J., and Jongmans, A. G. 1996. A micromorphological study of pedogenic processes in an evolutionary soil sequence formed on Late Quaternary rhyolitic tephra deposits, North Island, New Zealand. Quaternary International 34-36 (0): 249-261.

Balco, G., Stone, J. O. H., and Jennings, C. 2005. Dating Plio-Pleistocene glacial sediments using the cosmic-ray-produced radionuclides ^{10}Be and ^{26}Al. American Journal of Science 305 1-41.

Banerjee, S., Jeevankumar, S. 2007. Facies and depositional sequence of the Mesoproterozoic Rohtas Limestone: Eastern Son valley, Vindhyan basin. Journal of Asian Earth Sciences 30 (1): 82–92.

Basu, P. K., Biswas S., and Acharyya, S.K. 1987. Late Quaternary ash beds from Son and Narmada basins, Madhya Pradesh. Indian Minerals 41 66-72.

Bhattacharyya, A., Morad, S. 1993. Proterozoic braided ephemeral fluvial deposits: an example from the Dhandraul Sandstone Formation of the Kaimur Group, Son Valley, central India. Sedimentary Geology 84 (1-4): 101.

Beddoe-Stephens, B., Aspden, J. A., and Shepherd, T. J. 1983. Glass inclusions and melt compositions of the Toba Tuffs, northern Sumatra. Contributions to Mineralogy and Petrology 83 (3)**:** 278-287.

Bellier, O., and Sebrier, M. 1994. Relationship between tectonism and volcanism along the Great Sumatran Fault Zone deduced by spot image analyses. Tectonophysics 233 (3-4)**:** 215-231.

Blinkhorn, J., Parker, A. G., Ditchfield, P., Haslam, M., and Petraglia, M. 2012. Uncovering a landscape buried by the super-eruption of Toba, 74,000 years ago: A multi-proxy environmental reconstruction of landscape heterogeneity in the Jurreru Valley, south India. Quaternary International 258 (0)**:** 135-147.

Blott, S. J., and Pye, K. 2001. GRADISTAT: a grain size distribution and statistics package for the analysis of unconsolidated sediments. Earth Surface Processes and Landforms 26 (11)**:** 1237-1248.

Bobe, R., Behrensmeyer, A.K., Chapman, R.E. 2002. Faunal change, environmental variability and late Pliocene hominin evolution. Journal of Human Evolution 42: 475–497.

Bonadonna, C., Phillips, J.C. 2003. Sedimentation from strong volcanic plumes. J. Geophys. Res. 108 (B7): 2340.

Bonadonna, C., and Houghton, B. F. 2005. Total grain-size distribution and volume of tephra-fall deposits. Bulletin of Volcanology 67 (5)**:** 441-456.

Bonadonna, C., Ernst, G. G. J., and Sparks, R. S. J. 1998. Thickness variations and volume estimates of tephra fall deposits: the importance of particle Reynolds number. Journal of Volcanology and Geothermal Research 81 (3-4)**:** 173-187.

Bonadonna, C., Genco, R., Gouhier, M., Pistolesi, M., Cioni, R., Alfano, F., Hoskuldsson, A., and Ripepe, M. 2011. Tephra sedimentation during the 2010 Eyjafjallajökull eruption (Iceland) from deposit, radar, and satellite observations. J. Geophys. Res. 116 (B12)**:** B12202.

Bond, G., Broecker, W., Johnsen, S., McManus, J., Labeyrie, L., Jouzel, J., Bonani, G. 1993. Correlations between climate records from North Atlantic sediments and Greenland ice. Nature 365 (6442): 143.

Bridgland, D., Westaway, R. 2008. Climatically controlled river terrace staircases: A worldwide Quaternary phenomenon. Geomorphology 98 (3-4): 285–315.

Bühring, C., Sarnthein, M., and Leg 184 Shipboard Scientific Party 2000. Toba ash layers in the South China Sea: Evidence of contrasting wind directions during eruption ca. 74 ka. Geology 28 (3)**:** 275-278.

Campo, E.V., Duplessy, J.C., Rossignol-Strick, M. 1982. Climatic conditions deduced from a 150-kyr oxygen isotope-pollen record from the Arabian Sea. Nature 296 (5852): 56.

Cerling, T. E., Brown, F. H., and Bowman, J. R. 1985. Low-temperature alteration of volcanic glass: Hydration, Na, K, ^{18}O and Ar mobility. Chemical Geology: Isotope Geoscience section 52 (3-4)**:** 281-293.

Charman, D. J., West, S., Kelly, A., and Grattan, J. 1995. Environmental change and tephra deposition: The strath of Kildonan, Northern Scotland. Journal of Archaeological Science 22 (6)**:** 799-809.

Chen, C.-H., Yang, T.F., Song, S.-R., Iizuka, Y., Wei, K.-Y. 2000. Toba ash layers in the South China Sea: Evidence of contrasting wind directions during eruption ca. 74 ka: Comment and Reply: Comment. Geology 28 (11): 1055–1056.

Chesner, C. A. 1988. "The Toba Tuffs and Caldera complex, sumatra, Indonesia: Insights to magma bodies and eruptions.", Michigan Technology University.

Chesner, C. A. 1998. Petrogenesis of the Toba Tuffs, Sumatra, Indonesia. Journal of Petrology 39 (3)**:** 397-438.

Chesner, C. A. 2012. The Toba Caldera Complex. Quaternary International 258 (0)**:** 5-18.

Chesner, C. A., and Ettlinger, A. D. 1989. Composition of volcanic allanite from the Toba Tuffs, Sumatra, Indonesia. American Mineralogist 74 (7-8)**:** 750-758.

Chesner, C. A., and Rose, W. I. 1991. Stratigraphy Of The Toba-Tuffs And The Evolution Of The Toba-Caldera Complex, Sumatra, Indonesia. Bulletin Of Volcanology 53 (5)**:** 343-356.

Chesner, C. A., and Luhr, J. F. 2010. A melt inclusion study of the Toba Tuffs, Sumatra, Indonesia. Journal of Volcanology and Geothermal Research 197 (1-4)**:** 259-278.

Chesner, C. A., Sporleder, B. A., Bohnenstiehl, D. R., and Dolan, M. T. 1996. Post-caldera lavas at the Toba Caldera, Sumatra, Indonesia. Geological Society of America Abstracts with Programs 28 32.

Chesner, C. A., Boroughs, S. P., Storm, L. C., and McIntosh, W. C. 2000. Constraints on resurgence at the Toba Caldera, Sumatra, Indonesia. Geological Society of America Abstracts with Programs 3: 502.

Chesner, C. A., Rose, W. I., Deino, A., Drake, R., and Westgate, J. A. 1991. Eruptive history of Earth's largest Quaternary caldera (Toba, Indonesia) clarified. Geology 19 (3)**:** 200-203.

Clemens, S. C., and Prell, W. L. 2003. A 350,000 year summer-monsoon multi-proxy stack from the Owen Ridge, Northern Arabian Sea. Marine Geology 201 (1-3)**:** 35.

Collings, H. D. 1938. Pleistocene Site in the Malay Peninsula. Nature 142 (3595): 575-576.

Collins, B.D., Dunne, T. 1986. Erosion of tephra from the 1980 eruption of Mount St. Helens. Geological Society of America Bulletin 97 (7): 896–905.

Costa, A., Folch, A., Macedonio, G., Giaccio, B., Isaia, R., and Smith, V. C. 2012. Quantifying volcanic ash dispersal and impact of the Campanian Ignimbrite super-eruption. Geophys. Res. Lett. 39 (10)**:** L10310.

Crowley, S.S., Dufek, D.A., Stanton, R.W., Ryer, T.A. 1994. The effects of volcanic ash disturbances on a peat-forming environment; environmental disruption and taphonomic consequences. Palaios 9 (2): 158–174.

Davies, S. M., Elmquist, M., Bergman, J., Wohlfarth, B., and Hammarlund, D. 2007. Cryptotephra sedimentation processes within two lacustrine sequences from west central Sweden. The Holocene 17 (3)**:** 319-330.

Davies, S. M., Abbott, P. M., Pearce, N. J. G., Wastegaard, S., and Blockley, S. P. E. 2012. Integrating the INTIMATE records using tephrochronology: rising to the challenge. Quaternary Science Reviews 36 (0)**:** 11-27.

Delmelle, P., Villiéras, F., Pelletier, M., 2005. Surface area, porosity and water adsorption properties of fine volcanic ash particles. Bull. Volcanol. 67 (2): 160.

De Silva, S., Zandt, G., Trumbull, R., Viramonte, J. G., Salas, G., and JimÃ©nez, N. s. 2006. Large ignimbrite eruptions and volcano-tectonic depressions in the Central Andes: a thermomechanical perspective. Geological Society, London, Special Publications 269 (1)**:** 47-63.

Dehn, J., Farrel, J.W., and Schmincke, H.U. 1991. Neogene tephrochronology from site 758 on Ninety East ridge: Indonesian arc volcanism of the past 5 Ma. Proceedings of the Ocean Drilling Program, Scientific Results 121 273-295.

Diehl, J. F., Onstott, T. C., Chesner, C. A., and Knight, M. D. 1987. No short reversals of Brunhes Age recorded in the Toba Tuffs, north Sumatra, Indonesia. Geophys. Res. Lett. 14 (7)**:** 753-756.

Di Rita, F., Magri, D., 2009. Holocene drought, deforestation and evergreen vegetation development in the central Mediterranean: a 5500 year record from Lago Alimini Piccolo, Apulia, southeast Italy. The Holocene 19 (2): 295–306.

Durant, A. J., Rose, W. I., Sarna-Wojcicki, A. M., Carey, S., and Volentik, A. C. M. 2009. Hydrometeor-enhanced tephra sedimentation: Constraints from the 18 May 1980 eruption of Mount St. Helens. J. Geophys. Res. 114 (B3)**:** B03204.

Ersoy, O., Chinga, G., Aydar, E., Gourgaud, A., Evren Cubukcu, H., Ulusoy, I. 2006. Texture

discrimination of volcanic ashes from different fragmentation mechanisms: A case study, Mount Nemrut stratovolcano, eastern Turkey. Computers & Geosciences 32 (7): 936.

Ersoy, O., Sen, E., Aydar, E., Tatar, I., Çelik, H.H. 2010. Surface area and volume measurements of volcanic ash particles using micro-computed tomography (micro-CT): A comparison with scanning electron microscope (SEM) stereoscopic imaging and geometric considerations. Journal of Volcanology and Geothermal Research 196 (3-4), 281.

Fanning, K.A., Schink, D.R. 1969. Interaction of Marine Sediments with Dissolved Silica. Limnology and Oceanography 14 (0): 59–68.

Fauzi, McCaffrey, R., Wark, D., Sunaryo, and Prih Haryadi, P. Y. 1996. Lateral variation in slab orientation beneath Toba Caldera, northern Sumatra. Geophys. Res. Lett. 23 (5)**:** 443-446.

Favalli, M., Pareschi, M., Zanchetta, G. 2006. Simulation of syn-eruptive floods in the circumvesuvian plain (southern Italy). Bull. Volcanol. 68 (4): 349.

Fierstein, J., and Nathenson, M. 1992. Another look at the calculation of fallout tephra volumes. Bulletin of Volcanology 54 (2)**:** 156-167.

Floyd, P. A., and Winchester, J. A. 1978. Identification and discrimination of altered and metamorphosed volcanic rocks using immobile elements. Chemical Geology 21 (3-4)**:** 291-306.

Folch, A., Costa, A., Durant, A., and Macedonio, G. 2010. A model for wet aggregation of ash particles in volcanic plumes and clouds: 2. Model application. J. Geophys. Res. 115 (B9)**:** B09202.

Folk, R. L. 1966. A review of grain-size parameters. Sedimentology 6 (2)**:** 73-93.

Folk, R. L., and Ward, W. C. 1957. Brazos River bar [Texas]; a study in the significance of grain size parameters. Journal of Sedimentary Research 27 (1)**:** 3-26.

Fritz, W.J. 1980. Reinterpretation of the depositional environment of the Yellowstone "fossil forests." Geology 8 (7): 309–313.

Froese, D.G., Zazula, G.D., Reyes, A.V. 2006. Seasonality of the late Pleistocene Dawson tephra and exceptional preservation of a buried riparian surface in central Yukon Territory, Canada. Quaternary Science Reviews 25 (13-14), 1542.

Froggatt, P. C. 1982. Review of methods of estimating rhyolitic tephra volumes; applications to the Taupo volcanic zone, New Zealand. Journal of Volcanology and Geothermal Research 14 (3-4)**:** 301-318.

Gardner, J. E., Layer, P. W., and Rutherford, M. J. 2002. Phenocrysts versus xenocrysts in the youngest Toba Tuff: Impications for the petrogenesis of 2800 km3 of magma. Geology 30 (4)**:** 347-350.

Gasparotto, G., Spadafora, E., Summa, V., and Tateo, F. 2000. Contribution of grain size and compositional data from the Bengal Fan sediment to the understanding of Toba volcanic event. Marine Geology 162 (2-4)**:** 561-572.

Gathorne-Hardy, F. J., and Harcourt-Smith, W. E. H. 2003. The super-eruption of Toba, did it cause a human bottleneck? Journal of Human Evolution 45 (3)**:** 227-230.

Gatti, E., and Oppenheimer, C. 2012. Utilization of distal tephra records for understanding climatic and environmental consequences of the Youngest Toba Tuff. In: L. Giosan, D. Fuller, R. Flad, and P. Clift (Eds.), Climates, Past Landscapes and Civilizations, American Geophysical Union Monograph, Washington DC, In press.

Gatti, E., Durant, A. J., Gibbard, P. L., and Oppenheimer, C. 2011. Youngest Toba Tuff in the Son Valley, India: a weak and discontinuous stratigraphic marker. Quaternary Science Reviews 30 (27-28)**:** 3925-3934.

Gatti E., Mokhtar, S., Talib, K., Rashidi, A., Gibbard, P., Oppenheimer, C., 2012. Depositional processes of reworked tephra from the Late Pleistocene Younger Toba Tuff deposits in the Lenggong Valley, Malaysia, Quaternary Research, In Press, Corrected Proof.

Gatti, E., Achyuthan, H., Villa, I., Gibbard, P., and Oppenheimer, C. Submitted article. Geochemical patterns in distal and proximal Toba glass. Bulletin of Volcanology.

Ghiara, M. R., and Petti, C. 1995. Chemical alteration of volcanic glasses and related control by secondary minerals: Experimental studies. Aquatic Geochemistry 1 (4)**:** 329-354.

Gibling, M. R., Sinha, R., Roy, N. G., Tandon, S. K., and Jain, M. 2008. Quaternary fluvial and eolian deposits on the Belan river, India: paleoclimatic setting of Paleolithic to Neolithic archeological sites over the past 85,000 years. Quaternary Science Reviews 27 (3-4)**:** 391.

Gowda, I. G., Kirkpatrick, D. G., Lee, D. T., Naamad, A. 1983. Dynamic Voronoi Diagrams. IEEE Trans Inform Theory 29(0):724–731

Haslam, M., Clarkson, C., Petraglia, M., Korisettar, R., Jones, S., Shipton, C., Ditchfield, P., and Ambrose, S. H. 2010. The 74 ka Toba super-eruption and southern Indian hominins: archaeology, lithic technology and environments at Jwalapuram Locality 3. Journal of Archaeological Science 37 (12)**:** 3370-3384.

Haslam, M., Roberts, R. G., Shipton, C., Pal, J. N., Fenwick, J. L., Ditchfield, P., Boivin, N., Dubey, A. K., Gupta, M. C., and Petraglia, M. 2011. Late Acheulean hominins at the Marine Isotope Stage 6/5e transition in north-central India. Quaternary Research 75 (3)**:** 670-682.

Hayes, S. K., Montgomery, D. R., and Newhall, C. G. 2002. Fluvial sediment transport and deposition following the 1991 eruption of Mount Pinatubo. Geomorphology 45 (3-4)**:** 211.

Herzog, M., and Graf, H.-F. 2010. Applying the three-dimensional model ATHAM to volcanic plumes: Dynamic of large co-ignimbrite eruptions and associated injection heights for volcanic gases. Geophys. Res. Lett. 37 (19)**:** L19807.

Hildreth, W., and Drake, R. E. 1992. Volcán Quizapu, Chilean Andes. Bulletin of Volcanology 54 (2)**:** 93-125.

Horn, P., Muller-sohnius, D., Storzer, D., Zoller, L. 1993. K-Ar, fission-track-, and thermoluminescence ages of Quaternary volcanic tuffs and their bearing on Acheulian artifacts from Bori, Kukdi Valley, Pune District, India. Zeitschrift der Deutschen geologischen Gesellschaft 144 (0): 326–329.

Huang, C., Yue, Zhao, M., Wang, C., Chun, Wei, G. 2001. Cooling of the South China Sea by the Toba Eruption and correlation with other climate proxies ~71,000 years ago. Geophys. Res. Lett. 28 (20): 3915.

Imbert, T., and Desprairies, A. 1987. Neoformation of halloysite on volcanic glass in a marine environment. Clay minerals 22 179-185.

James, H.V.A., Petraglia, M.D. 2005. Modern Human Origins and the Evolution of Behavior in the Later Pleistocene Record of South Asia. Current Anthropology 46 (0): S3.

Jones, S. C. 2007. The Toba supervolcanic eruption: Tephra-fall deposits in India and palaeanthropological implications. In: M. D. Petraglia and B. Allchin (Eds.), The Evolution and History of Human Populations in South Asia. Springer, Berlin, pp. 173-200.

Jones, S. C. 2010. Palaeoenvironmental response to the ~74 ka Toba ash-fall in the Jurreru and Middle Son valleys in southern and north-central India. Quaternary Research 73 (2)**:** 336-350.

Jones, S. C. 2012. Local- and regional-scale impacts of the ~74 ka Toba supervolcanic eruption on hominin populations and habitats in India. Quaternary International 258 (0)**:** 100-118.

Jones, S. C., and Pal, J. N. 2005. The Middle Son Valley and the toba Supervolcanic eruption of 74 kyr BP: Youngest Toba Tuff Deposits and Palaeolithic Associations. Journal of Interdisciplinary Studies in History and Archaeology 2 (1)**:** 47-62.

Jones, S. C., and Pal, J. N. 2009. The Palaeolithic of the Middle Son valley, north-central India: Changes in hominin lithic technology and behaviour during the Upper Pleistocene. Journal of Anthropological Archaeology 28 (3)**:** 323.

Jouzel, J., Lorius, C., Petit, J.R., Genthon, C., Barkov, N.I., Kotlyakov, V.M., Petrov, V.M. 1987. Vostok ice core: a continuous isotope temperature record over the last climatic cycle (160,000 years). Nature 329 (6138): 403-408.

Kale, V. S., Patil D.N., Pawar N.J., and S.N., R. 1993. Discovery of a volcanic ash bed in the alluvial sediments at Morgaon, Maharashtra. Man and Environment 18 (0): 141-143.

Karmalkar, N. R., Ghate, S. N., Mishra, S., and S.N., R. 1998. Morphology of the volcanic ash from the Kukadi River section, Pune District, Maharashtra. J. Geol. Soc. India 51 (0): 213-218.

Kataoka, K. 2003. Volcaniclastic remobilization and resedimentation in distal terrestrial settings in response to large-volume rhylitic eruptions: Examples from the Plio-Pleistocene volcaniclastic sediments, central Japan. Journal of Geosciences (46)**:** 47-65.

Kataoka, K. 2005. Distal fluvio-lacustrine volcaniclastic resedimentation in response to an explosive silicic eruption: The Pliocene Mushono tephra bed, central Japan. Geological Society of America Bulletin 117 (1-2)**:** 3-17.

Kataoka, K. S., Manville, V., Nakajo, T., and Urabe, A. 2009. Impacts of explosive volcanism on distal alluvial sedimentation: Examples from the Pliocene-Holocene volcaniclastic successions of Japan. Sedimentary Geology 220 (3-4)**:** 306.

Khadkikar, A.S. 2003. Bedform migration and bar evolution in a late Quaternary monsoon-influenced river, Gujarat, western India. Sedimentary Geology 157 (3-4): 277.

Kilian, R., Biester, H., Behrmann, J., Baeza, O., Fesq-Martin, M., Hohner, M., Schimpf, D., Friedmann, A., Mangini, A. 2006. Millennium-scale volcanic impact on a superhumid and pristine ecosystem. Geology 34 (8): 609–612.

Klovan, J.E. 1966. The use of factor analysis in determining depositional environments from grain-size distributions. Journal of Sedimentary Research 36 (1), 115–125.

Knight, M. D., Walker, G. L., Ellwood, B. B., and Diehl, J. F. 1986. Stratigraphy, paleomagnetism, and magnetic fabric of the Toba tuffs: constraints on the sources and eruptive styles. Journal of Geophysical Research 91 (0): 355-382.

Koniger, S., and Stollhofen, H. 2001. Environmental and tectonic controls on preservation potential of distal fallout ashes in fluvio-lacustrine settings: the Carboniferous-Permian saar-Nahe Basin, south-west Germany. In : White, J., Riggs, N. (Eds), Spec. Publs int. Ass Sediment., Wiley-Blackwell, London, 30 (0): pp. 263-284.

Korisettar, R., Mishra, S., Rajaguru S.N., Gogte, V. D., Ganjoo, r. K., Venkatesan, T. R., Tandon, s. K., Somayajulu, B. L. K., and Kale, V. S. 1988. Age of the Bori volcanic ash and Lower Palaeolithic culture of the Kukdi Valley, Maharashtra. Bulletin of the Deccan College Postgraduate and Research Institute 48 135-138.

Kudrass, H. R., Hofmann, A., Doose, H., Emeis, K., and Erlenkeuser, H. 2001. Modulation and amplification of climatic changes in the Northern Hemisphere by the Indian summer monsoon during the past 80 k.y. Geology 29 (1)**:** 63-66.

S.C. Kuehn, D.G. Froese, P.A.R. Shane, INTAV Intercomparison Participants, 2011. The INTAV intercomparison of electron-beam microanalysis of glass by tephrochronology laboratories: Results and recommendations, Quaternary International 46(1–2):19-47.

Kuznetsova, E. P., Motenko, R. G., Vigasina, M. F., and Mel'chakova, L. V. 2009. IR spectroscopy and thermal study of volcanic ashes of different age: annual seminar on experimental mineralogy, petrology and geochemistry. Bull. Earth Sci. RAS 1 (27)**:** 83.

Lawrence, R.L., Ripple, W.J., 2000. Fifteen years of revegetation of Mount St. Helens: a landscape

scale analyses. Ecology 81 (10): 2742–2752.

Ledbetter, M. T., and Sparks, R. S. J. 1979. Duration of large-magnitude explosive eruptions deduced from graded bedding in deep-sea ash layers. Geology 7 (5): 240 - 244.

Lee, M.-Y., Chen, C.-H., Wei, K.-Y., Iizuka, Y., and Carey, S. 2004. First Toba supereruption revival. Geology 32 (1)**:** 61-64.

Leuschner, D.C., Sirocko, F. 2000. The low-latitude monsoon climate during Dansgaard-Oeschger cycles and Heinrich Events. Quaternary Science Reviews 19 (1-5): 243–254.

Lewin, J., Macklin, M.G., Johnstone, E. 2005a. Interpreting alluvial archives: sedimentological factors in the British Holocene fluvial record. Quaternary Science Reviews 24 (16-17): 1873–1889.

Lewis, L., Ditchfield, P., Pal, J. N., and Petraglia, M. 2012. Grain size distribution analysis of sediments containing Younger Toba tephra from Ghoghara, Middle Son valley, India. Quaternary International 258 (0)**:** 180-190.

Liang, X., Wei, G., Shao, L., Li, X., and Wang, R. 2001. Records of Toba eruptions in the South China Sea. Science in China Series D: Earth Sciences 44 (10)**:** 871-878.

Liu, Z., Colin, C., and Trentesaux, A. 2006. Major element geochemistry of glass shards and minerals of the Youngest Toba Tephra in the southwestern South China Sea. Journal of Asian Earth Sciences 27 (1)**:** 99-107.

Lotter, A.F., Birks, H.J.B., Zolitschka, B. 1995. Late-glacial pollen and diatom changes in response to two different environmental perturbations: volcanic eruption and Younger Dryas cooling. Journal of Paleolimnology 14 (1): 23.

Lowe, D. J. 2011. Tephrochronology and its application: A review. Quaternary Geochronology 6 (2)**:** 107-153.

Lowe, J. J., and Walker, M. J. C. 1984. Reconstructing Quaternary Environments, Longman Scientific and Technical, London, pp. 434.

Macedonio, G., Costa, A., and Longo, A. 2005. A computer model for volcanic ash fallout and assessment of subsequent hazard. Computers and Geosciences 31 (7)**:** 837-845.

Macklin, M.G., Fuller, I.C., Lewin, J., Maas, G.S., Passmore, D.G., Rose, J., Woodward, J.C., Black, S., Hamlin, R.H.B., Rowan, J.S. 2002. Correlation of fluvial sequences in the Mediterranean basin over the last 200 ka and their relationship to climate change. Quaternary Science Reviews 21 (14-15), 1633–1641.

Mandal, D. 1983. A note on the radiocarbon dates from the Middle Son Valley. In: Sharma G R, C.J.D. (Ed.), Palaeoenvironments and Prehistory in the Middle Son Valley. Abinash Prakashan, Allahabad, pp. 185–289.

Manville, V., Newton, E. H., and White, J. D. L. 2005. Fluvial responses to volcanism: resedimentation of the 1800a Taupo ignimbrite eruption in the Rangitaiki River catchment, North Island, New Zealand. Geomorphology 65 (1-2)**:** 49-70.

Manville, V., Németh, K., and Kano, K. 2009a. Source to sink: A review of three decades of progress in the understanding of volcaniclastic processes, deposits, and hazards. Sedimentary Geology 220 (3-4)**:** 136.

Manville, V., Segschneider, B., Newton, E., White, J. D. L., Houghton, B. F., and Wilson, C. J. N. 2009b. Environmental impact of the 1.8 ka Taupo eruption, New Zealand: Landscape responses to a large-scale explosive rhyolite eruption. Sedimentary Geology 220 (3-4)**:** 318.

Marel, H. W. 1947. Diatomaceous deposits at Lake Toba. Journal of Sedimentary Petrology 3 (17): 129-134.

Marel, H. W. 1948. Volcanic glass, allanite and zircon as characteristic minerals of the Toba rhyolite at Sumatra's East Coast. Journal of Sedimentary Petrology 18 (0)**:** 24-29.

Margari, V., Pyle, D. M., Bryant, C., and Gibbard, P. L. 2007. Mediterranean tephra stratigraphy revisited: Results from a long terrestrial sequence on Lesvos Island, Greece. Journal of Volcanology and Geothermal Research 163 (1-4)**:** 34.

Mastrolorenzo, G., Palladino, D. M., Vecchio, G., and Taddeucci, J. 2002. The 472 AD Pollena eruption of Somma-Vesuvius (Italy) and its environmental impact at the end of the Roman Empire. Journal of Volcanology and Geothermal Research 113 (1-2)**:** 19-36.

Masturyono, McCaffrey, R., Wark, D. A., Roecker, S. W., Fauzi, Ibrahim, G., and Sukhyar. 2001. Distribution of magma beneath the Toba caldera complex, north Sumatra, Indonesia, constrained by three-dimensional P wave velocities, seismicity, and gravity data. Geochem. Geophys. Geosyst. 2 (4).

Matthews, N. E., Smith, V. C., Costa, A., Durant, A. J., Pyle, D. M., and Pearce, N. J. G. 2012. Ultra-distal tephra deposits from super-eruptions: Examples from Toba, Indonesia and Taupo Volcanic Zone, New Zealand. Quaternary International 258 (0)**:** 54-79.

McCarthy, A. J., and Elders, C. F. 1997. Cenozoic deformation in Sumatra: oblique subduction and the development of the Sumatran Fault System. *In* "Geological Society Special Publication." pp. 355-363.

McLaren, P. 1981. An interpretation of trends in grain size measures. Journal of Sedimentary Research 51 (2), 611–624.

McLaren, P., Bowles, D. 1985. The effects of sediment transport on grain-size distributions. Journal of Sedimentary Research 55 (4), 457–470.

McMenamin, D.S., Kumar, S., Awramik, S.M. 1983. Microbial fossils from the Kheinjua Formation, Middle Proterozoic Semri Group (Lower Vindhyan) Son Valley area, central India. Precambrian Research 21(3-4): 247.

Miall, A. D. 1996. "The Geology of Fluvial Deposits.Sedimentary Facies, Basin Analysis, and Petroleum Geology." Springer-Verlag, Berlin.

Mishra, S., Venkatesan, T. R., Rajaguru, S. N., and Somayajulu, B. L. K. 1995. Earliest Acheulian Industry from Peninsular India. Current Anthropology 36 (5)**:** 847-851.

Mishra, S., Deo, S. G., Abbas, R., Naik, S., Shete, G., Aqrawal, N., and Rajaguru, S. 2009. Excavation at the Early site of Maharashtra (2000-2007). *In* "Recent Research Trend in South Asian Archaeology." K. Paddayya, Joglekar, P.P., Basa, K.K., Sawant, R. (Eds.), Pune., pp. 121-137.

Mokhtar, S. 2009. Debu Gunung Berapi di Lembah Lenggong, Perak. Journal Arkeologi Malaysia 22 (0)**:** 1-12.

Morad, S., Bhattacharyya, A., Al-Aasm, I. S., and Ramseyer, K. 1991. Diagenesis of quartz in the Upper Proterozoic Kaimur Sandstones, Son Valley, central India. Sedimentary Geology 73 (3-4)**:** 209.

Morgan, R. P. C. 1973. The influence on scale in climatic geomorphology: a case study of drainage density in West Malaysia. Geographiska annales. Series A, Physical Geography 55 (2)**:** 107-115.

Morley, M. W., and Woodward, J. C. 2011. The Campanian Ignimbrite (Y5) tephra at Crvena Stijena Rockshelter, Montenegro. Quaternary Research 75 (3)**:** 683-696.

Mullins, C. E. 1977. Magnetic susceptibility of the soil and its significance in soil science – A review. Journal of Soil Science 28 (2)**:** 223-246.

Nakayama, K. 2001. Subaerial liquefied flow of volcaniclastic sediments, central Japan. In: B. McCaffrey and B. Kneller and J. Peakall (Eds.), Particulate gravity currents, International Association of Sedimentologist Special Publication 31, pp. 233-244.

Nakayama, K., and Yoshikawa, S. 1997. Depositional processes of primary to reworked volcaniclastics on an alluvial plain; an example from the Lower Pliocene Ohta tephra bed of the Tokai Group, central Japan. Sedimentary Geology 107 (3-4)**:** 211.

Nammah, H., Larsen, F. E., McCool, D. K., Fritts Jr, R., and Molnau, M. 1986. Mt. St. Helens volcanic ash: Effect of incorporated and unincorporated ash of two particle sizes on runoff and erosion. Agriculture, Ecosystems & Environment 15 (1)**:** 63.

Nanson, G. C., and Croke, J. C. 1992. A genetic classification of floodplains. Geomorphology 4 (6)**:** 459-486.

Narcisi, B., Vezzoli, L. 1999. Quaternary stratigraphy of distal tephra layers in the Mediterranean--an overview. Global and Planetary Change 21(1-3): 31.

Németh, K., Cronin, S.J. 2007. Syn- and post-eruptive erosion, gully formation, and morphological evolution of a tephra ring in tropical climate erupted in 1913 in West Ambrym, Vanuatu. Geomorphology 86 (1-2): 115-130.

Ninkovich, D. 1979. Distribution, age and chemical composition of tephra layers in deep-sea sediments off western Indonesia. Journal of Volcanology and Geothermal Research 5 (1-2)**:** 67-86.

Ninkovich, D., Sparks, R., and Ledbetter, M. 1978b. The exceptional magnitude and intensity of the Toba eruption, Sumatra: An example of the use of deep-sea tephra layers as a geological tool. Bulletin of Volcanology 41 (3)**:** 286-298.

Ninkovich, D., Shackleton, N. J., Abdel-Monem, A. A., Obradovich, J. D., and Izett, G. 1978a. K-Ar age of the late Pleistocene eruption of Toba, north Sumatra. Nature 276 (5688)**:** 574-577.

Nishimura, S. 1981. The development of neo-tectonics in Sumatra, Indonesia. Paleolimnology of Lake Biwa & the Japanese Pleistocene 9 (0): 151-176.

Nishimura, S., Abe, E., Yokoyama, T., Wirasantosa, T., and Dharma, A. 1977. Danau Toba- The outline of Lake toba, North sumatra, Indonesia: Palaeolimnology of Lake Biwa. Japan Pleistocene 5 (0)**:** 313-332.

Nishimura, S., Abe, E., Nishida, J., Yokoyama, T., Dharma, A., Hehanussa, P., and Hehuwat, F. 1984. A gravity and volcanostratigraphic interpretation of the Lake Toba region, North Sumatra, Indonesia. Tectonophysics 109 (3-4)**:** 253-261,265-272.

Noble, D. C., Smith, V. C., and Peck, L. C. 1967. Loss of halogens from crystallized and glassy silicic volcanic rocks. Geochimica et Cosmochimica Acta 31 (2)**:** 215-223.

Oppenheimer, C. 2002. Limited global change due to the largest known Quaternary eruption, Toba ~74 kyr BP? Quaternary Science Reviews 21 (14-15)**:** 1593-1609.

Oppenheimer, S. 2009. The great arc of dispersal of modern humans: Africa to Australia. Quaternary International 202 (1-2)**:** 2-13.

Oppenheimer, S. 2012. A single southern exit of modern humans from Africa: Before or after Toba? Quaternary International 258 (0)**:** 88-99.

Page, B. G. N. 1979. A review of the main structural and magmatic features of northern Sumatra. Journal of the Geological Society 136 (5)**:** 569-579.

Pal, J. N., Williams M.A.J., Jaiswal M., and A.K., S. 2005. Infra Red Stimulated Luminescence ages fro prehistoric cultures in the son and Belan Valleys, North Central India. Journal of Interdisciplinary Studies in History and Archaeology 1 (0): 51-62.

Paredes, J.M., Foix, N., Colombo Piñol, F., Nillni, A., Allard, J.O., Marquillas, R.A. 2007. Volcanic and climatic controls on fluvial style in a high-energy system: The Lower Cretaceous Matasiete Formation, Golfo San Jorge basin, Argentina. Sedimentary Geology 202 (1-2): 96.

Passega, R. 1964. Grain size representation by CM patterns as a geologic tool. Journal of Sedimentary Research 34 (4): 830–847.

Pattan, J. N., Shane, P., and Banakar, V. K. 1999. New occurrence of Youngest Toba Tuff in abyssal sediments of the Central Indian Basin. Marine Geology 155 (3-4)**:** 243-248.

Pattan, J. N., Shane, P. A. R., Pearce, N. J. G., Banakar, V. K., and Parthiban, G. 2001. An occurrence of ~ 74 ka Youngest Toba tephra from the western continental margine of india. Current Science 80 (10)**:** 1322-1326.

Pattan, J. N., Prasad, M. S., and Babu, E. V. S. S. K. 2010. Correlation of the oldest Toba Tuff to sediments in the central Indian Ocean Basin. J. Earth Syst. Sci. 119 (4)**:** 531-539.

Pearce, N. J. G., Bendall, C. A., and Westgate, J. A. 2008a. Comment on "Some numerical considerations in the geochemical analysis of distal microtephra" by A.M. Pollard, S.P.E. Blockley and C.S. Lane. Applied Geochemistry 23 (5)**:** 1353-1364.

Pearce, N.J.G., Alloway, B.V., Westgate, J.A. 2008b. Mid-Pleistocene silicic tephra beds in the Auckland region, New Zealand: Their correlation and origins based on the trace element analyses of single glass shards. Quaternary International 178 (1): 16.

Pearce, N. J. G., Perkins, W. T., Westgate J.A., Gorton, M. P., Jackson, S. E., Neal, C. R., and Chenery, S. P. 1997. A compilation of new and published major and trace element data for NIST SRM 610 and NIST SRM 612 glass reference materials. Geostandards Newsletter-the Journal of Geostandards and Geoanalysis 21 (1)**:** 115-144.

Pelletier, J.D., DeLong, S.B., Cline, M.L., Harrington, C.D., Keating, G.N. 2008. Dispersion of channel-sediment contaminants in distributary fluvial systems: Application to fluvial tephra and radionuclide redistribution following a potential volcanic eruption at Yucca Mountain. Geomorphology 94 (1-2): 226.

Perrotta, A., and Scarpati, C. 2003. Volume partition between the plinian and co-ignimbrite air fall deposits of the Campanian Ignimbrite eruption. Mineralogy and Petrology 79 (1)**:** 67-78.

Petraglia, M., Korisettar, R., Boivin, N., Clarkson, C., Ditchfield, P., Jones, S., Koshy, J., Lahr, M. M., Oppenheimer, C., Pyle, D., Roberts, R., Schwenninger, J.-L., Arnold, L., and White, K. 2007. Middle Paleolithic Assemblages from the Indian Subcontinent Before and After the Toba Super-Eruption. Science 317 (5834)**:** 114-116.

Petraglia, M., Korisettar, R., Bai, M.K., Bovin, N., Janardhana, B., Clarkson, C., Cunningham, K., Ditchfield, P., Fuller, D., Hampson, J., Haslam, M., Jones, S., Koshy, J., Miracle, P., Oppenheimer, C., Roberts, R., White, K. 2009. Human occupation, adaptation and behavioral change in the Pleistocene and Holocene of south India: recent investigations in the Kurnool district, Andhra Pradesh. Eurasian Prehistory 6 (0): 119–166.

Petraglia, M. D., Korisettar, R., and Pal, J. N. 2012. The Toba volcanic super-eruption of 74,000 years ago: Climate change, environments, and evolving humans. Quaternary International 258 (0)**:** 1-4.

Pérez, F.L. 2009. The role of tephra covers on soil moisture conservation at Haleakala's crater

(Maui, Hawaii). CATENA 76 (3): 191.

Pollack, J.B., Toon, O.B., Sagan, C., Summers, A., Baldwin, B., Van Camp, W. 1976. Volcanic Explosions and Climatic Change: A Theoretical Assessment. J. Geophys. Res. 81 (6): 1071-1083.

Prell, W. L., and Kutzbach, J. E. 1987. Monsoon Variability Over the Past 150,000 Years. J. Geophys. Res. 92 (D7)**:** 8411-8425.

Prell, W. L., and Kutzbach, J. E. 1992. Sensitivity of the Indian monsoon to forcing parameters and implications for its evolution. Nature 360 (6405)**:** 647.

Pyle, D. M. 1989a. The thickness, volume and grainsize of tephra fall deposits. Bulletin of Volcanology 51 (1)**:** 1-15.

Pyle, D. M. 1989b. New estimates for the volume of the Minoan eruption. *In* "Thera and the Aegean World III " D. A. Hardy, J. Keller, V. P. Galanopoulos, N. C. Flemming, and T. H. Druitt (Eds.), The Thera Foundation, London.pp. 113-121.

Pyle, D. M., Ricketts, G. D., Margari, V., van Andel, T. H., Sinitsyn, A. A., Praslov, N. D., and Lisitsyn, S. 2006. Wide dispersal and deposition of distal tephra during the Pleistocene Campanian Ignimbrite/Y5 eruption, Italy. Quaternary Science Reviews 25 (21-22)**:** 2713-2728.

Pyne-O'Donnell, S. 2011. The taphonomy of Last Glacial–Interglacial Transition (LGIT) distal volcanic ash in small Scottish lakes. Boreas 40 (1)**:** 131-145.

Raj, R. 2007. Occurrence of volcanic ash in the Quaternary alluvial deposits, lower Narmada basin, western India. Journal of Earth System Science 117 (1): 41–48.

Rampino, M.R., Self, S. 1982. Historic eruptions of Tambora (1815), Krakatau (1883), and Agung (1963), their stratospheric aerosols, and climatic impact. Quaternary Research 18 (2): 127.

Rampino, M. R., and Self, S. 1992. Volcanic winter and accelerated glaciation following the Toba super-eruption. Nature 359 (6390)**:** 50.

Rampino, M. R., and Self, S. 1993. Climate-Volcanism Feedback and the Toba Eruption of ~74,000 Years Ago. Quaternary Research 40 (3)**:** 269.

Robock, A., Ammann, C. M., Oman, L., Shindell, D., Levis, S., and Stenchikov, G. 2009. Did the Toba volcanic eruption of ~74 ka B.P. produce widespread glaciation? J. Geophys. Res. 114 (D10)**:** 107-116.

Rose, W., Bonis, S., Stoiber, R., Keller, M., and Bickford, T. 1973. Studies of volcanic ash from two recent Central American eruptions. Bulletin of Volcanology 37 (3)**:** 338-364.

Rose, W. I. 1993. Comment on 'another look at the calculation of fallout tephra volumes' by Judy Fierstein and Manuel Nathenson. Bulletin of Volcanology 55 (5)**:** 372-374.

Rose, W. I., and Chesner, C. A. 1987. Dispersal of ash in the great Toba eruption, 75 ka. Geology 15 (10): 913-917.

Rose, W. I., and Chesner, C. A. 1990. Worldwide dispersal of ash and gases from earth's largest known eruption: Toba, Sumatra, 75 ka. Palaeogeography, Palaeoclimatology, Palaeoecology 89 (3): 269-275.

Rose, W. I., and Durant, A. J. 2009. Fine ash content of explosive eruptions. Journal of Volcanology and Geothermal Research 186 (1-2): 32-39.

Sarna-Wojcicki, A. M., and Davis, J. O. 1991. Quaternary Tephrochronology In: R. B. Morrison (Eds.), The Geology of North America, Quaternary nonglacial geology: Conterminous U.S. The Geological Society of America, Boulder, Colorado, pp. 93-116.

Sarna-Wojcicki, A. M., Meyer, C. E., Bowman, H. R., Timothy Hall, N., Russell, P. C., Woodward, M. J., and Slate, J. L. 1985. Correlation of the Rockland ash bed, a 400,000-year-old stratigraphic marker in northern California and western Nevada, and implications for middle Pleistocene paleogeography of central California. Quaternary Research 23 (2): 236-257.

Scaillet, B., Clemente, B., Evans, B. W., and Pichavant, M. 1998. Redox control of sulfur degassing in silicic magmas. J. Geophys. Res. 103 (B10): 23937-23949.

Scasso, R. A., Corbella, H., and Tiberi, P. 1994. Sedimentological analysis of the tephra from the 12–15 August 1991 eruption of Hudson volcano. Bulletin of Volcanology 56 (2): 121-132.

Schulz, H., von Rad, U., and Erlenkeuser, H. 1998. Correlation between Arabian Sea and Greenland climate oscillations of the past 110,000 years. Nature 393 (6680): 54-57.

Schulz, H., Emeis, K.-C., Erlenkeuser, H., von Rad, U., and Rolf, C. 2002. The Toba Volcanic Event and Interstadial/Stadial Climates at the Marine Isotopic Stage 5 to 4 Transition in the Northern Indian Ocean. Quaternary Research 57 (1): 22-31.

Scrivenor, J. B. 1930. A recent rhyolite-ash with sponge-spicules and diatoms in Malaya. Geological Magazine 67 (9): 385-393.

Segschneider, B., Landis, C. A., Manville, V., White, J. D. L., and Wilson, C. J. N. 2002. Environmental response to a large, explosive rhyolite eruption: sedimentology of post-1.8 ka pumice-rich Taupo volcaniclastics in the Hawke's Bay region, New Zealand. Sedimentary Geology 150 (3-4): 275.

Self, S. 2006. The effects and consequences of very large explosive volcanic eruptions. Philosophical Transactions of the Royal Society A: Mathematical, Physical and Engineering Sciences 364 (1845): 2073-2097.

Self, S., Rampino, M. R., Newton, M. S., and Wolff, J. A. 1984. Volcanological study of the great Tambora eruption of 1815. Geology 12 (11): 659-663.

Shane, P., Westgate, J., Williams, M., and Korisettar, R. 1995. New Geochemical Evidence for the Youngest Toba Tuff in India. Quaternary Research 44 (2): 200-204.

Sharma, G. R. 1980. History to prehistory. Archaeology of the Ganga Valley and the Vindhyas. Department of Ancient History, Culture and Archaeology, University of Allahabad, Allahabad.

Sharma, G. R., and Clark, J. D. 1983. Palaeoenvironments and Prehistory in the Middle Son Valley, Madhya Predesh, North Central India. Allahabad, Abinash Prakashan.

Shikazono, N., Takino, A., and Ohtani, H. 2005. An estimate of dissolution rate constant of volcanic glass in volcanic ash soil from the Mt. Fuji area, central Japan. Geochemical Journal 39 185-196.

Sigurdsson, H., Carey, S. 1989. Plinian and co-ignimbrite tephra fall from the the 1815 Eruption of Tambora Volcano. Bull. Volc. 51(4): 243.

Simonsen, L., Toft, J. 2006. Texture, composition and stratigraphy of volcanic ash beds in lower Palaeocene chalk from the North Sea Central Graben area. Marine and Petroleum Geology 23 (7): 767.

Singh, I. B. 1980. Precambrian sedimentary sequences of India: Their peculiarities and comparison with modern sediments. Precambrian Research 12 (1-4): 411.

Smith, V. C., Pearce, N. J. G., Matthews, N. E., Westgate, J. A., Petraglia, M. D., Haslam, M., Lane, C. S., Korisettar, R., and Pal, J. N. 2011. Geochemical fingerprinting of the widespread Toba tephra using biotite compositions. Quaternary International 246 (1-2): 97-104.

Song, S. R., Chen, C. H., Lee, M. Y., Yang, T. F., Iizuka, Y., and Wei, K. Y. 2000. Newly discovered eastern dispersal of the youngest Toba Tuff. Marine Geology 167 (3-4): 303.

Sparks, R. S. J., and Wilson, L. 1976. A model for the formation of ignimbrite by gravitational column collapse. Journal of the Geological Society 132 (4): 441-451.

Sparks, R. S. J., and Huang, T. C. 1980. The volcanological significance of deep-sea ash layers associated with ignimbrites. Geological Magazine 117 (5): 425-436.

Sparks, R. S. J., Moore, J. G., and Rice, C. J. 1986. The initial giant umbrella cloud of the May 18th, 1980, explosive eruption of Mount St. Helens. Journal of Volcanology and Geothermal Research 28 (3-4): 257-274.

Sparks, R. S. J., Bursik, M. I., Ablay, G. J., Thomas, R. M. E., and Carey, S. N. 1992. Sedimentation of tephra by volcanic plumes. Part 2: controls on thickness and grain-size variations of tephra fall deposits. Bulletin of Volcanology 54 (8): 685-695.

Stauffer, P. H. 1972. Cenozoic. In: D. J. Gobbett, and Hutchinson (Eds.), Geology of the Malay Peninsula (West Malaysia and Singapore), John Wiley and Sons, London, pp. 143-176.

Stauffer, P. H. 1973. Late Pleistocene age indicated fro volcanic ash in west Malaysia. Geological Society of Malaysia Newsletter 40 (0): 1-4.

Stauffer, P. H., Nishimura, S., and Batchelor, B. C. 1980. Volcanic ash in Malaya from catastrophic eruption of toba, sumatra, 30,000 years ago. *In* "Physical geology of Indonesian Island Arcs." S. Nishimura (Eds.), pp. 156-164, Kyoto.

Stokes, S., Lowe, D. J., and Froggatt, P. C. 1992. Discriminant function analysis and correlation of Late Quaternary rhyolitic tephra deposits from Taupo and Okataina volcanoes, New Zealand, using glass shard major element composition. Quaternary International 13-14 (0)**:** 103-117.

Stollhofen, H., Stanistreet, I.G., McHenry, L.J., Mollel, G.F., Blumenschine, R.J., Masao, F.T. 2008. Fingerprinting facies of the Tuff IF marker, with implications for early hominin palaeoecology, Olduvai Gorge, Tanzania. Palaeogeography, Palaeoclimatology, Palaeoecology 259 (4): 382.

Storey, M., Roberts, R. G., and Saidin, M. 2012. Astronomically calibrated $^{40}Ar/^{39}Ar$ age for the Toba supereruption and global synchronization of late Quaternary records. Proceedings of the National Academy of Sciences 109 (46)**:** 18684-18688.

Svensson, A., Bigler, M., Blunier, T., Clausen, H. B., Dahl-Jensen, D., Fischer, H., Fujita, S., Goto-Azuma, K., S.J. Johnsen, Kawamura, K., Kipfstuhl, S., Kohno, M., Parrenin, F., Popp, T., Rasmussen, S. O., Schwander, J., Seierstad, I., Severi, M., Steffensen, J. P., Udisti, R., Uemura, R., Vallelonga, P., Vinther, B. M., Wegner, A., Wilhelms, F., and Winstrup, M. 2012. Direct linking of Greenland and Antarctic ice cores at the Toba eruption (74 kyr BP). Clim. Past. Discuss. 8 (0): 5389-5427.

Telford, R.J., Barker, P., Metcalfe, S., Newton, A. 2004. Lacustrine responses to tephra deposition: examples from Mexico. Quaternary Science Reviews 23 (23-24): 2337.

Textor, C., Graf, H.-F., Herzog, M., and Oberhuber, J. M. 2003. Injection of gases into the stratosphere by explosive volcanic eruptions. J. Geophys. Res. 108 (D19)**:** 4606.

Thompson, R., Bradshaw, R. W., and Whitley, J. E. 1986. The distribution of ash in Icelandic lake sediments and the relative importance of mixing and erosion processes. Journal of Quaternary Science 1 (1)**:** 3-11.

Thorarinsson, S., and Sigvaldason, G. 1972. The Hekla Eruption of 1970. Bulletin of Volcanology 36 (2)**:** 269-288.

Timmreck, C., Graf, H.-F., Zanchettin, D., Hagemann, S., Kleinen, T., and Krüger, K. 2012. Climate response to the Toba super-eruption: Regional changes. Quaternary International 258 (0)**:** 30-44.

Timmreck, C., Graf, H.-F., Lorenz, S. J., Niemeier, U., Zanchettin, D., Matei, D., Jungclaus, J. H., and Crowley, T. J. 2010. Aerosol size confines climate response to volcanic super-eruptions. Geophys. Res. Lett. 37 (24)**:** L24705.

Todesco, M. 2004. Volcanic Eruption Induced Floods. A Rainfall-Runoff Model Applied to the Vesuvian Region (Italy). Natural Hazards 33 (2): 223.

Van Bemmelen, R. W. 1970. The Geology of Indonesia. *In* "General Geology of Indonesia and Adjacent Archipelagos 1A (second ed.)." M. Nijhoff (Eds.), The Hague, pp. 732.

van der Kaars, S., Bassinot, F., De Deckker, P., and Guichard, F. 2010. Changes in monsoon and ocean circulation and the vegetation cover of southwest Sumatra through the last 83,000 years: The record from marine core BAR94-42. Palaeogeography, Palaeoclimatology, Palaeoecology 296 (1-2)**:** 52-78.

van der Kaars, S., Williams, M. A. J., Bassinot, F., Guichard, F. o., Moreno, E., Dewilde, F., and Cook, E. J. 2012. The influence of the ~73 ka Toba super-eruption on the ecosystems of northern Sumatra as recorded in marine core BAR94-25. Quaternary International 258 (0)**:** 45-53.

Von Rad, U., Burgath, K.-P., Pervaz, M., and Schulz, H. 2002. Discovery of the Toba Ash (c. 70 ka) in a high-resolution core recovering millennial monsoonal variability off Pakistan. Geological Society, London, Special Publications 195 (1)**:** 445-461.

Wada, K. 1987. Minerals formed and mineral formation from volcanic ash by weathering. Chemical Geology 60 (1-4)**:** 17-28.

Walker, D. 1956. Studies on the Quaternary of the Malay Peninsula. Pt. I: Alluvial deposits of Perak and the relative levels of land and sea. Fed. Mus. J. 1-2 (0): 19-34.

Westaway, R., Mishra, S., Deo, S. G., and Bridgland, D. R. 2011. Methods for determination of the age of Pleistocene tephra, derived from eruption of Toba, in central India. . J. Earth Syst. Sci. 120, (3)**:** 503-530.

Westgate, J. A., and Gorton, M. P. 1981. Correlation techniques in tephra studies. *In* "Tephra Studies." S. Self, and R. S. J. Sparks (Eds.), D. Reidel, Dordrecht, pp. 73-94..

Westgate, J. A., Perkins, W. T., Fuge, R., Pearce, N. J. G., and Wintle, A. G. 1994. Trace-element analysis of volcanic glass shards by laser ablation inductively coupled plasma mass spectrometry: application to tephrochronological studies. Applied Geochemistry 9 (3)**:** 323-335.

Westgate, J. A., Shane, P. A. R., Pearce, N. J. G., Perkins, W. T., Korisettar, R., Chesner, C. A., Williams, M. A. J., and Acharyya, S. K. 1998. All Toba Tephra Occurrences across Peninsular India Belong to the 75,000 yr B.P. Eruption. Quaternary Research 50 (1)**:** 107-112.

Williams, M. 2012a. Did the ~73 ka Toba super-eruption have an enduring effect? Insights from genetics, prehistoric archaeology, pollen analysis, stable isotope geochemistry, geomorphology, ice cores, and climate models. Quaternary International 269 (0)**:** 87-93.

Williams, M. 2012b. The ~73 ka Toba super-eruption and its impact: History of a debate. Quaternary International 258 (0)**:** 19-29.

Williams, M. A. J., and Royce, K. 1982. Quaternary geology of the middle son valley, North Central India: Implications for prehistoric archaeology. Palaeogeography, Palaeoclimatology, Palaeoecology 38 (3-4)**:** 139.

Williams, M. A. J., and Royce, K. 1983. Alluvial History of the Middle Son Valley, North Central India. In: " G. R. Sharma, and J. D. Clark (Eds.). Paleo-environments and Prehistory in the Middle Son Valley, Madhya Pradesh, North Central India. Allahabad, Abinash Prakashan, pp. 9-22.

Williams, M. A. J., and Clarke, M. F. 1984. Late Quaternary environments in north-central India. Nature 308 633-635.

Williams, M. A. J., and Clarke, M. F. 1995. Quaternary geology and prehistoric environments in the Son and Belan Valleys, north central India. In: S. Wadia, R. Korisettar, and V. S. Kale (Eds.), Quaternary environments and geoarcheology of India. Geological Society of India, Bangalore, pp. 282-308.

Williams, M. A. J., Pal, J. N., Jaiswal, M., and Singhvi, A. K. 2006. River response to Quaternary climatic fluctuations: evidence from the Son and Belan valleys, north-central India. Quaternary Science Reviews 25 (19-20)**:** 2619-2631.

Williams, M. A. J., Ambrose, S. H., van der Kaars, S., Ruehlemann, C., Chattopadhyaya, U., Pal, J., and Chauhan, P. R. 2009. Environmental impact of the 73 ka Toba super-eruption in South Asia. Palaeogeography, Palaeoclimatology, Palaeoecology 284 (3-4)**:** 295-314.

Wilson, C. J. N. 2001. The 26.5 ka Oruanui eruption, New Zealand: an introduction and overview. Journal of Volcanology and Geothermal Research 112 (1-4)**:** 133-174.

Wilson, L., Huang, T.C. 1979. The influence of shape on the atmospheric settling velocity of volcanic ash particles. Earth and Planetary Science Letters 44 (2): 311.

Woods, A. W. 1988. The fluid dynamics and thermodynamics of eruption columns. Bulletin of Volcanology 50 (3)**:** 169-193.

Woods, A. W., and Wohletz, K. 1991. Dimensions and dynamics of co-ignimbrite eruption columns. Nature 350 (6315)**:** 225.

Xiao, X.Y., Shen, J., Wang, S.M., Xiao, H.F., Tong, G.B. 2011. The variation of the southwest monsoon from the high resolution pollen record in Heqing Basin, Yunnan Province, China for the last 2.78 Ma. Palaeogeography, Palaeoclimatology, Palaeoecology 287 (1-4): 45.

Yang, Q., Mayewski, P. A., Zielinski, G. A., Twickler, M., and Taylor, K. C. 1996. Depletion of atmospheric nitrate and chloride as a consequence of the Toba Volcanic Eruption. Geophys. Res. Lett. 23 (18)**:** 2513-2516.

Zanchetta, G., Sulpizio, R., Roberts, N., Cioni, R., Eastwood, W.J., Siani, G., Caron, B., Paterne, M., Santacroce, R. 2011. Tephrostratigraphy, chronology and climatic events of the Mediterranean basin during the Holocene: An overview. The Holocene 21 (1): 33–52.

Zielinski, G. A. 2000. Use of paleo-records in determining variability within the volcanism-climate system. Quaternary Science Reviews 19 (1-5)**:** 417.

Zielinski, G. A., Mayewski, P. A., Meeker, L. D., Whitlow, S., and Twickler, M. S. 1996a. A 110,000-Yr Record of Explosive Volcanism from the GISP2 (Greenland) Ice Core. Quaternary Research 45 (2)**:** 109-118.

Zielinski, G. A., Mayewski, P. A., Meeker, L. D., Whitlow, S., Twickler, M. S., and Taylor, K. 1996b. Potential Atmospheric Impact of the Toba Mega-Eruption ~71,000 Years Ago. Geophys. Res. Lett. 23.

Zobel, D.B., Antos, J.A. 1997. A decade of recovery of understory vegetation buried by volcanic tephra from Mount St. Helens. Ecological Monographs 67 (0): 317–344.

Appendix. Raw geochemical data

9.1 Internal Standards (in wt%) measured with LA-ICP-MS

Element	Chondrite	NIST 610	NIST 612	NIST614		KL2-G ref	T1-G ref	BIR-1 lit	BHVO-2 lit	BCR-2 lit
^{9}Be	0,04	465,6	37,74	1,12		0,9	2	0,58	0,9	1,75
^{24}Mg	143000	465,3	77,44	39,96666667		43800	22600	58493	43598	21648
^{27}Al	12900	10005,57	11164,6	10983,27333		69300	90000	82033,96397	71448,93636	71448,93636
^{30}Si	160000	328329,15	335916,8	0		234000	273000	224179	233247	252879
^{43}Ca	13500	81833,26	85262,5	81833		77200	50600	95056	81476	50887
^{45}Sc	8,64	441,1	41,05	2,03		32,3	26,7	44	32	33
^{51}V	85	441,7	39,22	1,03		370	190	313	317	416
^{60}Ni	16500	443,9	38,44	2		116	13	166	119	17,7
^{85}Rb	3,45	431,1	31,63	0,82		8,9	80	0,24	9,08	46,9
^{88}Sr	11,9	497,4	76,15	45,7		364	283	110	396	340
^{89}Y	2,25	449,9	38,25	0,83		26,8	23,2	17	26	37
^{90}Zr	5,54	439,9	35,99	0,95		159	147	14,5	172	188
^{93}Nb	0,375	419,4	38,06	0,89		15,8	9,1	0,55	18	11
^{137}Ba	3,41	424,1	37,74	3,09		123	382	6,4	131	677
^{139}La	0,367	457,4	35,77	0,71		13,2	69	0,58	15,2	24,9
^{140}Ce	0,957	447,8	38,35	0,79		32,9	127	1,85	37,5	52,9
^{141}Pr	0,137	429,8	37,16	0,78		4,71	12,1	0,37	5,29	6,57
^{143}Nd	0,711	430,8	35,24	0,76		21,7	40,7	2,35	24,5	28,7
^{147}Sm	0,231	450,5	36,72	0,73		5,55	6,52	1,1	6,07	6,57
^{153}Eu	0,087	461,1	34,44	0,77		1,95	1,21	0,52	2,07	1,96
^{157}Gd	0,306	419,9	36,95	0,72		6,1	5,2	1,97	6,24	6,75
^{159}Tb	0,058	442,8	35,92	0,68		0,93	0,82	0,38	0,936	1,07
^{163}Dy	0,381	426,5	35,97	0,77		5,35	4,44	2,5	5,31	6,41
^{165}Ho	0,0851	449,4	37,87	0,79		0,99	0,83	0,57	0,972	1,3
^{166}Er	0,249	426	37,43	0,8		2,64	2,42	1,63	2,54	3,66
^{169}Tm	0,0356	420,1	37,55	0,68		0,336	0,35	0,25	0,33	0,54
^{172}Yb	0,248	461,5	39,95	0,76		2	2,32	1,6	2	3,38
^{175}Lu	0,0381	434,7	37,71	0,77		0,296	0,35	0,25	0,274	0,51

^{178}Hf	0,179	417,7	34,77	0,75		4,14	3,9	0,56	4,1	4,8
^{181}Ta	0,026	376,6	39,77	0,86		0,97	0,45	0,06	1,4	0,82
^{208}Pb	3,65	413,3	38,96	3,74		2,2	13	3	1,6	11
^{232}Th	0,0425	450,6	37,23	0,81		1,03	30	0,03	1,2	6,2
^{238}U	0,0122	457,1	37,15	0,86		0,55	1,67	0,01	0,39	1,69

9.2 Rare elements geochemical analyses (LA-ICP-MS)

GLITTER4.0: Laser Ablation Analysis Results									
NB: Please note that all values for the internal standard(s) are reported in units of weight% oxide, all other values reported in ppm									
GLITTER!: Trace Element Concentrations MDL filtered.									
Element	**Chondrite**	**MRB-3_1**	**MRB-3_2**	**MRB-3_3**	**MRB-3_4**	**MRB-3_5**	**MRB-3_6**	**MRB-3_7**	**MRB-3_8**
^{9}Be	0,04	1,89	<2.18	6,26	2,71	1,1	2,72	<3.16	6,17
^{24}Mg	143000	0,066	0,066	0,066	0,066	0,066	0,066	0,066	0,066
^{27}Al	12900	78277,82	67905,57	103804,54	77833,88	30091,95	54824,66	82008,87	90319,96
^{30}Si	160000	294102,41	270534,88	526444,88	331753,66	122790,2	275113,59	339311,13	401194,78
^{43}Ca	13500	4948,01	4402,13	6736,02	5738,65	1450,42	3999,33	4361,55	4207,24
^{45}Sc	8,64	5,11	3,74	7,76	4,58	2,01	2,89	3,57	7,71
^{51}V	85	1,51	3,67	0,9	7,21	5,52	6,41	1,87	3,4
^{60}Ni	16500	0,55	2,67	<0.39	<1.26	1,91	<0.50	0,75	1,52
^{85}Rb	3,45	302,49	213,82	494,13	267,52	89,87	173,41	268,55	397,49
^{88}Sr	11,9	16,34	32,62	19,15	33,82	17,96	39,4	32,73	21,45
^{89}Y	2,25	32,78	20,17	42,59	26,33	8,41	14,17	27	41,56
^{90}Zr	5,54	73,69	54,55	83,91	51,89	26,29	38,79	66,43	72,1
^{93}Nb	0,375	15,29	9,87	24,54	12,3	4,5	8,63	13,68	18,58
^{137}Ba	3,41	55,16	302,77	74,63	247,14	203,73	400,14	235,93	77,75
^{139}La	0,367	18,39	20,79	24,61	20,68	10,1	18,7	21,89	23,65
^{140}Ce	0,957	39,66	39,59	64,48	43,31	19,83	39,67	45,45	50,65
^{141}Pr	0,137	4,21	3,89	6,29	4,62	1,79	3,54	4,38	5,03
^{143}Nd	0,711	15,03	12,22	21,17	15,66	7,13	13,4	15,8	21,47
^{147}Sm	0,231	3,56	2,97	5,58	3	1,27	2,66	3,9	4,29
^{153}Eu	0,087	0,2	0,216	0,259	0,319	0,119	0,251	0,304	0,249
^{157}Gd	0,306	4,07	2,47	5,08	2,93	0,95	1,63	3,19	4,84
^{159}Tb	0,058	0,656	0,438	0,989	0,642	0,125	0,353	0,738	0,93
^{163}Dy	0,381	4,47	2,8	7,02	4,24	1,22	2,22	4,11	6,53
^{165}Ho	0,0851	1,02	0,656	1,31	0,851	0,293	0,512	1,06	1,51
^{166}Er	0,249	2,6	2,05	4,34	2,52	0,808	1,32	2,92	3,56
^{169}Tm	0,0356	0,448	0,333	0,762	0,473	0,137	0,284	0,531	0,574
^{172}Yb	0,248	4,07	3,5	5,45	3,48	1,02	1,7	3,86	5,55
^{175}Lu	0,0381	0,622	0,524	0,844	0,544	0,167	0,311	0,571	0,86
^{178}Hf	0,179	2,63	2,29	3,44	2,74	1,05	1,76	2,9	3,3
^{181}Ta	0,026	1,55	0,98	2,65	1,37	0,457	0,801	1,47	2,08
^{208}Pb	3,65	43,77	33,81	64,14	40,16	20,3	30,07	43,98	56,32
^{232}Th	0,0425	27,63	18,53	41,01	25,92	8,8	15,79	27,86	37,41
^{238}U	0,0122	6,98	3,94	11,64	5,63	1,68	3,15	5,62	9,16
REE Chondrite normalised		**MRB-3_1**	**MRB-3_2**	**MRB-3_3**	**MRB-3_4**	**MRB-3_5**	**MRB-3_6**	**MRB-3_7**	**MRB-3_8**
La	0,367	50,1090	56,6485	67,0572	56,3488	27,5204	50,9537	59,6458	64,4414
Ce	0,957	41,4420	41,3689	67,3772	45,2560	20,7210	41,4525	47,4922	52,9258
Pr	0,137	30,7299	28,3942	45,9124	33,7226	13,0657	25,8394	31,9708	36,7153
Nd	0,711	21,1392	17,1871	29,7750	22,0253	10,0281	18,8467	22,2222	30,1969
Sm	0,231	15,4113	12,8571	24,1558	12,9870	5,4978	11,5152	16,8831	18,5714
Eu	0,087	2,2989	2,4828	2,9770	3,6667	1,3678	2,8851	3,4943	2,8621
Gd	0,306	13,3007	8,0719	16,6013	9,5752	3,1046	5,3268	10,4248	15,8170
Tb	0,058	11,3103	7,5517	17,0517	11,0690	2,1552	6,0862	12,7241	16,0345
Dy	0,381	11,7323	7,3491	18,4252	11,1286	3,2021	5,8268	10,7874	17,1391
Ho	0,0851	11,9859	7,7086	15,3937	10,0000	3,4430	6,0165	12,4559	17,7438
Er	0,249	10,4418	8,2329	17,4297	10,1205	3,2450	5,3012	11,7269	14,2972
Tm	0,0356	12,5843	9,3539	21,4045	13,2865	3,8483	7,9775	14,9157	16,1236
Yb	0,248	16,4113	14,1129	21,9758	14,0323	4,1129	6,8548	15,5645	22,3790
Lu	0,0381	16,3255	13,7533	22,1522	14,2782	4,3832	8,1627	14,9869	22,5722

Element	Chondrite	MRB-3_9	MRB-3_10						
^{9}Be	0,04	13,09	5,09						
^{24}Mg	143000	0,066	0,066						
^{27}Al	12900	91886,53	78035,2						
^{30}Si	160000	386432,56	345499,63						
^{43}Ca	13500	<3955.07	4328,99						
^{45}Sc	8,64	6,88	4,45						
^{51}V	85	6,91	1,7						
^{60}Ni	16500	2,67	0,77						
^{85}Rb	3,45	419,33	290,1						
^{88}Sr	11,9	17,9	34,95						
^{89}Y	2,25	60,81	27,52						
^{90}Zr	5,54	113,21	67,96						
^{93}Nb	0,375	23,52	14,2						
^{137}Ba	3,41	75,88	237,64						
^{139}La	0,367	26,8	22,2						
^{140}Ce	0,957	63,02	51,45						
^{141}Pr	0,137	6,46	4,64						
^{143}Nd	0,711	31,2	16,58						
^{147}Sm	0,231	4,66	3,49						
^{153}Eu	0,087	<0.00	0,351						
^{157}Gd	0,306	4,25	3,16						
^{159}Tb	0,058	1,44	0,743						
^{163}Dy	0,381	6,72	4,14						
^{165}Ho	0,0851	2,03	1,03						
^{166}Er	0,249	5,16	2,99						
^{169}Tm	0,0356	0,88	0,453						
^{172}Yb	0,248	7,48	3,64						
^{175}Lu	0,0381	1,25	0,529						
^{178}Hf	0,179	4,68	2,74						
^{181}Ta	0,026	2,47	1,52						
^{208}Pb	3,65	50,53	43,23						
^{232}Th	0,0425	43,35	26,91						
^{238}U	0,0122	9,23	6,34						
REE normalised	Chondrite	MRB-3_9	MRB-3_10						
La	0,367	73,0245	60,4905						
Ce	0,957	65,8516	53,7618						
Pr	0,137	47,1533	33,8686						
Nd	0,711	43,8819	23,3193						
Sm	0,231	20,1732	15,1082						
Eu	0,087	0.00	4,0345						
Gd	0,306	13,8889	10,3268						
Tb	0,058	24,8276	12,8103						
Dy	0,381	17,6378	10,8661						
Ho	0,0851	23,8543	12,1034						
Er	0,249	20,7229	12,0080						
Tm	0,0356	24,7191	12,7247						
Yb	0,248	30,1613	14,6774						
Lu	0,0381	32,8084	13,8845						

Element	Chondrite	BR-6_1	BR-6_2	BR-6_3	BR-6_4	BR-6_5	BR-6_6	BR-6_7	BR-6_8
^{9}Be	0,04	1,06	<0.00	<0.00	<0.67	1,93	1,45	4,11	<0.00
^{24}Mg	143000	0,061	0,061	0,061	0,061	0,061	0,061	0,061	0,061
^{27}Al	12900	34499,13	7365,98	12886,47	10663,25	20495,98	69590,71	59175,27	24171,42
^{30}Si	160000	145561,72	32782,83	63756,77	48506,52	94165,23	316853,63	299527,38	148638,83
^{43}Ca	13500	1944,56	325,36	1059,11	426,97	1205,9	3716,32	3425,15	1641,99
^{45}Sc	8,64	1,96	0,73	0,94	0,79	1,51	5,52	3,78	2,84
^{51}V	85	2,13	1,3	3,24	2,88	2,31	1,27	1,44	4,97
^{60}Ni	16500	1,52	0,55	2,29	1,89	1,73	1	0,41	<1.11
^{85}Rb	3,45	104,94	33,79	45,77	40,4	70,79	312,48	276,39	87,69
^{88}Sr	11,9	23,73	3,89	6,27	1,71	8,86	12,12	13,92	15,53
^{89}Y	2,25	9,57	2,02	3,81	4,2	5,85	34,26	27,46	7,63
^{90}Zr	5,54	31,23	7,68	13,78	11,53	19,73	46,75	49,06	27,25
^{93}Nb	0,375	5,4	1,95	2,27	2,31	3,84	15,12	13,96	4,13
^{137}Ba	3,41	264,54	41,17	48,97	9,04	90,47	38,27	43,79	139,34
^{139}La	0,367	12,23	2,31	3,59	2,34	5,45	19,16	16,09	8,24
^{140}Ce	0,957	24,55	4,92	7,64	5,34	12,12	56,95	36,91	16,51
^{141}Pr	0,137	2,26	0,441	0,733	0,568	1,09	4,28	3,67	1,64
^{143}Nd	0,711	7,77	1,51	2,63	1,92	3,37	15,83	13,56	5,25
^{147}Sm	0,231	1,79	0,201	0,443	0,581	0,69	3,61	3,19	0,99
^{153}Eu	0,087	0,139	0,042	0,036	0,0215	0,058	0,131	0,116	0,145
^{157}Gd	0,306	1,21	0,186	0,464	0,478	0,73	3,54	3,57	1,09
^{159}Tb	0,058	0,214	0,0443	0,102	0,085	0,165	0,82	0,635	0,165
^{163}Dy	0,381	1,33	0,281	0,553	0,578	0,85	5,41	3,6	0,69
^{165}Ho	0,0851	0,335	0,072	0,128	0,148	0,174	1,04	0,823	0,243
^{166}Er	0,249	1,14	0,194	0,354	0,397	0,79	3,14	2,77	0,75
^{169}Tm	0,0356	0,168	0,0395	0,0619	0,0642	0,125	0,548	0,494	0,108
^{172}Yb	0,248	1,32	0,297	0,574	0,532	0,8	4,45	3,51	0,98
^{175}Lu	0,0381	0,197	0,0537	0,092	0,075	0,138	0,651	0,536	0,156
^{178}Hf	0,179	1,13	0,231	0,475	0,497	0,92	2,44	2,14	0,93
^{181}Ta	0,026	0,536	0,125	0,224	0,217	0,363	1,69	1,51	0,522
^{208}Pb	3,65	16,34	3,89	7,75	8,15	10,8	40,51	38,31	14,13
^{232}Th	0,0425	9,69	2,08	4,02	3,89	6,6	31,51	26,36	8,81
^{238}U	0,0122	2,01	0,466	0,934	0,958	1,42	7,38	6,99	1,91
REE Chondrite normalised		BR-6_1	BR-6_2	BR-6_3	BR-6_4	BR-6_5	BR-6_6	BR-6_7	BR-6_8
La	0,367	33,3243	6,2943	9,7820	6,3760	14,8501	52,2071	43,8420	22,4523
Ce	0,957	25,6531	5,1411	7,9833	5,5799	12,6646	59,5089	38,5684	17,2518
Pr	0,137	16,4964	3,2190	5,3504	4,1460	7,9562	31,2409	26,7883	11,9708
Nd	0,711	10,9283	2,1238	3,6990	2,7004	4,7398	22,2644	19,0717	7,3840
Sm	0,231	7,7489	0,8701	1,9177	2,5152	2,9870	15,6277	13,8095	4,2857
Eu	0,087	1,5977	0,4828	0,4138	0,2471	0,6667	1,5057	1,3333	1,6667
Gd	0,306	3,9542	0,6078	1,5163	1,5621	2,3856	11,5686	11,6667	3,5621
Tb	0,058	3,6897	0,7638	1,7586	1,4655	2,8448	14,1379	10,9483	2,8448
Dy	0,381	3,4908	0,7375	1,4514	1,5171	2,2310	14,1995	9,4488	1,8110
Ho	0,0851	3,9365	0,8461	1,5041	1,7391	2,0447	12,2209	9,6710	2,8555
Er	0,249	4,5783	0,7791	1,4217	1,5944	3,1727	12,6104	11,1245	3,0120
Tm	0,0356	4,7191	1,1096	1,7388	1,8034	3,5112	15,3933	13,8764	3,0337
Yb	0,248	5,3226	1,1976	2,3145	2,1452	3,2258	17,9435	14,1532	3,9516
Lu	0,0381	5,1706	1,4094	2,4147	1,9685	3,6220	17,0866	14,0682	4,0945

Element	Chondrite	BR-6_9							
^{9}Be	0,04	0,93							
^{24}Mg	143000	0,061							
^{27}Al	12900	7752,71							
^{30}Si	160000	42632,48							
^{43}Ca	13500	250,23							
^{45}Sc	8,64	0,97							
^{51}V	85	2,74							
^{60}Ni	16500	1,28							
^{85}Rb	3,45	30,78							
^{88}Sr	11,9	0,95							
^{89}Y	2,25	3,34							
^{90}Zr	5,54	12,66							
^{93}Nb	0,375	2,07							
^{137}Ba	3,41	6,16							
^{139}La	0,367	1,99							
^{140}Ce	0,957	3,72							
^{141}Pr	0,137	0,362							
^{143}Nd	0,711	1,35							
^{147}Sm	0,231	0,33							
^{153}Eu	0,087	<0.0074							
^{157}Gd	0,306	0,226							
^{159}Tb	0,058	0,033							
^{163}Dy	0,381	0,5							
^{165}Ho	0,0851	0,108							
^{166}Er	0,249	0,307							
^{169}Tm	0,0356	0,062							
^{172}Yb	0,248	0,329							
^{175}Lu	0,0381	0,087							
^{178}Hf	0,179	0,461							
^{181}Ta	0,026	0,217							
^{208}Pb	3,65	4,52							
^{232}Th	0,0425	3,26							
^{238}U	0,0122	0,725							
REE	Chondrite	BR-6_9							
La	0,367	5,4223							
Ce	0,957	3,8871							
Pr	0,137	2,6423							
Nd	0,711	1,8987							
Sm	0,231	1,4286							
Eu	0,087								
Gd	0,306	0,7386							
Tb	0,058	0,5690							
Dy	0,381	1,3123							
Ho	0,0851	1,2691							
Er	0,249	1,2329							
Tm	0,0356	1,7416							
Yb	0,248	1,3266							
Lu	0,0381	2,2835							

Element	Chondrite	BTS-12_1	BTS-12_2	BTS-12_3	BTS-12_4	BTS-12_5	BTS-12_6	BTS-12_7	BTS-12_8
^{9}Be	0,04	<1.97	3,24	0,35	4,04	1,76	<3.52	1,42	2,31
^{24}Mg	143000	0,054	0,054	0,054	0,054	0,054	0,054	0,054	0,054
^{27}Al	12900	61429,39	55008,45	43304,85	63735,7	58540,45	57837,32	33632,83	57568,7
^{30}Si	160000	231872,42	247096,03	222189,09	265561,31	242483,11	271451	159648,69	327175,81
^{43}Ca	13500	2860,63	3082,43	2717,8	3500,35	4825,69	3572,6	821,45	4678,2
^{45}Sc	8,64	3,4	3,26	2,85	4,1	4,35	3,17	2,32	3,92
^{51}V	85	3,29	2,96	4,01	2,47	2,46	0,84	5,06	2,41
^{60}Ni	16500	2	1,98	1,2	0,27	1,17	<0.72	<0.39	1,32
^{85}Rb	3,45	179,63	175,12	153,66	201,72	174,65	197,57	116,25	227,7
^{88}Sr	11,9	29,23	26,36	25,56	35,91	50,84	27,99	20,17	33,25
^{89}Y	2,25	17,52	15,98	9,37	20,8	14,39	19,15	9,12	14,74
^{90}Zr	5,54	48,73	55,47	41,79	68,03	45,39	48,34	44,25	45,64
^{93}Nb	0,375	9,74	10,3	8,42	11,07	9,08	9,26	8,56	12,23
^{137}Ba	3,41	324	277,54	336,62	349,93	425,46	282,99	200,28	360,07
^{139}La	0,367	18,05	17,4	14,33	21,7	20,14	19,54	10,76	17,61
^{140}Ce	0,957	36,17	34,39	33,96	41,13	40,12	39,75	19,84	44,31
^{141}Pr	0,137	3,57	3,1	2,85	4,39	3,87	3,57	2,01	3,72
^{143}Nd	0,711	13,84	12,02	9,29	15,25	12,84	12,71	6,95	11,61
^{147}Sm	0,231	2,79	2,39	1,74	2,24	2,34	2,77	2,06	2,27
^{153}Eu	0,087	0,27	0,25	0,217	0,258	0,409	0,312	0,124	0,321
^{157}Gd	0,306	2,28	1,4	1,55	2,73	2,25	3,23	1,39	1,76
^{159}Tb	0,058	0,3	0,425	0,23	0,49	0,398	0,542	0,255	0,382
^{163}Dy	0,381	2,58	2,41	1,69	2,66	2,31	2,59	1,4	2,32
^{165}Ho	0,0851	0,708	0,578	0,296	0,626	0,367	0,64	0,282	0,51
^{166}Er	0,249	1,87	1,65	0,857	2,2	1,52	1,67	1	1,56
^{169}Tm	0,0356	0,196	0,291	0,172	0,299	0,227	0,288	0,157	0,24
^{172}Yb	0,248	2,76	2,3	1,41	2,64	2,2	2,25	0,94	1,79
^{175}Lu	0,0381	0,338	0,335	0,193	0,383	0,281	0,39	0,163	0,274
^{178}Hf	0,179	1,97	1,66	1,21	2,34	2,01	2,07	1,52	1,77
^{181}Ta	0,026	0,97	0,892	0,66	1,02	0,81	0,93	0,546	1,043
^{208}Pb	3,65	35,93	28,76	26,03	35,51	28,99	32,33	20,06	35,22
^{232}Th	0,0425	18,5	16,16	11,72	20,79	17,51	19,56	10,41	17,16
^{238}U	0,0122	4,13	3,38	2,99	4,3	3,33	4,27	2,42	4,87
REE normalised	**Chondrite**	**BTS-12_1**	**BTS-12_2**	**BTS-12_3**	**BTS-12_4**	**BTS-12_5**	**BTS-12_6**	**BTS-12_7**	**BTS-12_8**
La	0,367	49,1826	47,4114	39,0463	59,1281	54,8774	53,2425	29,3188	47,9837
Ce	0,957	37,7952	35,9352	35,4859	42,9781	41,9227	41,5361	20,7315	46,3009
Pr	0,137	26,0584	22,6277	20,8029	32,0438	28,2482	26,0584	14,6715	27,1533
Nd	0,711	19,4655	16,9058	13,0661	21,4487	18,0591	17,8762	9,7750	16,3291
Sm	0,231	12,0779	10,3463	7,5325	9,6970	10,1299	11,9913	8,9177	9,8268
Eu	0,087	3,1034	2,8736	2,4943	2,9655	4,7011	3,5862	1,4253	3,6897
Gd	0,306	7,4510	4,5752	5,0654	8,9216	7,3529	10,5556	4,5425	5,7516
Tb	0,058	5,1724	7,3276	3,9655	8,4483	6,8621	9,3448	4,3966	6,5862
Dy	0,381	6,7717	6,3255	4,4357	6,9816	6,0630	6,7979	3,6745	6,0892
Ho	0,0851	8,3196	6,7920	3,4783	7,3561	4,3126	7,5206	3,3137	5,9929
Er	0,249	7,5100	6,6265	3,4418	8,8353	6,1044	6,7068	4,0161	6,2651
Tm	0,0356	5,5056	8,1742	4,8315	8,3989	6,3764	8,0899	4,4101	6,7416
Yb	0,248	11,1290	9,2742	5,6855	10,6452	8,8710	9,0726	3,7903	7,2177
Lu	0,0381	8,8714	8,7927	5,0656	10,0525	7,3753	10,2362	4,2782	7,1916

Element	Chondrite	BTS-12_9	BTS-12_10						
^{9}Be	0,04	0,83	<0.00						
^{24}Mg	143000	0,054	0,054						
^{27}Al	12900	48309,7	31068,77						
^{30}Si	160000	218671,78	85964,74						
^{43}Ca	13500	3401,28	510,14						
^{45}Sc	8,64	3,01	2,09						
^{51}V	85	8,12	7,71						
^{60}Ni	16500	0,67	3,41						
^{85}Rb	3,45	154,42	56,87						
^{88}Sr	11,9	23,74	5,72						
^{89}Y	2,25	14,85	4,05						
^{90}Zr	5,54	45,16	31,73						
^{93}Nb	0,375	9,68	7,57						
^{137}Ba	3,41	246,06	65,83						
^{139}La	0,367	15,92	5,86						
^{140}Ce	0,957	32,26	10,3						
^{141}Pr	0,137	3,3	1,2						
^{143}Nd	0,711	12,9	3,39						
^{147}Sm	0,231	2,03	0,44						
^{153}Eu	0,087	0,161	0,225						
^{157}Gd	0,306	2,12	0,57						
^{159}Tb	0,058	0,365	0,068						
^{163}Dy	0,381	2,65	1,14						
^{165}Ho	0,0851	0,53	0,216						
^{166}Er	0,249	1,49	0,69						
^{169}Tm	0,0356	0,222	0,104						
^{172}Yb	0,248	1,72	0,77						
^{175}Lu	0,0381	0,278	0,098						
^{178}Hf	0,179	1,87	1,12						
^{181}Ta	0,026	0,905	0,556						
^{208}Pb	3,65	58,09	18,51						
^{232}Th	0,0425	23,29	6,94						
^{238}U	0,0122	4,23	1,65						
REE	Chondrite	BTS-12_9	BTS-12_10						
La	0,367	43,3787	15,9673						
Ce	0,957	33,7095	10,7628						
Pr	0,137	24,0876	8,7591						
Nd	0,711	18,1435	4,7679						
Sm	0,231	8,7879	1,9048						
Eu	0,087	1,8506	2,5862						
Gd	0,306	6,9281	1,8627						
Tb	0,058	6,2931	1,1724						
Dy	0,381	6,9554	2,9921						
Ho	0,0851	6,2280	2,5382						
Er	0,249	5,9839	2,7711						
Tm	0,0356	6,2360	2,9213						
Yb	0,248	6,9355	3,1048						
Lu	0,0381	7,2966	2,5722						

Element	Chondrite	BTS-12_1	BTS-12_2	BTS-12_3	BTS-12_4	BTS-12_5	BTS-12_6	BTS-12_7	BTS-12_8
^{9}Be	0,04	<1.97	3,24	0,35	4,04	1,76	<3.52	1,42	2,31
^{24}Mg	143000	0,054	0,054	0,054	0,054	0,054	0,054	0,054	0,054
^{27}Al	12900	61429,39	55008,45	43304,85	63735,7	58540,45	57837,32	33632,83	57568,7
^{30}Si	160000	231872,42	247096,03	222189,09	265561,31	242483,11	271451	159648,69	327175,81
^{43}Ca	13500	2860,63	3082,43	2717,8	3500,35	4825,69	3572,6	821,45	4678,2
^{45}Sc	8,64	3,4	3,26	2,85	4,1	4,35	3,17	2,32	3,92
^{51}V	85	3,29	2,96	4,01	2,47	2,46	0,84	5,06	2,41
^{60}Ni	16500	2	1,98	1,2	0,27	1,17	<0.72	<0.39	1,32
^{85}Rb	3,45	179,63	175,12	153,66	201,72	174,65	197,57	116,25	227,7
^{88}Sr	11,9	29,23	26,36	25,56	35,91	50,84	27,99	20,17	33,25
^{89}Y	2,25	17,52	15,98	9,37	20,8	14,39	19,15	9,12	14,74
^{90}Zr	5,54	48,73	55,47	41,79	68,03	45,39	48,34	44,25	45,64
^{93}Nb	0,375	9,74	10,3	8,42	11,07	9,08	9,26	8,56	12,23
^{137}Ba	3,41	324	277,54	336,62	349,93	425,46	282,99	200,28	360,07
^{139}La	0,367	18,05	17,4	14,33	21,7	20,14	19,54	10,76	17,61
^{140}Ce	0,957	36,17	34,39	33,96	41,13	40,12	39,75	19,84	44,31
^{141}Pr	0,137	3,57	3,1	2,85	4,39	3,87	3,57	2,01	3,72
^{143}Nd	0,711	13,84	12,02	9,29	15,25	12,84	12,71	6,95	11,61
^{147}Sm	0,231	2,79	2,39	1,74	2,24	2,34	2,77	2,06	2,27
^{153}Eu	0,087	0,27	0,25	0,217	0,258	0,409	0,312	0,124	0,321
^{157}Gd	0,306	2,28	1,4	1,55	2,73	2,25	3,23	1,39	1,76
^{159}Tb	0,058	0,3	0,425	0,23	0,49	0,398	0,542	0,255	0,382
^{163}Dy	0,381	2,58	2,41	1,69	2,66	2,31	2,59	1,4	2,32
^{165}Ho	0,0851	0,708	0,578	0,296	0,626	0,367	0,64	0,282	0,51
^{166}Er	0,249	1,87	1,65	0,857	2,2	1,52	1,67	1	1,56
^{169}Tm	0,0356	0,196	0,291	0,172	0,299	0,227	0,288	0,157	0,24
^{172}Yb	0,248	2,76	2,3	1,41	2,64	2,2	2,25	0,94	1,79
^{175}Lu	0,0381	0,338	0,335	0,193	0,383	0,281	0,39	0,163	0,274
^{178}Hf	0,179	1,97	1,66	1,21	2,34	2,01	2,07	1,52	1,77
^{181}Ta	0,026	0,97	0,892	0,66	1,02	0,81	0,93	0,546	1,043
^{208}Pb	3,65	35,93	28,76	26,03	35,51	28,99	32,33	20,06	35,22
^{232}Th	0,0425	18,5	16,16	11,72	20,79	17,51	19,56	10,41	17,16
^{238}U	0,0122	4,13	3,38	2,99	4,3	3,33	4,27	2,42	4,87
REE normalised	**Chondrite**	**BTS-12_1**	**BTS-12_2**	**BTS-12_3**	**BTS-12_4**	**BTS-12_5**	**BTS-12_6**	**BTS-12_7**	**BTS-12_8**
La	0,367	49,1826	47,4114	39,0463	59,1281	54,8774	53,2425	29,3188	47,9837
Ce	0,957	37,7952	35,9352	35,4859	42,9781	41,9227	41,5361	20,7315	46,3009
Pr	0,137	26,0584	22,6277	20,8029	32,0438	28,2482	26,0584	14,6715	27,1533
Nd	0,711	19,4655	16,9058	13,0661	21,4487	18,0591	17,8762	9,7750	16,3291
Sm	0,231	12,0779	10,3463	7,5325	9,6970	10,1299	11,9913	8,9177	9,8268
Eu	0,087	3,1034	2,8736	2,4943	2,9655	4,7011	3,5862	1,4253	3,6897
Gd	0,306	7,4510	4,5752	5,0654	8,9216	7,3529	10,5556	4,5425	5,7516
Tb	0,058	5,1724	7,3276	3,9655	8,4483	6,8621	9,3448	4,3966	6,5862
Dy	0,381	6,7717	6,3255	4,4357	6,9816	6,0630	6,7979	3,6745	6,0892
Ho	0,0851	8,3196	6,7920	3,4783	7,3561	4,3126	7,5206	3,3137	5,9929
Er	0,249	7,5100	6,6265	3,4418	8,8353	6,1044	6,7068	4,0161	6,2651
Tm	0,0356	5,5056	8,1742	4,8315	8,3989	6,3764	8,0899	4,4101	6,7416
Yb	0,248	11,1290	9,2742	5,6855	10,6452	8,8710	9,0726	3,7903	7,2177
Lu	0,0381	8,8714	8,7927	5,0656	10,0525	7,3753	10,2362	4,2782	7,1916

Element	Chondrite	KgL12_1	KgL12_2	KgL12_3	KgL12_4	KgL12_5	KgL12_6	KgL12_7	KgL12_8
^{9}Be	0,04	11,2	3,03	1,43	0,86	41,4	3,67	6,84	<0.00
^{24}Mg	143000	0,068	0,068	0,068	0,068	0,068	0,068	0,068	0,068
^{27}Al	12900	1191297,63	91027,41	48189,48	38231,59	1489432,88	93462,54	100810,88	31128,4
^{30}Si	160000	1526008,13	379958,97	165830,5	177215,69	3272651	456228,66	535000,88	149284,02
^{43}Ca	13500	350575,91	5193,57	2613,11	3062,11	427525,97	6579,62	4992,53	3302,24
^{45}Sc	8,64	25,82	5,97	2,6	2,57	24,93	6,07	6,69	<1.56
^{51}V	85	<5.69	2,66	5,19	1,88	<8.87	1,57	1,57	15,41
^{60}Ni	16500	3,42	1,44	1,23	0,3	14,06	0,8	<0.65	<1.01
^{85}Rb	3,45	15,68	430,9	141,85	150,28	24,2	426,44	493,2	132,57
^{88}Sr	11,9	3280,7	21,38	21,83	23,16	4014,16	38,1	25,04	8,58
^{89}Y	2,25	1,83	39,86	11,52	10,8	2,54	32,91	41,48	12,42
^{90}Zr	5,54	<0.00	73,48	49,71	32,4	3,14	81	83,44	39,48
^{93}Nb	0,375	0,21	22,56	9,32	8,01	<0.40	19,34	24,82	6,17
^{137}Ba	3,41	1807,22	82,67	209,06	232,9	2317,68	253,94	80,98	149,62
^{139}La	0,367	64,69	22,61	11,43	12,58	85,12	27,91	26,23	10,58
^{140}Ce	0,957	91,18	54,95	26,66	28,43	127,01	65,05	66,59	19,89
^{141}Pr	0,137	6,66	5,7	2,47	2,49	9,22	5,76	6,64	2,68
^{143}Nd	0,711	17,86	20,87	7,84	8,94	27,1	20,44	22,76	5,38
^{147}Sm	0,231	2	4,04	1,91	1,56	1,91	4,87	5,74	1,02
^{153}Eu	0,087	13,72	0,316	0,256	0,19	20,42	0,388	0,255	0,138
^{157}Gd	0,306	1,36	4,43	1,57	1,38	2,52	4,65	4,96	1,3
^{159}Tb	0,058	0,172	0,887	0,262	0,258	<0.00	0,922	0,918	0,36
^{163}Dy	0,381	0,96	6,2	1,72	1,67	0,34	5,14	7,03	1,93
^{165}Ho	0,0851	0,072	1,44	0,384	0,345	<0.21	1,15	1,59	0,38
^{166}Er	0,249	<0.00	4,59	1,22	1,18	<0.72	3,64	4,46	0,89
^{169}Tm	0,0356	<0.05	0,702	0,214	0,181	0,02	0,587	0,834	0,204
^{172}Yb	0,248	0,077	6,25	1,81	1,53	<0.45	4,8	5,85	1,61
^{175}Lu	0,0381	<0.06	0,793	0,265	0,23	0,084	0,696	0,858	0,261
^{178}Hf	0,179	<0.274	3,62	1,88	1,3	<0.49	3,69	3,71	1,2
^{181}Ta	0,026	<0.063	2,34	0,911	0,737	<0.112	1,94	2,47	0,66
^{208}Pb	3,65	132,86	59,1	28,55	23,85	251,9	54,74	65,93	15,81
^{232}Th	0,0425	<0.168	39,5	11,96	12,51	0,09	34,26	43,76	12,58
^{238}U	0,0122	0,055	10,34	3,14	2,98	<0.23	8,72	12,26	2,82
REE Chondrite normalised		KgL12_1	KgL12_2	KgL12_3	KgL12_4	KgL12_5	KgL12_6	KgL12_7	KgL12_8
La	0,367	176,2670	61,6076	31,1444	34,2779	231,9346	76,0490	71,4714	28,8283
Ce	0,957	95,2769	57,4190	27,8579	29,7074	132,7168	67,9728	69,5820	20,7837
Pr	0,137	48,6131	41,6058	18,0292	18,1752	67,2993	42,0438	48,4672	19,5620
Nd	0,711	25,1195	29,3530	11,0267	12,5738	38,1153	28,7482	32,0113	7,5668
Sm	0,231	8,6580	17,4892	8,2684	6,7532	8,2684	21,0823	24,8485	4,4156
Eu	0,087	157,7011	3,6322	2,9425	2,1839	234,7126	4,4598	2,9310	1,5862
Gd	0,306	4,4444	14,4771	5,1307	4,5098	8,2353	15,1961	16,2092	4,2484
Tb	0,058	2,9655	15,2931	4,5172	4,4483		15,8966	15,8276	6,2069
Dy	0,381	2,5197	16,2730	4,5144	4,3832	0,8924	13,4908	18,4514	5,0656
Ho	0,0851	0,8461	16,9213	4,5123	4,0541		13,5135	18,6839	4,4653
Er	0,249		18,4337	4,8996	4,7390		14,6185	17,9116	3,5743
Tm	0,0356		19,7191	6,0112	5,0843	0,5618	16,4888	23,4270	5,7303
Yb	0,248	0,3105	25,2016	7,2984	6,1694		19,3548	23,5887	6,4919
Lu	0,0381		20,8136	6,9554	6,0367	2,2047	18,2677	22,5197	6,8504

Element	Chondrite	KgL12_9	KgL12_10						
^{9}Be	0,04	<0.00	1,64						
^{24}Mg	143000	0,068	0,068						
^{27}Al	12900	61425,49	79806,89						
^{30}Si	160000	300646	437419,03						
^{43}Ca	13500	5279,03	5302,63						
^{45}Sc	8,64	3,24	5,92						
^{51}V	85	1,99	1,76						
^{60}Ni	16500	<0.79	0,7						
^{85}Rb	3,45	231,69	329,27						
^{88}Sr	11,9	42,48	35,41						
^{89}Y	2,25	20,49	28,53						
^{90}Zr	5,54	82,73	82,31						
^{93}Nb	0,375	11,15	16,26						
^{137}Ba	3,41	401,44	287,24						
^{139}La	0,367	24,93	23,98						
^{140}Ce	0,957	47,65	56,26						
^{141}Pr	0,137	4,43	5						
^{143}Nd	0,711	18,69	18,4						
^{147}Sm	0,231	3,92	3,78						
^{153}Eu	0,087	0,26	0,381						
^{157}Gd	0,306	1,65	3,23						
^{159}Tb	0,058	0,45	0,716						
^{163}Dy	0,381	2,36	4,42						
^{165}Ho	0,0851	0,78	0,949						
^{166}Er	0,249	2,05	2,77						
^{169}Tm	0,0356	0,397	0,504						
^{172}Yb	0,248	3,06	3,85						
^{175}Lu	0,0381	0,431	0,505						
^{178}Hf	0,179	2,64	3						
^{181}Ta	0,026	1,08	1,56						
^{208}Pb	3,65	32,26	50,39						
^{232}Th	0,0425	21,21	29,85						
^{238}U	0,0122	4,76	7,48						
REE Chondrite normalised		KgL12_9	KgL12_10						
La	0,367	67,9292	65,3406						
Ce	0,957	49,7910	58,7879						
Pr	0,137	32,3358	36,4964						
Nd	0,711	26,2869	25,8790						
Sm	0,231	16,9697	16,3636						
Eu	0,087	2,9885	4,3793						
Gd	0,306	5,3922	10,5556						
Tb	0,058	7,7586	12,3448						
Dy	0,381	6,1942	11,6010						
Ho	0,0851	9,1657	11,1516						
Er	0,249	8,2329	11,1245						
Tm	0,0356	11,1517	14,1573						
Yb	0,248	12,3387	15,5242						
Lu	0,0381	11,3123	13,2546						

Element	Chondrite	KgL3-3_1	KgL3-3_2	KgL3-3_3	KgL3-3_4	KgL3-3_5	KgL3-3_6	KgL3-3_7	KgL3-3_8
^{9}Be	0,04	0,81	1,91	<0.00	<0.00	0,51	3,45	<5.88	6,6
^{24}Mg	143000	0,063	0,063	0,063	0,063	0,063	0,063	0,063	0,063
^{27}Al	12900	83014,59	64046,21	78282,66	67539,83	47604,82	78570,35	71522,09	61870,35
^{30}Si	160000	336167,19	299783,53	303185,25	269569,91	141334,36	371288,25	304988,19	276797,34
^{43}Ca	13500	6349,68	5117,94	7054,62	3588,28	2175,33	4927,87	4093,82	5105,94
^{45}Sc	8,64	4,47	2,92	4,04	3,48	2,32	3,24	3	3,41
^{51}V	85	1,09	0,7	1,66	3,69	5,25	1,83	<1.18	2,26
^{60}Ni	16500	1,03	0,58	1,4	3,33	3,66	0,7	<1.20	22,88
^{85}Rb	3,45	284,74	220,17	263,42	246,38	93,93	309,22	207,33	199,43
^{88}Sr	11,9	47,55	44,04	38,92	10,36	11,95	29,76	46,59	43,46
^{89}Y	2,25	26,97	18,91	24,75	25,06	7,89	30,08	20,17	15,66
^{90}Zr	5,54	90,8	58,64	82	54,48	38,36	69,04	54,03	60,12
^{93}Nb	0,375	14,44	12,01	15,52	14	8,31	15,22	11,04	11,07
^{137}Ba	3,41	476,11	549,93	447,21	66,38	164,35	247,21	540,4	462,15
^{139}La	0,367	30,39	26,19	26,02	15,39	9,2	24,74	26,57	21,99
^{140}Ce	0,957	58,65	52,26	52,75	34,68	24,82	52,26	49,34	45,94
^{141}Pr	0,137	5,53	4,77	4,67	3,52	1,9	5,16	4,65	3,93
^{143}Nd	0,711	19,9	16,3	15,01	11,57	6,25	19,2	14,73	13,82
^{147}Sm	0,231	3,73	2,8	4,56	2,85	1,36	3,24	3,72	3,14
^{153}Eu	0,087	0,345	0,404	0,353	0,166	0,197	0,226	0,408	0,266
^{157}Gd	0,306	3,39	2,63	2,28	2,6	0,98	4,16	2,41	3,15
^{159}Tb	0,058	0,686	0,485	0,7	0,561	0,202	0,71	0,512	0,426
^{163}Dy	0,381	4,04	2,67	3,24	3,71	1,41	5,01	3,11	2,85
^{165}Ho	0,0851	1,09	0,622	0,81	0,852	0,257	1,11	0,741	0,66
^{166}Er	0,249	3,01	2,01	2,51	2,6	0,788	3,26	2,06	1,74
^{169}Tm	0,0356	0,56	0,309	0,444	0,437	0,138	0,601	0,294	0,222
^{172}Yb	0,248	3,68	2,7	2,81	3,43	0,876	4,44	2,58	2,31
^{175}Lu	0,0381	0,593	0,42	0,413	0,496	0,136	0,695	0,406	0,364
^{178}Hf	0,179	2,97	2,31	3,17	2,56	1,39	3,28	2,61	2,49
^{181}Ta	0,026	1,31	1,12	1,3	1,68	0,784	1,55	1,08	1,06
^{208}Pb	3,65	44,24	36,37	40,61	39,21	19,42	47,38	32,36	32,32
^{232}Th	0,0425	28,13	21,14	27,29	25,88	11,25	30,55	21,92	19,65
^{238}U	0,0122	5,43	4,28	5,08	5,82	2,15	7,25	3,73	4,02
REE Chondrite normalised		KgL3-3_1	KgL3-3_2	KgL3-3_3	KgL3-3_4	KgL3-3_5	KgL3-3_6	KgL3-3_7	KgL3-3_8
La	0,367	82,8065	71,3624	70,8992	41,9346	25,0681	67,4114	72,3978	59,9183
Ce	0,957	61,2853	54,6082	55,1202	36,2382	25,9352	54,6082	51,5569	48,0042
Pr	0,137	40,3650	34,8175	34,0876	25,6934	13,8686	37,6642	33,9416	28,6861
Nd	0,711	27,9887	22,9255	21,1111	16,2729	8,7904	27,0042	20,7173	19,4374
Sm	0,231	16,1472	12,1212	19,7403	12,3377	5,8874	14,0260	16,1039	13,5931
Eu	0,087	3,9655	4,6437	4,0575	1,9080	2,2644	2,5977	4,6897	3,0575
Gd	0,306	11,0784	8,5948	7,4510	8,4967	3,2026	13,5948	7,8758	10,2941
Tb	0,058	11,8276	8,3621	12,0690	9,6724	3,4828	12,2414	8,8276	7,3448
Dy	0,381	10,6037	7,0079	8,5039	9,7375	3,7008	13,1496	8,1627	7,4803
Ho	0,0851	12,8085	7,3090	9,5182	10,0118	3,0200	13,0435	8,7074	7,7556
Er	0,249	12,0884	8,0723	10,0803	10,4418	3,1647	13,0924	8,2731	6,9880
Tm	0,0356	15,7303	8,6798	12,4719	12,2753	3,8764	16,8820	8,2584	6,2360
Yb	0,248	14,8387	10,8871	11,3306	13,8306	3,5323	17,9032	10,4032	9,3145
Lu	0,0381	15,5643	11,0236	10,8399	13,0184	3,5696	18,2415	10,6562	9,5538

Element	Chondrite	KgL3-3_9	KgL3-3_10						
^{9}Be	0,04	<0.00	4,3						
^{24}Mg	143000	0,063	0,063						
^{27}Al	12900	67715,77	96041,64						
^{30}Si	160000	330481,94	493351,19						
^{43}Ca	13500	4487,56	5980,42						
^{45}Sc	8,64	4,11	5,26						
^{51}V	85	1,05	<1.21						
^{60}Ni	16500	1,15	2,38						
^{85}Rb	3,45	248,44	391,95						
^{88}Sr	11,9	36,51	35,24						
^{89}Y	2,25	21,01	34,43						
^{90}Zr	5,54	67,25	91,89						
^{93}Nb	0,375	11,44	19,53						
^{137}Ba	3,41	392,88	209,82						
^{139}La	0,367	24,94	26,35						
^{140}Ce	0,957	46,81	59,23						
^{141}Pr	0,137	4,57	5,5						
^{143}Nd	0,711	18,85	19,4						
^{147}Sm	0,231	2,15	4,63						
^{153}Eu	0,087	0,33	0,41						
^{157}Gd	0,306	2,64	3,52						
^{159}Tb	0,058	0,339	0,8						
^{163}Dy	0,381	3,65	4,77						
^{165}Ho	0,0851	0,76	1,23						
^{166}Er	0,249	2,49	3,31						
^{169}Tm	0,0356	0,457	0,659						
^{172}Yb	0,248	2,76	4,86						
^{175}Lu	0,0381	0,462	0,702						
^{178}Hf	0,179	2,36	3,47						
^{181}Ta	0,026	1,02	1,83						
^{208}Pb	3,65	34,74	59,23						
^{232}Th	0,0425	24,02	36,32						
^{238}U	0,0122	4,87	8,85						
REE	Chondrite	KgL3-3_9	KgL3-3_10						
La	0,367	67,9564	71,7984						
Ce	0,957	48,9133	61,8913						
Pr	0,137	33,3577	40,1460						
Nd	0,711	26,5120	27,2855						
Sm	0,231	9,3074	20,0433						
Eu	0,087	3,7931	4,7126						
Gd	0,306	8,6275	11,5033						
Tb	0,058	5,8448	13,7931						
Dy	0,381	9,5801	12,5197						
Ho	0,0851	8,9307	14,4536						
Er	0,249	10,0000	13,2932						
Tm	0,0356	12,8371	18,5112						
Yb	0,248	11,1290	19,5968						
Lu	0,0381	12,1260	18,4252						

Element	Chondrite	3-11_1	3-11_2	3-11_3	3-11_4	3-11_5	3-11_6	3-11_7	3-11_8
^{9}Be	0,04	0,85	2,59	2,5	1,58	<0.00	5,15	1,99	0,75
^{24}Mg	143000	0,048	0,048	0,048	0,048	0,048	0,048	0,048	0,048
^{27}Al	12900	37566,18	49978,39	64344,36	65758,44	16128,25	71707,49	45313,56	24089,62
^{30}Si	160000	159453,42	247240,89	283282,56	347963,97	71822,57	428851,84	214428,95	108430,84
^{43}Ca	13500	2448,7	3571,37	4045,87	4321,29	1209,85	4660,29	2823,78	1852,32
^{45}Sc	8,64	1,8	3,13	4,21	4,12	0,86	5,34	3,18	1,39
^{51}V	85	1,07	0,7	0,81	1,04	0,85	<0.57	0,72	0,57
^{60}Ni	16500	0,39	0,68	<0.94	<0.43	<0.34	1,26	0,35	0,39
^{85}Rb	3,45	138,77	262,57	280,21	349,21	75,48	399,71	206,14	94,83
^{88}Sr	11,9	21,14	9,66	13,89	14,05	5,98	15,55	9,39	15,34
^{89}Y	2,25	11,38	20,5	28,12	28,02	7,91	28,88	20,77	7,38
^{90}Zr	5,54	32	42,48	60,33	52,53	16,76	58,61	36,39	20,59
^{93}Nb	0,375	6,87	13,11	14,34	17,18	3,86	20,68	10,29	4,15
^{137}Ba	3,41	223,61	45,4	47,49	52,89	16,49	51,57	39,58	140,54
^{139}La	0,367	11,76	13,27	16,86	16,87	5	18,65	12,4	8,43
^{140}Ce	0,957	25,56	33,64	38,53	45,15	10,6	53,62	28,1	17,61
^{141}Pr	0,137	2,36	3,37	4,13	4,25	1,18	4,81	2,73	1,49
^{143}Nd	0,711	7,63	11,86	13,99	14,38	4,27	16,33	10,42	5,29
^{147}Sm	0,231	1,64	3,06	3,32	3,72	1,31	3,88	2,16	0,93
^{153}Eu	0,087	0,214	0,128	0,067	0,189	0,037	0,192	0,109	0,129
^{157}Gd	0,306	1,48	3,03	2,94	3,73	1,42	3,78	2,1	1,24
^{159}Tb	0,058	0,252	0,483	0,613	0,659	0,164	0,661	0,453	0,118
^{163}Dy	0,381	1,63	3,47	4,34	4,2	1,51	4,45	3,47	1,29
^{165}Ho	0,0851	0,396	0,853	0,96	0,918	0,303	0,98	0,714	0,277
^{166}Er	0,249	1,14	2,35	3,21	3,03	0,8	3,07	1,9	0,751
^{169}Tm	0,0356	0,208	0,412	0,509	0,481	0,168	0,543	0,36	0,149
^{172}Yb	0,248	1,47	3,1	4,04	3,91	1,13	4,14	2,71	1,05
^{175}Lu	0,0381	0,231	0,452	0,554	0,57	0,175	0,571	0,424	0,157
^{178}Hf	0,179	1,24	1,91	2,39	2,41	0,74	2,65	1,8	0,79
^{181}Ta	0,026	0,595	1,36	1,5	1,77	0,456	2,08	1,152	0,412
^{208}Pb	3,65	20,56	34,52	39,96	44,45	10,54	56,16	28,98	14,49
^{232}Th	0,0425	11,08	20,15	26,98	26,97	8,39	29,43	20,46	8,27
^{238}U	0,0122	2,42	5,78	6,85	8,36	1,87	9,99	5,01	1,88
REE Chondrite normalised		**3-11_1**	**3-11_2**	**3-11_3**	**3-11_4**	**3-11_5**	**3-11_6**	**3-11_7**	**3-11_8**
La	0,367	32,0436	36,1580	45,9401	45,9673	13,6240	50,8174	33,7875	22,9700
Ce	0,957	26,7085	35,1515	40,2612	47,1787	11,0763	56,0293	29,3626	18,4013
Pr	0,137	17,2263	24,5985	30,1460	31,0219	8,6131	35,1095	19,9270	10,8759
Nd	0,711	10,7314	16,6807	19,6765	20,2250	6,0056	22,9677	14,6554	7,4402
Sm	0,231	7,0996	13,2468	14,3723	16,1039	5,6710	16,7965	9,3506	4,0260
Eu	0,087	2,4598	1,4713	0,7701	2,1724	0,4253	2,2069	1,2529	1,4828
Gd	0,306	4,8366	9,9020	9,6078	12,1895	4,6405	12,3529	6,8627	4,0523
Tb	0,058	4,3448	8,3276	10,5690	11,3621	2,8276	11,3966	7,8103	2,0345
Dy	0,381	4,2782	9,1076	11,3911	11,0236	3,9633	11,6798	9,1076	3,3858
Ho	0,0851	4,6533	10,0235	11,2808	10,7873	3,5605	11,5159	8,3901	3,2550
Er	0,249	4,5783	9,4378	12,8916	12,1687	3,2129	12,3293	7,6305	3,0161
Tm	0,0356	5,8427	11,5730	14,2978	13,5112	4,7191	15,2528	10,1124	4,1854
Yb	0,248	5,9274	12,5000	16,2903	15,7661	4,5565	16,6935	10,9274	4,2339
Lu	0,0381	6,0630	11,8635	14,5407	14,9606	4,5932	14,9869	11,1286	4,1207

Element	Chondrite	3-11_9	3-11_10						
^{9}Be	0,04	1,52	2,7						
^{24}Mg	143000	0,048	0,048						
^{27}Al	12900	30752,85	57877,44						
^{30}Si	160000	172193,23	306834,03						
^{43}Ca	13500	2084,95	3720,14						
^{45}Sc	8,64	1,89	4,02						
^{51}V	85	1,14	<0.42						
^{60}Ni	16500	0,31	0,92						
^{85}Rb	3,45	162,87	303,21						
^{88}Sr	11,9	5,64	11,52						
^{89}Y	2,25	13,4	25,27						
^{90}Zr	5,54	28,99	49,51						
^{93}Nb	0,375	8,21	14,7						
^{137}Ba	3,41	34,24	49,17						
^{139}La	0,367	8,29	15,4						
^{140}Ce	0,957	21,36	39,93						
^{141}Pr	0,137	1,95	3,77						
^{143}Nd	0,711	7,28	13,26						
^{147}Sm	0,231	1,62	2,89						
^{153}Eu	0,087	0,088	0,208						
^{157}Gd	0,306	1,37	3,17						
^{159}Tb	0,058	0,315	0,606						
^{163}Dy	0,381	1,85	3,49						
^{165}Ho	0,0851	0,475	0,93						
^{166}Er	0,249	1,54	2,87						
^{169}Tm	0,0356	0,236	0,487						
^{172}Yb	0,248	1,69	3,69						
^{175}Lu	0,0381	0,27	0,594						
^{178}Hf	0,179	0,952	2,23						
^{181}Ta	0,026	0,864	1,48						
^{208}Pb	3,65	21,85	42,98						
^{232}Th	0,0425	12,72	25,3						
^{238}U	0,0122	3,85	7,07						
REE Chondrite normalised		**3-11_9**	**3-11_10**						
La	0,367	22,5886	41,9619						
Ce	0,957	22,3197	41,7241						
Pr	0,137	14,2336	27,5182						
Nd	0,711	10,2391	18,6498						
Sm	0,231	7,0130	12,5108						
Eu	0,087	1,0115	2,3908						
Gd	0,306	4,4771	10,3595						
Tb	0,058	5,4310	10,4483						
Dy	0,381	4,8556	9,1601						
Ho	0,0851	5,5817	10,9283						
Er	0,249	6,1847	11,5261						
Tm	0,0356	6,6292	13,6798						
Yb	0,248	6,8145	14,8790						
Lu	0,0381	7,0866	15,5906						

Element	Chondrite	BTS-3_1	BTS-3_2	BTS-3_3	BTS-3_4	BTS-3_5	BTS-3_6	BTS-3_7	BTS-3_8
^{9}Be	0,04	0,52	4,23	<3.66	1,47	2,77	4	1,98	1,96
^{24}Mg	143000	0,063	0,063	0,063	0,063	0,063	0,063	0,063	0,063
^{27}Al	12900	70759,88	70112,55	83521,98	71562,75	83221,66	98612,5	43989,51	85444,43
^{30}Si	160000	321600,16	339781,19	405928,16	364738,38	413469	420279	203376,53	390209,31
^{43}Ca	13500	4646,78	5729,48	5158,71	5132,58	5358,65	5291,92	2411,33	6053,06
^{45}Sc	8,64	3,81	2,56	4,68	3,64	5,33	5,9	2,02	5,39
^{51}V	85	0,85	3,65	1,24	0,99	1,92	1,72	3,79	<1.04
^{60}Ni	16500	0,48	<1.17	<0.53	0,52	1,13	0,54	0,97	0,8
^{85}Rb	3,45	253,4	280,02	280,68	268,84	402,62	418,26	161,88	326,19
^{88}Sr	11,9	41,9	39,04	47,47	46,28	18,13	20,76	15,38	36,25
^{89}Y	2,25	20,93	22,85	25,39	21,99	39,46	47,34	14,08	30,78
^{90}Zr	5,54	55,43	55,83	78,93	65,81	75,58	85,02	44,11	74,19
^{93}Nb	0,375	13,11	13,99	15,25	12,89	19,5	21,18	9,02	15,97
^{137}Ba	3,41	395,84	402,48	476,53	423,36	59,5	76,77	148,92	279,37
^{139}La	0,367	22,84	22,74	27,76	23,88	20,84	25,98	12,54	25,63
^{140}Ce	0,957	51,64	48,17	57,36	52,9	52,48	55,92	24,76	54,24
^{141}Pr	0,137	4,68	4,29	5,05	4,77	4,92	5,77	2,49	5,31
^{143}Nd	0,711	16,62	14,95	18,82	16,53	20,65	23,44	9,32	16,96
^{147}Sm	0,231	2,9	2,68	3,85	3,16	5,22	5,81	1,9	3,42
^{153}Eu	0,087	0,329	0,6	0,384	0,325	0,27	0,244	0,158	0,204
^{157}Gd	0,306	2,92	2,67	4,34	2,85	4,68	4,44	1,14	3,21
^{159}Tb	0,058	0,502	0,57	0,712	0,593	0,854	1,07	0,342	0,566
^{163}Dy	0,381	2,99	2,89	3,61	3,4	5,41	6,78	1,88	5,42
^{165}Ho	0,0851	0,83	0,82	0,87	0,737	1,04	1,54	0,44	1,06
^{166}Er	0,249	2,21	2,05	2,75	2,27	3,67	4,37	1,66	3,01
^{169}Tm	0,0356	0,353	0,353	0,558	0,339	0,666	0,834	0,256	0,568
^{172}Yb	0,248	2,81	2,83	3,42	3,19	5,09	5,6	1,63	4,41
^{175}Lu	0,0381	0,433	0,478	0,466	0,459	0,712	0,99	0,27	0,542
^{178}Hf	0,179	2,16	2,28	2,84	2,42	3,16	3,95	1,48	3,38
^{181}Ta	0,026	1,26	1,13	1,23	1,23	2,14	2,46	0,997	1,67
^{208}Pb	3,65	37,72	38,21	44,52	39,85	55,36	55,71	25,28	47,69
^{232}Th	0,0425	21,64	22,27	25,63	21,65	35,36	40,45	14,08	31,28
^{238}U	0,0122	4,96	5,61	5,42	5,06	9,69	9,59	3,33	6,78
REE Chondrite normalised		**BTS-3_1**	**BTS-3_2**	**BTS-3_3**	**BTS-3_4**	**BTS-3_5**	**BTS-3_6**	**BTS-3_7**	**BTS-3_8**
La	0,367	62,2343	61,9619	75,6403	65,0681	56,7847	70,7902	34,1689	69,8365
Ce	0,957	53,9603	50,3344	59,9373	55,2769	54,8380	58,4326	25,8725	56,6771
Pr	0,137	34,1606	31,3139	36,8613	34,8175	35,9124	42,1168	18,1752	38,7591
Nd	0,711	23,3755	21,0267	26,4698	23,2489	29,0436	32,9677	13,1083	23,8537
Sm	0,231	12,5541	11,6017	16,6667	13,6797	22,5974	25,1515	8,2251	14,8052
Eu	0,087	3,7816	6,8966	4,4138	3,7356	3,1034	2,8046	1,8161	2,3448
Gd	0,306	9,5425	8,7255	14,1830	9,3137	15,2941	14,5098	3,7255	10,4902
Tb	0,058	8,6552	9,8276	12,2759	10,2241	14,7241	18,4483	5,8966	9,7586
Dy	0,381	7,8478	7,5853	9,4751	8,9239	14,1995	17,7953	4,9344	14,2257
Ho	0,0851	9,7532	9,6357	10,2233	8,6604	12,2209	18,0964	5,1704	12,4559
Er	0,249	8,8755	8,2329	11,0442	9,1165	14,7390	17,5502	6,6667	12,0884
Tm	0,0356	9,9157	9,9157	15,6742	9,5225	18,7079	23,4270	7,1910	15,9551
Yb	0,248	11,3306	11,4113	13,7903	12,8629	20,5242	22,5806	6,5726	17,7823
Lu	0,0381	11,3648	12,5459	12,2310	12,0472	18,6877	25,9843	7,0866	14,2257

Element	Chondrite	Tej_1	Tej_2	Tej_3	Tej_4	Tej_5	Tej_6	Tej_7	Tej_8
^{9}Be	0,04	<0.00	<0.00	2,55	0,47	1,1	1,19	<0.00	1,5
^{24}Mg	143000	0,051	0,051	0,051	0,051	0,051	0,051	0,051	0,051
^{27}Al	12900	57090,16	35581,34	39867,28	54155,83	57321,8	47089,06	62228,83	47418,52
^{30}Si	160000	200934,73	133032,95	188143,14	273206,63	240237,39	216830,69	277115,88	234805,47
^{43}Ca	13500	4802,09	2440,08	2847,88	4492,16	4564,36	2746,55	4797,75	2688,03
^{45}Sc	8,64	3,4	1,88	2,5	3,13	3,05	1,45	1,64	2,27
^{51}V	85	0,89	2,22	1,85	0,93	1,46	0,81	2,06	1,3
^{60}Ni	16500	0,59	0,51	0,78	<0.54	0,45	0,65	0,98	0,61
^{85}Rb	3,45	164,71	103,42	139,43	176,29	186,97	139,88	244,79	175,02
^{88}Sr	11,9	28,53	17,4	24,12	39,4	25,61	32,87	31,96	22,7
^{89}Y	2,25	16,57	10,64	11,84	13,87	17,95	13,03	20,08	17,46
^{90}Zr	5,54	42,73	33,32	34,84	52,03	50,15	41,06	55,28	43,71
^{93}Nb	0,375	7,96	5,56	6,85	8,82	9,56	6,77	10,85	8,39
^{137}Ba	3,41	281,07	189,89	229,15	429,66	308,72	360,61	280,38	151,08
^{139}La	0,367	17,22	11,3	12,75	18,78	18,36	17,48	20,53	14,5
^{140}Ce	0,957	33,5	22,08	26,97	40,24	36,43	32,56	43,42	29,61
^{141}Pr	0,137	2,91	2,16	2,57	3,48	3,78	3,24	4,07	2,98
^{143}Nd	0,711	11,24	7,56	9,46	10,6	13,3	9,96	14,27	11,43
^{147}Sm	0,231	1,74	1,52	1,87	2,78	2,68	2	2,44	1,88
^{153}Eu	0,087	0,105	0,161	0,169	0,302	0,255	0,311	0,25	0,25
^{157}Gd	0,306	2,35	1,57	1,47	1,75	2,01	1,2	2,53	2,08
^{159}Tb	0,058	0,359	0,217	0,243	0,345	0,324	0,262	0,47	0,368
^{163}Dy	0,381	2,38	1,57	1,59	2,16	2,99	1,65	3,59	2,8
^{165}Ho	0,0851	0,67	0,323	0,367	0,42	0,615	0,429	0,619	0,61
^{166}Er	0,249	1,89	1,05	1,23	1,4	1,95	1,3	2,26	1,65
^{169}Tm	0,0356	0,242	0,173	0,176	0,228	0,343	0,201	0,408	0,286
^{172}Yb	0,248	1,76	1,37	1,35	1,76	2,32	1,73	2,98	2,46
^{175}Lu	0,0381	0,326	0,221	0,267	0,279	0,387	0,285	0,423	0,335
^{178}Hf	0,179	2,02	1,17	1,29	1,7	2,03	1,7	2,48	1,78
^{181}Ta	0,026	0,72	0,512	0,706	0,749	0,97	0,714	1,15	0,89
^{208}Pb	3,65	24,32	16,29	20,49	28,15	26,55	20,76	36,8	24,36
^{232}Th	0,0425	16,77	10,93	11,85	15,38	17,65	14,07	21,99	16,71
^{238}U	0,0122	3,18	2,1	2,63	3,32	3,28	2,45	5,31	3,7
REE Chondrite normalised		**Tej_1**	**Tej_2**	**Tej_3**	**Tej_4**	**Tej_5**	**Tej_6**	**Tej_7**	**Tej_8**
La	0,367	46,9210	30,7902	34,7411	51,1717	50,0272	47,6294	55,9401	39,5095
Ce	0,957	35,0052	23,0721	28,1818	42,0481	38,0669	34,0230	45,3710	30,9404
Pr	0,137	21,2409	15,7664	18,7591	25,4015	27,5912	23,6496	29,7080	21,7518
Nd	0,711	15,8087	10,6329	13,3052	14,9086	18,7060	14,0084	20,0703	16,0759
Sm	0,231	7,5325	6,5801	8,0952	12,0346	11,6017	8,6580	10,5628	8,1385
Eu	0,087	1,2069	1,8506	1,9425	3,4713	2,9310	3,5747	2,8736	2,8736
Gd	0,306	7,6797	5,1307	4,8039	5,7190	6,5686	3,9216	8,2680	6,7974
Tb	0,058	6,1897	3,7414	4,1897	5,9483	5,5862	4,5172	8,1034	6,3448
Dy	0,381	6,2467	4,1207	4,1732	5,6693	7,8478	4,3307	9,4226	7,3491
Ho	0,0851	7,8731	3,7955	4,3126	4,9354	7,2268	5,0411	7,2738	7,1680
Er	0,249	7,5904	4,2169	4,9398	5,6225	7,8313	5,2209	9,0763	6,6265
Tm	0,0356	6,7978	4,8596	4,9438	6,4045	9,6348	5,6461	11,4607	8,0337
Yb	0,248	7,0968	5,5242	5,4435	7,0968	9,3548	6,9758	12,0161	9,9194
Lu	0,0381	8,5564	5,8005	7,0079	7,3228	10,1575	7,4803	11,1024	8,7927

Element	Chondrite	Tej_9	Tej_10						
^{9}Be	0,04	1,49	<2.43						
^{24}Mg	143000	0,051	0,051						
^{27}Al	12900	40549,58	58745,41						
^{30}Si	160000	173580,42	283988						
^{43}Ca	13500	2055,74	3996,71						
^{45}Sc	8,64	2,12	2,33						
^{51}V	85	<1.18	1,08						
^{60}Ni	16500	0,61	0,26						
^{85}Rb	3,45	132,6	206,12						
^{88}Sr	11,9	23,92	34,81						
^{89}Y	2,25	12,68	17,46						
^{90}Zr	5,54	42,01	42,85						
^{93}Nb	0,375	6,86	9,97						
^{137}Ba	3,41	220,26	351,7						
^{139}La	0,367	14,61	20,33						
^{140}Ce	0,957	27,2	41,39						
^{141}Pr	0,137	2,41	3,74						
^{143}Nd	0,711	9,86	12,6						
^{147}Sm	0,231	1,71	2,43						
^{153}Eu	0,087	0,225	0,289						
^{157}Gd	0,306	1,57	1,94						
^{159}Tb	0,058	0,292	0,368						
^{163}Dy	0,381	2,04	3,07						
^{165}Ho	0,0851	0,586	0,62						
^{166}Er	0,249	1,37	1,73						
^{169}Tm	0,0356	0,283	0,307						
^{172}Yb	0,248	1,74	2,4						
^{175}Lu	0,0381	0,274	0,388						
^{178}Hf	0,179	1,74	2,19						
^{181}Ta	0,026	0,624	0,998						
^{208}Pb	3,65	18,52	30,08						
^{232}Th	0,0425	14,44	19,05						
^{238}U	0,0122	2,54	4,1						
REE Chondrite normalised		**Tej_9**	**Tej_10**						
La	0,367	39,8093	55,3951						
Ce	0,957	28,4222	43,2497						
Pr	0,137	17,5912	27,2993						
Nd	0,711	13,8678	17,7215						
Sm	0,231	7,4026	10,5195						
Eu	0,087	2,5862	3,3218						
Gd	0,306	5,1307	6,3399						
Tb	0,058	5,0345	6,3448						
Dy	0,381	5,3543	8,0577						
Ho	0,0851	6,8860	7,2855						
Er	0,249	5,5020	6,9478						
Tm	0,0356	7,9494	8,6236						
Yb	0,248	7,0161	9,6774						
Lu	0,0381	7,1916	10,1837						

Element	Chondrite	KgL2-5_1	KgL2-5_2	KgL2-5_3	KgL2-5_4	KgL2-5_5	KgL2-5_6	KgL2-5_7	KgL2-5_8
^{9}Be	0,04	2,77	3,12	<2.79	1,5	1,78	1,15	<3.43	0,78
^{24}Mg	143000	0,067	0,067	0,067	0,067	0,067	0,067	0,067	0,067
^{27}Al	12900	80680,3	84212,85	100388,49	79042,34	79289,84	101215,55	97857,91	72096,44
^{30}Si	160000	367750,06	355564,63	484838	389444,28	386748,25	436103,81	446147,03	362046
^{43}Ca	13500	5447,01	6029,38	6587,61	6387,58	6012,29	5923,1	6465,04	5488,47
^{45}Sc	8,64	3,64	3,99	6,66	4,03	4,51	4,62	4,88	4,14
^{51}V	85	1,03	<0.70	1,08	0,87	1,16	<0.97	1,2	1,61
^{60}Ni	16500	0,34	1,27	0,75	<0.26	<0.80	<0.73	0,87	<0.45
^{85}Rb	3,45	300,99	284,88	493,48	297,43	314,13	365,21	457,52	269,27
^{88}Sr	11,9	47,28	40,91	18,6	47,83	41,33	45,08	24,38	47,36
^{89}Y	2,25	24,58	28,25	45,82	24,43	24,53	36,79	48,66	20,35
^{90}Zr	5,54	74,17	83,82	87,69	71,22	65,23	99,16	85,04	74,67
^{93}Nb	0,375	15,53	14,77	25,46	15,63	16,26	18,17	23,17	13,65
^{137}Ba	3,41	520,78	485,74	69,65	562,21	467,79	316,93	78,15	663,2
^{139}La	0,367	26,64	27,75	26,94	28,66	25,57	30,53	27,34	29,11
^{140}Ce	0,957	60,21	57,79	67,19	62,69	60,68	61,45	61,07	62,06
^{141}Pr	0,137	5,75	5,8	6,96	5,87	5,73	6,25	6,29	5,69
^{143}Nd	0,711	19,41	19,35	25,47	19,92	17,29	21,56	23,03	18,03
^{147}Sm	0,231	3,69	3,91	6,04	3,71	3,41	4,77	4,81	3,64
^{153}Eu	0,087	0,531	0,388	0,282	0,467	0,434	0,462	0,273	0,405
^{157}Gd	0,306	3,46	3,92	5,57	3,46	2,65	4,56	6,25	2,61
^{159}Tb	0,058	0,662	0,765	1,22	0,584	0,613	0,738	0,96	0,635
^{163}Dy	0,381	3,83	4,27	7,42	3,81	3,46	5,52	6,72	3,47
^{165}Ho	0,0851	0,819	0,98	1,63	0,806	0,955	1,27	1,53	0,592
^{166}Er	0,249	2,52	2,77	5,09	2,52	2,55	3,66	4,91	2,07
^{169}Tm	0,0356	0,464	0,535	0,796	0,397	0,445	0,656	0,676	0,385
^{172}Yb	0,248	3,39	3,48	5,86	3,42	3,12	4,89	6,4	2,53
^{175}Lu	0,0381	0,523	0,574	0,977	0,454	0,569	0,771	0,94	0,437
^{178}Hf	0,179	2,7	3,24	4,05	3,14	2,73	3,97	3,72	2,8
^{181}Ta	0,026	1,5	1,38	2,92	1,47	1,53	1,98	2,48	1,42
^{208}Pb	3,65	45,01	42,21	69,28	44,25	48,18	51,28	63,22	44,68
^{232}Th	0,0425	24,95	26,35	44,81	26,63	26,2	37,37	44,4	23,61
^{238}U	0,0122	5,56	5,52	12,08	5,79	6,3	7,8	10,04	5,25
REE Chondrite normalised		**KgL2-5_1**	**KgL2-5_2**	**KgL2-5_3**	**KgL2-5_4**	**KgL2-5_5**	**KgL2-5_6**	**KgL2-5_7**	**KgL2-5_8**
La	0,367	72,5886	75,6131	73,4060	78,0926	69,6730	83,1880	74,4959	79,3188
Ce	0,957	62,9154	60,3866	70,2090	65,5068	63,4065	64,2111	63,8140	64,8485
Pr	0,137	41,9708	42,3358	50,8029	42,8467	41,8248	45,6204	45,9124	41,5328
Nd	0,711	27,2996	27,2152	35,8228	28,0169	24,3179	30,3235	32,3910	25,3586
Sm	0,231	15,9740	16,9264	26,1472	16,0606	14,7619	20,6494	20,8225	15,7576
Eu	0,087	6,1034	4,4598	3,2414	5,3678	4,9885	5,3103	3,1379	4,6552
Gd	0,306	11,3072	12,8105	18,2026	11,3072	8,6601	14,9020	20,4248	8,5294
Tb	0,058	11,4138	13,1897	21,0345	10,0690	10,5690	12,7241	16,5517	10,9483
Dy	0,381	10,0525	11,2073	19,4751	10,0000	9,0814	14,4882	17,6378	9,1076
Ho	0,0851	9,6240	11,5159	19,1539	9,4712	11,2221	14,9236	17,9788	6,9565
Er	0,249	10,1205	11,1245	20,4418	10,1205	10,2410	14,6988	19,7189	8,3133
Tm	0,0356	13,0337	15,0281	22,3596	11,1517	12,5000	18,4270	18,9888	10,8146
Yb	0,248	13,6694	14,0323	23,6290	13,7903	12,5806	19,7177	25,8065	10,2016
Lu	0,0381	13,7270	15,0656	25,6430	11,9160	14,9344	20,2362	24,6719	11,4698

Element	Chondrite	KgL2-5_9	KgL2-5_10						
^{9}Be	0,04	5,88	7,15						
^{24}Mg	143000	0,067	0,067						
^{27}Al	12900	85221,43	85646,46						
^{30}Si	160000	471674,88	488406,75						
^{43}Ca	13500	7026,11	5638,62						
^{45}Sc	8,64	5,14	5,31						
^{51}V	85	1,43	0,91						
^{60}Ni	16500	<0.74	1,17						
^{85}Rb	3,45	377,78	443,02						
^{88}Sr	11,9	38,51	21,02						
^{89}Y	2,25	30,76	37,12						
^{90}Zr	5,54	78,46	76,79						
^{93}Nb	0,375	17,89	22,55						
^{137}Ba	3,41	327,62	78,65						
^{139}La	0,367	26,12	23,49						
^{140}Ce	0,957	62,45	58,24						
^{141}Pr	0,137	5,8	5,61						
^{143}Nd	0,711	19,58	20,49						
^{147}Sm	0,231	4,27	5,04						
^{153}Eu	0,087	0,316	0,317						
^{157}Gd	0,306	3,78	4,75						
^{159}Tb	0,058	0,722	0,57						
^{163}Dy	0,381	4,09	5,9						
^{165}Ho	0,0851	0,94	1,36						
^{166}Er	0,249	2,91	3,56						
^{169}Tm	0,0356	0,458	0,649						
^{172}Yb	0,248	3,79	5,14						
^{175}Lu	0,0381	0,606	0,843						
^{178}Hf	0,179	2,9	2,97						
^{181}Ta	0,026	1,93	2,4						
^{208}Pb	3,65	54,15	59,32						
^{232}Th	0,0425	31,68	38,84						
^{238}U	0,0122	7,73	10,63						
REE Chondrite normalised		**KgL2-5_9**	**KgL2-5_10**						
La	0,367	71,1717	64,0054						
Ce	0,957	65,2560	60,8568						
Pr	0,137	42,3358	40,9489						
Nd	0,711	27,5387	28,8186						
Sm	0,231	18,4848	21,8182						
Eu	0,087	3,6322	3,6437						
Gd	0,306	12,3529	15,5229						
Tb	0,058	12,4483	9,8276						
Dy	0,381	10,7349	15,4856						
Ho	0,0851	11,0458	15,9812						
Er	0,249	11,6867	14,2972						
Tm	0,0356	12,8652	18,2303						
Yb	0,248	15,2823	20,7258						
Lu	0,0381	15,9055	22,1260						

9. 3 Major components internal standards and calibration (EPMA)

Signal(s) Used : Na Ka, Si Ka, K Ka, Ca Ka, Ti Ka, Fe Ka, Al Ka, Mg Ka, P Ka, Ba La, Ce La, Cr Ka, Mn Ka, Sr La, Rb La

Spectromers Conditions : Sp1 LTAP, Sp2 TAP, Sp3 LPET, Sp3 LPET, Sp3 LPET, Sp5 LIF, Sp2 TAP, Sp4 TAP, Sp3 LPET, Sp5 LIF, Sp5 LIF, Sp5 LIF, Sp5 LIF, Sp3 LPET, Sp3 LPET
Full Spectromers Conditions : Sp1 LTAP(2d= 0,K= 0), Sp2 TAP(2d= 0,K= 0), Sp3 LPET(2d= 0,K= 0), Sp3 LPET(2d= 0,K= 0), Sp3 LPET(2d= 0,K= 0), Sp5 LIF(2d= 0,K= 0), Sp2 TAP(2d= 0,K= 0), Sp4 TAP(2d= 0,K= 0), Sp3 LPET(2d= 0,K= 0), Sp5 LIF(2d= 0,K= 0), Sp5 LIF(2d= 0,K= 0), Sp5 LIF(2d= 0,K= 0), Sp5 LIF(2d= 0,K= 0), Sp3 LPET(2d= 0,K= 0), Sp3 LPET(2d= 0,K= 0)

Column Conditions : Cond 1 : 15keV 2nA , Cond 2 : 15keV 10nA
Cond 1 : Na Ka, Si Ka, K Ka, Ca Ka, Ti Ka, Fe Ka, Al Ka, Mg Ka
Cond 2 : P Ka, Ba La, Ce La, Cr Ka, Mn Ka, Sr La, Rb La

Date : 1-Sep-2010

User Name : sx

Setup Name : EGatti_Glass_Aug_2010.qtiSet

DataSet Comment : 1

Comment :

Analysis Date : 31/08/2010 19:37:02

Project Name : Emma Gatti

Sample Name : 27_Aug_2010
Pha Parameters
:

	Bias	Gain	Dtime	Blin	Wind	Mode
Sp1(Na Ka)	1300	2639	3	560	768	Inte
Sp2(Si Ka)	1308	2714	3	560	1404	Inte
Sp3(K Ka)	1850	895	3	560	791	Inte
Sp3(Ca Ka)	1850	895	3	560	791	Inte
Sp3(Ti Ka)	1850	895	3	560	791	Inte
Sp5(Fe Ka)	1859	425	3	560	738	Inte
Sp2(Al Ka)	1308	2714	3	560	1404	Inte
Sp4(Mg Ka)	1317	2819	3	560	4960	Inte
Sp3(P Ka)	1850	895	3	560	791	Inte
Sp5(Ba La)	1859	425	3	560	738	Inte
Sp5(Ce La)	1859	425	3	560	738	Inte
Sp5(Cr Ka)	1859	425	3	560	738	Inte
Sp5(Mn Ka)	1859	425	3	560	738	Inte
Sp3(Sr La)	1850	895	3	560	791	Inte
Sp3(Rb La)	1850	895	3	560	791	Inte

Peak Position : Sp1 46379 (-600, 400), Sp2 27737 (-500, 500), Sp3 42751 (-300, 250), Sp3 38393 (-300, 250), Sp3 31437 (-350, 250), Sp5 48088 (-250, 300), Sp2 32460 (-500, 500), Sp4 38521 (-500, 500), Sp3 70286 (-700, 600), Sp5 68937 (-500, 500), Sp5 63617 (-200, 350), Sp5 56870 (-250, 300), Sp5 52205 (200, 1.0221), Sp3 78354 (-300, 300), Sp3 83565 (1)

Current Sample Position : X = -13171 Y = 3888 Z = -100

Standard Name :

Na On Jad

Si On Si Glass

K On KSp

Ca On Diopside

Ti On Rutile

Fe On Fayalite

Al On Cor

Mg On Periclase

P On Apatite

Ba On Benitoite

Ce On CeAl2

Cr On Cr

Mn On Mn

Sr On Celest

Rb On Rb Glass

Standard composition :

Jad = O : 47.5%, Na : 11.3%, Al : 13.2%, Si : 27.8%, Fe : 0.2%

Si Glass = O : 48.0939%, F : 0.64%, Na : 4.2066%, Mg : 0.006%, Al : 5.5989%, Si : 34.8755%, K : 3.6358%, Ca : 0.1072%, Ti : 0.1079%, Mn : 0.0465%, Fe : 2.6817%

KSp = O : 46.1%, Na : 0.8%, Al : 9.7%, Si : 30.3%, K : 12.8%, Fe : 0.3%

Diopside = O : 44.5%, Mg : 11.2%, Si : 25.9%, Ca : 18.4%

Rutile = Ti : 59.95%, O : 40.05%

Fayalite = O : 31.405%, Si : 13.783%, Fe : 54.812%

Cor = O : 47.1%, Al : 52.9%

Periclase = O : 39.7%, Mg : 60.3%

Apatite = O : 38.1%, F : 3.4%, P : 18.4%, Cl : 0.4%, Ca : 39.7%

Benitoite = O : 34.8%, Si : 20.4%, Ti : 11.6%, Ba : 33.2%

CeAl2 = Ce : 72.1959%, Al : 27.8041%

Cr = Cr : 100.%

Mn = Mn : 100.%

Celest = O : 34.7%, S : 17.4%, Sr : 47.1%, Ba : 0.8%

Rb Glass = O : 30.026%, Al : 7.165%, Ge : 37.544%, Rb : 9.52%, Ca : 15.745%

Calibration file name :

Na : Jad_Na192.calDat

Si : Si Glass_Si041.calDat

K : KSp_K143.calDat

Ca : Diopside_Si_Ca195.calDat

Ti : Rutile_Ti157.calDat

Fe : Fayalite_Fe154.calDat

Al : Cor_Al_Al041.calDat

Mg : Periclase_Mg_Mg027.calDat

P : Apatite_P048.calDat

Ba : Benitoite_Ba_Ba019.calDat

Ce : CeAl2_Ce008.calDat

Cr : Cr_Cr163.calDat

Mn : Mn_Mn168.calDat

Sr : Celest_Sr063.calDat

Rb : Rb Glass_Rb002.calDat

Beam Size : 15, 15 µm

9.4 Major components geochemical analyses (EPMA)

Element	BTS3/1	BTS3/2	BTS3/3	BTS3/4	BTS3/5	BTS3/6	BTS3/7	BTS3/8	BTS3/9	BTS3/10	BTS3/11	BTS3/12	BTS3/13	BTS3/14	BTS3/15
Na_2O	3,2311	2,9863	3,3368	3,1026	3,1638	3,2671	3,164	1,0906	3,1023	3,1876	2,5656	3,1166	2,8421	2,8866	3,1845
SiO_2	75,8637	75,3822	75,3104	74,0233	75,1733	76,3076	75,6084	75,5874	74,8892	75,8842	70,7782	74,7481	74,524	74,1139	75,0771
K_2O	5,0218	5,2068	5,0452	5,1835	5,0419	5,3076	5,2347	4,7513	5,1116	5,1404	5,3424	5,0314	5,2016	5,2943	5,0205
CaO	0,7654	0,7025	0,7261	0,7422	0,772	0,6885	0,694	0,7727	0,7368	0,7451	0,7705	0,763	0,7436	0,823	0,7701
TiO_2	0,0447	0,0281	0,0735	0,0574	0,0426	0,0888	0,0109	0,0561	0,0009	0,0447	0,0595	-0,0112	0,0602	0,0641	0,0617
FeO	0,782	0,7819	0,7561	0,891	1,0766	0,8745	0,8651	0,8476	0,9766	0,8233	0,8902	1,1686	0,7924	0,6933	0,8259
Al_2O_3	11,8873	11,9673	11,97	12,1441	11,6576	12,0884	11,8914	12,1054	12,0392	11,9829	11,6293	11,8928	11,6765	11,7876	12,0797
MgO	0,059	0,0426	0,0359	0,0426	0,0921	0,0294	0,0721	0,1064	0,0197	0,0458	0,0753	0,0493	0,121	0,1015	0,0525
P_2O_5	-0,0031	0,0145	0,0237	0,0159	0,024	-0,0143	0,0122	0,0041	0,0183	0,0123	0,0006	0,0079	0,0031	0,0155	0,0005
BaO	-0,0233	0,1183	0,0216	-0,0812	0,0859	-0,0216	0,0431	0,0817	0,1404	0,0108	0,1296	-0,0465	0	0,0973	0,1188
Ce_2O_3	-0,0556	0,0905	-0,0217	-0,0034	0,0575	-0,0409	-0,0996	-0,0595	0,0122	0,0275	0,0818	0,0042	0,0241	-0,0146	-0,009
Cr_2O_3	-0,0172	0,0149	0,052	0,0013	0,0356	-0,0189	0,0193	-0,017	0,0402	0,0216	-0,0203	-0,0258	-0,0124	0,039	-0,0275
MnO	0,0415	0,0706	-0,0014	-0,0115	0,0954	0,0478	0,1091	0,0476	0,0708	0,0849	0,0755	0,0564	0,0521	0,0867	0,051
SrO	-0,051	-0,0249	-0,046	-0,0311	-0,017	-0,0316	-0,0197	-0,024	-0,0368	-0,0565	-0,05	-0,0156	-0,0381	-0,0644	0,0013
Rb_2O	-0,9446	-0,9205	-0,9586	-0,9147	-0,9647	-0,907	-0,8991	-0,9009	-0,9169	-0,9297	-0,9397	-0,8834	-0,9519	-0,9348	-0,9294
Total	97,6965	97,4064	97,3515	96,2039	97,3183	98,6997	97,7242	95,4509	97,1581	98,0112	92,3986	96,8385	96,0407	96,0028	97,2434

Element	BTS12 / 1	BTS12 / 2	BTS12 / 3	BTS12 / 4	BTS12 / 5	BTS12 / 6	BTS12 / 7	BTS12 / 8	BTS12 / 9	BTS12 / 10	BTS12 / 11	BTS12 / 12	BTS12 / 13	BTS12 / 14	BTS12 / 15	BTS12 / 16
Na_2O	2,9595	3,2161	2,7794	2,949	2,9592	3,0927	2,4223	2,8791	2,9968	2,4588	2,6868	3,1005	3,1139	3,2333	3,0466	1,7819
SiO_2	74,2623	75,3436	72,3871	75,2148	76,0565	75,8156	69,4914	74,9882	76,2163	70,4214	75,241	74,6326	75,3382	75,0356	75,4749	76,1617
K_2O	5,0745	5,3158	4,6541	5,3028	5,1146	5,3089	5,059	5,2582	5,0141	4,8423	5,1748	5,121	4,8928	5,2517	5,2511	4,9203
CaO	0,8391	0,5805	0,6765	0,8122	0,7999	0,8523	0,6154	0,76	0,6441	0,797	0,8019	0,8016	0,8165	0,7927	0,8044	0,8157
TiO_2	0,0048	0,0356	0,0045	0,0407	0,0347	0,0559	0,0909	0,0199	0,0417	0,028	0,0314	0,0563	0,0322	0,0382	0,0488	0,0229
FeO	0,9987	0,4278	1,0449	0,7689	0,9779	0,7693	0,5211	0,782	0,6112	0,8234	0,7603	1,0141	0,7984	0,8919	0,8982	0,8322
Al_2O_3	12,1404	11,4307	12,007	11,8903	12,0753	11,8002	10,9588	12,1163	11,7835	11,4521	11,5864	11,9568	12,2165	12,0503	11,6542	11,9664
MgO	0,0163	0,0163	0,0033	0,0783	0,144	0,0098	0,1042	0,0229	0,0359	0,1172	0,0587	0,0164	0,0653	0,1175	0,0065	0,0486
P_2O_5	0,0038	0,0017	-0,004	0,0124	0,0242	-0,0009	0,0149	0,0131	0,0087	0,0033	0,0034	0,0188	0,0083	0,0094	0,0009	0,0034
BaO	0,0971	-0,0216	0,043	0,0466	0,1186	0,0433	-0,0216	0,1514	0,0753	-0,1294	-0,0648	0,0216	-0,0215	0,0539	0,1402	-0,108
Ce_2O_3	0,0035	0,0287	0,0814	-0,0916	0,0569	0,0071	-0,0641	0,0882	0,0615	-0,0298	0,0051	0,0251	0,049	-0,0404	0,0719	-0,0597
Cr_2O_3	0,023	0,0096	0,0232	-0,0024	0,0113	-0,0356	0,012	0,0047	-0,0027	-0,057	-0,0365	-0,0098	-0,0115	0,001	0,0524	0,0083
MnO	0,107	0,0772	0,052	0,1056	0,03	0,0976	0,0619	0,0167	0,1604	0,1236	0,0755	0,096	0,089	0,0575	-0,0157	0,0155
SrO	0,0066	-0,0183	-0,0459	-0,0411	-0,0538	-0,046	-0,0144	-0,0132	-0,0131	-0,0197	-0,0026	-0,0223	-0,0563	-0,0236	-0,0249	-0,0406
Rb_2O	-0,9352	-0,9454	-0,9365	-0,9103	-0,9485	-0,9073	-0,8932	-0,9286	-0,9279	-0,9486	-0,935	-0,9504	-0,9831	-0,9421	-0,8995	-0,9112
Total	96,5366	96,4836	93,7563	97,2216	98,403	97,8526	89,3518	97,1007	97,6494	91,0673	96,4253	96,8608	97,42	97,533	97,4501	96,5768

Element	KgL2 / 1	KgL2 / 2	KgL2 / 3	KgL2 / 4	KgL2 / 5	KgL2 / 6	KgL2 / 7	KgL2 / 8	KgL2 / 9	KgL2 / 10	KgL2 / 11	KgL2 / 12	KgL2 / 13	KgL2 / 14	KgL2 / 15
Na_2O	3,0144	-0,011	3,106	2,9365	2,9455	2,8436	2,8787	3,2091	0,0172	3,0905	1,7883	2,4937	2,076	2,8114	3,3323
SiO_2	74,6995	104,3165	74,8619	73,8986	74,0989	74,6158	72,0656	75,8888	104,0855	75,4812	75,2938	69,0309	74,8564	75,456	74,3874
K_2O	4,964	-0,0316	4,8395	5,2984	5,3508	5,0862	4,8845	5,1458	-0,0083	4,9594	5,1649	4,5173	5,2206	5,5016	5,0396
CaO	0,6839	-0,0394	0,7178	0,7846	0,7975	0,6294	0,7234	0,7639	-0,0045	0,7736	0,7214	0,7244	0,7355	0,7466	0,6565
TiO_2	0,0304	0,0194	0,0765	0,0912	0,0933	0,115	0,0729	0,0475	0,007	0,0783	0,0615	0,0522	0,0551	0,0551	0,0647
FeO	0,7865	0,0511	0,9111	0,667	0,8879	0,9837	0,7308	0,7083	0,0642	0,7474	0,8966	1,0211	0,6974	0,6714	0,7002
Al_2O_3	12,1543	0,0201	12,1311	12,0602	12,2283	11,8781	11,1822	12,1527	0,0779	11,6764	11,8135	12,1312	12,1045	12,0688	12,1373
MgO	0,0751	0,0096	0,1079	0,0293	0,1337	0,0195	0,0619	0,0815	0,0159	0,0913	0,0419	0,0358	0,0712	0,078	0,0457
P_2O_5	0,0046	0,0066	0,0083	0,0017	0,006	-0,0009	0,0005	-0,0107	0,017	0,0039	-0,0047	0,0702	0,0179	-0,0038	-0,0162
BaO	0,1181	-0,0216	-0,129	0,0645	-0,0115	0,043	0,1075	-0,0323	-0,0757	0,0107	-0,0116	0,0232	0,1516	-0,0108	-0,2093
Ce_2O_3	0,1314	-0,0639	-0,1002	-0,0047	0,0325	0,0047	0,0023	0,0878	-0,0631	-0,0246	0,0474	-0,0494	0,02	-0,0262	-0,0025
Cr_2O_3	-0,0302	0,0099	-0,002	0,0144	0,006	-0,0017	-0,002	-0,021	-0,0074	0,0141	-0,0066	0,0037	0,0244	0,0064	-0,024
MnO	0,0766	-0,0288	0,0231	0,0252	0,107	0,0926	0,0045	0,0727	0,0307	0,0407	0,133	0,0838	0,1164	0,1002	0,0625
SrO	-0,0628	-0,0646	-0,0105	-0,0222	-0,0293	-0,0497	-0,017	-0,0236	-0,0074	-0,0587	-0,0818	0,0057	-0,0552	-0,0131	-0,0681
Rb_2O	-0,9364	-0,9132	-0,9155	-0,9805	-0,9419	-0,9112	-0,9248	-0,9263	-0,8873	-0,9513	-0,9508	-0,9384	-0,9487	-0,9405	-0,9186
Total	96,739	104,4332	96,7832	95,8715	96,6874	96,3117	92,7148	98,1581	104,3152	96,9676	95,9622	90,1932	96,147	97,4955	96,4263

Element	KgL2-12 / 1	KgL2-12 / 2	KgL2-12 / 3	KgL2-12 / 4	KgL2-12 / 5	KgL2-12 / 6	KgL2-12 / 7	KgL2-12 / 8	KgL2-12 / 9	KgL2-12 / 10	KgL2-12 / 11	KgL2-12 / 12	KgL2-12 / 13	KgL2-12 / 14	KgL2-12 / 15	KgL2-12 / 16	KgL2-12 / 17
Na_2O	0,0266	3,1274	2,8511	3,3396	-0,0272	-0,0185	3,1477	3,0638	3,0034	3,157	7,1821	3,3342	6,9711	3,1283	3,1687	3,0217	6,1919
SiO_2	102,9873	74,4323	66,7799	75,4967	102,0633	103,1073	74	75,7082	75,2231	74,4551	61,581	75,0114	61,2343	74,4908	74,5508	72,8272	57,9962
K_2O	-0,0211	4,963	12,8291	4,996	0,0108	-0,0088	5,1552	5,0735	4,9625	4,8804	0,8185	5,108	0,8093	5,0976	5,0139	5,0643	0,6171
CaO	0,0407	0,7941	0,1994	0,6475	0,004	-0,0133	0,7736	0,6973	0,7871	0,6637	6,4462	0,6846	7,3245	0,7863	0,8125	0,8479	8,7435
TiO_2	0,0118	0,0508	-0,034	0,037	-0,0054	-0,0076	0,0644	-0,0012	-0,0148	0,0488	-0,0036	0,0331	0,0006	0,0473	0,0783	0,018	0,012
FeO	-0,054	1,0592	0,1628	0,594	-0,1225	0,0496	0,8378	0,8464	1,0042	0,8845	0,2512	1,072	-0,0101	0,7091	0,9278	0,7192	0,1877
Al_2O_3	0,1608	12,1016	18,7351	11,9364	0,0427	0,0276	11,6977	11,5015	11,8581	11,7271	25,1319	11,9339	25,2803	12,0512	11,6975	11,7797	26,1199
MgO	0,0032	0,0784	-0,0227	0,0749	0,0478	-0,0064	0,0588	0,0555	0,0457	0,062	-0,0133	0,0688	0,01	0,0719	0,0884	0,0748	0,0233
P_2O_5	-0,0219	0,0132	0,0033	0,0144	0,0146	0,0119	0,0136	0,0102	0,0171	0,0108	-0,0124	-0,0006	0,0173	-0,0024	0,0044	0,0014	0,0155
BaO	0	-0,043	0,3014	0,0537	-0,0324	-0,0117	0,0323	-0,0431	0,043	0	-0,0465	0,043	0,0323	0,2475	0,1931	-0,0117	0,1184
Ce_2O_3	-0,002	-0,0739	0,0278	-0,0697	0,0386	0,0718	0,0518	-0,0185	0	0,0078	-0,0754	-0,0685	0,0352	-0,0313	-0,0187	-0,0493	0,0411
Cr_2O_3	0,0007	0,0066	0,063	-0,0051	-0,0271	-0,0305	-0,0345	-0,0115	-0,0098	0,0056	-0,0132	-0,0012	-0,0007	0,0452	-0,0056	-0,049	-0,0171
MnO	-0,0241	0,145	-0,0059	0,0981	0,0246	0,004	0,0323	0,0638	0,0595	0,075	-0,0252	0,0452	-0,0241	0,096	0,0752	0,0377	0,0344
SrO	0,0199	-0,0564	-0,012	0,0562	-0,0124	-0,0135	-0,0603	-0,0262	0,0196	-0,0353	0,063	-0,0406	0,0028	-0,042	-0,0026	-0,0384	0,0334
Rb_2O	-0,8999	-0,91	-0,9445	-0,928	-0,8922	-0,8669	-0,9128	-0,9005	-0,945	-0,8976	-1,015	-0,9304	-1,0495	-0,9623	-0,9268	-0,9738	-1,0464
Total	103,251	96,7716	101,9527	97,2883	102,2463	103,2722	95,8652	97,0202	97,0234	95,9779	101,4739	97,3343	101,7177	96,7712	96,6104	94,392	100,1343

Element	KgL3 / 1	KgL3 / 2	KgL3 / 3	KgL3 / 4	KgL3 / 5	KgL3 / 6	KgL3 / 7	KgL3 / 8	KgL3 / 9	KgL3 / 10	KgL3 / 11	KgL3 / 12	KgL3 / 13	KgL3 / 14	KgL3 / 15
Na_2O	3,0931	3,1816	2,8463	2,8745	3,334	2,8049	2,9772	2,9264	6,9281	3,1077	6,2449	3,1626	2,869	3,1981	3,1366
SiO_2	74,3512	75,3082	74,0219	74,1072	74,9952	71,0294	74,3738	73,0762	60,6906	73,9671	58,3207	74,4527	73,99	74,2981	74,9078
K_2O	4,9559	5,1427	5,0404	5,2382	4,8904	4,8178	5,1453	4,9418	0,7933	4,9282	0,527	5,2088	5,5485	5,0254	5,0376
CaO	0,8559	0,8664	0,6097	0,8577	0,6677	0,6377	0,7441	0,6835	7,2002	0,828	8,5492	0,8178	0,8537	0,8269	0,8474
TiO_2	-0,0024	0,0172	0,0638	0,0395	0,0755	0,0574	0,1016	0,0698	-0,0192	0,0428	-0,0042	0,0704	0,0469	0,0274	0,0992
FeO	0,6088	0,6354	0,8899	0,9427	0,8337	0,8732	0,7492	1,0518	0,1458	0,763	-0,1227	1,0545	0,8729	0,6221	0,8703
Al_2O_3	11,7288	11,7221	11,6995	11,9541	11,8165	11,5387	11,7475	12,0421	25,1787	11,9132	26,6745	12,1533	11,7718	11,8896	11,8579
MgO	0,0359	0,0065	0,0685	0,0785	0,0327	0,0685	0,0522	0,0914	-0,0133	0,1012	0,0597	0,0523	0,1173	0,0815	0,0359
P_2O_5	0,0064	0,0028	0,0307	-0,0044	-0,0185	0,0135	0,0182	0,0211	0,0153	-0,0062	0,0112	-0,0078	0,0029	0,0142	-0,0024
BaO	-0,0215	0,2045	-0,07	-0,0968	0,1176	0,0862	0,0538	-0,0431	-0,0108	0,1076	0,0815	-0,1397	0,1292	0,0699	0,1513
Ce_2O_3	0,0059	-0,0662	0,0319	0,0458	0,0249	-0,1048	-0,0302	-0,0059	-0,0259	0,0263	0,0191	-0,0246	0,0506	-0,0085	0,0072
Cr_2O_3	-0,0452	-0,0907	-0,0223	0,0708	-0,0515	-0,0113	0,0039	0,0081	-0,0024	0,0284	-0,0515	-0,0063	0,0005	-0,0161	0,0391
MnO	0,0553	0,0097	0,0766	0,0278	0,054	0,0298	0,0498	0,0974	0,0097	0,0391	-0,0081	0,0588	0,057	-0,0068	0,0619
SrO	-0,0432	-0,0196	-0,0426	-0,0183	-0,013	-0,0013	-0,0301	-0,0407	0,0278	-0,0026	0,0557	0,0524	-0,0419	-0,0142	-0,0553
Rb_2O	-0,9566	-0,9341	-0,9614	-0,921	-0,905	-0,8965	-0,9478	-0,9464	-1,0401	-0,9408	-1,0609	-0,9277	-0,9323	-0,9054	-0,9054
Total	95,6972	97,097	95,379	96,2367	96,8422	91,9571	96,0167	95,0096	100,9894	95,8524	100,5434	97,0837	96,3103	96,053	97,0522

Element	JWP3-11/1	JWP3-11/2	JWP3-11/3	JWP3-11/4	JWP3-11/5	JWP3-11/6	JWP3-11/7	JWP3-11/8	JWP3-11/9	JWP3-11/10	JWP3-11/11	JWP3-11/12	JWP3-11/13	JWP3-11/14	JWP3-11/15
Na_2O	3.1450	2.9693	3.5437	2.9948	3.1774	3.1481	3.2042	3.0844	3.1765	3.0695	3.5776	3.3210	3.4282	3.3097	3.3100
SiO_2	74.3881	68.6847	76.1958	73.7225	72.8102	74.7037	74.6102	74.3000	75.0125	73.9902	75.2083	75.5354	74.9034	73.6822	75.8691
K_2O	5.0654	4.3871	4.8344	4.9081	4.4234	4.8722	5.1489	5.1581	5.0309	4.9899	4.9717	5.0110	5.1358	4.6917	4.8903
CaO	0.6567	0.6618	0.6873	0.6205	0.7217	0.7389	0.7638	0.8152	0.5726	0.8194	0.6741	0.6391	0.7452	0.6412	0.6645
TiO_2	0.0614	0.0202	0.0475	0.0536	0.0409	0.0710	0.0652	0.0445	0.0078	0.0755	0.0523	0.0334	0.0637	0.0628	0.0430
FeO	1.0176	0.6867	1.0889	0.7510	1.0932	0.6727	1.0224	0.8049	0.9537	0.7349	0.8898	0.6671	1.0182	0.4273	0.7971
Al_2O_3	12.0689	10.4998	12.1337	11.6378	11.4742	11.6355	11.9931	11.9119	11.8631	11.8112	12.3454	11.7023	11.6585	11.6587	11.8368
MgO	0.0654	0.0686	0.0688	-0.0065	0.0687	0.0425	0.0720	0.0195	0.0620	-0.0228	0.0393	0.0750	0.0491	0.0650	0.0588
P_2O_5	0.0172	0.0066	-0.0048	-0.0069	0.0082	0.0100	-0.0107	-0.0083	-0.0092	0.0156	0.0135	0.0160	0.0070	0.0129	0.0119
BaO	-0.0801	0.0466	0.0645	0.0580	-0.0967	0.2084	0.1166	0.0466	-0.0348	-0.0700	0.1719	0.0465	-0.0696	-0.0108	0.0116
Ce_2O_3	-0.0108	0.0365	0.0231	0.0008	-0.0454	0.0936	-0.1023	0.0267	0.0207	0.0909	0.0313	-0.0381	0.0232	0.0035	-0.0466
Cr_2O_3	-0.0605	0.0204	-0.0098	0.0595	-0.0200	0.0187	0.0037	-0.0132	0.0174	-0.0061	0.0249	-0.0074	0.0029	-0.0142	0.0587
MnO	0.0990	0.0495	0.0906	0.0471	0.0999	0.1283	0.0475	-0.0168	0.0496	0.0501	0.1040	0.0616	0.0639	0.1160	0.1430
SrO	-0.0223	-0.0454	-0.0511	-0.0663	-0.0210	-0.0338	-0.0469	0.0284	-0.0480	-0.0596	-0.0079	-0.0821	-0.0325	-0.0196	-0.0340
Rb_2O	-0.9347	-0.9401	-0.9277	-0.8919	-0.9221	-0.9331	-0.9101	-0.9449	-0.9289	-0.9470	-0.9308	-0.9464	-0.9062	-0.9381	-0.9395
Total	96.5847	88.1378	98.7783	94.8536	93.9178	96.3435	97.0475	96.2403	96.7667	95.6471	98.1041	97.1084	97.0989	94.6709	97.6948

Element	BR6/1	BR6/2	BR6/3	BR6/4	BR6/5	BR6/6	BR6/7	BR6/8	BR6/9	BR6/10	BR6/11	BR6/12	BR6/13	BR6/14	BR6/15
Na_2O	3.3748	3.4115	6.9127	3.2768	3.1516	3.0402	3.1513	2.5310	3.1368	1.9732	3.3450	3.0170	3.0219	3.0630	2.1424
SiO_2	74.3727	74.2062	60.7375	72.4466	74.2833	74.5214	73.7132	62.1390	72.7587	52.3446	74.8098	74.3737	73.6881	75.7562	61.2427
K_2O	4.6454	4.8378	0.7039	4.9141	4.9452	5.2556	4.9905	3.8022	4.6227	2.9128	5.0076	5.3659	4.6613	5.0367	4.6938
CaO	0.7538	0.5794	7.5325	0.5835	0.8211	0.7166	0.7624	0.6922	0.9163	0.5367	0.7799	0.8175	0.9492	0.8036	0.7034
TiO_2	0.0099	0.0683	0.0096	0.0078	0.0180	0.0193	0.0539	0.0713	0.0852	0.0795	0.0487	0.0933	0.0830	0.0780	0.0500
FeO	1.0201	0.5385	0.2868	1.0443	0.9611	0.5657	0.8177	0.7826	1.0281	0.8871	0.8880	0.7638	1.0704	0.6012	0.6263
Al_2O_3	12.2077	11.7077	25.0997	11.6118	11.4961	11.5573	11.4352	10.1710	11.6178	8.9002	11.9765	11.6560	11.5193	11.9377	9.4809
MgO	0.0327	0.0327	-0.0100	0.0327	0.0653	0.0456	0.1273	0.1370	0.0885	0.1925	0.0196	0.0750	0.1047	0.0424	0.0423
P_2O_5	0.0066	0.0096	0.0094	-0.0059	0.0048	-0.0076	0.0016	0.0167	0.0081	0.0350	0.0271	0.0105	0.0264	-0.0008	0.0182
BaO	0.1612	-0.1291	-0.0350	-0.0322	-0.0233	0.0234	0.0645	0.0816	0.1750	0.1858	0.0752	-0.0215	0.2441	0.0862	-0.0108
Ce_2O_3	0.0313	0.0493	-0.0675	-0.0372	0.0671	-0.0396	0.0082	0.0008	-0.0140	-0.0169	-0.0434	-0.0905	0.0453	-0.0322	-0.0082
Cr_2O_3	0.0256	-0.0340	0.0357	0.0354	-0.0172	-0.0082	0.0110	-0.0214	-0.0228	0.0314	0.0591	0.0320	-0.0066	0.0497	0.0027
MnO	0.0452	0.0813	0.0284	0.1018	-0.0335	0.0446	0.0112	0.0747	0.0892	0.0845	0.0231	0.0459	0.0494	0.0703	0.1003
SrO	-0.0144	-0.0039	0.0480	-0.0446	0.0128	-0.0326	0.0222	0.0298	0.0128	-0.0028	-0.0511	-0.0288	-0.0057	0.0026	-0.0183
Rb_2O	-0.9166	-0.9265	-10.205	-0.9097	-0.8853	-0.9656	-0.8849	-0.9872	-0.9254	-0.9757	-0.9305	-0.9179	-0.9578	-0.9072	-0.9279
Total	96.6872	95.5224	101.4042	94.0549	95.8265	95.7897	95.1703	80.5300	94.5392	68.1633	97.0596	96.2505	95.4630	97.5278	79.1030

Element	MRB3 / 1	MRB3 / 2	MRB3 / 3	MRB3 / 4	MRB3 / 5	MRB3 / 6	MRB3 / 7	MRB3 / 8	MRB3 / 9	MRB3 / 10	MRB3 / 11	MRB3 / 12	MRB3 / 13	MRB3 / 14	MRB3 / 15
Na_2O	3.2996	3.3163	2.9769	3.0157	3.2322	3.4709	3.0315	3.1725	2.9065	3.0956	3.1599	3.0808	3.1753	3.0326	3.3241
SiO_2	74.6966	73.8381	73.0840	75.1957	72.4957	74.2346	74.8945	73.7287	70.6581	74.8748	73.9969	74.5918	71.8785	73.2037	73.8389
K_2O	4.9556	5.0502	4.9905	5.0520	4.7596	4.5201	5.1032	5.0207	4.3616	5.0758	5.0005	5.2891	5.0497	5.1408	5.1875
CaO	0.8490	0.8205	0.8674	0.7876	0.7235	0.6595	0.7335	0.7394	0.7560	0.7550	0.6668	0.7473	0.7333	0.8318	0.6586
TiO_2	0.0359	0.0365	0.0652	0.0159	0.0240	0.0713	0.0547	0.0879	0.0581	0.0537	0.0315	0.0632	0.0451	0.0096	0.0229
FeO	0.8840	0.6319	0.9414	0.8081	1.0666	0.6775	0.9178	0.6298	0.7891	0.7985	0.9853	0.7379	0.9694	0.8773	1.0348
Al_2O_3	12.3120	11.8440	11.8997	11.8994	11.4962	11.7453	11.5755	11.7696	11.1126	11.8871	11.9393	11.8108	11.5647	11.8319	11.6088
MgO	0.0982	0.0588	0.0982	0.0684	0.0720	0.0621	0.0587	0.0848	0.0751	0.0425	0.0163	0.0750	0.0980	0.0588	0.0164
P_2O_5	0.0146	0.0187	0.0115	-0.0116	0.0116	0.0055	0.0060	0.0004	-0.0010	0.0309	0.0024	0.0088	-0.0032	0.0014	0.0053
BaO	-0.0431	0.0108	0.1399	-0.1183	0.1075	0.0323	0.0647	-0.0323	0.0933	0.0323	-0.0215	-0.0108	-0.0215	0.1516	-0.0108
Ce_2O_3	-0.0518	0.0307	0.0157	0.0188	0.0266	0.0557	0.0730	-0.0137	-0.0335	-0.0454	-0.0498	0.0208	0.0204	0.0883	0.1032
Cr_2O_3	-0.0113	0.0047	-0.0011	0.0037	0.0015	0.0017	-0.0225	0.0073	-0.0249	0.0193	-0.0335	-0.0142	-0.0697	0.0026	0.0076
MnO	0.0327	0.0232	0.0178	0.0620	0.0499	0.0003	0.0431	0.0885	0.0655	0.0027	0.1090	0.0611	-0.0320	0.0673	0.1043
SrO	-0.0013	-0.0671	-0.0355	-0.0366	-0.0288	-0.0262	0.0275	-0.0445	-0.0199	-0.0235	-0.0158	-0.0406	-0.0735	-0.0085	-0.0433
Rb_2O	-0.9188	-0.8456	-0.9233	-0.9310	-0.9237	-0.8722	-0.9333	-0.9206	-0.9337	-0.9432	-0.9336	-0.9374	-0.9671	-0.9500	-0.9488
Total	97.1782	95.6844	95.1082	96.9273	94.0670	95.5368	96.5837	95.3296	90.8759	96.6681	95.9079	96.4866	93.5344	95.2977	95.9124

Element	Tejpur/1	Tejpur/2	Tejpur/3	Tejpur/4	Tejpur/5	Tejpur/6	Tejpur/7	Tejpur/8	Tejpur/9	Tejpur/10	Tejpur/11	Tejpur/12	Tejpur/13	Tejpur/14	Tejpur/15
Na_2O	2.9947	3.0949	4.2822	3.0656	2.9962	2.9983	3.0643	3.1139	2.9601	4.1942	3.3020	2.9263	0.1480	3.0565	3.0222
SiO_2	73.6086	74.3868	52.6870	72.7517	75.2743	74.8031	74.7646	74.4110	74.3810	53.0995	74.6737	73.0041	99.7105	74.4392	74.2693
K_2O	5.1567	5.2501	0.2471	5.1116	5.3122	5.0815	5.1837	4.8738	5.1184	0.3409	5.2204	5.1674	0.0641	4.9115	4.9840
CaO	0.8243	0.6614	12.4008	0.7446	0.6899	0.6766	0.7837	0.7811	0.7587	12.6787	0.6202	0.9179	0.0517	0.8189	0.7586
TiO_2	0.0700	0.0505	0.1020	0.0505	0.0132	0.0869	0.0427	0.0265	0.0442	0.1373	0.0861	0.0382	-0.0048	0.0274	0.0343
FeO	0.9668	1.0140	0.6035	1.1301	0.9043	1.0467	0.9441	0.5636	1.0394	0.1931	0.9204	1.0315	0.0306	0.6320	1.0120
Al_2O_3	11.9954	11.8608	27.8533	11.6943	11.9445	11.2407	11.7105	11.5915	11.7420	28.8183	11.8637	11.6604	0.5550	11.5954	11.6812
MgO	0.0686	0.0033	0.0760	0.0556	0.0784	0.0261	0.0816	0.0586	0.0652	0.1908	0.0065	0.0622	0.0541	0.0587	0.0425
P_2O_5	0.0061	0.0042	0.0081	0.0078	0.0134	-0.0131	-0.0033	0.0048	0.0089	0.0049	0.0101	0.0084	-0.0132	0.0136	0.0075
BaO	0.1280	0.0645	0.0816	0.0467	0.1395	0.0931	-0.1167	0.0754	0.0000	0.0539	0.0116	0.2449	0.0433	0.1723	0.0858
Ce_2O_3	0.0953	-0.0665	-0.0899	-0.0981	-0.0980	-0.0127	0.0204	0.0263	-0.0184	0.0380	-0.0428	0.0416	-0.0560	-0.0341	0.0207
Cr_2O_3	-0.0201	-0.0278	0.0259	0.0077	0.0012	-0.0700	-0.0026	0.0271	0.0154	0.0396	-0.0135	0.0220	0.0000	0.0022	0.0054
MnO	0.0222	0.1070	0.0061	0.0860	0.0859	0.0056	0.0745	0.0666	-0.0340	-0.0153	0.0667	0.0769	-0.0120	0.0545	0.0719
SrO	0.0057	-0.0249	-0.0091	0.0028	-0.0366	-0.0622	-0.0738	-0.0484	-0.0445	0.0601	-0.0638	0.0227	-0.0423	-0.0039	-0.0091
Rb_2O	-0.9488	-0.9175	-10.533	-0.9193	-0.9529	-0.9354	-0.9615	-0.9194	-0.9166	-10.555	-0.8959	-0.9610	-0.9210	-0.9568	-0.9174
Total	95.9424	96.4975	98.3737	94.7552	97.4531	96.0586	96.6701	95.6201	96.1333	99.8494	96.7814	95.2245	100.6572	95.7822	95.9953